Photon counting in the microwave domain and its applications to superconducting qubit readout

Dissertation

zur Erlangung des Grades

des Doktors der Naturwissenschaften

der Naturwissenschaftlich-Technischen Fakultät

der Universität des Saarlandes

von

Andrii Sokolov

Saarbrücken

2023

Tag des Kolloquiums:	18. Dezember 2023
Dekan:	Prof. Dr. Ludger Santen
Berichterstatter:	Prof. Dr. Frank Wilhelm-Mauch
	Prof. Dr. Gernot Alber
	Prof. Dr. Giovanna Morigi
Vorsitz:	Prof. Dr. Prof. Christoph Becker
Akad. Mitarbeiter:	Dr. Philipp Hövel

"No one knows the reason for all this, but it is probably quantum."

Terry Pratchett, *Pyramids*

"This is all good, but what is actually quantum here?"

Leonid Yatsenko, a good question in the annual conference of the Institute of Physics in Kyiv

Abstract

This thesis theoretically explores new schemes in microwave photon detection and superconducting qubit readout. We review the commonly used dispersive readout with a homodyne detection and describe the quantization of the system. The use of photodetectors for the readout may simplify its scaling. We introduce two such schemes. In the first one, coherent radiation is used as a probe which is measured by a photon-number-resolving detector. In the second one, the probe is in a single-photon Fock state. A detector that is only able to distinguish between the presence and absence of photons is used. We also provide a simple formula for the measurement-induced qubit decoherence given that the resonator is occupied by coherent and thermal photons. We use Langevin equations in our treatment of the dispersive readout, which allows one to have a self-containing theory of the system. Finally, we consider a microwave photodetector that is able to count photons up to two by using two-photon transition.

Zusammenfassung

Diese Dissertation untersucht theoretisch neue Schemata zur Detektion von Mikrowellen-Photonen und zur Messung von supraleitenden Qubits. Wir diskutieren die häufig verwendete dispersive Messung von supraleitenden Qubits mittels homodyner Detektion und beschreiben die Quantisierung des Systems. Die Verwendung von Fotodetektoren kann die Skalierung der Messung vereinfachen. Wir stellen zwei solcher Schemata vor. Im ersten Fall wird für das Testsignal kohärente Strahlung verwendet, die mit einem Photonenzahl-auflösenden Detektor gemessen wird. Im zweiten Fall befindet sich das Testsignal in einem Einzelphotonen-Fock-Zustand. Es wird ein Detektor verwendet, der lediglich zwischen der Anwesenheit und Abwesenheit von Photonen unterscheiden kann. Wir stellen auch eine einfache Formel der messinduzierten Qubit-Dekohärenz vorausgesetzt, der Resonator ist mit thermischen und kohärenten Photonen besetzt. Wir verwenden Langevin-Gleichungen in unserer Untersuchung der dispersiven Messung, was es ermöglicht, eine selbst enthaltende Theorie des Systems zu entwickeln. Abschließend betrachten wir einen Mikrowellen-Fotodetektor, der bis zu zwei Photonen durch Zwei-Photonen-Absorption zählen kann.

Publication List

- A. Sokolov
  Optimal conditions for high-fidelity dispersive readout of a qubit with a photon-number-resolving detector
  Phys. Rev. A 93, 032323 (2016)

- A. M. Sokolov and E. V. Stolyarov
  Single-photon limit of dispersive readout of a qubit with a photodetector
  Phys. Rev. A 101, 042306 (2020)

- A. M. Sokolov and F. K. Wilhelm
  Superconducting detector that counts microwave photons up to two
  Phys. Rev. Appl. 14.6, 064063 (2020)

Acknowledgments

First of all, I would like to thank my supervisor, Prof. Frank Wilhelm-Mauch, with whom I got the pleasure to work. He was very supportive even in highly complicated circumstances, including not only physics. His knowledge of the field and literature and his physical intuition were indispensable. Secondly, I would like to thank my Ukrainian supervisor, Oleksandr Chumak. While I wasn't able to finish my PhD study in Kyiv, he still was able to teach me a lot about organizing my work, writing style, and of course some physics—most importantly, the Langevin equation formalism.

I also need to thank Andrii Semenov, who suggested that I should apply for the DAAD scholarship. This resulted—contrary to our initial plans!—in my visit to Saarbrücken and then, in my enrollment as a PhD student there. Here I thank Olya and her parents for taking care of my son during my stays in Germany. I thank my father, who supported my family in the hard times before I got a job in Saarbrücken.

Next, I would like to thank all my colleagues from the Frank's group, and especially some of them. I thank Raphael Schmit, with whom we had a lot of fun teaching theoretical mechanics and statistical physics. I would like to acknowledge pleasant breaks we had with Raphael, Susanna Kirchhoff, Federico Roy, Peter Schuhmacher, and with other my office roommates. Also I thank Annette Messinger and Elie Assémat, with whom we had great time bouldering in the Dudweiler climbing hall during my DAAD stay in 2016.

I thank Eugene Stolyarov, who worked on the single-photon readout with me and had enough patience to finish this work. I thank the people who read the manuscript and provided feedback: Peter Schuhmacher, Raphael Schmit, Eugene Stolyarov, Federico Roy, and Susanna Kirchhoff. I am indebted to Oleksandr Chumak who has found a missing factor in my early comparisons of the qubit decoherence rate with the literature.

Also, I thank Prof. Tero Heikkilä, who kindly allowed me to spend quite some time tackling my thesis while I was employed to work on projects with him. Then, I should thank Ksjusha for her constant everyday support in the last years of finishing my thesis. Finally, I probably won't be able to finish it, if not the Ukrainian Armed Forces deterring the full-scale Russian invasion. Of those who currently fights, special thanks to Volodymyr Demyanovych, with whom we hiked a lot in the better times, and Bohdan Lepyavko and Danylo Butenko, with whom we started our PhD journey in physics back in 2011.

Contents

List of Figures

To Orest

Chapter I

Introduction

Quantum technologies are rapidly developing nowadays. In fact, the pace and the character of the developments are extraordinary enough for the situation to be called the "second quantum revolution". The "first quantum revolution" happened when the laws of quantum mechanics were used to build devices such as lasers, transistors, or Magnetic Resonance Imaging (MRI) machines. While quantum mechanics is needed to design these devices, their function can be described by the classical physics. A laser emits light that mostly behaves as classical (yet highly coherent) radiation, a transistor operates on classical currents, and an MRI machine provides an image of classical tissues using classical radiation as a probe. In contrast, in the second quantum revolution, the devices are built that need to manipulate quantum objects. A quantum computer operates on complex superposition states to perform a calculation. In quantum cryptography, quantum states of light or matter are used to prevent eavesdropping. Non-classical states of a probe are used in quantum sensing, which allows one to gain superior resolution.

One much simpler example of a device that detects and manipulates quantum states of light is a single-photon detector. That is a device which is able to detect a tiniest possible portion of electromagnetic energy in some mode, a single photon. We introduce one type of single-photon detectors, the Josephson photomultiplier (JPM), in Sec. 5. In Ch. VIII, we present our original results concerning a JPM that is able to count up to two photons. Our JPM can operate in the range from 1 to 20 GHz; the JPMs demonstrated so far detect photons around 4.8 GHz [1] and from 4.4 to 5.9 GHz [2]. The state of radiation in these ranges is typically detected by measuring its phase and amplitude; a photodetector, however, measures the radiation intensity. We mention some possible uses for a photodetector in Ch. VIII.

One application of the detectors is worth mentioning here: it is the dispersive readout of a superconducting qubit. A qubit (QUantum BIT) is an elementary piece of quantum information. Unlike the classical bit, which adopts values of either "0" or "1", a qubit can be in a superposition of two states $|\downarrow\rangle$ and $|\uparrow\rangle$ (in this thesis, we adopt physical labeling for the states of the qubit). Besides, multiple qubits can be in an entangled state. Quantum systems are needed to implement multiple qubits. One promising implementation is a superconducting qubit, which is briefly introduced in Sec. 1.3. The readout of a qubit is the process of quantum measurement which collapses the superposition state of the qubit and determines which state—$|\downarrow\rangle$ or $|\uparrow\rangle$—it occupies after the collapse. In the dispersive readout, radiation is used as a probe; typically, to infer the state of the qubit, the phase shift of the probe radiation is determined with a homodyne detection. This type of readout is briefly introduced in Sec. 3.1 and its theory is given in Ch. III. Alternatively, one can use a photodetector to gain information on the photon number in the probe. Two original schemes that use photodetectors are discussed in Chs. IV and Ch. VII. A distinctive feature of our

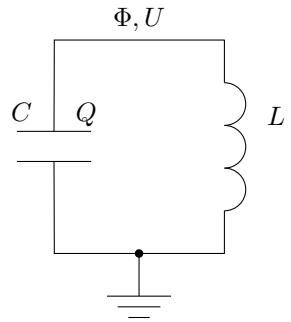

FIGURE 1.1: LC circuit

theoretical description of these schemes is the use of Langevin equations (see Sec. 6.1 for a brief introduction).

In the course of quantum measurement, a superposition state collapses turning into a mere statistical mixture. This is is due to the decoherence of a system. We study the measurement-induced decoherence in the dispersive readout and its dependence on the temperature in Ch. V.

In the following subsections, we provide some broader background for the rest of the thesis, and introduce the concepts and techniques that we use throughout it. While doing that we further refer to the relevant parts of the thesis.

1 Superconducting quantum circuits

In a superconducting state, conducting electrons form Cooper pairs in a collective state called a condensate. A condensate can be described by a wavefunction similar to a single-particle wavefunction. The condensate wavefunction is highly coherent in time and space, which leads to various macroscopic quantum effects—including the Josephson effect important for us. Besides, this coherence means one can quantize the degrees of freedom of an electric circuit.

1.1 Quantization of the LC circuit

Here we review the quantization procedure of an electric circuit on a basic example of the LC circuit (see Fig. 1.1).

First we need to write out the Hamiltonian of the classical system. It is convenient to use the node flux [3]

$$\Phi(t) = \int_{-\infty}^{t} dt' U(t') \tag{1.1}$$

as the generalized coordinate of the system. Here U denotes a voltage drop on some branch of the circuit and $\Phi(-\infty) = 0$. The Lagrangian of the circuit is equal to the difference of its kinetic and potential energies. For our choice of coordinate, the Lagrangian of the LC circuit reads

$$\mathcal{L} = \frac{C\dot{\Phi}^2}{2} - \frac{\Phi^2}{2L}. \tag{1.2}$$

Node flux Φ and the respective voltage U are depicted in Fig. 1.1. The generalized momentum of the circuit is

$$Q = \frac{\partial \mathcal{L}}{\partial \dot{\Phi}} = C\dot{\Phi} \tag{1.3}$$

the charge of the upper plane of the capacitance C. Legendre transform yields the Hamiltonian:

$$H = Q\dot{\Phi} - \mathcal{L} = \frac{Q^2}{2C} + \frac{\Phi^2}{2L}. \tag{1.4}$$

We could have guessed the Hamiltonian for the LC circuit right away. However, for more complex circuits it is hard to do that. It is always safe to start from the Lagrangian.

Now we quantize the system. The conjugate variables Φ and Q are promoted to operators with the commutator

$$[\Phi, Q] = i\hbar. \tag{1.5}$$

This procedure is known as canonical quantization. It can be motivated by mentioning that a commutator of two dynamical variables is proportional to their Poisson bracket [4]. The reduced Planck constant $\hbar = h/2\pi$ arises in the relation for the theory to agree with experiment.

Let us write out the Hamiltonian in terms of the ladder operators. We introduce the creation operator of a photon,

$$a^\dagger = Q\sqrt{\frac{\rho}{2\hbar}} - i\frac{\Phi}{\sqrt{2\hbar\rho}} \tag{1.6}$$

with $\rho = \sqrt{L/C}$, and the photon annihilation operator

$$a = Q\sqrt{\frac{\rho}{2\hbar}} + i\frac{\Phi}{\sqrt{2\hbar\rho}} \tag{1.7}$$

Note we call an excitation in the harmonic oscillator a photon. Using the commutation relation (1.5), the Hamiltonian can be rewritten as

$$H = \hbar\omega_\mathrm{r}\left(a^\dagger a + \frac{1}{2}\right), \tag{1.8}$$

where $\omega_\mathrm{r} = 1/\sqrt{LC}$.

The LC circuit can be used to model a single mode of a microwave resonator. We will use the Hamiltonian (1.8) in what follows. We also write out useful identities:

$$\Phi = i\sqrt{\frac{\hbar\rho}{2}}(a^\dagger - a), \tag{1.9}$$

$$Q = \sqrt{\frac{\hbar}{2\rho}}(a^\dagger + a). \tag{1.10}$$

According to the definition we have chosen, a is proportional to the negative-frequency component of the voltage Q/C in the circuit.

More complex circuits can be quantized analogously. For that, each element potential and kinetic energies are written out; the respective variables are then linked to each other by the Kirchhoff's laws, which leaves a set of independent variables of a circuit. This procedure is carried out in Sec. II.1 and Appendix VIII.A. Note that for a circuit with multiple degrees of freedom, a canonical momentum might depend on a set of node fluxes, so Eq. (1.3) becomes a system of linear equations. Then solving it for $\dot{\Phi}$s and plugging them into the Legendre transform (1.4) often requires quite a bit of algebra. A more elegant approach is used in Appendix VIII.A that only requires differentiation of the expressions for Qs to determine H.

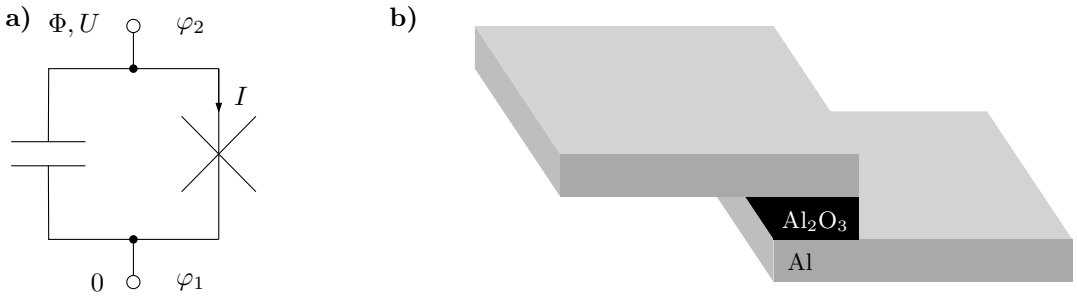

FIGURE 1.2: a) Real Josephson junction at low temperatures can be represented as an ideal junction (cross) and a shunting capacitance. b) Typical structure of a Josephson junction used on an aluminum superconducting chip [5].

1.2 Josephson junction

Most interesting electric circuits contain a nonlinear element. In the superconducting circuits, a Josephson junction is used to provide nonlinearity.

Usually, a Josephson junction used is formed by two superconductors separated by a thin dielectric (see Fig. 1.2). The dielectric is so thin that the Cooper pairs are able to tunnel through it. Peculiarly, the resulting dc current is present even when no voltage is applied across the junction. On the other hand, an ac current arises even with an applied dc voltage. These effects were predicted [6] by B. Josephson.

Here we give a hand-waving explanation of the formula for the Josephson current [7, 8]. Let us consider an ideal Josephson junction (the right branch in Fig. 1.2a). Density of superconducting current inside a superconductor is set by $\nabla\varphi$, where φ is the condensate phase. Analogously, current through the barrier should depend only on the phase difference across it:

$$I = f(\varphi_2 - \varphi_1). \tag{1.11}$$

Let us inverse time. This changes the sign of I. According to the Schrödinger equation for the condensate wavefunction, this also changes the sign of φ_1 and φ_2. Therefore, f is an odd function. Moreover, as adding 2π to the phases should not change anything, f has a period of 2π. Current can not be infinite, so f has a maximum and a minimum. The general form of f which satisfies these requirements is

$$I = \sum_{n=1,2,\ldots} I_{n-1} \sin n(\varphi_2 - \varphi_1). \tag{1.12}$$

In the most common case, the current is given by

$$I = I_0 \sin(\varphi_2 - \varphi_1) \tag{1.13}$$

with $I_0 > 0$. Experimentally, this relation can be checked by observing, e.g., Shapiro steps [9]. We have seen in Sec. 1.1 that it is convenient to treat an electric circuit in terms of node flux Φ (1.1). It turns out that node flux is proportional to the condensate phase. A Cooper pair at the top electrode in Fig. 1.2a has an energy $E_2 = -2eU$ given that its energy is $E_1 = 0$ at the bottom electrode. Here U is the voltage drop on the junction and $e > 0$ is the absolute value of the electron charge. Approximately, the Schrödinger equation $i\hbar\dot{\psi}_2 = E_2\psi_2$ holds for the condensate wavefunction at the top electrode $\psi_2 \propto \exp i\varphi_2$. It yields $\psi_2 \propto \exp \int_{-\infty}^{t} dt' E_2/i\hbar$. From these relations

and Eq. (1.1) it follows that the drop of node flux is

$$\Phi = \Phi_0(\varphi_2 - \varphi_1)/2\pi, \tag{1.14}$$

where $\Phi_0 = h/2e$ is the flux quantum and

$$I = I_0 \sin 2\pi\Phi/\Phi_0. \tag{1.15}$$

Equations (1.14)–(1.15) with the node flux definition (1.1) constitute the Josephson law. A simple phenomenological derivation of the Josephson effect is given in Ref. [10]. For a microscopic derivation and a list of literature about the topic, check Ref. [11]. For an application-focused introduction, see Refs. [12, 13].

To write out the Lagrangian of a circuit which includes a Josephson junction, we need its potential energy. It can be calculated, up to a constant, as

$$E = \int_0^t dt' U I = -E_\mathrm{J} \cos 2\pi\Phi/\Phi_0, \tag{1.16}$$

where

$$E_\mathrm{J} = I_0\Phi_0/2\pi \tag{1.17}$$

is Josephson energy. Due to our choice of sign in Eq. (1.13), the potential energy (1.16) is minimized with $\varphi_2 - \varphi_1 = 0$. It is the junction stationary state in the absence of external fields. In that state, no supercurrent flows in a circuit with such junctions.[1]

1.3 Superconducting qubits

A harmonic oscillator driven by a classical tone evolves with a displacement operator [15]. Hence if the evolution starts in a coherent state, such as a vacuum state, only other coherent states are reachable. However, if we probe a system in a coherent state through a linear coupling, the probe state evolves just as if it is driven classically (see Sec. III.1 and Ref. [16]). We cannot see any quantum effects in such a setup. Therefore, an LC circuit manipulated by a classical drive cannot be used as a qubit.

One possibility to overcome this is to introduce a nonlinearity into the LC circuit. As the resulting spectrum is non-equidistant, it is possible to address two selected energy levels with a coherent drive to create non-classical states. On a more general level, introducing nonlinearities lifts the Ehrenfest theorem restriction, and quantum effects might be visible directly in the expectation values of the system coordinates.[2] In every architecture (see, for example, Ref. [18] for a review) of superconducting qubits, Josephson junctions are used to provide nonlinearity.

A device that functions as a qubit is designed and operated such as in the logical operations with it only the two lowest levels $|\downarrow\rangle$ and $|\uparrow\rangle$ matter. While sometimes one also needs to take account of the higher levels, in this thesis we use the two-level approximation. Hence the qubit Hamiltonian we use reads

$$H_\mathrm{q} = \frac{1}{2}\hbar\omega_\mathrm{q}\sigma_\mathrm{z}, \tag{1.18}$$

[1] That is not true for a π junction, for which Eq. (1.13) becomes $I = -I_0 \sin(\varphi_2 - \varphi_1)$ and its energy is minimized at $\phi_2 - \phi_1 = \pi$. For example, if a superconducting ring is interrupted by a π junction, a current loops in the ring even with no external fields applied. To treat that system, one can use the definition of node flux in terms of the condensate phase [14]. However, π junctions are harder to make and their use is beyond the scope of this thesis. For the systems we consider, both definitions are equivalent.

[2] One can as well use an *extrinsic* nonlinearity to prepare a quantum state in a linear system. Along these lines, squeezed quantum states of a mechanical oscillator were used to encode a qubit [17].

where σ_z is such that $\sigma_z|\downarrow\rangle = -|\downarrow\rangle$ and $\sigma_z|\uparrow\rangle = |\uparrow\rangle$.

While the times a superconducting qubit can store a quantum state are small as compared to their ion or atomic counterparts [19], superconducting qubits nevertheless possess a number of other outstanding qualities. Namely, their resonance frequency and coupling to other systems are set by design; besides, the qubit is controlled and read out by a convenient microwave equipment. This makes superconducting qubits promising building blocks for a quantum computer.

2 Light-matter coupling in circuit quantum electrodynamics

Here we write out the Hamiltonians of capacitive and inductive coupling between a resonator and a qubit.

Capacitive coupling boils down (see Appendix VIII.A, Sec. II.1 and Ref. [14]) to the terms proportional to $Q_r Q_q$ in the Hamiltonian, where Q_r and Q_q are charge-like generalized momenta of the resonator and the qubit, respectively. In what follows, we also use the flux-like generalized coordinate of the qubit system Φ_q. Usually the wavefunctions of the qubit ground state $\langle\Phi_q|\downarrow\rangle$ and of its excited state $\langle\Phi_q|\uparrow\rangle$ differ in parity. Hence the only non-zero matrix elements of $Q_q = -i\hbar d/d\Phi_q$ are $\langle\uparrow|Q_q|\downarrow\rangle$ and $\langle\downarrow|Q_q|\uparrow\rangle$. Then, using Eq. (1.10) for the resonator variable, one arrives at

$$H_{\text{cap}} = g\hbar(a^\dagger + a)(\sigma_+ + \sigma_-), \tag{1.19}$$

where $\sigma_+ = |\uparrow\rangle\langle\downarrow|$ and $\sigma_- = |\downarrow\rangle\langle\uparrow|$. Inductive coupling gives rise to the terms proportional to $\Phi_r\Phi_q$. Analogous reasoning gives

$$H_{\text{ind}} = g\hbar(a^\dagger - a)(\sigma_+ - \sigma_-). \tag{1.20}$$

The Hamiltonian

$$H = \frac{1}{2}\hbar\omega_q\sigma_z + g\hbar(a^\dagger + a)(\sigma_+ + \sigma_-) + \hbar\omega_r\left(a^\dagger a + \frac{1}{2}\right) \tag{1.21}$$

and the Hamiltonians equivalent to it are called the Rabi Hamiltonians. In the next section, we will use the Hamiltonian (1.21) in the interaction picture:

$$H \to U^\dagger H U - i\hbar U^\dagger \dot{U} = g\hbar(a^\dagger e^{i\omega_r t} + a e^{-i\omega_r t})(\sigma_+ e^{i\omega_q t} + \sigma_- e^{-i\omega_q t}), \tag{1.22}$$

where $U = \exp\frac{1}{i\hbar}H_0 t$ with $H_0 = \frac{1}{2}\hbar\omega_q\sigma_z + \hbar\omega_r\left(a^\dagger a + \frac{1}{2}\right)$.

The signs in Hamiltonians (1.19) and (1.20) depend on the convention taken in the definitions (1.6)–(1.7) of a and $a^\dagger$. In fact, in the case of isolated qubit and resonator the Hamiltonians can be transformed one into another. This can be shown by rotating the qubit Bloch sphere around the z axis by $\pi/2$ and applying the unitary transformation $\exp(-ia^\dagger a\pi/2)$ to the resonator variables. Another effect of the transformation is that the signs in Eqs. (1.9)–(1.10) interchange. This also changes the initial conditions for a, $a^\dagger$ and $\sigma_\pm$. Hence the dynamics generated by H_{cap} and H_{ind} is different, even though we can transform one Hamiltonian into another. Still, the dynamics has the same steady-state limit and the quantities derived from the coefficients in the Hamiltonian are the same for both systems. If, however, another subsystem interacts with the qubit or the resonator, there is no unitary transform to turn the full Hamiltonian with the capacitive coupling into the one with the inductive coupling. Capacitive and inductive couplings are no longer equivalent in that case [20]. Nevertheless, they

become equivalent if one applies a commonly used approximation, which is described below.

2.1 Rotating-wave approximation

Often, the rotating-wave approximation (RWA) can be used to describe interaction. In the RWA, one neglects the fast-oscillating term $g\sigma_- a e^{-i(\omega_\mathrm{q}+\omega_\mathrm{r})t}$ and its Hermitian conjugate in the Rabi Hamiltonian (1.22). These terms lead to the contributions to the dynamical equations of two types.

First are the terms proportional to $1/(\omega_\mathrm{q}+\omega_\mathrm{r})$. They arise, for example, on integration of the last two terms in

$$\dot{\sigma_\mathrm{z}} = -2ig\Big(\sigma_+ a e^{i(\omega_\mathrm{q}-\omega_\mathrm{r})t} - a^\dagger \sigma_- e^{-i(\omega_\mathrm{q}-\omega_\mathrm{r})t} + \sigma_+ a^\dagger e^{i(\omega_\mathrm{q}+\omega_\mathrm{r})t} - \sigma_- a e^{-i(\omega_\mathrm{q}+\omega_\mathrm{r})t}\Big). \quad (1.23)$$

The equation follows from the interaction picture Hamiltonian (1.22). The result of integration is often negligible to the contribution of the terms with $\sigma_+ a$ and $a^\dagger \sigma_-$. Indeed, this contribution is proportional to $1/(\omega_\mathrm{q}-\omega_\mathrm{r})$ and usually it holds that

$$\omega_\mathrm{q}, \omega_\mathrm{r} \gg |\omega_\mathrm{q} - \omega_\mathrm{r}|. \quad (1.24)$$

If the condition (1.24) does not hold, the frequencies of the qubit and the resonator shift significantly due to the fast-oscillating terms. The resulting shift is known as the Bloch-Siegert shift.

Second type of the contribution of the fast-oscillating terms is an addition to σ_z and $a^\dagger a$. Taking the condition (1.24) into account,

$$\dot{\sigma_\mathrm{z}} \approx -2ig\big(\sigma_+ a e^{i(\omega_\mathrm{q}-\omega_\mathrm{r})t} - a^\dagger \sigma_- e^{-i(\omega_\mathrm{q}-\omega_\mathrm{r})t}\big). \quad (1.25)$$

Also,

$$\frac{d}{dt}\big(\sigma_+ a e^{i(\omega_\mathrm{q}-\omega_\mathrm{r})t} - a^\dagger \sigma_- e^{-i(\omega_\mathrm{q}-\omega_\mathrm{r})t}\big) = -ig\big[a^\dagger a \sigma_\mathrm{z} + \tfrac{1}{2}(\sigma_\mathrm{z}+1) + a^2 \sigma_\mathrm{z}\big], \quad (1.26)$$

where it was taken into account that $\sigma_+^2 = 0$. On integration, the term $-iga^2\sigma_\mathrm{z}$ is proportional to $g/2\omega_\mathrm{r}$. It does not contribute when

$$\omega_\mathrm{q}, \omega_\mathrm{r} \gg g \quad (1.27)$$

and the Eqs. (1.25)–(1.26) can be solved to yield σ_z. Otherwise, the term contributes to σ_z and, as can be shown analogously, to $a^\dagger a$.

Under the conditions (1.24) and (1.27), the Rabi Hamiltonian (1.21) simplifies to

$$H = \frac{1}{2}\hbar\omega_\mathrm{q}\sigma_\mathrm{z} + g\hbar(\sigma_+ a + a^\dagger \sigma_-) + \hbar\omega_\mathrm{r}\left(a^\dagger a + \frac{1}{2}\right), \quad (1.28)$$

which is known as the Jaynes-Cummings Hamiltonian. This Hamiltonian can be easily diagonalized—see Ref. [19], for example. The diagonalization with a unitary transform is discussed in the next section.

2.2 Dispersive transformation

One way to diagonalize the Jaynes-Cummings Hamiltonian (1.28) is via a unitary transformation. It is shown in Refs. [21] and [22], that the Hamiltonian is diagonalized

with

$$U = \exp\big\{ -(2\sqrt{N})^{-1} \arctan\big[2\lambda\sqrt{N}(\sigma_+ a - a^\dagger \sigma_-)\big]\big\}, \tag{1.29}$$

$$N = a^\dagger a + \frac{1}{2}(\sigma_\mathrm{z} + 1), \tag{1.30}$$

$$\lambda = g/(\omega_\mathrm{q} - \omega_\mathrm{r}). \tag{1.31}$$

However, this transformation often is not practical. The Hamiltonians for real problems include the coupling of the resonator to the outer world. Such a Hamiltonian is hard to diagonalize. We resort to a perturbation theory in λ. Assume the coupling is weak and a few photons occupy the resonator,

$$4\lambda^2(n_\mathrm{ch} + 1) \ll 1, \tag{1.32}$$

where n_ch denotes the characteristic number of photons in the resonator. The condition can be rewritten into two:

$$n_\mathrm{ch} \ll n_\mathrm{crit}, \quad \lambda^2 \ll 1, \tag{1.33}$$

where $n_\mathrm{crit} = 1/4\lambda^2$ is called the critical photon number. When the condition (1.32) holds, a first-order perturbation theory suffices. The exact transformation (1.29) simplifies to

$$U_\mathrm{d} = \exp\big[-\lambda\sigma_+ a + \lambda a^\dagger \sigma_- + O(\lambda^3)\big]. \tag{1.34}$$

The transformation (1.34) is called dispersive. It acts on Eqs. (1.28) as follows:

$$H \to U_\mathrm{d}^\dagger H U_\mathrm{d} \approx H_\mathrm{q} + \tilde{H}_\mathrm{qr} + H_\mathrm{r} \tag{1.35}$$

$$= \tilde{H}_\mathrm{q} + H_\mathrm{r} = H_\mathrm{q} + \tilde{H}_\mathrm{r}, \tag{1.36}$$

where

$$\tilde{H}_\mathrm{qr} = \lambda\hbar g\sigma_\mathrm{z}\left(a^\dagger a + \frac{1}{2}\right) \tag{1.37}$$

is the Hamiltonian of a parametric qubit-resonator coupling, and

$$\tilde{H}_\mathrm{q} = \frac{1}{2}\hbar\tilde{\omega}_\mathrm{q}\sigma_\mathrm{z}, \tag{1.38}$$

$$\tilde{H}_\mathrm{r} = \hbar\tilde{\omega}_\mathrm{r}\left(a^\dagger a + \frac{1}{2}\right) \tag{1.39}$$

are the effective qubit and resonator Hamiltonians. We have denoted

$$\tilde{\omega}_\mathrm{q} = \omega_\mathrm{q} + 2\chi\left(a^\dagger a + \frac{1}{2}\right) \tag{1.40}$$

the dressed qubit frequency, and

$$\tilde{\omega}_\mathrm{r} = \omega_\mathrm{r} + \chi\sigma_\mathrm{z} \tag{1.41}$$

the dressed resonator frequency. Here $\chi = g\lambda$ is known as the dispersive shift. It follows from our analysis that expressions (1.35)–(1.36) are correct to the first order of λ. A more intricate treatment, given in Ref. [21], shows that they hold to λ^2.

Several qualitative features of the dynamics of our system follow from the form of the dressed Jaynes-Cummings Hamiltonian given by Eqs. (1.35)–(1.41). It follows from Eqs. (1.36), (1.38), and (1.40) that the qubit frequency acquires a Stark

shift, which depends on the number of photons in the resonator. On the other hand, Eqs. (1.36), (1.39), and (1.41) show that the resonator acquires a shift in its frequency, which depends on the state of the qubit. The shift is also known as the dispersive pull. It should be stressed that the energy exchange between the qubit and the resonator is negligible when the condition (1.32) holds. The parametric coupling is the only effect of the qubit-resonator interaction.

A similar reasoning can be carried out one step beyond the RWA[3]. As explained in Ch. VI, if the rapidly-oscillating terms of the Rabi Hamiltonian are small and $\omega_{\mathrm{q}} \sim \omega_{\mathrm{r}}$, one can still use the dispersive Hamiltonian (1.36). The dispersive shift is then renormalized by the Bloch-Siegert shift. Along these lines, we describe the photon transport through the qubit-resonator system in Ch. VI. Then in Ch. VII we use these results to seek a speedup of the single-photon dispersive readout of a qubit.

3 Dispersive readout

Qubit readout is one of the most important processes in quantum information technologies. First of all, qubit readout occurs when the results of a computation are read out. The possibility to read out a qubit is a basic requirement for quantum computation [24]. During the computation, a qubit state can be ruined by decoherence. To avoid this, it is proposed to encode a logical qubit in several physical qubits. This redundancy is then used in a process called quantum error correction, which is able to undo the effect of decoherence on the logical qubit [25]. Quantum error correction codes take the result of the qubit readout as input. Besides, one can initialize a qubit by measurement, if, after the measurement, the qubit stays in the same eigenstate it was detected in. This requirement constitutes a quantum-non-demolition (QND) measurement [26]. It is usually desirable for the measurement to be QND, as this avoids noises from the detector back-action [26]. In any case, it is important for the measurement to be fast and robust.

The dispersive readout of a superconducting qubit [19] is a promising setup to achieve these goals. While other readout techniques have been proposed (see the references in Ref. [27]), it is the dispersive measurement that is both highly-QND and can be made rather fast and high-fidelity. During the measurement a qubit is coupled to a cavity off-resonantly. This results in the absence of energy exchange between them; however, the resonance of the cavity gets shifted either to the blue or to the red side, depending on whether the qubit is in the excited or in the ground state. This is expressed by the dispersive Hamiltonian (1.36),

$$H = \frac{1}{2}\hbar\omega_{\mathrm{q}}\sigma_{\mathrm{z}} + \hbar(\omega_{\mathrm{r}} + \chi\sigma_{\mathrm{z}})\left(a^{\dagger}a + \frac{1}{2}\right). \tag{1.42}$$

The shift is used to infer the qubit state by measuring the resonator transmission or reflection. Dispersive readout is QND for well-chosen parameters, when the Hamiltonian (1.42) is valid. In this case, $\dot{\sigma_{\mathrm{z}}} = \frac{1}{i\hbar}[\sigma_{\mathrm{z}}, H] = 0$ and the qubit state does not change after collapse.

In practice there are several factors limiting the QND nature of the scheme. First, the qubit Rabi oscillations [28] were neglected when making the dispersive approximation. Secondly, in reality, to control and read out the qubit, the resonator is coupled to waveguides (this is modeled in Chs. III and VI). These waveguides provide an important source of relaxation for the qubit: this resonator-assisted relaxation is known

[3] It was shown by Braak [23] that the Rabi Hamiltonian (1.21) can be exactly diagonalized. However, it is not clear how to use his results if the system interacts with the outer world.

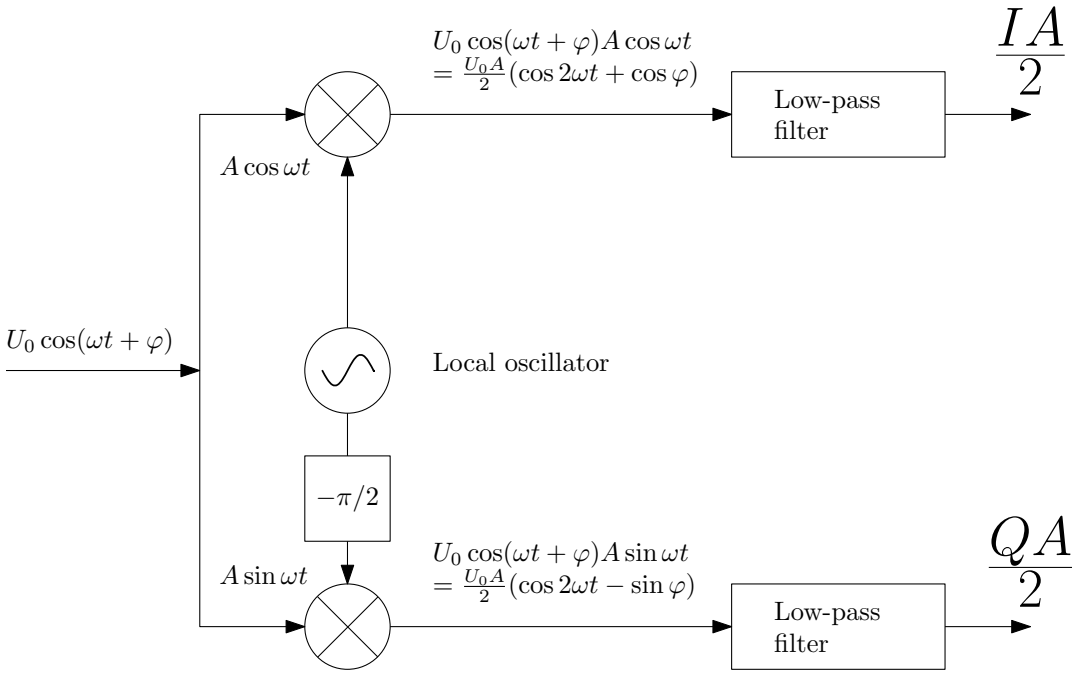

FIGURE 1.3: Homodyne measurement. The input signal is $U_0\cos(\omega t+\varphi)=I\cos\omega t+Q\sin\omega t$, where $I=U_0\cos\varphi$ and $Q=-U_0\sin\varphi$. The signal is multiplied with the local oscillator with different phases on the frequency mixers. A mixer is depicted as a cross inside a circle. (Physically, multiplication of signals in a mixer is achieved by using a nonlinearity [30].) The low-pass filters separate the components proportional to I and Q.

as the Purcell relaxation (see Refs. [28, 29]). Finally, the other sources of relaxation were also neglected in the bare Hamiltonian (1.28).

3.1 Homodyne readout

Most implementations of the dispersive measurement infer the state (ground or excited) of the qubit by, roughly speaking, a shift in the coherent-state radiation which is either transmitted through the cavity or reflected by it. Namely, after several amplification stages at different temperatures, the phase shift is detected with a room-temperature homodyning. With the homodyne detection, one determines the I and Q components of the signal with respect to the signal incident on the resonator (see Fig. 1.3). The local oscillator in the homodyne detector is in phase with the signal incident on the resonator due to the use of a frequency standard which synchronizes both sources [31]. We find the expressions for average values of I and Q in Ch. III. To have less noise in the output, a quantum-limited parametric amplifier is used in the first cold stage of amplification [32]. A quantum-limited amplifier only adds an amount of noise close to the limit imposed by the quantum physics [33, 34]. Such amplifiers were used to demonstrate quantum jumps [35], reversal of the measurement-induced decoherence [36] and other outstanding phenomena (see Ref. [37]). However, the approach still has disadvantages. It is not simple to use a parametric amplifier in the same cryostat with the qubit and the cavity, as this introduces an additional non-reciprocal element and a pump. Non-reciprocal elements which are used today are bulky, and the pump is hard to isolate from the rest of the circuitry. This makes it hard to scale the readout to bigger number of qubits [37].

3.2 Photodetector readout

Recently, an alternative scheme of the dispersive measurement was put forward [37] and implemented [2]. The idea is to use a detector absorbing a microwave photon, like the detectors routinely used in optics. Then the cavity is driven on one of its shifted frequencies $\omega_r \pm g\lambda$ [see Eqs. (1.39) and (1.41)] or close to it. Depending on whether the qubit is in $|\uparrow\rangle$ or $|\downarrow\rangle$, the photons mostly pass through the cavity or reflect off it. One infers the state of the qubit ($|\uparrow\rangle$ or $|\downarrow\rangle$) by the number of the detector clicks. A detector can be placed on-chip, and the setup scales well for the readout of several and more qubits. Numerous detectors of microwave photons were proposed (see e.g. Refs. [38–40]), and some were demonstrated [1, 2, 41–48]. Most of the detectors in the references can not provide any information besides the presence or absence of photons. Such detectors are called vacuum detectors. In Refs. [2, 29, 37], the qubit state is determined based on whether the detector clicked or not. We consider the readout with a Fock-state probe and a vacuum detector in Ch. VII. In Ch. IV we consider the readout with a detector that is able to distinguish the number of incident photons—a photon-number-resolving-detector. A continuous coherent probe is used. It is found that the use of a photon-number-resolving detector improves the performance of that scheme. A photodetector with limited number resolution, which is able to count microwave photons up to two, is considered in Ch. VIII.

3.3 Measurement-induced decoherence

Quantum measurement is always accompanied by decoherence. The latter results in a superposition of eigenstates turning into a mere statistical mixture. Setup for a dispersive readout with a coherent radiation is a convenient system to study this process. When the cavity is driven by a coherent radiation, it becomes occupied by a coherent state whose number of photons fluctuates. As the qubit frequency depends on the cavity photon number, fluctuations of the photon number result in the qubit phase becoming more and more random—hence the qubit decoheres. We provide a simple formula for the rate of this measurement-induced decoherence in Ch. V. Apart from the drive photons, the formula takes into account the thermal ones.

4 Measures of readout performance

It is possible that the qubit readout does not identify a state of the qubit correctly. Common measures to quantify the readout performance are readout contrast and fidelity. Also, sometimes it is more convenient to use the probability of erroneous readout. All these measures are closely related.

4.1 Contrast

Probabilistic measurement contrast [37] is defined as

$$C = P_{\uparrow|\uparrow} - P_{\uparrow|\downarrow}. \tag{1.43}$$

$P_{m|i}$ is the probability of inferring the qubit to be in state $|m\rangle$ while it is in state $|i\rangle$. Note C is not the probability of a correct measurement result, as it does not comprise

Section 4 was published in "A. M. Sokolov and E. V. Stolyarov, Phys. Rev. A 101, 042306 (2020)". Copyright (2020) by the American Physical Society. The majority of the text was written by A. M. Sokolov.

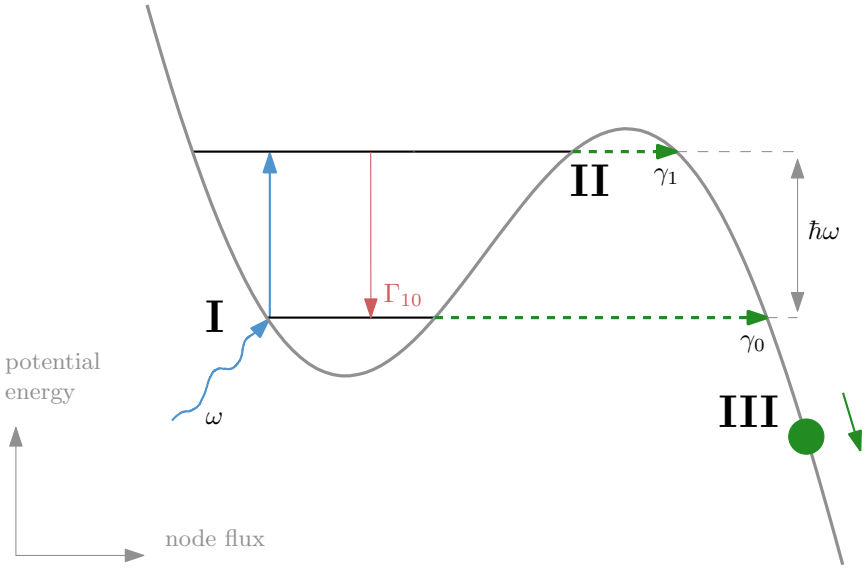

FIGURE 1.4: JPM operation and sources of errors. Working steps: I) a photon of frequency ω excites the JPM, II) the JPM tunnels to the continuum of states to the left, III) the JPM "rolls down" the potential. Non-zero tunneling rate γ_0 results in false counts, while the non-radiative relaxation Γ_{10} can result in absence of a click even if photons are present.

the probabilities of the qubit to be prepared in each state[4]. The contrast (1.43) is also dubbed fidelity sometimes [49–52]. It is however more consistent to reserve the term fidelity for the other, yet related, quantity.

4.2 Fidelity and error probability

We define the measurement fidelity as the probability of a correct measurement result. Let $P_\downarrow$ and $P_\uparrow$ denote the probabilities to measure $|\downarrow\rangle$ and $|\uparrow\rangle$, respectively. Then the fidelity is

$$F = 1 - P_\downarrow P_{\uparrow|\downarrow} - P_\uparrow P_{\downarrow|\uparrow} \tag{1.44}$$

We know nothing about the qubit initial state prior to readout. Hence it is reasonable to set $P_{\downarrow,\uparrow} = 1/2$ and

$$F = 1 - (P_{\uparrow|\downarrow} + P_{\downarrow|\uparrow})/2. \tag{1.45}$$

That's the formula given, for example, in Ref. [53]. Taking into account that $P_{\uparrow|\uparrow} + P_{\uparrow|\downarrow} = 1$, we express fidelity (1.45) in terms of the probabilistic contrast (1.43):

$$F = (1 + C)/2. \tag{1.46}$$

It is often convenient to argue in terms of the probability of an erroneous readout

$$\varepsilon = 1 - F. \tag{1.47}$$

5 Josephson photomultiplier

A Josephson photomultiplier (JPM) is a microwave photon detector which is based on the Josephson junction. It functions as follows (see Fig. 1.4). We start with the JPM in the ground state. Tunneling from that state occurs rarely. A photon excites the JPM. Tunneling rate of the excited state is much higher than from the ground one, $\gamma_1 \gg \gamma_0$. After the tunneling, the JPM "rolls down" the potential on the other side of the barrier. While first it accelerates, soon the speed of rolling down becomes constant, due to dissipation to other degrees of freedom. The JPM acquires a macroscopic voltage drop $\dot{\Phi} = \text{const}$ across its contacts. This voltage can be detected by a voltmeter and is interpreted as a click. This JPM is a vacuum detector: that is, it can only distinguish a vacuum state from the states with one or more photons.

One can modify JPM to count photons to two. This is discussed in Ch. VIII.

5.1 Detector performance

Here we overview how to measure the likelihood of the detector working properly and estimate these measures for the JPM. There are several possibilities for the detector to give an incorrect result. First, it can fail to give a click when a photon is present. The probability to have a click when a photon is present is called the *bright count probability*. Second, the detector can fire if no photons are present. For the detector which counts up to two photons, there is also a possibility to identify a single-photon state as a multi-photon one. We call the probability of these processes the *false count probability*. These measures can be combined to yield the *probability of a detection error*.

Let us estimate the bright count probability $P_{\mathrm{b}}^{0/1}$ for the JPM. Given that we have waited long enough, a photon is most probably absorbed by the JPM. However, this does not necessarily give a click: a photon could get stuck in the ground state due to the JPM relaxation. For each small period of time Δt, a part $\gamma_1 P_1 \Delta t$ of the occupation P_1 of the excited level tunnels, while a part $\Gamma_{10} P_1 \Delta t$ decays non-radiatively. After the excited state gets depleted, the ground one is occupied with a probability

$$P_0(t_{\mathrm{opt}}) \approx \Gamma_{10}/(\Gamma_{10} + \gamma_1). \tag{1.48}$$

Ratios like this one are known as branching ratios. We neglected tunneling from the ground state. P_0 is taken at optimal time t_{opt}, which is a tradeoff between increasing the false counts due to the ground state tunneling and partial depletion of the excited state. It follows that,

$$P_{\mathrm{b}}^{0/1}(t_{\mathrm{opt}}) = 1 - P_0(t_{\mathrm{opt}}) \approx \gamma_1/(\Gamma_{10} + \gamma_1). \tag{1.49}$$

This expression was also given in Ref. [54].

It is easy to estimate the false count probability for the JPM. When there are no photons, the JPM stays in the ground state. However, from there it can still tunnel and give a click. Occupation of the ground state is $\exp -\gamma_0 t$, hence the false count probability is

$$P_{\mathrm{f}}^{0/1}(t) = 1 - e^{-\gamma_0 t}. \tag{1.50}$$

Now we give an expression for the probability of detection error. A detection error can occur if there was a photon, but the detector did not fire, or when there were no

[4] In Ref. [49] the quantity we call here the measurement contrast was erroneously claimed to equal the probability of correct measurement result.

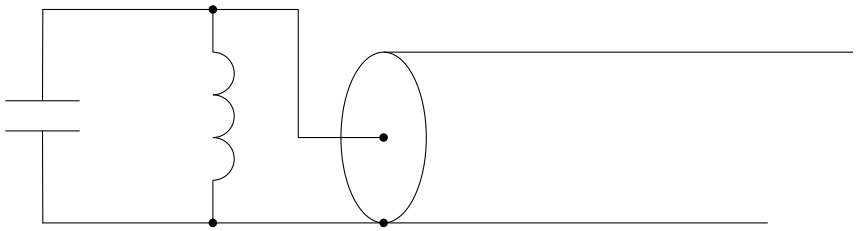

FIGURE 1.5: Damped LC circuit. The dissipation results from the energy being absorbed by the waveguide.

photons and it fired. The probability of error is

$$\varepsilon = P_0 P_{\mathrm{f}}^{0/1} + P_1(1 - P_{\mathrm{b}}^{0/1}) \tag{1.51}$$

where P_N is a probability of an input state with N photons to occur. If nothing is known about the resonator state beforehand, $P_0 = P_1 = 1/2$ and

$$\varepsilon = \frac{1}{2}\big(P_{\mathrm{f}}^{0/1} + 1 - P_{\mathrm{b}}^{0/1}\big) \tag{1.52}$$

If the time dependence of both $P_{\mathrm{f}}^{0/1}$ and $P_{\mathrm{b}}^{0/1}$ is known, one can find the optimal time for which ε is minimal.

6 Some methods to treat the open quantum systems

We have already encountered dissipation rate Γ_{10} in the JPM in the previous section, but have not considered how to model the dissipation. Any dissipation occurs due to the leakage to the external degrees of freedom. Hence the systems where dissipation cannot be neglected are called the open systems. In this section, we present two methods of how to treat such systems.

6.1 Langevin equations

Langevin equations is a versatile tool for modeling random dissipative processes. Using Langevin equations is especially useful when a correlator of some quantities is sought. Here, as an example, we derive the Langevin equation for a damped quantum resonator.

We model damping by the interaction with a semi-infinite waveguide (see Fig. 1.5). Usually, in the circuit quantum electrodynamics (QED) [19], majority of the resonator damping is indeed caused by coupling to a waveguide. Moreover, often that is a very good model for other sources of dissipation as well [55].

The Hamiltonian of the system reads

$$H = \hbar\omega_{\mathrm{r}}\left(a^\dagger a + \frac{1}{2}\right) + \hbar\int_0^\infty dk f_k(a^\dagger b_k + b_k^\dagger a) + \hbar\int_0^\infty dk\,\omega_k b_k^\dagger b_k. \tag{1.53}$$

The Hamiltonian of the resonator is given according to Eq. (1.8). Operators $b_k^\dagger$ and b_k create and annihilate a photon with a wavevector k. Each mode is represented by a Hamiltonian of a harmonic oscillator in Eq. (1.53). The infinite part of the waveguide energy is omitted in the Hamiltonian. The waveguide is assumed to be dispersionless,

$$\omega_k = vk, \tag{1.54}$$

where v is the speed of propagating photons. The coupling between the resonator and the waveguide is written in the RWA. We discuss a derivation of the waveguide and the coupling Hamiltonians in the context of circuit QED in Ch. II.

From the Hamiltonian (1.53), one obtains the equation of motion for operators of photon annihilation in the waveguides:

$$\dot{b}_k = \frac{1}{i\hbar}[b_k, H], \tag{1.55}$$

$$\dot{b}_k = -i\omega_k b_k - i f_k a. \tag{1.56}$$

Their formal integral is given by

$$b_k(t) = b_k(0)e^{-i\omega_k t} - i f_k \int_0^t dt' e^{-i\omega_k(t-t')} a(t'). \tag{1.57}$$

The equation states that the field in the waveguides consists of the free-oscillations part and the part describing the influence of the resonator.

Now we obtain the Langevin equation for a. It follows from the Hamiltonian (1.53) that

$$\dot{a} = -i\omega_{\mathrm{r}} a - i \int_0^\infty dk f_k b_k(t). \tag{1.58}$$

Using Eq. (1.57), one splits the integral in Eq. (1.58),

$$-i \int_0^\infty dk f_k b_k(t) = -i \int_0^\infty dk f_k b_k(0) e^{-i\omega_k t} - \int_0^t dt' \int_0^\infty dk f_k^2 e^{-ivk(t-t')} a(t'). \tag{1.59}$$

The dispersion relation (1.54) was used.

To arrive at the Langevin equation, some approximations are required. First, the integral over k in the second term can be extended to $-\infty$. Indeed, $a(t')$ varies approximately as $\exp(-i\omega_{\mathrm{r}} t' - \kappa t'/2)$, where $\kappa > 0$ is the damping constant we will determine. Hence in the region of negative k the expression under the integral oscillates fast. After the integration over t', this region contributes only negligibly—if the coupling f_k does not have sudden peaks there, and the resonator is of high quality factor with $\kappa \ll \omega_{\mathrm{r}}$. In fact, to continue, we assume that the coupling is constant. The integration over t' yields a result proportional to $1/(vk - \omega_{\mathrm{r}} + i\kappa/2)$. Its absolute value has a narrow peak in a region around $k = \omega_{\mathrm{r}}/v$. Hence we assume that $f_k \approx f$ in this region that provides the major contribution to the integral. Using that $\int_{-\infty}^{+\infty} dk\, e^{-ikv(t-t')} = 2\pi\delta(t-t')/v$, one arrives at

$$\dot{a}(t) \approx \left(-i\omega_{\mathrm{r}} - \frac{\kappa}{2}\right) a(t) - i f \int_0^\infty dk\, b_k(0) e^{-i\omega_k t}, \quad t > 0, \tag{1.60}$$

where $\kappa = 2\pi f^2/v$ is the decay rate of the resonator. An argument very similar to ours is presented in Ch. 6.3 of Ref. [15]. Extension of integration limits is also used in Appendix D of Ref. [56] in a related argument.

Equation (1.60) is the Langevin equation for a. The last term on the right-hand side of the equation is a Langevin noise source; the dissipation is accompanied by noise. Note also, that the evolution of a in each instant of time depends only on its value at the very instant. In other words, we have arrived at the Markov approximation [57]. Ultimately, it arises as we have assumed that the system does not feel the reservoir internal structure.

One may wonder, why not just carry out the integral over wavevectors k in Eq. (1.59), without extending its lower limit? The integration yields

$$\int_0^\infty dk f_k^2 e^{-ivk(t-t')} = \frac{\pi f^2}{v}\Big[\,\mathrm{PV}\,\frac{1}{i\pi(t-t')} + \delta(t-t')\Big], \tag{1.61}$$

where we have assumed that $f_k \approx f$, and PV denotes the Cauchy principal value. The second term in the brackets allows to recover the Langevin equation (1.60) on integrating over t'. The first term there, however, provides then a divergence. Limiting the time resolution can avoid the divergence [56]; but in any case, this term only adds up to the resonator frequency ω_r. Hence, we can use the cheap trick described for obtaining (1.60), but we then mind that the renormalized ω_r appears in our results. On the other hand, when ω_r is determined by measuring the resonator response to a signal traveling by the attached waveguides (see Chs. III and IV), it is this renormalized frequency that is measured anyway.

We expect that the same holds for other similar parameters when we use this cheap trick throughout the thesis. We use Langevin equations in Chs. III–VII for the problems related to qubit readout.

6.2 Lindblad master equation

Lindblad master equations are the equations on density matrix which are often used to treat an open quantum system. As compared to the Langevin equations, this method is usually easier and also allows one to find the dynamics of a (mixed) quantum state. Here we review two ways of deriving the Lindblad master equation.

The first way is mostly mathematical and is based on two properties of density matrices and one physical assumption. First, trace of a density matrix is always unity. This is because the diagonal elements of a density matrix are probabilities of the respective states to occur; they should sum up to unity. Second, density matrix always stays positive. That is, all elements are non-negative in the diagonalized matrix. Again, this is due to the diagonal elements being probabilities. More than that, if a part of a density matrix is evolved by the equations we seek, the whole density matrix should stay positive. Finally, the physical assumption is that, in each instant of time, the evolution of a density matrix depends only on the density matrix in that instant of time; i.e., we assume the evolution is Markovian and we neglect any memory in our system. The equation for the density matrix ρ that satisfies the above requirements is [58, 59]

$$\dot\rho = \frac{1}{i\hbar}[H,\rho] + \sum_{i=1}^{N^2-1}\gamma_i\left(L_i\rho L_i^\dagger - \frac{1}{2}[L_i^\dagger L_i,\rho]_+\right) \tag{1.62}$$

for an open system with N levels. Here H is a Hamiltonian which governs the unitary part of the system dynamics. L_i are called the jump operators. One can check that for $L_i = |m\rangle\langle n|$ with the states $|n\rangle$ and $|m\rangle$ such as their energies $E_n > E_m$, the rate γ_i is the rate of the decay $n \to m$; and for $L_j = |n\rangle\langle n|$, the rate γ_j is the pure dephasing rate of $|n\rangle$.

The second way [59, 60] to derive the Lindblad equation is more physical. One considers a system weakly coupled to a huge thermal reservoir. The Born-Markov approximation is used, which neglects the changes in the reservoir due to the system evolution and neglects the system memory. This yields the Redfield equation. The latter can be transformed into the Lindblad equation (1.62) by applying the secular approximation. In the secular approximation one neglects the processes that link populations $\langle n|\rho|n\rangle$ and coherences $\langle n|\rho|m\rangle$, where $n \neq m$. For the relaxation rates much

smaller than the frequency separation between the levels, these processes are manifested by rapidly oscillating terms in the Redfield equations and are neglected [61]. One peculiar thing follows about the Redfield equation: without the secular approximation the Redfield equation does not guarantee that ρ_{nn} are always non-negative. Due to this and the fact that the Lindblad equation is much simpler, the Lindblad equation is used much more often than the Redfield equation. We use the Lindblad equation in Ch. VIII to model non-unitary processes in the JPM. We also derive a Redfield equation for a tunneling model that links coherences and populations in Appendix VIII.C. We check that dismissing the rapidly oscillating terms in it gives rise to the Lindblad equation for the JPM in Appendix VIII.D.

Chapter II

Quantization of the waveguide-resonator system

In Sec. I.6.1 the simplest case of a direct coupling of a waveguide and a resonator was shown in Fig. 1.5. However, in circuit QED, a resonator is usually coupled to a waveguide capacitively. A direct coupling provides damping that only depends on the waveguide wave impedance (this can be explained by mentioning that a waveguide can be replaced by a resistance equal to the waveguide impedance). Standard impedances of convenient and widely used coaxial waveguides provide too much of damping. This compromises coherence of a qubit coupled to the resonator due to the Purcell effect [28]. A capacitor allows one to achieve reasonable values of damping. In this chapter, we consider a single waveguide coupled capacitively to a resonator, which interacts with a qubit inductively (see Fig. 2.1). It is straightforward to generalize our treatment for the case of two waveguides coupled to the resonator, which is usually the case in practice. As for the capacitive qubit-resonator coupling, one needs to explicitly include a qubit into the treatment in that case [20]; however, the general idea of our treatment stays the same.

A coupling capacitance we have is a point-like inhomogeneity in the waveguide. Using the field expansion with zero current at the point of coupling yields the A^2 term [62]. A more convenient approach allows one to avoid this term, as discussed in the reference. In that approach, one finds the normal modes of an inhomogeneous waveguide and uses that expansion to define the creation and annihilation operators. In Ref. [63] the normal modes of a waveguide are identified numerically to treat an ultrastrong coupling of a qubit and a resonator. However, the system studied in the reference is different from that of ours: it is an inhomogeneous transmission-line resonator that is coupled galvanically to a flux qubit. Our treatment bears some resemblance to Refs. [20, 62, 64], but still the method we use is different. Unlike Refs. [20, 62] we treat the coupling capacitance in the continuous limit, without resorting to the discrete representation of the waveguide. This is also the approach used in Sec. 2.2 of Ref. [64], but there an exotic Lagrangian coordinate is chosen—the full charge of the segment of a waveguide from its start to a point x. Here we develop an analytical theory that treats a point-like coupling capacitor right in the continuous limit; we use the conventional Lagrangian variable of node flux at point x of a waveguide.

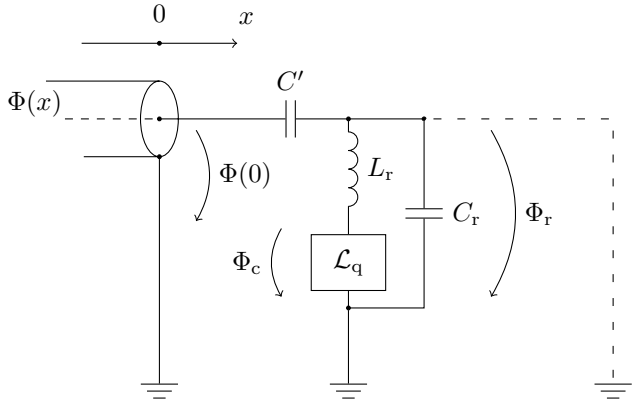

FIGURE 2.1: Waveguide-resonator system. A waveguide is loaded by a resonator. The latter includes an arbitrary system with Lagrangian $\mathcal{L}_\mathrm{q}$. Arrows indicate the direction of drop in node flux. Resonator short circuit (long-dashed) provides a convenient set of line modes.

1 Lagrangian, Hamiltonian, and first quantization

Lagrangian of the system reads

$$\mathcal{L}_{\mathrm{w},0} = \mathcal{L}_\mathrm{w} + \mathcal{L}_0, \tag{2.1}$$

$$\mathcal{L}_\mathrm{w} = \int_{-\infty}^{+\infty} dx\, \theta(-x-)\Big(\frac{\varkappa\dot\Phi^2}{2} - \frac{(\partial_x\Phi)^2}{2\ell}\Big), \tag{2.2}$$

$$\mathcal{L}_0 = \frac{C'(\dot\Phi(0) - \dot\Phi_\mathrm{r})^2}{2} + \mathcal{L}_{\mathrm{r,qr}} + \mathcal{L}_\mathrm{q}, \tag{2.3}$$

$$\mathcal{L}_{\mathrm{r,qr}} = \frac{C_\mathrm{r}\dot\Phi_\mathrm{r}^2}{2} - \frac{(\Phi_\mathrm{r} - \Phi_\mathrm{c})^2}{2L_\mathrm{r}}. \tag{2.4}$$

Above and in what follows, $x\pm$ stands for $x \pm \varepsilon$, where ε is positive infinitesimal. $\mathcal{L}_\mathrm{w}$ is the Lagrangian of the line. $\varkappa$ and ℓ stand for the distributed capacitance and inductance of the waveguide. $\Phi(x)$ denotes the node flux in the point x of the line. $\mathcal{L}_0$ is the Lagrangian of the point-like system: it describes the cavity-line coupling, the resonator, and the qubit. Lagrangian of the qubit and the qubit-resonator coupler is denoted by $\mathcal{L}_\mathrm{q}$. The coupling is through the node flux Φ_c. Lagrangian of the resonator is denoted by $\mathcal{L}_{\mathrm{r,qr}}$. It includes a qubit-resonator coupling term. Drop of the node flux across the resonator capacitance is Φ_r. For the system described it is possible to write out the Hamiltonian of the waveguide-resonator coupling without knowledge of $\mathcal{L}_\mathrm{q}$ [20].

The generalized momenta of the system are

$$P(x) = \frac{\delta\,\mathcal{L}}{\delta\dot\Phi(x)} = \theta(-x-)\varkappa\dot\Phi(x) + \delta(x)Q(0), \tag{2.5}$$

$$Q_\mathrm{r} = \frac{\partial\,\mathcal{L}_{\mathrm{w},0}}{\partial\dot\Phi_\mathrm{r}} = -Q(0) + C_\mathrm{r}\dot\Phi_\mathrm{r}, \tag{2.6}$$

$$Q_\mathrm{q} = \frac{\partial\,\mathcal{L}_\mathrm{q}}{\partial\dot\Phi_\mathrm{q}}, \tag{2.7}$$

where

$$Q(0) = C'(\dot\Phi(0) - \dot\Phi_\mathrm{r}) \tag{2.8}$$

is a shortcut notation for the point charge at $x = 0$, and $P(x)$ is the charge density in the point x of the waveguide. Q_r is the total charge of the resonator top node. Φ_q stands for the set of qubit variables, and Q_q stands for the respective generalized momenta.

On performing the Legendre transform

$$H_{\mathrm{w},0} = \int_{-\infty}^{0+} dx \dot{\Phi} P + \dot{\Phi}_\mathrm{r} Q_\mathrm{r} + \dot{\Phi}_\mathrm{q} Q_\mathrm{q} - \mathcal{L}_{\mathrm{w},0}, \tag{2.9}$$

one obtains the Hamiltonian

$$H_{\mathrm{w},0} = H_\mathrm{w} + H_0, \tag{2.10}$$

$$H_\mathrm{w} = \int_{-\infty}^{+\infty} dx\, \theta(-x-) \Big(\frac{P^2}{2\varkappa} + \frac{(\partial_x \Phi)^2}{2\ell} \Big), \tag{2.11}$$

$$H_0 = \frac{Q^2(0)}{2\tilde{C}'} + H_\mathrm{wr} + H_\mathrm{r,qr} + H_\mathrm{q}, \tag{2.12}$$

$$H_\mathrm{wr} = Q_\mathrm{r} Q(0)/C_\mathrm{r}, \tag{2.13}$$

$$H_\mathrm{r,qr} = \frac{Q_\mathrm{r}^2}{2C_\mathrm{r}} + \frac{(\Phi_\mathrm{r} - \Phi_\mathrm{c})^2}{2L_\mathrm{r}}, \tag{2.14}$$

$$H_\mathrm{q} = \dot{\Phi}_\mathrm{q} Q_\mathrm{q} - \mathcal{L}_\mathrm{q}, \tag{2.15}$$

where $\tilde{C}' = (1/C' + 1/C_\mathrm{r})^{-1}$. The first term in Eq. (2.12) is known as the A^2 term [62].

Next, we promote the canonical variables to operators. This imposes commutation relations:

$$[\Phi(y), P(y)] = i\hbar\, \delta(x - y), \tag{2.16}$$

$$[\Phi_\mathrm{r}, Q_\mathrm{r}] = i\hbar, \quad [\Phi_\mathrm{q}, Q_\mathrm{q}] = i\hbar. \tag{2.17}$$

Other pairs of variables commute.

2 Second quantization of the waveguide

Now let us rewrite the waveguide Hamiltonian in terms of the photon creation and annihilation operators. To do it, one expands the line field by an orthogonal set of modes. A boundary condition at the line end generates such a set. In choosing a convenient mode set, we will modify the true boundary condition by short-circuiting the resonator. This allows us to include the A^2 term into the mode expansion.

For completeness, we first obtain the true boundary condition at $x = 0$. The waveguide dynamics is governed by the equations

$$\dot{P}(x) = \tfrac{1}{i\hbar}[P(x), H], \quad \dot{\Phi}(x) = \tfrac{1}{i\hbar}[\Phi(x), H]. \tag{2.18}$$

From the last equation it follows that

$$\dot{\Phi}(0) = \frac{Q(0)}{\tilde{C}'} + \frac{Q_\mathrm{r}}{C_\mathrm{r}}, \tag{2.19}$$

while the first one yields

$$\dot{P}(x) = \frac{1}{i\hbar\ell} \int_{-\infty}^{+\infty} dx' \left(\partial_{x'} [P(x), \Phi(x')] \right) \theta(-x'-) \partial_{x'} \Phi(x'). \tag{2.20}$$

Carrying out a partial integration and using the commutator (2.16) results in

$$\dot{P}(x) = \frac{1}{\ell}\partial_x[\theta(-x-)\partial_x\Phi]. \tag{2.21}$$

Taking $\lim_{\epsilon\to 0}\int_{-\epsilon}^{\epsilon} dx$ of both sides while expressing $P(x)$ with Eq. (2.5) gives

$$\dot{Q}(0) = -\frac{1}{\ell}\partial_x\Phi(0). \tag{2.22}$$

Note that the sign differs from that given in Ref. [20], as our waveguide spans the region of negative x. From Eqs. (2.19) and (2.22) the boundary condition follows,

$$\frac{1}{\ell}\partial_x\Phi(0) = -\tilde{C}'\ddot{\Phi}(0) + \frac{\tilde{C}'}{C_\mathrm{r}}\dot{Q}_\mathrm{r}. \tag{2.23}$$

One can also obtain this boundary condition by considering the Kirchhoff's laws at $x = 0$.

Now we expand $\Phi(x)$ in terms of the wave equation eigenfunctions that satisfy the boundary condition (2.23) while short-circuiting the resonator (see Fig. 2.1). The wave equation reads

$$\ddot{\Phi} = v^2\partial_x^2\Phi, \quad v = 1/\sqrt{\varkappa\ell}, \quad x < 0. \tag{2.24}$$

It can be obtained from Eqs. (2.18) and (2.21). The general solution of the wave equation is

$$\Phi(x,t) = \Phi_\rightarrow(t - x/v) + \Phi_\leftarrow(t + x/v). \tag{2.25}$$

It is convenient to introduce $\varphi_{\rightleftarrows}(\omega)$ the Fourier transforms of $\Phi_{\rightleftarrows}(\tau)$, so that

$$\Phi_{\rightleftarrows}(\tau) = \frac{1}{\sqrt{2\pi}}\int_{-\infty}^{+\infty} d\omega e^{i\omega\tau}\varphi_{\rightleftarrows}(\omega). \tag{2.26}$$

With the resonator short-circuited, no current flows through C_r and $\dot{Q}_\mathrm{r} = 0$. In terms of $\varphi_{\rightleftarrows}(\omega)$, the boundary condition (2.23) with $\dot{Q}_\mathrm{r} \equiv 0$ reads

$$(1 - i\tilde{C}'Z_\mathrm{c}\omega)\varphi_\rightarrow = (1 + i\tilde{C}'Z_\mathrm{c}\omega)\varphi_\leftarrow \tag{2.27}$$

with $Z_\mathrm{c} = \sqrt{\ell/\varkappa}$ the characteristic impedance of the line. Introducing $\varphi = \varphi_\rightarrow(1 - i\tilde{C}'Z_\mathrm{c}\omega)(1 + \tilde{C}'^2Z_\mathrm{c}^2\omega^2)^{-1/2}$ and using Eqs. (2.26) we rewrite Eq. (2.25) as

$$\Phi_\mathrm{f}(x,t) = \sqrt{\frac{2}{\pi}}\int_0^\infty d\omega e^{i\omega t}\varphi(\omega)\cos\left(\frac{\omega}{v}x - \Delta_\omega\right) + \text{h. c.}, \tag{2.28}$$

$$\tan\Delta_\omega = \tilde{C}'Z_\mathrm{c}\omega. \tag{2.29}$$

It follows that the linear dispersion relation

$$\omega = vk \tag{2.30}$$

holds. In obtaining Eq. (2.28), it was used that since Φ is Hermitian, $\varphi^\dagger(-\omega) = \varphi(\omega)$. Also, as Φ is continuous, the expansion is valid up to and including $x = 0$. Subscript "f" signifies that the field is free of influence of the resonator degree of freedom. In

this case $\dot{\varphi} = 0$ and the use of Eq. (2.5) yields the charge density

$$P_{\mathrm{f}}(x,t) = i\varkappa(x)\sqrt{\frac{2}{\pi}}\int_0^\infty d\omega e^{i\omega t}\,\omega\varphi(\omega)\cos\Big(\frac{\omega}{v}x - \Delta_\omega\Big) + \text{h. c.}, \tag{2.31}$$

$$\varkappa(x) = \varkappa\theta(-x-) + \tilde{C}'\delta(x). \tag{2.32}$$

With C' at the line end, $x = 0$ is no longer a voltage node and a current antinode, as some current can flow into C'. This is more pronounced for higher frequencies, where the impedance of the capacitor is lower.

Based on expansions (2.28) and (2.31), we make a change of variables

$$\Phi(x,t) = i\int_0^\infty d\omega\sqrt{\frac{\hbar Z_{\mathrm{c}}}{\pi\omega}}[b(\omega,t) - b^\dagger(\omega,t)]\cos\Big(\frac{\omega}{v}x - \Delta_\omega\Big), \tag{2.33}$$

$$P(x,t) = \varkappa(x)\int_0^\infty d\omega\sqrt{\frac{\hbar Z_{\mathrm{c}}\omega}{\pi}}[b^\dagger(\omega,t) + b(\omega,t)]\cos\Big(\frac{\omega}{v}x - \Delta_\omega\Big) \tag{2.34}$$

for $x \le 0$. It is convenient to rewrite the Hamiltonian of the line and the effective coupling capacitor $\tilde{C}'$:

$$\begin{aligned}
&\int_{-\infty}^{0-} dx\Big(\frac{P^2}{2\varkappa} + \frac{(\partial_x\Phi)^2}{2\ell}\Big) + \int_{0-}^{0+} dx\frac{Q^2(x)}{2\tilde{C}'}\delta(x)\\
&\qquad = \lim_{\substack{\varepsilon,\eta\to 0\\ \eta>\varepsilon>0}}\Bigg[\int_{-\infty}^{0-\varepsilon} dx\Big(\frac{1}{2}\frac{P^2}{\varkappa\theta(-x-\eta) + \tilde{C}'\delta(x)} + \frac{(\partial_x\Phi)^2}{2\ell}\Big)\\
&\qquad\qquad + \int_{0-\varepsilon}^{0+\eta} dx\frac{1}{2}\frac{[\varkappa\dot{\Phi}\theta(-x-\eta) + Q\delta(x)]^2}{\varkappa\theta(-x-\eta) + \tilde{C}'\delta(x)}\Bigg]\\
&\qquad\qquad = \int_{-\infty}^{0+} dx\Bigg[\frac{P^2}{2\varkappa(x)} + \frac{(\partial_x\Phi)^2}{2\ell}\theta(-x-)\Bigg] = H_{\mathrm{w,c}}.
\end{aligned} \tag{2.35}$$

Further we need the orthogonality relations for the modes we expand the fields in:

$$\begin{aligned}
\frac{2}{\pi v}\int_{-\infty}^{0} dx\frac{\varkappa(x)}{\varkappa}\cos\Big(\frac{\omega'}{v}x + \Delta_{\omega'}\Big)\cos\Big(\frac{\omega''}{v}x + \Delta_{\omega''}\Big)\\
= \delta(\omega' - \omega'') + \delta(\omega' + \omega''),
\end{aligned} \tag{2.36}$$

$$\begin{aligned}
\frac{2}{\pi v}\int_{-\infty}^{0} dx\sin\Big(\frac{\omega'}{v}x + \Delta_{\omega'}\Big)\sin\Big(\frac{\omega''}{v}x + \Delta_{\omega''}\Big)\\
= \delta(\omega' - \omega'') - \delta(\omega' + \omega'').
\end{aligned} \tag{2.37}$$

Using those with the expansions (2.33)–(2.34), one arrives at

$$H_{\mathrm{w,c}} = \hbar\int_0^\infty d\omega\,\omega b^\dagger(\omega)b(\omega), \tag{2.38}$$

where we have dropped the constant, yet diverging, part of the energy.

$b(\omega)$ and $b^\dagger(\omega)$ are the operators of creation and annihilation of a photon with frequency ω in the waveguide. Indeed, one can show that the operators have the appropriate commutation relations. First we express $b(\omega)$ in terms of the fields:

$$b(\omega) = \sqrt{\frac{Z_{\mathrm{c}}}{\hbar\omega\pi}}\int_{-\infty}^{0} dx(P - i\omega\Phi)\cos\Big(\frac{\omega}{v}x + \Delta_\omega\Big). \tag{2.39}$$

Then use of the orthogonality relation (2.36) and the commutator (2.16) yields

$$[b(\omega'), b^\dagger(\omega)] = \delta(\omega - \omega'). \tag{2.40}$$

Now we express H_{wr} in terms of creation and annihilation operators. It follows from Eqs. (2.34) and (2.5) that

$$Q(0) = \tilde{C}' \int_0^\infty d\omega e^{i\omega t} \sqrt{\frac{\hbar Z_{\mathrm{c}} \omega}{\pi}} [b^\dagger(\omega) + b(\omega)] \cos \Delta_\omega. \tag{2.41}$$

It is more common to work with the annihilation operator

$$b_k = \sqrt{v}\, b(kv) \tag{2.42}$$

of a photon with wavevector k and its conjugate $b_k^\dagger$. The last equation follows from the fact that the number of photons $\langle b_k^\dagger b_k \rangle dk$ in an interval dk is the same as in the respective interval $d\omega$, $\langle b^\dagger(\omega) b(\omega) \rangle d\omega$; here dk and $d\omega$ can be related using the dispersion relation (2.30). Substituting expression (2.41) to (2.13) and rewriting in terms of b_k and $b_k^\dagger$ gives rise to

$$H_{\mathrm{wr}} = v Q_{\mathrm{r}} \int_0^\infty dk \frac{\tilde{C}'}{C_{\mathrm{r}}} \sqrt{\frac{\hbar Z_{\mathrm{c}} k}{\pi}} (b_k^\dagger + b_k) \cos \Delta_{kv}. \tag{2.43}$$

Rewriting (2.38) in terms of b_k and $b_k^\dagger$ yields

$$H_{\mathrm{w,c}} = \hbar \int_0^\infty dk\, \omega_k b_k^\dagger b_k. \tag{2.44}$$

In what follows, we will also need the expression for voltage of the right-propagating wave,

$$U_\rightarrow(x,t) = \frac{P_\rightarrow(x,t)}{\varkappa(x)} = \int_0^\infty dk \sqrt{\frac{\hbar Z_{\mathrm{c}} v^2 k}{\pi}} (b_k^\dagger e^{-ikx - \Delta_{vk}} + \text{h. c.}), \tag{2.45}$$

where it was used that $b_k \propto e^{-ivkt}$ to pick the terms that describe the right-propagating waves from Eq. (2.34). The expressions for the left-propagating voltage $U_\leftarrow$ and for $\Phi_\rightarrow$ and $\Phi_\leftarrow$ can be obtained analogously.

Chapter III

Qubit readout with a homodyne detector

In the homodyne readout, one measures the quadratures of the signal transmitted[1] through the resonator. We reviewed the homodyne measurement of the quadratures in Sec. I.3.1. From those quadratures the qubit state can be inferred. In this chapter, we calculate the expressions for the average values of the quadratures.

1 Continuous measurement

For simplicity, we assume that the resonator is driven continuously. The drive is turned on in the initial instant of time $t = 0$. Its amplitude slowly, as compared to the inverse transition frequencies of the system, approaches its steady-state value. One then waits until the transients settle down and measures the transmitted signal in its steady state. In Chs. IV and V, we will also consider a continuous measurement. Hence the Hamiltonian and some of the results presented below are used in those chapters.

2 Hamiltonian

Hamiltonian of the system reads:

$$H = H_{\rm q} + H_{\rm qr} + H_{\rm r} + H_{\rm rI} + H_{\rm rII} + H_{\rm I} + H_{\rm II}, \tag{3.1}$$

where

$$H_{\rm q} = \frac{1}{2}\hbar[\omega_q + F(t)]\sigma_{\rm z}, \tag{3.2}$$

$$H_{\rm r} = \hbar\omega_{\rm r}\left(a^\dagger a + \frac{1}{2}\right), \tag{3.3}$$

$$H_{\rm qr} = \hbar g(\sigma_+ a + \text{h. c.}) \tag{3.4}$$

are the Hamiltonians of the qubit, resonator and the qubit-resonator interaction, respectively. The qubit longitudinally couples to the classical noise $F(t)$, for which $\langle F(t)\rangle = 0$. Inclusion of $F(t)$ phenomenologically[2] models loss of the qubit coherence

[1] The reflected signal can be used as well, but that requires additional complexity in the experimental setup.

[2] For microscopic models, see Refs. [65, 66].

that is unrelated to its coupling to the resonator—what we call the *natural* decoherence. Hamiltonians of the waveguide fields are

$$H_\alpha = \hbar \int_0^\infty dk\, \omega_k b_k^{\alpha\dagger} b_k^\alpha, \quad \alpha = \mathrm{I}, \mathrm{II} \tag{3.5}$$

according to Eq. (2.44). Here $b_k^{\mathrm{I}\dagger}, b_k^{\mathrm{I}}$ and $b_k^{\mathrm{II}\dagger}, b_k^{\mathrm{II}}$ are the operators of creation and annihilation of a photon with a wavevector k in the first and the second transmission line, respectively. Modes of transmission lines constitute a heat bath the resonator photon relaxes to. The terms responsible for interaction of the waveguides with the resonator are

$$H_{\mathrm{r}\alpha} = \hbar \int_0^\infty dk f_k (a^\dagger b_k^\alpha + \text{h. c.}). \tag{3.6}$$

Equation (3.6) is obtained from Eq. (2.43). The expression (1.10) is used for Q_{r} and the RWA is made.

2.1 Driving with coherent radiation

Here we split the mode operators of the first waveguide into the operators of the drive and the operator of the rest.

To drive a circuit QED system, radiation of a room-temperature classical generator is attenuated in several stages at lower and lower temperatures [5, 31], thus avoiding the thermal noise. Hence we assume that at $t = 0$ the first waveguide field is in the coherent state [67]

$$|\{c_k\}\rangle = \exp\left(\int_0^\infty dk\, b_k^{\mathrm{I}\dagger} c_k - \text{h. c.}\right)|0\rangle. \tag{3.7}$$

Here $c_k = v\,(2\pi)^{-1} \int_{-\infty}^{\infty} dt e^{ivkt}(c + c^*)$ is the Fourier transform of a signal $c(t) + c^*(t)$ with the negative-frequency part

$$c(t) = \int_0^\infty dk\, c_k e^{-i\omega_k t}, \tag{3.8}$$

where $\omega_k = vk$ according to the dispersion relation (2.30). As can be shown by a simple generalization of Sec. 5 treatment, the average voltage incident at the resonator is proportional to the signal $c + c^*$.

Now we split out the drive operators, similarly to what was done in Ref. [16] for the laser driving. Consider the displacement operator

$$D(t) = \exp\left(\int_0^\infty dk\, b_k^{\mathrm{I}\dagger} c_k e^{-i\omega_k t} - \text{h. c.}\right). \tag{3.9}$$

If one moves to the displaced frame by transforming the system wavefunction $|\psi\rangle \to D|\psi\rangle$, the initial condition on $|\psi\rangle$ is $|0\rangle$ as $D(0)|0\rangle = |\{c_k\}\rangle$. However, an additional interaction term arises in the Hamiltonian (3.1):

$$H_{\mathrm{I}} + H_{\mathrm{rI}} \to D^\dagger (H_{\mathrm{I}} + H_{\mathrm{rI}}) D - i\hbar D^\dagger \dot{D} = H_{\mathrm{I}} + H_{\mathrm{rI}} + H_{\mathrm{rd}}. \tag{3.10}$$

Here $H_{\mathrm{rd}} = \int_0^\infty dk (f_k a^\dagger c_k e^{-i\omega_k t} + \text{h. c.})$ is the Hamiltonian of the drive-resonator coupling. The transformation (3.9) can be shown to be composed of moving into the interaction picture, displacing each b_k by c_k and moving out of the interaction picture. This sequence is also the simplest way to obtain the Hamiltonian (3.10).

As discussed in Sec. 1, we assume that $c(t = 0) = 0$. On the other hand, we measure the transmitted signal in the steady state. At these times the drive can be considered monochromatic, i.e.,

$$c(t) \approx c(0)e^{-i\omega_{\mathrm{d}}t} \text{ for } t \gg \kappa^{-1}. \tag{3.11}$$

Here we formally define $c(0)$ so that $c_k = c(0)\delta(k - \omega_{\mathrm{d}}/v)$, where the dispersive relation (2.30) is used. In our convention $|c(0)|^2$ is the average density, per unit length, of photons in the incident flux. After all, by plugging the monochromatic c_k into H_{rd} from Eq. (3.10), we arrive at the drive Hamiltonian in the steady state continuous measurement:

$$H_{\mathrm{rd}} \approx \hbar f[a^\dagger c(t) + \text{h. c.}], \tag{3.12}$$

where $f = f_{\omega_{\mathrm{d}}/v}$.

For clarity, we write out the displaced full Hamiltonian:

$$H \to H_{\mathrm{q}} + H_{\mathrm{qr}} + H_{\mathrm{r}} + H_{\mathrm{rI}} + H_{\mathrm{rII}} + H_{\mathrm{rd}} + H_{\mathrm{I}} + H_{\mathrm{II}}. \tag{3.13}$$

2.2 Full Hamiltonian in the dispersive frame

We diagonalize the Jaynes-Cummings Hamiltonian $H_{\mathrm{q}} + H_{\mathrm{qr}} + H_{\mathrm{r}}$ with the dispersive transform (1.34), which yields the dispersive Hamiltonian (1.36). To transform the full Hamiltonian (3.1) we express the bare operators σ_{z} and a in terms of their dressed counterparts,

$$a \to U_{\mathrm{d}}^\dagger a U_{\mathrm{d}} = a + \lambda\sigma_- + O(\lambda^2), \tag{3.14}$$

$$\sigma_{\mathrm{z}} \to \sigma_{\mathrm{z}} - 2\lambda(\sigma_+ a + a^\dagger \sigma_-) + O(\lambda^2), \tag{3.15}$$

and use Eq. (1.35). This yields the full system dressed Hamiltonian:

$$\begin{aligned} H \to U_{\mathrm{d}}^\dagger H U_{\mathrm{d}} = {} & H_{\mathrm{q}} + \tilde{H}_{\mathrm{qr}} + H_{\mathrm{r}} \\ & + H_{\mathrm{rI}} + H_{\mathrm{rII}} + H_{\mathrm{rd}} \\ & + H_{F\mathrm{qr}} + H_{\mathrm{qI}} + H_{\mathrm{qII}} + H_{\mathrm{qd}} \\ & + H_{\mathrm{I}} + H_{\mathrm{II}} + o(\lambda) \end{aligned} \tag{3.16}$$

with

$$H_{\mathrm{q}\alpha} = \lambda\hbar \int_0^\infty dk f_k(\sigma_+ b_k^\alpha + \text{h. c.}), \tag{3.17}$$

$$H_{\mathrm{qd}} = \lambda\hbar f[\sigma_+ c(t) + \text{h. c.}], \tag{3.18}$$

$$H_{F\mathrm{qr}} = -\lambda\hbar F(t)(\sigma_+ a + \text{h. c.}), \tag{3.19}$$

and $\tilde{H}_{\mathrm{qr}}$ defined in Eq. (1.37).

Direct interaction between the dressed qubit and resonator vanishes in Eq. (3.16); however, qubit-bath and qubit-drive couplings appear. Due to these couplings, the dressed qubit and resonator are effective systems both interacting with transmission lines. Moreover, now the noise in the qubit transition frequency $F(t)$ causes not only the longitudinal decoherence of the qubit but also transitions of both the qubit and the resonator [68]. In the following sections and in Chs. IV and V, we work in the dressed picture.

3 Outgoing voltage in terms of the resonator field

According to Eq. (2.45), the operator of voltage of the right-propagating wave in the second waveguide is

$$U^{\mathrm{II}}_{\rightarrow}(x,t) = \frac{P_{\rightarrow}(x,t)}{\varkappa(x)} = \int_0^\infty dk \sqrt{\frac{\hbar Z_{\mathrm{c}} v^2 k}{\pi}} b^{\mathrm{II}}_k e^{ikx + i\Delta_{vk}} + \text{h. c.}. \tag{3.20}$$

One can find, analogously to the derivation of Eq. (1.57), that

$$b^{\mathrm{II}}_k(t) = b^{\mathrm{II}}_k(0) e^{-i\omega_k t} - i \int_0^t dt' f_k e^{-i\omega_k (t-t')} (a + \lambda\sigma_-)_{t'}. \tag{3.21}$$

Substituting Eq. (3.21) into Eq. (3.20) and using that the second waveguide is initially in the vacuum state, we have

$$\langle U^{\mathrm{II}}_{\rightarrow}(x,t)\rangle = -i \int_0^\infty dk f_k \sqrt{\frac{\hbar Z_{\mathrm{c}} v^2 k}{\pi}} \int_0^t dt' \langle a + \lambda\sigma_-\rangle_{t'} e^{-i\omega_k (t-t') + ikx + i\Delta_{vk}} + \text{c. c.}. \tag{3.22}$$

We assume that the incoming signal bands and the system resonances are sufficiently narrow. Then, analogously to the derivation of Eq. (1.60), we can extend the integral over k to the negative values and replace k in Eq. (3.22) with the wavevectors giving the main contribution to the integral:

$$\langle U^{\mathrm{II}}_{\rightarrow}(x,t)\rangle \approx -i \sqrt{\frac{\hbar Z_{\mathrm{c}} v}{\pi}} \int_0^t dt' \int_{-\infty}^\infty dk\, e^{-i\omega_k (t-t') + ikx} \times \langle f e^{i\Delta_{\omega_{\mathrm{r}}}} \sqrt{\omega}_{\mathrm{r}} a + \lambda f_{\mathrm{q}} e^{i\Delta_{\omega_{\mathrm{q}}}} \sqrt{\omega}_{\mathrm{q}} \sigma_- \rangle_{t'} + \text{c. c.}, \tag{3.23}$$

where

$$f = f_{\omega_{\mathrm{d}}/v} \approx f_{\omega_{\mathrm{r}}/v}, \quad f_{\mathrm{q}} = f_{\omega_{\mathrm{q}}/v}. \tag{3.24}$$

Using that $\int_{-\infty}^\infty dk\, e^{-i\omega_k (t-t') + ikx} = 2\pi v^{-1} \delta(t - t' + x/v)$ yields

$$\langle U^{\mathrm{II}}_{\rightarrow}(x,t)\rangle \approx -i \sqrt{\frac{4\pi\hbar Z_{\mathrm{c}}}{v}} \int_0^t dt' \delta(t' - t + \frac{x}{v}) \times \langle f e^{i\Delta_{\omega_{\mathrm{r}}}} \sqrt{\omega}_{\mathrm{r}} a + \lambda f_{\mathrm{q}} e^{i\Delta_{\omega_{\mathrm{q}}}} \sqrt{\omega}_{\mathrm{q}} \sigma_- \rangle_{t'} + \text{c. c.} \tag{3.25}$$

With no loss of generality, we seek an expression for the voltage at the very beginning of the waveguide:

$$\langle U^{\mathrm{II}}_{\rightarrow}(x = 0^+, t)\rangle = -i \sqrt{\frac{4\pi\hbar Z_{\mathrm{c}}}{v}} \langle f e^{i\Delta_{\omega_{\mathrm{r}}}} \sqrt{\omega}_{\mathrm{r}} a + \lambda f_{\mathrm{q}} e^{i\Delta_{\omega_{\mathrm{q}}}} \sqrt{\omega}_{\mathrm{q}} \sigma_- \rangle_t + \text{c. c.} \tag{3.26}$$

for $t > 0$.

Strictly speaking, the voltage depends on both the resonator and the qubit states. This coincides with the view of them as effective systems both connected to the waveguide. However, as the rotating-wave approximation dictates the qubit and resonator frequencies to be of the same order, the qubit term in Eq. (3.26) is negligible due to λ being small. Therefore,

$$\langle U^{\mathrm{II}}_{\rightarrow}(x = 0^+, t)\rangle \approx -i \sqrt{\hbar \omega_{\mathrm{r}} Z_{\mathrm{c}} \kappa} \langle a(t)\rangle e^{i\Delta_{\omega_{\mathrm{r}}}} + \text{c. c.}, \quad t > 0, \tag{3.27}$$

where

$$\kappa = 4\pi f^2/v \tag{3.28}$$

will be shown to be the resonator decay rate. Note, that after the qubit wavefunction collapse, σ_- vanishes and Eq. (3.27) becomes exact. The phase shift $\Delta_{\omega_\mathrm{r}}$ is due to the coupling capacitor; see the explanation for Eq. (2.31).

4 Evolution of the resonator field

Here we find an explicit expression for $a(t)$ the annihilation operator of the resonator photon. First, let us obtain the Langevin equation for it. The evolution equation for the operator reads

$$\dot{a}(t) = -i\tilde{\omega}_\mathrm{r}(t)a(t) - i\int_0^\infty dk f_k(b_k^\mathrm{I} + b_k^\mathrm{II})_t - ifc(t) + i\lambda F(t)\sigma_-(t) + o(\lambda), \tag{3.29}$$

with $\tilde{\omega}_\mathrm{r}$ defined in Eq. (1.41). Analogously to the derivation of Eq. (1.60), we obtain

$$\begin{aligned}\dot{a}(t) = \left(-i\tilde{\omega}_\mathrm{r}(t) - \frac{\kappa}{2}\right)a(t) - ifc(t) - \lambda\frac{\kappa}{2}\sigma_-(t) \\ - i\int_0^\infty dk f_k[b_k^\mathrm{I}(0) + b_k^\mathrm{II}(0)]e^{-i\omega_k t} + i\lambda F(t)\sigma_-(t) + o(\lambda),\end{aligned} \tag{3.30}$$

where κ (3.28) is the resonator decay rate.

Now we find the formal solution of the equation. Notice that $\tilde{\omega}_\mathrm{r}(t)$ is constant in the accuracy of Eq. (3.30). Indeed, it is $\sigma_\mathrm{z}(t)$ that leads to changes in $\tilde{\omega}_\mathrm{r}(t)$; it can be found that $\dot{\sigma_\mathrm{z}}(t) = O(\lambda)$. Therefore $\tilde{\omega}_\mathrm{r}(t) = \omega_\mathrm{r} + g\lambda\sigma_\mathrm{z}(t) = \mathrm{const} + o(\lambda)$. It is then simple to write down the formal solution of Eq. (3.30):

$$\begin{aligned}a(t) = a(0)e^{-(i\tilde{\omega}_\mathrm{r}+\kappa/2)t} - \int_0^t dt' e^{-(i\tilde{\omega}_\mathrm{r}+\kappa/2)(t-t')}\Bigg(i\int_0^\infty dk f_k[b_k^\mathrm{I}(0) + b_k^\mathrm{II}(0)]e^{-i\omega_k t'} \\ + ifc(t') + \lambda\frac{\kappa}{2}\sigma_-(t') - i\lambda F(t')\sigma_-(t')\Bigg).\end{aligned} \tag{3.31}$$

Note that the exponents in the solution cannot be just expanded to the first order in λ. The term under the integral proportional to $c(t)$ oscillates with frequency $\omega_\mathrm{r} - \omega_\mathrm{d}$, which can be small or zero. This makes the $O(\lambda)$ term in the exponent under the integral matter.

We confine ourselves to the case of a steady state of the resonator field. Assume the drive is turned on before the preparation of a qubit state, and the qubit is prepared at time $t = 0$. Changing the qubit state shifts the cavity resonance, which leads to transients in the resonator field [69]; those transients fade for times

$$t \gg \kappa^{-1}. \tag{3.32}$$

As the drive is turned on before the qubit preparation, the respective transients have faded for those times too. In that case the resonator can be considered to be in a

steady state, and the formal solution (3.31) takes the form

$$a(t) = -\int_{-\infty}^{t} dt' e^{-(i\tilde{\omega}_\mathrm{r}+\kappa/2)(t-t')}\Bigg(i\int_0^\infty dk f_k[b_k^\mathrm{I}(0)+b_k^\mathrm{II}(0)]e^{-i\omega_k t'} + ifc(t') + \lambda\frac{\kappa}{2}\sigma_-(t') - i\lambda F(t')\sigma_-(t')\Bigg). \quad (3.33)$$

The last two terms under the integral in Eq. (3.33) contribute in the order of λ^2, as $\sigma_-(t)$ oscillates with the qubit frequency ω_q. Still, we estimate their contribution in detail—to be sure that the integration does not yield any factor to make the contribution matter. First, we assume that the coupling is strong, $\kappa \lesssim g$. Then the contribution of the third integrand in Eq. (3.33) is smaller than λ^2:

$$\int_{-\infty}^{t} dt' e^{-(i\tilde{\omega}_\mathrm{r}+\kappa/2)(t-t')}\lambda\frac{\kappa}{2}\sigma_-(t') \sim \frac{\kappa}{g}\frac{g\lambda}{|\omega_\mathrm{q}-\omega_\mathrm{r}|} \lesssim \lambda^2. \quad (3.34)$$

This is beyond the accuracy with which Eq. (3.33) was obtained and should not be accounted for. In what follows we also show that the last integrand in Eq. (3.33) contributes negligibly in the relevant expectation values.

Integration of the drive and bath terms in Eq. (3.33) gives rise to a solution of Eq. (3.30):

$$a(t) \approx \frac{fc(0)e^{-i\omega_\mathrm{d}t}}{\tilde{\omega}_\mathrm{dr}+i\kappa/2} + \int_0^\infty dk\frac{f_k}{\tilde{\omega}_\mathrm{kr}+i\kappa/2}[b_k^\mathrm{I}(0)+b_k^\mathrm{II}(0)]e^{-i\omega_k t} + i\lambda\sigma_-(t)\int_{-\infty}^{t} dt' e^{(i\omega_\mathrm{qr}-\kappa/2)(t-t')}F(t')e^{i\int_{t'}^{t}dt''F(t'')}, \quad (3.35)$$

$$\tilde{\omega}_{\beta\mathrm{r}} = \omega_\beta - \tilde{\omega}_\mathrm{r}, \quad \beta = k, \mathrm{d}. \quad (3.36)$$

To obtain the last term, we have used that $\sigma_-(t')e^{-i\omega_\mathrm{q}(t-t')-i\int_t^{t'}dt''F(t'')}$ varies slowly. In addition, we have neglected the dispersive shift $g\lambda$ to the bare qubit-resonator detuning $\omega_\mathrm{qr} = \omega_\mathrm{q} - \omega_\mathrm{r}$. The first term of the expression (3.35) describes the drive-induced part of the field. Note that it depends on the σ_z by means of the dressed frequency $\tilde{\omega}_\mathrm{r}$, which enables dispersive readout of the qubit. The second term describes the influence of the waveguide fluctuations. The last term describes the resonator transitions due to the fluctuations in the qubit frequency [68]. They arise due to the dressing by the qubit. Apart from the last term, the expression (3.35) was obtained in Ref. [27] in the bare picture for the case of a single reservoir with discrete modes.

Now we calculate $\langle a(t)\rangle$, which will allow us to find the voltage in the second waveguide (3.27). As it was already noted, σ_z should be considered constant in the approximation Eq. (3.30) is obtained. Then the average of each term of the sum in expression (3.35) splits as

$$\langle(\omega_{k\mathrm{r}} - g\lambda\sigma_\mathrm{z}(0) + i\kappa/2)^{-1}b_k^\alpha(0)\rangle = \langle(\tilde{\omega}_{k\mathrm{r}}+i\kappa/2)^{-1}\rangle\langle b_k^\alpha(0)\rangle \quad (3.37)$$

and vanishes, as initially both waveguides are in the vacuum state in the displaced picture. Then, we neglect the last term in Eq. (3.35). Correlation between σ_- and F arises only in the next order of λ [one can check that from Eq. (5.15) that we write out later]. Hence one can split the average in the last term of Eq. (3.35). Assuming

that F is Gaussian-distributed, we estimate the average of the integral there as

$$\int_{-\infty}^{t} dt' e^{(i\omega_{\rm qr}+\kappa/2)(t'-t)} \langle F(t') e^{i\int_{t'}^{t} dt'' F(t'')} \rangle \approx -\frac{i\Gamma_0}{\omega_{\rm qr}+i\Gamma_0+i\kappa/2}. \tag{3.38}$$

Here we have used an identity from Appendix A. Then, we have assumed that F is a white noise with $\langle F(t')F(t'')\rangle = \langle F^2\rangle \delta(t'-t'')$. That allows us to find $\langle \big(\int_t^{t'} dt'' F\big)^2\rangle \approx (t'-t)\langle F^2\rangle = 2(t'-t)\Gamma_0$. Later in Ch. V, we show that Γ_0 is the rate of the qubit natural decoherence [70]. Similarly to Eq. (3.34), we find with Eq. (3.38) that the last term of Eq. (3.35) is negligible when $\Gamma_0 \lesssim g$. In that regime, we expect this term to be of same magnitude even for non-Gaussian F. So, on neglecting it and using Eq. (3.37), we obtain:

$$\langle a(t)\rangle = \Big\langle \frac{f c(0) e^{-i\omega_{\rm d} t}}{\tilde{\omega}_{\rm dr}+i\kappa/2} \Big\rangle. \tag{3.39}$$

5 Quadratures of the outgoing voltage

It is natural to express the voltage measured (3.27) in terms of the amplitude of the incident wave voltage

$$U^{\rm I}_{\rightarrow}(x,t) = \int_0^\infty dk \sqrt{\frac{\hbar Z_{\rm c} v^2 k}{\pi}} (b^{\rm I}_k e^{ikx+i\Delta_{vk}} + \text{h. c.}) \tag{3.40}$$

in the frame that was not displaced by D (3.9). In this frame the state of the first waveguide is $|\{c_k\}\rangle$ (3.7). Using that $c_k = c(0)\delta(k-\omega_{\rm d}/v)$, one obtains, analogously to the derivation of Eq. (3.25):

$$\langle U^{\rm I}_{\rightarrow}(x,t)\rangle \approx \sqrt{\frac{\hbar Z_{\rm c} v \omega_{\rm d}}{\pi}} c(t) e^{ikx+i\Delta_{\omega_{\rm d}}} - i\sqrt{\frac{\hbar Z_{\rm c}}{\pi v}} \int_0^t dt' \delta(t'-t+\frac{x}{v}) \ldots + \text{c. c.} \tag{3.41}$$

The second term zeroes, as $x<0$ in the first waveguide. Average voltage just at the first port of the resonator is given by

$$\langle U^{\rm I}_{\rightarrow}(x=0^-,t)\rangle = U^{\rm I}_0 \cos(\omega_{\rm d} t + \Delta_{\omega_{\rm r}}), \tag{3.42}$$

where $U^{\rm I}_0 = 4fc(0)\sqrt{\hbar\omega_{\rm r} Z_c/\kappa}$ is the voltage amplitude that was expressed similarly to the prefactor in Eq. (3.27). For simplicity, we assumed $c(0)$ to be real. Drive and resonator frequencies were assumed to be close to each other, $|\omega_{\rm d}-\omega_{\rm r}| \ll \omega_{\rm r}$. Substituting Eq. (3.39) into Eq. (3.27) and using Eq. (3.42) we obtain

$$\langle U^{\rm II}_{\rightarrow}(x=0^+,t)\rangle = U^{\rm I}_0 \big[\langle I\rangle \cos(\omega_{\rm d} t + \Delta_{\omega_{\rm r}}) - \langle Q\rangle \sin(\omega_{\rm d} t + \Delta_{\omega_{\rm r}})\big], \tag{3.43}$$

where $\langle I\rangle$ is the dimensionless component in phase with the drive and $\langle Q\rangle$ is the quadrature component. They are defined by means of the operators

$$I = -\frac{\kappa^2/4}{(\omega_{\rm dr}-g\lambda\sigma_{\rm z})^2+\kappa^2/4}, \tag{3.44}$$

$$Q = \frac{(\omega_{\rm dr}-g\lambda\sigma_{\rm z})\kappa/2}{(\omega_{\rm dr}-g\lambda\sigma_{\rm z})^2+\kappa^2/4}. \tag{3.45}$$

In Ref. [71] expressions for "effective qubit measurement operators" are given. They coincide, for the case of a steady-state resonator, $t \gg \kappa^{-1}$, with Eqs. (3.44) and (3.45).

We also provide explicit expressions for the average quadratures. Applying the identity

$$f(\sigma_z) = \frac{1+\sigma_z}{2} f(1) + \frac{1-\sigma_z}{2} f(-1) \tag{3.46}$$

to the quadratures (3.44) and (3.45) we obtain for their expectation values

$$\langle I \rangle = \frac{1+\langle\sigma_z\rangle}{2} \frac{\kappa^2/4}{(\omega_{dr}-g\lambda)^2+\kappa^2/4} + \frac{1-\langle\sigma_z\rangle}{2} \frac{\kappa^2/4}{(\omega_{dr}+g\lambda)^2+\kappa^2/4}, \tag{3.47}$$

$$\langle Q \rangle = -\frac{1+\langle\sigma_z\rangle}{2} \frac{(\omega_{dr}-g\lambda)\kappa/2}{(\omega_{dr}-g\lambda)^2+\kappa^2/4} - \frac{1-\langle\sigma_z\rangle}{2} \frac{(\omega_{dr}+g\lambda)\kappa/2}{(\omega_{dr}+g\lambda)^2+\kappa^2/4}. \tag{3.48}$$

Dependencies of the quadratures on detuning for the qubit in either of two eigenstates are given on Fig. 3.1.

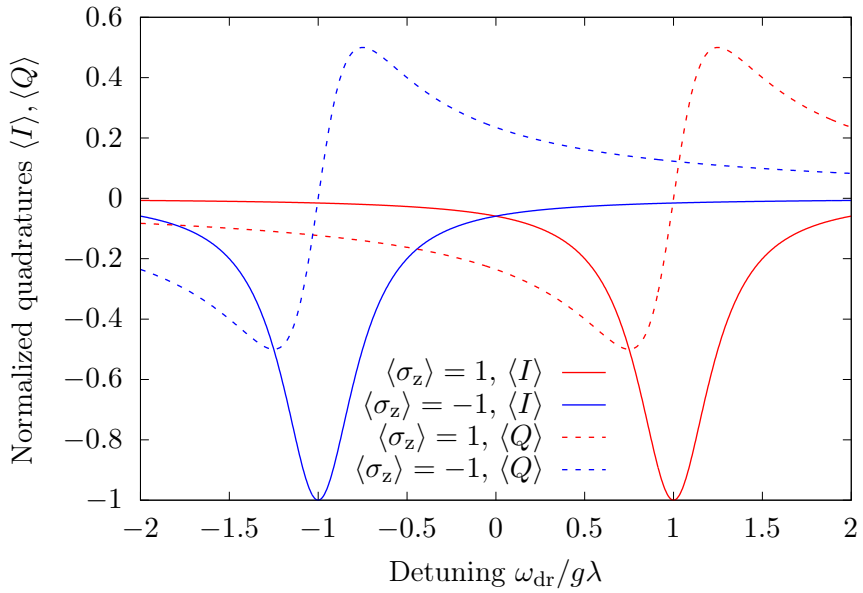

FIGURE 3.1: Dependence of the quadratures of transmitted voltage on detuning. Detuning ω_{dr} is given in units of $g\lambda$ the qubit Stark shift per one photon. Quadratures $\langle I\rangle$, $\langle Q\rangle$ are given in the units of amplitude of the incident voltage on the first port, $\langle U^{I}_{\rightarrow}(x=0^-, t=0)\rangle$. The resonator decay rate is $\kappa = g\lambda/2$.

Appendices

A Some averages involving Gaussian noise

Here we derive two known identities for averages that involve Gaussian-distributed noise x. First, simply by averaging with respect to the distribution, we prove the following identity:

$$\begin{aligned}\langle e^x \rangle &= \frac{1}{\sqrt{2\pi\langle x^2\rangle}} \int_{-\infty}^{+\infty} dx\, e^x \exp\left(-\frac{x^2}{2\langle x^2\rangle}\right) \\ &= \frac{1}{\sqrt{2\pi\langle x^2\rangle}} \int_{-\infty}^{+\infty} dx\, e^{\langle x^2\rangle/2} \exp\left(-\frac{(x-\langle x^2\rangle)^2}{2\langle x^2\rangle}\right) = \exp\frac{\langle x^2\rangle}{2}. \quad (3.A.1)\end{aligned}$$

We also prove another identity that we use in the main text. Introducing $X(t) = \int_{t_0}^{t} dt' x(t')$, we calculate that

$$\langle x(t) e^{X(t)} \rangle = \left\langle \frac{d}{dt} e^{X(t)} \right\rangle = \frac{1}{2}\left(\frac{d}{dt}\langle X^2\rangle\right) \exp\frac{\langle X^2\rangle}{2}, \quad (3.A.2)$$

where we have applied Eq. (3.A.1) for Gaussian-distributed X. The latter fact holds since a sum of Gaussian-distributed random values is again a Gaussian random variable. Another way to derive Eq. (3.A.2) is provided in §2.2 of Ref. [72].

Chapter IV

Qubit readout with a photon-number-resolving detector

In this chapter, we determine the optimal parameters for a simple scheme of dispersive readout of a qubit. In this scheme, continuous coherent radiation and a photodetector is used. Qubit state is inferred by detecting the photon number transmitted through the cavity. The use of a photodetector for the dispersive readout was already investigated in Refs. [2, 37]. There, the detector absorbs the cavity photons when the cavity is already populated. We consider the case of continuous drive and permanent resonator leakage, which is easier to achieve experimentally. Moreover, in the reference, the vacuum detector is studied: that is, a detector that cannot provide any information besides presence or absence of photons. In contrast, we deal with a detector able to distinguish any number of incident photons. We will show that, in the setup we consider, such a detector allows one to perform the measurement with a better accuracy.

We study the performance of a simple scheme for the dispersive readout with a photodetector. Readout accuracy can be characterized with the measurement contrast. We find the measurement parameters maximizing the contrast: the drive-resonator detuning and the ratio of a pull in the cavity resonance $g\lambda$ to the resonator leakage rate. The drive frequency is usually taken to match the pulled cavity resonance [27, 37, 69]. However, we show that this may result in a suboptimal contrast. We find the optimal detuning and resonator leakage. Surprisingly, they vary with the measurement duration. The other approach is to estimate the readout accuracy with the signal-to-noise ratio (SNR) in the photon count. Maximization of the SNR yields the parameters which are constant and simpler to use. The circumstances when these parameters result in close-to-optimal contrast are determined. We use our findings to estimate the duration of the readout for different physical realizations of the scheme.

1 Measurement scheme

We consider the following system (see Fig. 4.1a). A qubit interacts with one of the resonator modes. From the one side, the resonator is driven with a classical quasi-monochromatic pump. On the other side, a photon-number-resolving detector is placed. Photons leak out from the resonator by both sides. Both the detector and the drive source do not reflect the photons. Either of them may be connected to the

Chapter IV—except for Secs. 2 and 4.2, some excerpts from other sections, and Appendix A—was published in "A. Sokolov, Phys. Rev. A 93, 032323 (2016)".

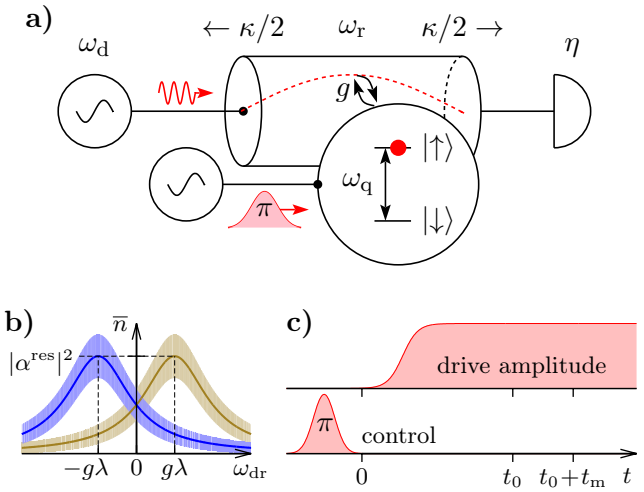

FIGURE 4.1: a) Schematic of the system which consists of: generators, a resonator coupled to a qubit, and a photocounter. b) Average number of photons transmitted, for the qubit in the ground state (blue line) and in the excited state (golden line). The root-mean-square deviation in the photon number is shown by the fill of respective color. c) Measurement sequence (times not to scale).

cavity by means of waveguides. Alternatively, the detector may be coupled directly to the resonator. The qubit state is controlled by a separate line.

We now describe the measurement sequence (see Fig. 4.1c). First the system is thermalized. Qubit relaxes into the ground state. Any mutual coherence between the qubit, the resonator, and the waveguide modes dies out. In case the measurement is to be carried out with the excited qubit, a π-pulse [70] is applied to the qubit at time $t = 0$. At the same time, the resonator drive is turned on. Some time after that, at $t = t_0$, one begins to count the detected photons. The time is chosen so that all transients in the cavity have faded and the drive can be considered monochromatic. The sequence ends at $t = t_0 + t_m$. It can be repeated to decrease the probability of an erroneous inferring of the qubit state.

Let us discuss one subtleness in the model. As it was already mentioned, the drive source is considered perfectly absorbing. It can be equivalently replaced [55] by a continuation to infinity of the waveguide that connects the cavity to the source. A wave generated by the source is then considered to come from the infinite waveguide. The same reasoning holds for the detector, which is also perfectly absorbing.

As the measurement sequence is very similar to that considered in Ch. III, we will use the Hamiltonian and some results from that section.

2 Photocounting statistics

To characterize the measurement, we need to know the dependence of photocounting statistics on the qubit state. Here we find the probability of a given count of detected photons, the average count, and the mean square deviation of the count. These quantities are found for the simplest case of the qubit occupying one of its eigenstates.

First we introduce a useful notation. Consider the density of photons [73, 74] that are traveling to the right in the second waveguide:

$$\langle \rho_{tr}(x,t)\rangle = \frac{1}{2\pi}\int_0^\infty \int_0^\infty dkdl \langle b_k^{II\dagger}(t) b_l^{II}(t)\rangle e^{-i(k-l)x}, \quad x > 0. \tag{4.1}$$

Here x is a distance from the second port of the resonator.

Photocounting statistics is given in terms of the photon density (4.1) as follows. The probability to detect n photons is given by [75–77]

$$P(n) = \Big\langle \mathrm{T}{:}\frac{W^n}{n!}e^{-W}{:}\Big\rangle, \tag{4.2}$$

where T:X: denotes the prescription of normal and time ordering of X, e.g.

$$\mathrm{T}{:}b^\dagger(t_1)b(t_1)b^\dagger(t_2)b(t_2){:} = \begin{cases} b^\dagger(t_1)b^\dagger(t_2)b(t_2)b(t_1), & t_1 < t_2 \\ b^\dagger(t_2)b^\dagger(t_1)b(t_1)b(t_2), & t_1 \geq t_2 \end{cases} \tag{4.3}$$

and

$$W = \eta v \int_{t_0}^{t_0+t_\mathrm{m}} dt' \langle \rho_\mathrm{tr}(t') \rangle \tag{4.4}$$

is number of photons absorbed by the detector. Here η is the efficiency of a photon counter, v is the speed of light, and t_m is the duration of the photocounting process. $v\langle\rho_\mathrm{tr}\rangle$ is the photon flux incident to the detector.

Now we find an expression for $P(n)$. This is accomplished by doing several simplifications. First, we place the detector at the beginning of the second waveguide. Secondly, thermal fluctuations in the waveguides are neglected. And lastly, we consider the qubit to occupy one of its eigenstates.

Let us express the sums over bath operators in Eq. (4.1) in terms of the resonator and qubit operators and the bath operators at time $t = 0$. We assume the detector placed at the very beginning of the second waveguide. This corresponds to $x = 0^+$ in Eq. (4.1). Any other placement shifts the phase of the radiation incident to the detector, which changes nothing for the photocounter. Taking an integral over all modes in Eq. (3.21) one obtains, analogously to the derivation of Eq. (3.26):

$$\Big(\int_0^\infty dk\, b_k^\mathrm{II}(t) e^{ikx} \Big)_{x=0^+} \approx \int_0^\infty dk\, b_k^\mathrm{II}(0) e^{-i\omega_k t} - \frac{2\pi i f}{v}(a + \lambda\sigma_-)_t \tag{4.5}$$

for $t > 0$. Up to a constant factor, the integral in the left-hand side of the equation is known as the output operator of the field [57]. As we have assumed a constant coupling f to the cavity as in Eq. (3.24), this operator depends only on the resonator state at the same instant of time: The equation describes our system in the Markov approximation, just as Eqs. (1.60) and (3.26) do.

Under reasonable conditions, $b_k^\mathrm{I}(0)$ and $b_k^\mathrm{II}(0)$ do not enter the expression for $P(n)$. Recall we have separated the drive out of the waveguide operators, by transforming the Hamiltonian with the displacement operator (3.9). In the resulting picture, we assume the waveguides to occupy the vacuum state $|0_\mathrm{w}\rangle$ at the initial instant of time $t = 0$. This is a viable assumption, for both optical and superconducting realizations. In optics, high frequencies make the number of thermal photons negligible at room temperature. Superconducting realizations operate in the microwave domain; however, the system is put inside a cryostat maintaining very low temperatures. At such temperatures, the effect of thermal radiation is negligible as well. Finding the expectation value of a normal-ordered expression with respect to $|0_\mathrm{w}\rangle$ zeroes any terms

containing $b_k^{\mathrm{I,II}}(0)$ or the conjugates. We have then

$$P(n) = \langle q|\langle 0_{\mathrm{w}}|\mathrm{T}{:}\frac{W^n}{n!}e^{-W}{:}|0_{\mathrm{w}}\rangle|q\rangle = \langle q|\mathrm{T}{:}\frac{\tilde{W}^n}{n!}e^{\tilde{W}}{:}|q\rangle, \tag{4.6}$$

$$\tilde{W} = \eta v \int_{t_0}^{t_0+t_{\mathrm{m}}} dt' \langle \tilde{\rho}_{\mathrm{tr}}(t')\rangle, \tag{4.7}$$

$$\langle \tilde{\rho}_{\mathrm{tr}}\rangle = \langle \rho_{\mathrm{tr}}|_{b_k(0)^{\mathrm{I,II}(\dagger)}\equiv 0}\rangle, \tag{4.8}$$

where $|q\rangle$ is the state vector of the qubit. As the resonator field is in the steady state given by Eq. (3.35), averages of our system do not depend on the initial state of the resonator. With the prescription (4.8), we express the photon density (4.1) in Eq. (4.2) in terms of the drive-induced part of the resonator field and the qubit operators. Using Eqs. (4.5) and (3.35), we arrive at

$$\langle \tilde{\rho}_{\mathrm{tr}}(t)\rangle = \frac{4\pi^2 f^2}{v^2}\big(|\tilde{\alpha}|^2 + \lambda\sigma_+\alpha + \lambda\alpha^*\sigma_-\big)_t + o(\lambda), \tag{4.9}$$

$$\tilde{\alpha}(t) = \frac{fc(0)e^{-i\omega_{\mathrm{d}}t}}{\tilde{\omega}_{\mathrm{dr}} + i\kappa/2}, \quad \alpha = \tilde{\alpha}\big|_{\lambda=0}. \tag{4.10}$$

In Eq. (4.9), we omit the term in $\langle\sigma_+ a\rangle$ induced by the noise F in the qubit frequency. Analogously to the derivation of Eq. (3.39), we find that this term is of order λ^2 when the qubit decoherence is slower than the coherent exchange between the qubit and the resonator, $\Gamma_0 \lesssim g$.

The photon flux can be considered unaltering on the interval from t_0 to $t_0 + t_{\mathrm{m}}$. One notices that the first term in Eq. (4.9) is constant by the definition (4.10) of $\tilde{\alpha}$. Subsequent time-dependent terms do not contribute substantially after integration in Eq. (4.7): one has

$$\int_{t_0}^{t_0+t_{\mathrm{m}}} dt' \lambda\sigma_+(t')\alpha(t') \sim \frac{\lambda}{\omega_{\mathrm{q}} - \omega_{\mathrm{d}}} \sim \lambda^2 \tag{4.11}$$

at least, and the same estimate for $\lambda\alpha^*\sigma_-$. Therefore,

$$\tilde{W} = \eta t_{\mathrm{m}} \frac{\kappa}{2}|\tilde{\alpha}|^2, \tag{4.12}$$

where we have used the expression for the resonator decay rate Eq. (3.28).

Let us discuss when it is possible to consider the resonator to be in the steady state. First, all transients in the resonator should vanish before the measurement begins. The condition for this is given by Eq. (3.32), in which t should be substituted with t_0. For clarity, we rewrite it here:

$$t_0 \gg \kappa^{-1}. \tag{4.13}$$

Second, during the measurement, the qubit should remain in the state in which it was set up. In the first-order approximation in λ, the measurement does not affect the qubit occupying one of its eigenstates. However, taking account of the next orders in λ shows the qubit excitation can leak to the waveguides through the resonator [21, 27, 28]. Moreover, our model does not account for the relaxation sources other than the waveguides (see Ref. [78], for example). Here it is sufficient to characterize all those processes with the longitudinal relaxation time T_1. Then the condition we have been talking about reads

$$t_0, t_{\mathrm{m}} \ll T_1. \tag{4.14}$$

The condition (4.14) is given in assumption of the single-shot measurement. However, it changes if one is free to perform a sequence of short measurements. In this case, one collects photons in N bins, each lasting t_m/N; a bin is carried out with a "fresh" qubit, prepared in a given state. The sum of all photons collected in bins obeys the same formula (4.2). Therefore, our further arguments apply for the case of sequential measurement, with t_m denoting the sum of bin durations. An analog of Eq. (4.14) for this case is

$$t_0, t_\mathrm{m}/N \ll T_1. \tag{4.15}$$

We calculate the expectation value in Eq. (4.6) for the qubit in one of its eigenstates. σ_z in Eq. (4.10) can be substituted either with 1 or -1 for $q = \uparrow$ or $\downarrow$, respectively. One arrives at the Poisson distribution

$$P_q(n) = \frac{(\overline{n}_q)^n}{n!} e^{-\overline{n}_q} \tag{4.16}$$

with

$$\overline{n}_q = \eta t_\mathrm{m} \frac{\kappa}{2} \langle q|\tilde{\alpha}^* \tilde{\alpha}|q\rangle \tag{4.17}$$

the average count of detected photons for the qubit in either of eigenstates $q = \uparrow, \downarrow$.

The mean-square deviation of a Poisson-distributed quantity is well known; it is equal to the average value of a quantity. Thus,

$$\overline{\Delta n^2}_q = \overline{n}_q. \tag{4.18}$$

We express the average count (4.17) in terms of the system parameters explicitly. Substituting Eq. (4.10) into Eq. (4.17) and rearranging, one has

$$\overline{n}_\uparrow = \frac{\eta t_m (\kappa/2)^3 \, |\alpha^\mathrm{res}|^2}{(\omega_\mathrm{dr} - g\lambda)^2 + \kappa^2/4}, \quad \overline{n}_\downarrow = \frac{\eta t_m (\kappa/2)^3 \, |\alpha^\mathrm{res}|^2}{(\omega_\mathrm{dr} + g\lambda)^2 + \kappa^2/4} \tag{4.19}$$

with

$$|\alpha^\mathrm{res}|^2 = 4f^2 |c|^2/\kappa^2 \tag{4.20}$$

the average number of photons that enter the cavity at resonance.

By Eq. (4.19), the statistics (4.16) has symmetries: $\omega_\mathrm{dr} \to -\omega_\mathrm{dr}$, "$\uparrow$" $\to$ "$\downarrow$" and analogous for $g\lambda$. This is a consequence of neglecting relaxation. Readout characteristics are set by the statistics; as they cannot depend on qubit states labeling, they are even functions of ω_dr and $g\lambda$. Hence it is enough to consider the case of positive detuning and pull,

$$\omega_\mathrm{dr}, g\lambda > 0. \tag{4.21}$$

Statistics of the photocounts, given by Eqs. (4.16)–(4.18), is the same as if coherent light was detected; it is possible to show that the state of the radiation in the second waveguide is a coherent state indeed. The qubit and the resonator are coupled dispersively, which means they don't exchange energy. The resonator can be considered as not interacting with the qubit, even though its frequency becomes shifted. A standalone resonator driven by a continuous monochromatic pump is known to reside in the coherent state [76]; radiation in the very state leaks to the waveguides. In a more formal way, this is shown in Refs. [79] and [80] using the master equation formalism.

With the photocounting statistics obtained, in the next two sections we characterize the robustness of the qubit measurement.

3 Signal-to-noise ratio

In this section, we calculate SNR of a count of detected photons, and the conditions optimizing the ratio. The conditions for the maximal SNR is determined for two cases. First, we suppose one has a measurement setup with a fixed dispersive pull $g\lambda$ and a fixed resonator damping rate κ. With respect to $g\lambda$ and κ, an optimal detuning $\omega_{\rm dr}$ is found. In the other case, either κ or $g\lambda$ can be varied as well.

We define SNR in our measurement as follows. A useful signal is the difference between the average photocounts for the qubit in the excited and the ground states. In both cases, the number of the photons detected fluctuates around its mean (see Fig. 4.1b). Noise in the signal is then given by the sum of fluctuations in both cases. That is,

$$\mathrm{SNR} = \frac{|\overline{n}_\uparrow - \overline{n}_\downarrow|}{\sqrt{\overline{\Delta n^2}_\uparrow} + \sqrt{\overline{\Delta n^2}_\downarrow}}. \tag{4.22}$$

A somewhat different expression is given in Ref. [53] in a similar context. While there is no substantial quantitative difference in using those two, for our purposes the form (4.22) results in cleaner math. Particularly, it is this form that appears naturally in the expression for contrast in Sec. 4.4.

For Poissonian statistics we have, Eq. (4.22) simplifies. Substituting Eq. (4.18) into it and rationalizing the denominator gives rise to

$$\mathrm{SNR} = \sqrt{\overline{n}_\uparrow} - \sqrt{\overline{n}_\downarrow}. \tag{4.23}$$

While deriving the last expression, we have used that $\overline{n}_\uparrow > \overline{n}_\downarrow$ due to Eq. (4.21). A different expression for SNR is widely used in the literature on cavity quantum electrodynamics with superconducting circuits [31, 68, 79, 81]. It is obtained for the homodyne measurement.

We proceed to determine the conditions of maximum of SNR given by this expression.

3.1 Optimizing with respect to detuning

Let us consider the case of fixed resonator damping rate κ and fixed dispersive pull $g\lambda$. Also, we require that the average number of photons that dwell in the cavity at resonance, $|\alpha^{\rm res}|^2$ (4.20), is maintained constant. With a varying detuning, this can be achieved by the appropriate choice of the drive power, which changes ϵ^2 proportionally. Under these circumstances, we find the detuning that maximizes SNR.

Here it is convenient to introduce a set of dimensionless notations. With the notations, the mean counts (4.19) are expressed as

$$\overline{n}_\uparrow = \frac{\tau_{\rm m}}{(D-X)^2+1}, \quad \overline{n}_\downarrow = \frac{\tau_{\rm m}}{(D+X)^2+1}, \tag{4.24}$$

where

$$\tau_{\rm m} = \eta\frac{\kappa}{2}|\alpha^{\rm res}|^2 t_{\rm m} \tag{4.25}$$

is the dimensionless measurement time. $\tau_{\rm m}$ gives the average count of photons absorbed by the detector in case the drive is resonant with the cavity. Also,

$$D = \frac{\omega_{\rm dr}}{\kappa/2} \tag{4.26}$$

is the dimensionless detuning, and

$$X = \frac{g\lambda}{\kappa/2} \tag{4.27}$$

is the dimensionless dispersive pull.

With Eq. (4.24), Eq. (4.23) takes the form

$$\mathrm{SNR} = \sqrt{\tau_\mathrm{m}} \left(1/\sqrt{(D-X)^2+1} - 1/\sqrt{(D+X)^2+1} \right). \tag{4.28}$$

Now we find the optimal detuning D^opt. Carrying out the derivative of the SNR (4.28) and equating it to zero one arrives at

$$\frac{D^\mathrm{opt}+X}{\left[(D^\mathrm{opt}+X)^2+1\right]^{3/2}} - \frac{D^\mathrm{opt}-X}{\left[(D^\mathrm{opt}-X)^2+1\right]^{3/2}} = 0. \tag{4.29}$$

Due to Eq. (4.21), $D^\mathrm{opt}, X > 0$. Therefore, the equation could have a real solution only if

$$D^\mathrm{opt} > X. \tag{4.30}$$

In Appendix A it is shown that a critical point from Eq. (4.29) is indeed a point of maximum. Another inequality,

$$D^\mathrm{opt} < \sqrt{X^2+1}, \tag{4.31}$$

is of use. It can be obtained by multiplying the left- and the right-hand sides of the inequality $\sqrt{D^\mathrm{opt}+X} > \sqrt{D^\mathrm{opt}-X}$ by the first and the second term from Eq. (4.29) and performing some algebra. It is difficult to obtain an analytical solution to Eq. (4.29). We have found numerically[1] its roots in the range given by Eqs. (4.30) and (4.31). The resulting dependence of D^opt on X is shown in Fig. 4.2. One can check that the given solutions satisfy Eq. (4.31). It is also seen that only at large X the optimal detuning is $D \approx X$.

This discrepancy with an intuitive choice of detuning can be explained. Just as it seems, probing the cavity at one of its resonances maximizes the difference of transmitted photons between the qubit eigenstates (see Fig. 4.1b). However, there is a shot noise in the photon number for both eigenstates, which needs to be accounted for. It turns out that with a proper detuning, the sum of noises decreases more than the difference in photon number. This increases SNR, as compared to the resonant probe case.

The difference $D^\mathrm{opt} - X$ is plotted in Fig. 4.3, and the effect on SNR of the optimal choice of detuning is illustrated. The difference between the optimal ($D = D^\mathrm{opt}$) and the naive ($D = X$) detuning is appreciable for the whole range of X given in the plot; in contrast, the interval where the increase in SNR is noticeable is substantially narrower. It is worth using the optimal D under the conditions of weak measurement, $X < 1$, as for a stronger measurement the increase in SNR is less than 1%. Note that in the weak-measurement interval of X the ratio $\mathrm{SNR}/\sqrt{\tau_\mathrm{m}}$ still reaches 0.5.

Let us obtain an approximation of D^opt for big X. As in this case the value of D^opt is close to X, we expand the equation on D^opt (4.29) in series in

$$\xi = D^\mathrm{opt} - X, \tag{4.32}$$

[1] The MATLAB/OCTAVE codes for the numerics in this chapter are available as a part of the GitLab repository [82].

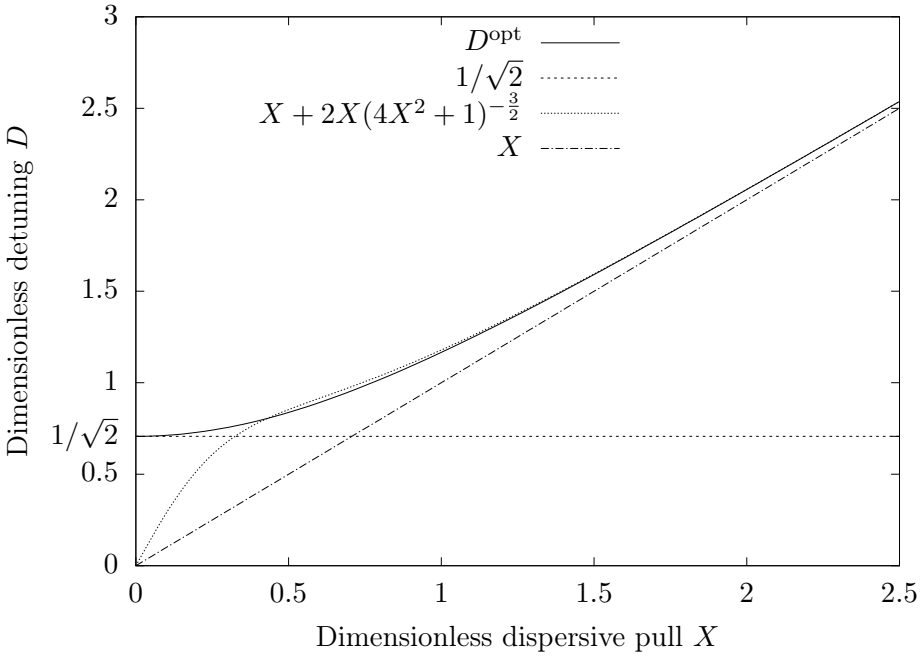

FIGURE 4.2: Optimal dimensionless detuning D (4.26) and some approximations to it, as functions of the dimensionless dispersive pull X (4.27).

leaving the terms up to the linear one. Assuming $\xi \ll 4X$, one obtains

$$\frac{1}{\left[(2X+\xi)^2+1\right]^{3/2}} = \frac{1}{(4X^2+1)^{3/2}}\left(1 - \frac{3}{2}\frac{4X\xi}{4X^2+1}\right) + o\left(\frac{4X\xi}{4X^2+1}\right). \tag{4.33}$$

Substituting the expression to Eq. (4.29) and omitting the terms quadratic in ξ one can solve the resulting linear equation on ξ. This gives

$$D^{\mathrm{opt}} - X = \xi \approx \frac{2X(4X^2+1)}{8X^2 + (4X^2+1)^{5/2} - 1}, \tag{4.34}$$

$$\xi^2 \ll [X + (4X)^{-1}]^2/16, \quad \xi^2 \ll 1. \tag{4.35}$$

The first inequality in Eq. (4.35) is the condition of the little-o term in Eq. (4.33) being negligible; the assumption of $\xi \ll 4X$ we have used deriving Eq. (4.33) follows from this inequality. The other condition in Eq. (4.35) arises when the second term in Eq. (4.29) is approximated by ξ. Expression (4.34) has the anticipated asymptote,

$$D^{\mathrm{opt}} - X \underset{X\to\infty}{\longrightarrow} 0. \tag{4.36}$$

From Eq. (4.34), a simpler approximation can be obtained,

$$D^{\mathrm{opt}} \approx X + 2X(4X^2+1)^{-3/2}, \tag{4.37}$$

which is the one shown in Fig. 4.2. For practical purposes it works well for $X > 0.4$, a range of use even better than that of Eq. (4.34). However, one can check that the latter expression, being better grounded mathematically, fits the exact solution of Eq. (4.29) in a nicer fashion, albeit in more narrow range of X.

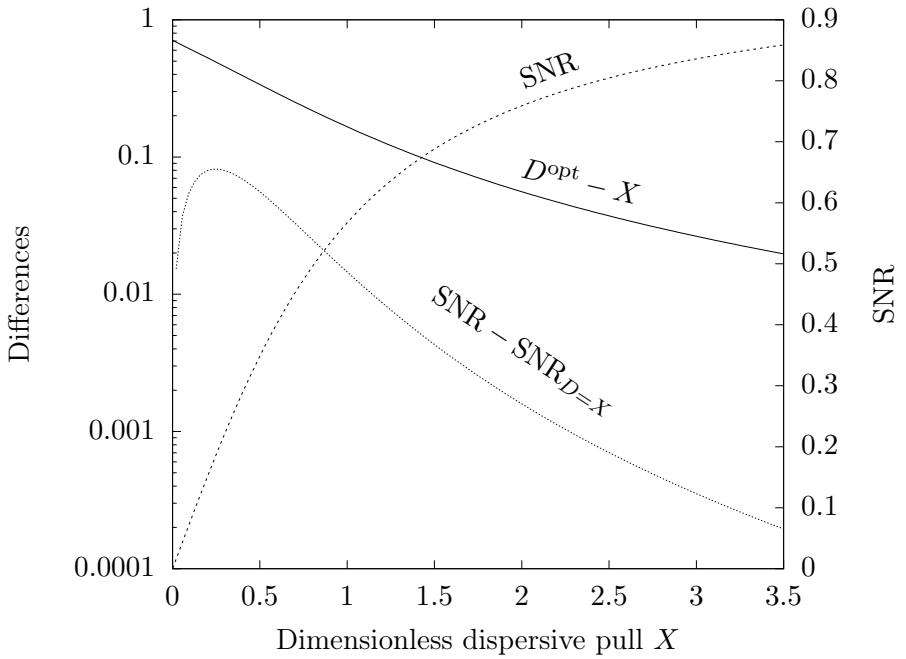

FIGURE 4.3: Comparison of the optimal-SNR ($D = D^{\mathrm{opt}}$) and the naive ($D = X$) drive-resonator detuning. SNR^1 denotes the SNR for $\tau_{\mathrm{m}} = 1$. As defined in Eqs. (4.26) and (4.27), D and X are the dimensionless detuning and dispersive pull, respectively.

Now consider the case of small X. We assume that $D > X$. An approximate identity takes place, up to linear terms in X:

$$\frac{D}{\left[(D \pm X)^2 + 1\right]^{3/2}} \approx \frac{D}{(D^2+1)^{3/2}} \left(1 \mp \frac{3DX}{D^2+1}\right). \tag{4.38}$$

We substitute Eq. (4.38) into Eq. (4.29) and find the solution of the resulting equation. This gives the small-X approximation,

$$D^{\mathrm{opt}} \approx 1/\sqrt{2}, \quad X^2 \ll 1. \tag{4.39}$$

In the case of $X \gg 1$, SNR has a simple dependence on the resonator leakage κ. By Eq. (4.36), the optimal detuning in this case is $D = X$ and Eq. (4.28) reduces to

$$\mathrm{SNR} = \sqrt{\tau_{\mathrm{m}}}. \tag{4.40}$$

From Eqs. (4.25) and (4.40) it follows that, at a fixed number of photons for the cavity in resonance, $|\alpha^{\mathrm{res}}|^2 = \mathrm{const}$, SNR increases with the damping rate κ as square root. Physically, this means that as far as the resonator decay rate is negligible to the dispersive pull, one can increase the decay rate to allow more photons to leak out of the cavity; this improves SNR.

SNR is determined by the interplay of two effects that depend on the resonator decay rate. Increasing κ allows more photons to leak out of the cavity. On the other hand, decreasing κ improves the resolution of the two spectral peaks corresponding to the qubit eigenstates. Therefore, one anticipates there is an optimal value of the decay rate. We will determine it in the next subsection.

3.2 Optimizing with respect to detuning and the pull/damping ratio

Here we consider the situation when, apart from the detuning, one is able to vary the ratio of the dispersive pull to the cavity damping rate. As before, the average number of cavity photons at resonance (4.20) is maintained constant. We show how the upper bound on SNR for the measurement can be approached.

The assumption of the variable pull/damping ratio $g\lambda/\kappa$ is quite plausible. The ratio can be varied in two ways. First, κ can be set on the design stage of an experiment. Fabrication of both optical and superconducting resonators is quite reproducible and the leakage rate can be chosen with an appreciable precision. Second, for the superconducting experiments, it is usually possible to tune the qubit frequency $\omega_{\rm q}$ *in situ* [18]. By varying $\omega_{\rm q}$ one changes λ (1.31) and hence the pull/damping ratio.

Let us introduce the dimensionless detuning and decay rate

$$\Delta = \frac{\omega_{\rm dr}}{g\lambda}, \quad K = \frac{\kappa/2}{g\lambda}. \tag{4.41}$$

In these notations the mean counts (4.19) are given by

$$\overline{n}_{\uparrow} = \frac{K^3 T_{\rm m}}{(\Delta-1)^2+K^2}, \quad \overline{n}_{\downarrow} = \frac{K^3 T_{\rm m}}{(\Delta+1)^2+K^2}, \tag{4.42}$$

where we have introduced the dimensionless time

$$T_{\rm m} = \eta\, g\lambda\, |\alpha^{\rm res}|^2 t_{\rm m}. \tag{4.43}$$

With Eqs. (4.42)–(4.43), SNR (4.23) is expressed as

$$\mathrm{SNR} = \sqrt{T_{\rm m}}\cdot K^{3/2}\left(\frac{1}{\sqrt{(\Delta-1)^2+K^2}} - \frac{1}{\sqrt{(\Delta+1)^2+K^2}}\right). \tag{4.44}$$

Equation (4.43) suggests the optical range is favorable for our scheme. To see this, one can rewrite Eq. (4.43),

$$T_{\rm m} = \frac{1}{4}\frac{|\alpha^{\rm res}|^2}{n^{\rm cr}}\eta|\omega_{\rm q}-\omega_{\rm r}|t_{\rm m}, \tag{4.45}$$

and the condition (1.32) for the measurement being non-demolition,

$$(n_{\rm ch}+1)/n_{\rm cr} \ll 1, \quad n_{\rm cr} = (2\lambda)^{-2}, \tag{4.46}$$

in terms of a critical number $n_{\rm cr} = (2\lambda)^{-2}$. The physical meaning of $n_{\rm cr}$ is that the dispersive regime breaks down at this number of excitations. The ratio $|\alpha^{\rm res}|^2/n_{\rm cr}$ is small by condition (4.46). For the same values of the ratio, bigger $|\omega_{\rm q}-\omega_{\rm r}|$ results in higher $T_{\rm m}$ and better readout. However, by the condition (1.24) the difference should be much smaller than the characteristic frequencies of the system. Therefore, high frequencies are favorable.

We find the maximum of SNR with respect to K and Δ. Equating partial derivatives to zero gives the set of equations

$$\frac{\Delta+1}{\left[(\Delta+1)^2+K^2\right]^{3/2}} = \frac{\Delta-1}{\left[(\Delta-1)^2+K^2\right]^{3/2}}, \tag{4.47}$$

$$\frac{3(\Delta+1)^2+K^2}{\left[(\Delta+1)^2+K^2\right]^{3/2}} = \frac{3(\Delta-1)^2+K^2}{\left[(\Delta-1)^2+K^2\right]^{3/2}} \tag{4.48}$$

which determine the critical point. Note Eq. (4.47) is the same as Eq. (4.29), despite being written in other notations. The solution of Eqs. (4.47)-(4.48) reads

$$\Delta = \sqrt{5}/2, \quad K = \sqrt{3}/2. \tag{4.49}$$

One can check that, at the Δ and K given, SNR reaches global maximum.

Using the definitions (4.41) and Eq. (4.44), we express $\omega_{\rm dr}$, κ, and SNR in terms of $g\lambda$:

$$\omega_{\rm dr} \approx 1.118 g\lambda, \quad \kappa = 1.732 g\lambda, \tag{4.50}$$

$$\mathrm{SNR} \approx 0.570\sqrt{\eta t_{\rm m}\, g\lambda |\alpha^{\rm res}|^2}. \tag{4.51}$$

Note that using an asymmetrical cavity one can increase SNR (4.51) substantially. In this case, the overall damping is $\kappa^{\rm I}+\kappa^{\rm II}$, where $\kappa^{\rm I}$ and $\kappa^{\rm II}$ are the rates cavity photons leak through the first and the second port. If the number of resonator photons is fixed, increasing $\kappa^{\rm I}$ only widens the resonator spectrum; thus one makes the rate as small as possible. On the other hand, $\kappa^{\rm II}$ gives the rate photons arrive at the detector. In the best case of $\kappa^{\rm I} \ll \kappa^{\rm II}$ one changes $\kappa/2$ to $\kappa^{\rm II}$ in the prefactor of the expression (4.17), while in the other occurrences κ is substituted with $\kappa^{\rm II}$. This doubles the dimensionless time $T_{\rm m}$ (4.43). Meanwhile, the optimal value of $\kappa^{\rm II}$ is the same as the optimal κ of the symmetrical case. We have an increase in SNR by the ratio of $\sqrt{2}$. The resulting value is the upper limit for SNR in the measurement we consider,

$$\mathrm{SNR} < 0.806\sqrt{\eta t_{\rm m}\, g\lambda |\alpha^{\rm res}|^2}. \tag{4.52}$$

We have investigated how to achieve the maximum SNR. However, SNR quantifies the measurement robustness only heuristically. Note that we haven't even specified the way one distinguishes upper and lower states of the qubit. Besides, the notion (4.22) of SNR takes into account only the two first moments $\overline{n}$ and $\overline{n^2}$ of the photon count. SNR cannot give a full description of fluctuations that obey Poisson statistics (4.16) and thus have non-vanishing moments of higher orders.

In the next section, we consider the measurement in finer detail and give a precise characteristic of its performance.

4 Contrast of the thresholding measurement

In this section, we consider the thresholding measurement of the qubit. An analytical expression for contrast of the measurement is given, in terms of the system parameters. With it, we determine conditions for the maximum contrast. Also, it is shown that, for big measurement times, one obtains maximum in contrast by maximizing SNR.

The easiest way to discriminate the state of the qubit by the number of photocounts is by a *threshold count*, which is set between the counts most probable for each eigenstate. Then, if the number of detected photons is less than the threshold,

the qubit is considered to occupy the ground state; and it is considered to be in the excited state in the opposite case.

4.1 Threshold count

It is natural to set the threshold count n_{th} to be the least number of photons detected, for which the probability of the qubit to reside in the upper state $|\uparrow\rangle$ is bigger than the probability to reside in the lower state $|\downarrow\rangle$ (see Fig. 4.4).

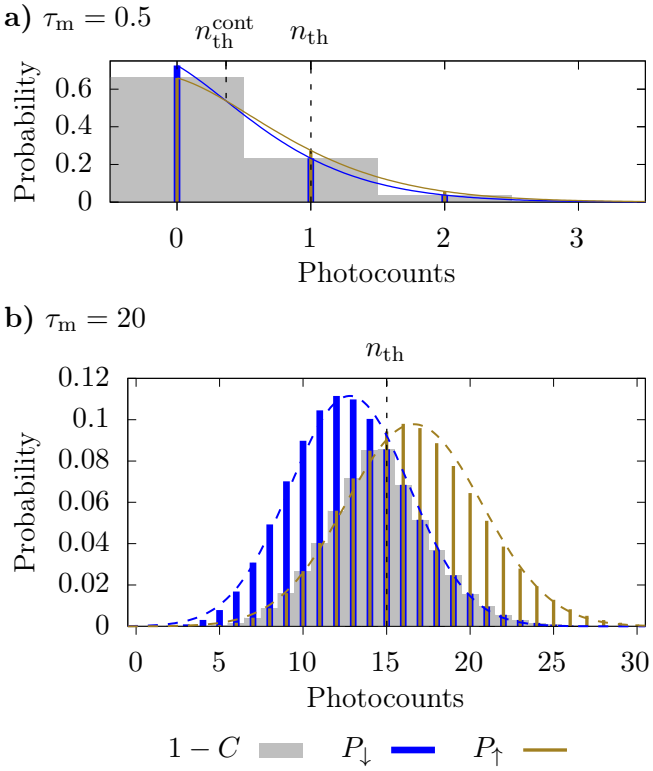

FIGURE 4.4: Probabilities of the qubit to reside in either of its eigenstates as a function of photocounts. Golden bars stand for the probabilities $P_{\uparrow}$ of the qubit being in the excited state, $|\uparrow\rangle$. Blue bars stand for the probabilities $P_{\downarrow}$ of the qubit being in the ground state, $|\downarrow\rangle$. n_{th}, the minimal number of counts to consider the qubit being in the excited state, is marked on the axes. The gray area equals $1-C$, which is twice the probability of erroneous measurement due to the definition (1.43) of contrast C and Eqs. (1.45)–(1.47). For both subfigures, $D = 0.6$ and $X = 0.15$. Each subfigure is plotted for a measurement time such that: a) Half a photon will be detected on average with the resonant drive. Solid lines show the continuation of the Poisson distribution to the real values. b) Twenty photons will be detected on average with the resonant drive. Dashed lines show the Gaussian approximation to the distributions.

To determine n_{th}, we first find its continuous analog: the point of intersection $n_{\mathrm{th}}^{\mathrm{cont}}$ of extrapolations of $P_{\uparrow}(n)$ and $P_{\downarrow}(n)$ to the real values. These are given by

$$P_q^{\mathrm{cont}}(n) = \frac{(\overline{n}_q)^n \, e^{-\overline{n}_q}}{\Gamma(n+1)}, \quad q = \uparrow, \downarrow . \tag{4.53}$$

In other words, $n_{\mathrm{th}}^{\mathrm{cont}}$ is defined by

$$P_{\uparrow}^{\mathrm{cont}}(n_{\mathrm{th}}^{\mathrm{cont}}) = P_{\downarrow}^{\mathrm{cont}}(n_{\mathrm{th}}^{\mathrm{cont}}). \tag{4.54}$$

By performing simple algebra, one can solve the equation and obtain

$$n_{\mathrm{th}}^{\mathrm{cont}} = \frac{\overline{n}_{\uparrow} - \overline{n}_{\downarrow}}{\log \overline{n}_{\uparrow} - \log \overline{n}_{\downarrow}}. \tag{4.55}$$

Plots of continuous distributions $P_{\uparrow,\downarrow}^{\mathrm{cont}}$ are given in Fig. 4.4a, with the positions of $n_{\mathrm{th}}^{\mathrm{cont}}$ and n_{th} marked.

The threshold count n_{th} can be found from $n_{\mathrm{th}}^{\mathrm{cont}}$. The peak of $P_{\uparrow}^{\mathrm{cont}}$ is higher and is located to the right of that of $P_{\downarrow}^{\mathrm{cont}}$. Also, as Eq. (4.55) shows, there is only one point where the probabilities are equal. It follows then, from graphical considerations, that $P_{\uparrow}^{\mathrm{cont}}(n) > P_{\downarrow}^{\mathrm{cont}}(n)$ for $n > n_{\mathrm{th}}^{\mathrm{cont}}$. Therefore,

$$n_{\mathrm{th}} = \lceil n_{\mathrm{th}}^{\mathrm{cont}} \rceil = \left\lceil \frac{\overline{n}_{\uparrow} - \overline{n}_{\downarrow}}{\log \overline{n}_{\uparrow} - \log \overline{n}_{\downarrow}} \right\rceil, \tag{4.56}$$

where $\lceil x \rceil$ denotes the first integer not less than x.

4.2 Poorly-resolving measurement

Consider the poorly-resolving measurement, in which distributions $P_{\uparrow}$ and $P_{\downarrow}$ almost overlap. The condition for the distributions to be very close is

$$\overline{n}_{\uparrow} - \overline{n}_{\downarrow} \ll \sqrt{\overline{n}_{\uparrow}} + \sqrt{\overline{n}_{\downarrow}}. \tag{4.57}$$

Here, we have used that the width of each distribution is $\sqrt{\Delta n^2}$, which reduces to $\sqrt{n}$ by Eq. (4.18). In terms of SNR (4.22), condition (4.57) takes a simple form:

$$\mathrm{SNR} \ll 1. \tag{4.58}$$

Consider the case of $X \ll 1$. With a reasonable choice of detuning, $D \sim 1$, the condition (4.57) simplifies, giving

$$2X\sqrt{\tau_{\mathrm{m}}} \ll 1. \tag{4.59}$$

It is interesting to determine the threshold count in the poorly-resolving measurement. To find the threshold, we consider the cases of $n_{\downarrow} > 1$ and $n_{\uparrow} < 1$ separately. In the case of $n_{\downarrow} > 1$, it follows from Eq. (4.57) that $\overline{n}_{\uparrow} - \overline{n}_{\downarrow} \ll \overline{n}_{\uparrow}, \overline{n}_{\downarrow}$. This gives an approximation for the logarithm in Eq. (4.55):

$$\log \frac{n_{\uparrow}}{n_{\downarrow}} \approx \frac{\overline{n}_{\uparrow} - \overline{n}_{\downarrow}}{\overline{n}_{\downarrow}} \approx \frac{\overline{n}_{\uparrow} - \overline{n}_{\downarrow}}{\overline{n}_{\uparrow}}. \tag{4.60}$$

Substituting the approximation into Eq. (4.56), one has

$$n_{\mathrm{th}} \approx \lceil \tau_{\mathrm{m}} \rceil, \quad n_{\downarrow} > 1. \tag{4.61}$$

It was taken into account that, according to Eq. (4.57), the distributions vary slowly in the vicinity of their maxima; thus the one-count difference in the threshold does not affect robustness of measurement substantially. In the case of small counts, the

threshold is

$$n_{\rm th} = 1, \quad n_\uparrow < 1. \tag{4.62}$$

Condition (4.59) can be used to distinguish the inferior case of poorly-resolving measurement. In such a measurement, the best one can do to discriminate the state of the qubit, is to consider counts to the right of the distributions maxima to indicate the qubit in $|\uparrow\rangle$, and counts to the left to indicate the qubit in $|\downarrow\rangle$. It follows from Eq. (4.59), that this regime can be evaded by increasing the measurement time. Moreover, by increasing the duration of measurement one can reach a measurement contrast which is arbitrary close to unity. This will be shown in the following subsection.

4.3 Contrast

If the number of detected photons is not less than the threshold count $n_{\rm th}$ (4.56) and one determines the qubit to be in the upper state, there is still a possibility that the qubit is in the lower state, and vice versa (see Fig. 4.4b). We quantify this possibility by the measurement contrast. According to the definition of the contrast (1.43) and that of $n_{\rm th}$,

$$C = \sum_{n=0}^{n_{\rm th}-1} [P_\downarrow(n) - P_\uparrow(n)]. \tag{4.63}$$

The sums in the definition can be expressed in terms of the incomplete Gamma function,

$$\Gamma(n, x) = \int_x^\infty dt\, t^{n-1} e^{-t}. \tag{4.64}$$

It is shown in Appendix B, that

$$\Gamma(n, x) = e^{-x}(n-1)! \sum_{n=0}^{n-1} \frac{x^n}{n!} \tag{4.65}$$

for n integer. We apply Eq. (4.65) to each sum with the probabilities given by Eq. (4.16). One arrives at

$$C = \frac{\Gamma(n_{\rm th}, \overline{n}_\downarrow) - \Gamma(n_{\rm th}, \overline{n}_\uparrow)}{\Gamma(n_{\rm th})}. \tag{4.66}$$

Contrast as a function of measurement time has discontinuities in the first derivative (see Fig. 4.5). This is explained in the following way. Increasing the duration of measurement shifts the distributions (compare Figs. 4.4a and 4.4b), which moves the threshold count $n_{\rm th}$ as well. Increment of $n_{\rm th}$ adds an additional term to the sums in Eq. (4.63), abruptly changing the derivative of C. This gives a graphical method to determine the threshold count for a given measurement duration. A number of cusps in the contrast plot, up to the given time, gives the threshold count.

As a special case, the contrast of a vacuum detector can be obtained from Eq. (4.63). Such a detector clicks (with a probability η) when at least one photon is absorbed. In this case, we decide that the qubit is in the upper state. In the opposite case, if no photons were detected during the measurement, one decides that the qubit is in the lower state. The situation is captured by $n_{\rm th} = 1$. Then Eq. (4.63) reduces to

$$C_{1/0} = e^{-\overline{n}_\downarrow} - e^{-\overline{n}_\uparrow}. \tag{4.67}$$

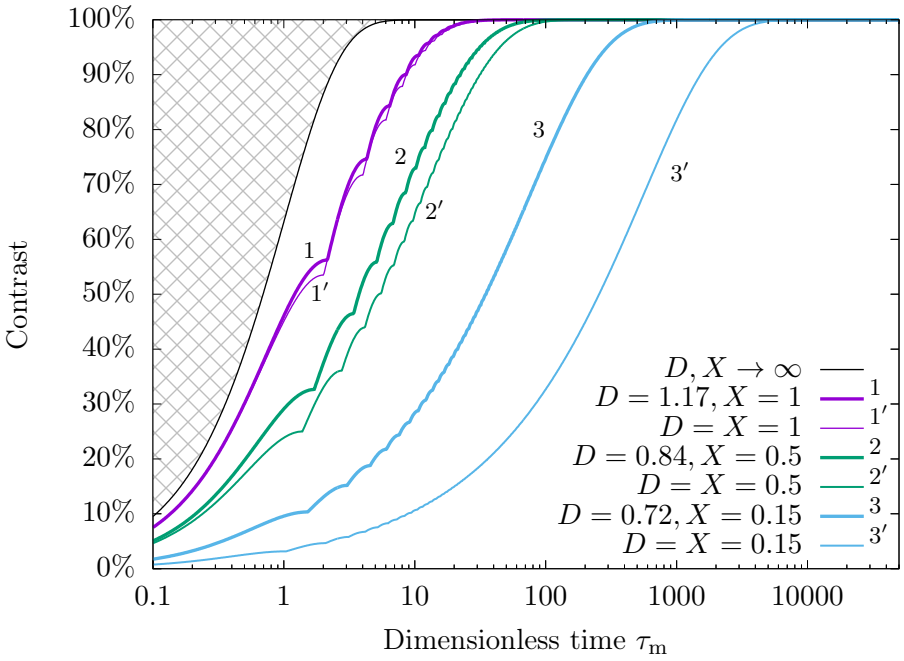

FIGURE 4.5: Measurement contrast as a function of a dimensionless time τ_m: the highest contrast for a given τ_m (the uppermost black curve), contrast for D maximizing SNR (thick solid lines), contrast for naive choice of detuning $D = X$ (thin solid lines), contrast when using the vacuum detector and $D = 0.84$, $X = 0.5$ (dashed line). The dimensionless time τ_m (4.25) equals the mean photon count for the resonant drive.

Contrast (4.67) is presented in Fig. 4.5. By Eq. (4.24), it has a maximum for the time of measurement

$$\tau_{m\,1/0}^{\mathrm{opt}} = \left(\frac{\log \overline{n}_\uparrow - \log \overline{n}_\downarrow}{\overline{n}_\uparrow - \overline{n}_\downarrow} \right) \Bigg|_{\tau_m = 1} . \tag{4.68}$$

For longer measurement it becomes more likely to detect a "false" photon in case the qubit is in the lower state. Hence the degradation of the contrast $C_{1/0}$ after the measurement duration rises above $\tau_{m\,1/0}^{\mathrm{opt}}$. It follows from Eqs. (4.56) and (4.68) that n_{th} increments quite in time one reaches the maximum contrast of the detection with $n_{\mathrm{th}} = 1$.

In Ref. [37], contrast for the related measurement with the vacuum detector was obtained; the quantity is called the measurement contrast there. Formally, expression (4.67) coincides with that of the mentioned work, when the latter is taken in the limit of negligible number of dark counts. However, a different measurement sequence is considered in the reference. There, a photon is allowed to leave the resonator only after the cavity has been already pumped. This is in contrast to the case of continuous drive and permanent leakage considered in this work. Hence the difference in the expressions for resonator occupancy. As a consequence, the time (4.68) maximizing contrast (4.67) is different in our case.

For a given τ_m, contrast is limited by a value that approaches unity with increasing of τ_m. To find this limiting value, we first find detuning D and dispersive pull X that maximize the contrast. It follows from its definition (4.64), that incomplete Gamma function $\Gamma(n, x)$ increases with decreasing of x. Therefore, contrast (4.66) increases with increasing $\overline{n}_\uparrow$ and decreasing $\overline{n}_\downarrow$. Indeed, it is seen from Fig. 4.4, that as the

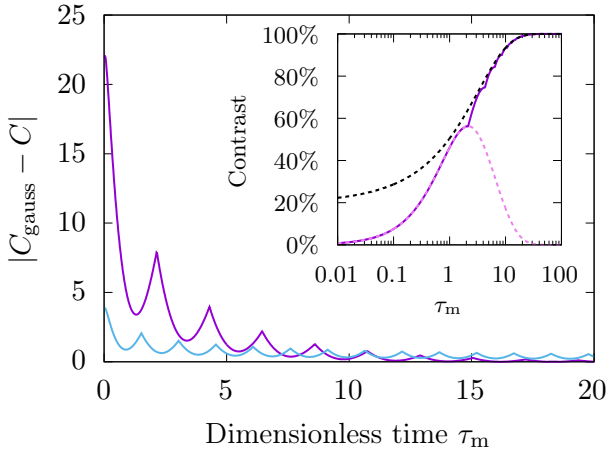

FIGURE 4.6: Accuracy of the Gaussian approximation to the contrast and the contrast of measurement with the vacuum detector. On the main plot, two curves give the absolute error of the approximation. Color convention as in Fig. 4.5: $D = 1.17, X = 1$ for the violet curve, and $D = 0.72, X = 0.15$ for the blue one. The blue curve is below the violet one for small τ_{m}. On the inset, the actual, the Gaussian-approximated, and the contrast for the vacuum detector are shown. Black dashed curve stands for the approximation; violet curve stands for the actual contrast. Contrast of the readout with the vacuum detector is given with a pink dashed curve. Measurement parameters are the same as for the violet curves on the main plot and in Fig. 4.5.

distance between distributions becomes bigger, their overlap shrinks. It follows from Eq. (4.24) that $\overline{n}_{\uparrow}$ reaches its maximum of τ_{m} at $D = X$, while $\overline{n}_{\downarrow}$ reaches its minimum of zero at $D \to \infty$ or $X \to \infty$. Therefore, C has its highest value at $D, X \to \infty$. According to the definition (4.27) of X, the regime can be approached in the case of small resonator decay, $\kappa \ll g\lambda$. Now we calculate the threshold count n_{th} in this limiting case. It follows from Eq. (4.55) that the continuous threshold approaches zero, $\lim_{D,X\to\infty} n_{\text{th}}^{\text{cont}} = 0$. However, $n_{\text{th}}^{\text{cont}}$ is strictly greater than zero for any D, X. One concludes that $n_{\text{th}} = \lceil n_{\text{th}}^{\text{cont}} \rceil = 1$. Using Eq. (4.67) with $\overline{n}_{\downarrow} = 0$ and $\overline{n}_{\uparrow} = \tau_{\text{m}}$, we obtain the limiting contrast,

$$C_{\tau_{\text{m}}}^{\max} = 1 - e^{-\tau_{\text{m}}}. \tag{4.69}$$

It is shown in Fig. 4.5 with a solid black curve. Note that at big X no photons are transmitted through the resonator in case the qubit pushes the cavity out of resonance. In this limit the vacuum and the photo-number-resolving detectors do not differ. However, $C_{\tau_{\text{m}}}^{\max}$ is by no means the limit on the contrast at physical time t_{m}. The real limit will be found below, along the lines of finding the bound on SNR in Sec. 3.2.

It is also shown in the figure how the choice of detuning maximizing SNR improves contrast, as compared to the "naive" choice $D = X$. First, it is seen that there is no need to use detuning other than $D = X$ for stronger measurements beginning with $X = 1$. This was already shown by analyzing SNR in Sec. 3.1. In the case of smaller X, consider a measurement reaching 95% contrast. For $X = 0.5$, one would need the measurement to last 1.5 times less if the detuning maximizing SNR is used. And for $X = 0.15$ such choice of detuning shortens the measurement more than sevenfold! Given such performance, it is natural to pose certain questions: Is there some connection between the conditions of maximum of SNR and contrast?

Would there be any further advantage in using the detuning *maximizing contrast*? We address these questions below.

4.4 Gaussian approximation

Consider a Gaussian approximation to the threshold count and contrast. We will show that in this approximation contrast is expressed in terms of SNR.

One obtains the approximation as follows. For a long measurement and lots of photocounts,

$$\overline{n}_\uparrow, \overline{n}_\downarrow \gg 1, \tag{4.70}$$

Poisson distributions $P_\uparrow$ and $P_\downarrow$ are well-approximated with Gaussians:

$$P_q(n) \approx \frac{1}{\sqrt{2\pi\overline{\Delta n^2}_q}} \exp\left[-\frac{(n-\overline{n}_q)^2}{2\overline{\Delta n^2}_q}\right], \quad q = \uparrow, \downarrow . \tag{4.71}$$

The approximation is shown in Fig. 4.4b. With it, contrast (4.63) is expressed as

$$C \approx \frac{1}{\sqrt{\pi}} \int_{x_\uparrow}^{x_\downarrow} dx\, e^{-x^2} = \frac{1}{2}\operatorname{erf} x_\downarrow - \frac{1}{2}\operatorname{erf} x_\uparrow, \tag{4.72}$$

where the limits of integration are given by

$$x_q = \frac{n_{\rm th}^{\rm gauss} - n_q}{\sqrt{2\overline{\Delta n^2}_q}}, \quad q = \uparrow, \downarrow, \tag{4.73}$$

and the Gaussian threshold count is

$$n_{\rm th}^{\rm gauss} = \sqrt{\overline{n}_\uparrow \overline{n}_\downarrow \left(1 + \frac{\log \overline{n}_\uparrow - \log \overline{n}_\downarrow}{\overline{n}_\uparrow - \overline{n}_\downarrow}\right)} \approx \sqrt{\overline{n}_\uparrow \overline{n}_\downarrow}. \tag{4.74}$$

To derive the approximate identity in Eq. (4.74), it was taken into account that $n_{\rm th}$ (4.56) is huge compared to unity due to the condition (4.70). Also, we have used the error function

$$\operatorname{erf} x = \frac{2}{\sqrt{\pi}} \int_0^x dx' e^{-x'^2} \tag{4.75}$$

to express the integral in Eq. (4.72) in a convenient form. A comparison between Eq. (4.72) and the exact expression for contrast is given in Fig. 4.6. For both sets of system parameters given on the figure, accuracy of the approximation grows with increase of measurement time. This is quite natural, as increasing the duration of measurement increases the average number of photons detected, which makes the Gaussian approximations to $P_\uparrow$ and $P_\downarrow$ more accurate. Gaussian distributions (4.71) have different width, hence the complex expression for the threshold count (4.74). This also means that the Gaussian theory with a symmetrical distributions given in [50] does not reproduce the Gaussian approximation presented here.

Using Eq. (4.74), one expresses the parameters of the error function in Eq. (4.72) in terms of SNR (4.28):

$$x_\uparrow \approx -\mathrm{SNR}/\sqrt{2}, \quad x_\downarrow \approx \mathrm{SNR}/\sqrt{2}. \tag{4.76}$$

The detuning which maximizes Gaussian contrast coincides with that maximizing SNR.

Equations (4.72), and (4.76)) constitute the expression for contrast which is formally equivalent to that given in Ref. [50]. To show this, one should change our definition of SNR in accordance to the reference. There, SNR is defined as a ratio of signal and noise *powers*. Thus to arrive at the formula given in Ref. [50], one should square the right-hand side of the SNR definition (4.22). Still, we have derived the expression for a different case: The distributions (4.71) are of Poissonian width set by Eq. (4.18) contrary to the same-width case considered in the reference; The distributions are sufficiently narrow, by Eqs. (4.70) and (4.18).

We have shown that the maxima of SNR and contrast coincide for long measurement times. Next we are going to investigate the exact conditions for maximum contrast.

4.5 Maximizing contrast with respect to detuning

In this subsection, we find the detuning that maximizes measurement contrast. Here the duration of measurement, the dispersive pull, and the resonator decay rate are fixed. Just as before, we assume the average number of cavity photons at resonance (4.20) is maintained constant.

The threshold count (4.56) changes in steps with the measurement duration. One then expects that the optimal detuning has discontinuities in points where the threshold changes. This behavior is illustrated in Fig. 4.7.

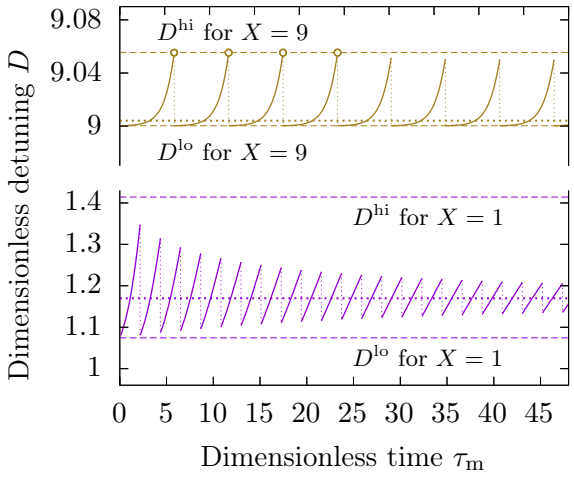

FIGURE 4.7: Dependence of the dimensionless optimal detuning on the dimensionless measurement duration for a fixed dispersive pull and resonator leakage: the detuning maximizing contrast for $X = 9$ (top solid) and $X = 1$ (bottom solid), the detuning maximizing SNR (bold dotted), and the upper and lower bounds on the detuning (dashed). The lower bound is not reached, despite the way it looks. The points marked with empty circles are not reached too.

Let us consider durations τ_{m} between the discontinuities. Here, n_{th} is constant; points where contrast C has extrema are found by equating the first derivative of C to zero, $\partial C/\partial D|_{n_{\mathrm{th}}\equiv\mathrm{const}} = 0$. Carrying out the derivative of the expression (4.66), the condition for extremum resolves to

$$\frac{D^{\mathrm{opt}} + X}{D^{\mathrm{opt}} - X} \cdot e^{\overline{n}_{\uparrow} - \overline{n}_{\downarrow}} = \left(\frac{\overline{n}_{\uparrow}}{\overline{n}_{\downarrow}}\right)^{n_{\mathrm{th}}+1}. \tag{4.77}$$

It is shown in Appendix C that the extrema given by the equation are the points of maximal contrast. The solution of Eq. (4.77) gives the optimal detuning between two "jumps".

Abrupt change of D^{opt} takes place in two cases. First, it occurs when the contrast for the next threshold count $n_{\mathrm{th}}+1$ exceeds that for the current one, n_{th}. Strictly speaking, as $C(\tau_{\mathrm{m}})$ is continuous, at the point of jump there exist two values of D^{opt}. This is the case for the curve with $X=1$ in Fig. 4.7, and the transitions after the fourth one for the curve with $X=9$. On the other hand, beginning with some measurement duration τ_{m}, there can be no detuning satisfying Eq. (4.77) at the present n_{th}. This case is realized in the first four transitions occurring for $X=9$, as illustrated in Fig. 4.7. In both cases, n_{th} increments by one and D^{opt} switches to the value given by Eq. (4.77) with the threshold incremented.

The last case allows us to find upper and lower bounds on oscillations of the optimal detuning. Consider the interval between two jumps. On the interval D^{opt} changes continuously, governed by Eq. (4.77); with it, the continuous threshold $n_{\mathrm{th}}^{\mathrm{cont}}$ (4.55) changes. According to the definition (4.56) of the threshold count, n_{th} increases when $n_{\mathrm{th}}^{\mathrm{cont}}$ passes by the current threshold. The value D^{opt} reaches prior to the increment is the highest possible. One can find this highest possible value. We substitute n_{th} in Eq. (4.77) with $n_{\mathrm{th}}^{\mathrm{cont}}$, given by Eq. (4.55). The substitution gives rise to the equation

$$(D+X)\big[(D-X)^2+1\big]=(D-X)\big[(D+X)^2+1\big]. \tag{4.78}$$

Solution of the equation sets the upper bound on D^{opt}:

$$D^{\mathrm{opt}}\le D^{\mathrm{hi}},\quad D^{\mathrm{hi}}=\sqrt{X^2+1}. \tag{4.79}$$

As at the point of jump $n_{\mathrm{th}}=n_{\mathrm{th}}^{\mathrm{cont}}+1$, the value D^{opt} approaches to after the switch can be found in an analogous way. We substitute n_{th} in Eq. (4.77) with $n_{\mathrm{th}}^{\mathrm{cont}}+1$, which results in the equation

$$(D+X)\big[(D-X)^2+1\big]^2=(D-X)\big[(D+X)^2+1\big]^2. \tag{4.80}$$

The equation reduces to the quartic equation. It has one real positive root. The root is the lower bound on D^{opt}:

$$D^{\mathrm{opt}}>D^{\mathrm{lo}},\quad D^{\mathrm{lo}}=\sqrt{1/3(2\sqrt{X^4+X^2+1}+X^2-1)}. \tag{4.81}$$

Knowledge of the upper and lower bounds speeds up dramatically the numerical procedures to obtain D^{opt}.

We briefly review the numerical procedures used. The simplest way to determine D^{opt} is to calculate C for D changing from D^{lo} to D^{hi} with small steps, and choose the detuning resulting in the biggest contrast. The plot for $X=1$ in Fig. 4.7 was obtained this way. In the calculations, the interval from D^{lo} to D^{hi} was divided in 1000 steps. However, for $X=9$, variations of C are too small to use this method. The respective curve in Fig. 4.7 was calculated by solving Eq. (4.77) for each τ_{m}. In both cases, τ_{m} was changing with a step of 0.1. As D^{opt} is quite steep just before a jump, we determine each point of a jump as precise as possible. In the case D^{opt} reaches D^{hi}, a switch occurs when $n_{\mathrm{th}}^{\mathrm{cont}}$ becomes equal to the current threshold. In the other case, the time is found using the fact that the contrasts for n_{th} and $n_{\mathrm{th}}+1$ are equal at the time of a switch.

4.6 Maximizing contrast with respect to detuning and the pull/damping ratio: the upper bound on the measurement contrast

Here we give the detuning and the ratio of dispersive pull to resonator leakage which result in optimal contrast. The average number of cavity photons at resonance is kept fixed. The resulting contrast is the biggest possible contrast for the scheme considered. Using the optimal parameters, we show the possibility for high-contrast single-shot readout in various realizations of the scheme.

We use the expressions of mean counts (4.42) in terms of Δ and K (4.41). A typical dependence of contrast (4.66) on those parameters is given in Fig. 4.8.

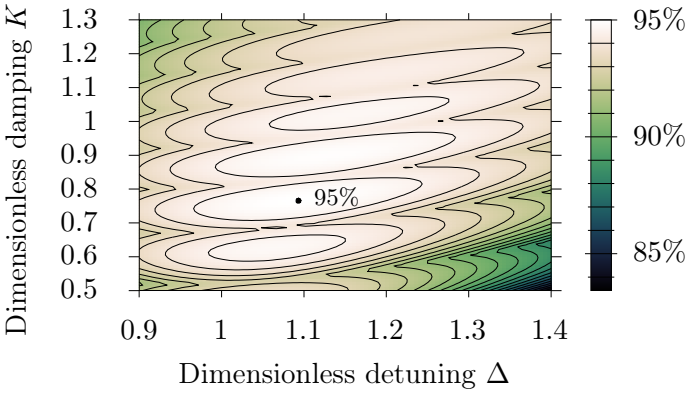

FIGURE 4.8: Contrast at dimensionless time $T_{\mathrm{m}} = 11.29$ vs. dimensionless detuning Δ and dimensionless resonator leakage K. The dimensionless quantities as defined in Eqs. (4.41) and (4.43).

One can write out the equations on a stationary point of contrast. Carrying out the partial derivatives $\partial C/\partial\Delta$ and $\partial C/\partial K$ and equating them to zero gives rise to the following set of equations:

$$\frac{\Delta+1}{\Delta-1}\cdot e^{\overline{n}_\uparrow-\overline{n}_\downarrow}=\left(\frac{\overline{n}_\uparrow}{\overline{n}_\downarrow}\right)^{n_{\mathrm{th}}+1}, \tag{4.82}$$

$$\frac{3(\Delta+1)^2+K^2}{3(\Delta-1)^2+K^2}\cdot e^{\overline{n}_\uparrow-\overline{n}_\downarrow}=\left(\frac{\overline{n}_\uparrow}{\overline{n}_\downarrow}\right)^{n_{\mathrm{th}}+1}. \tag{4.83}$$

As before, n_{th} is assumed constant during the differentiation. It follows from the equations that

$$K^2=3\Delta^2-3,\quad \Delta\neq\pm1. \tag{4.84}$$

With this, the mean counts (4.42) can be expressed in terms of Δ alone:

$$\overline{n}_\uparrow=T_{\mathrm{m}}\frac{\sqrt{27}}{2}\frac{(\Delta+1)\sqrt{\Delta^2-1}}{2\Delta+1}, \tag{4.85}$$

$$\overline{n}_\downarrow=T_{\mathrm{m}}\frac{\sqrt{27}}{2}\frac{(\Delta-1)\sqrt{\Delta^2-1}}{2\Delta-1}. \tag{4.86}$$

Plots of optimal Δ and K in Fig. 4.9a are obtained with Eqs. (4.82) and (4.84)–(4.86). This is done analogous to the calculation of $X=9$ plot in Fig. 4.7. The key difference is that Eqs. (4.85) and (4.86) are used to calculate contrast (4.66). Also, here we have checked numerically that the computed critical points are the points of maxima.

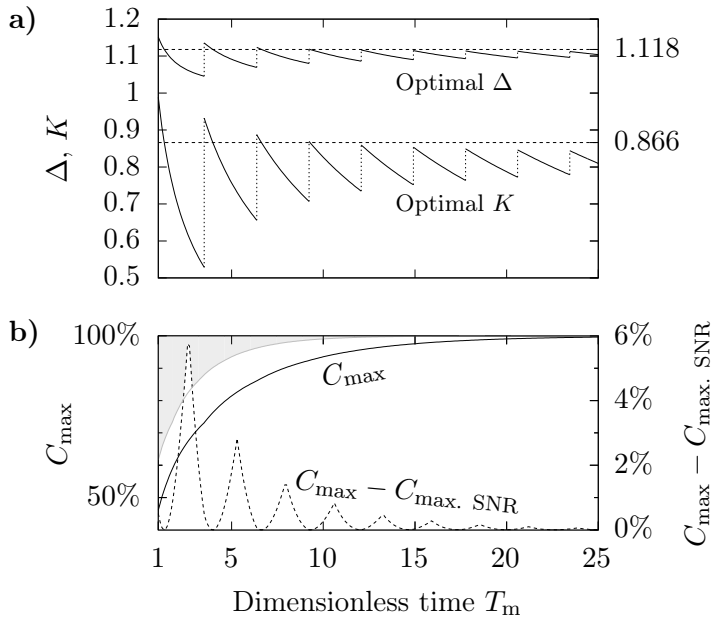

FIGURE 4.9: a) Top curves: dimensionless detuning Δ maximizing contrast (solid curve) and SNR (dashed line). Lower curves: dimensionless decay rate K of the resonator that maximizes contrast (solid curve) and SNR (dashed line). The dimensionless quantities as defined in Eqs. (4.41). b) Maximal contrast for symmetrical resonator (black solid), maximal contrast for asymmetrical resonator (gray solid), and the difference between the optimal contrast and the contrast reached with the parameters maximizing SNR (dashed). Both plots a) and b) are given vs. the time T_{m} (4.43).

The asymmetrical resonator with a negligible first-port leakage can be tackled in the same way as in Sec. 3.2. It was shown that the dimensionless time T_{m} (4.43) is multiplied by the factor of two in this case, so that a given contrast is reached quicker. This gives the upper bound on contrast for the measurement with various ratios of port leakage rates. The bound is shown in Fig. 4.9b, as well as the contrast for the case of symmetrical resonator. Numerical estimations for the measurement duration are given in Table 4.1.

It is important to use the photon-number-resolving detector to achieve a high-contrast readout. The vacuum detector provides the optimal contrast only up to the first jump in parameter values. After the jump, the optimal contrast is achieved with $n_{\mathrm{th}} \geq 2$, which is impossible for the vacuum detector. The possibility to resolve a photon number matters starting from a contrast of about 73%.

Note the naive detuning ($\Delta = 1$) and the optimal K result in a non-substantial loss of contrast. The loss is below 1% for a contrast higher than 75%. That is not surprising. We have already discussed in Sec. 3.1 that the naive detuning provides a close-to-optimal contrast for $g\lambda > \kappa/2$ ($K < 1$). One can see from Fig. 4.9 that the optimal K satisfies this condition for any reasonable value of the contrast.

TABLE 4.1: Estimations for measurement time for different realizations of cavity QED: transmon superconducting qubit coupled to 1D resonator, quantum dot (QD) in a nanocavity, Bose-Einstein condensate (BEC) in a 3D optical cavity, and an ensemble of nitrogen defect spins in diamond coupled to a 1D microwave resonator. Efficiency of the detector is $\eta = 0.9$.

Qubit	g[1] (MHz)	$\lvert\omega_q - \omega_r\rvert$ (GHz)	$\lvert\alpha^{res}\rvert^2$	t_m for C of 95%	99%	T_1[1]
Transmon [32]	86	1[1]	1[1]	0.7 μs	1.2 μs	20 μs
QD [83]	21000	1000	10	1.2 ns	2.0 ns	11 ns
BEC [84]	1000	1000	1000	5.1 ns	11.0 ns	53 ns
N defects [85]	17	0.1	0.01	17.6 μs	30.6 μs	20 s

[1] Value from reference.

5 Maximizing contrast vs maximizing signal-to-noise ratio

In this section, we discuss how using the parameters maximizing contrast compares to the use of those maximizing SNR, in terms of the resulting contrast.

First, for big measurement times, maximizing SNR results in the maximum of contrast. We have shown this in Sec. 4.4, using the Gaussian asymptotics to contrast.

For smaller times, it depends on whether one is free to choose only the drive-resonator detuning, or both the detuning and the resonator decay rate.

Consider the case one is able to choose a detuning only. For this case, we have performed a numerical comparison of the contrast $C_{\max}$ reached with the optimal detuning, and the contrast $C_{\text{max. SNR}}$ the detuning maximizing SNR results in. A non-vanishing difference $C_{\max} - C_{\text{max. SNR}}$ occurs near the point of threshold change. It is found that the maximal difference is slightly bigger than 1%. Such a gain is achieved for pulls $X \approx 0.5 \div 1$. The contrasts reached under these circumstances are about $50\% \div 60\%$.

If, in addition to detuning, it is possible to set the dispersive pull or the resonator leakage, the gain becomes bigger. As shown in Fig. 4.9b, use of the parameters maximizing contrast rather than SNR pays off with a moderate increase of contrast, for a range of measurement durations. Namely, a gain about 6% occurs in the measurement reaching contrast about 65%. And even for contrast of about 95% the increase can be close to 1%.

6 Conclusion

We have determined the optimal system parameters for the dispersive qubit readout using a fully-absorbing, photon-number-resolving detector.

Probing the cavity on one of its resonances may result in suboptimal measurement performance. This can be explained in terms of SNR in the difference in photon counts for the $|\downarrow\rangle$ and $|\uparrow\rangle$ qubit states. Photon counts fluctuate due to the photon shot noise. The difference is maximized for a resonance probe, but, with detuning, it decreases slower than the noise in it. Hence there is an optimal detuning that maximizes the SNR. The need to detune is most pronounced in the weak measurement, when the dispersive pull is smaller than the cavity decay rate, $g\lambda < \kappa/2$. Consider the case

when only the detuning can be varied. Then, the optimal detuning can be determined by Fig. 4.3. For a very weak measurement, $g\lambda \ll \kappa/2$, we have obtained asymptotics for the optimal detuning: $\omega_{\mathrm{dr}} = \kappa\sqrt{2}/4$.

To obtain these results, it is sufficient to maximize a simple characteristic of the measurement, SNR, which is given by Eq. (4.22). It turns out that the detuning maximizing contrast (4.63) results in almost the same values of contrast. For sufficiently long measurement durations that result in high contrast, we have proved that the conditions of maxima of SNR and contrast coincide. As for the moderate contrasts, the difference in contrast is not substantial.

The situation is different if one is able to tune the $g\lambda/\kappa$ ratio. One can use the ratio that maximizes SNR if aiming at more than 95% contrast. A contrast very close to the optimal one is then achieved, while the optimal $g\lambda/\kappa$ is the same for measurements of any duration. For a shorter measurement, it is better to use $g\lambda/\kappa$ that maximizes contrast. It is given in Fig. 4.9a. For each measurement duration, there is a distinct $g\lambda/\kappa$ ratio. (This does not mean the ratio should be changed throughout the measurement.) As for the drive-resonator detuning, it can be chosen as $\omega_{\mathrm{dr}} = g\lambda$. This results in almost the same contrast as the exact value of optimal detuning.

The photon-number-resolving detector is advantageous for the readout. With a vacuum detector, one needs a longer measurement to achieve contrasts starting with 73%.

Single-shot readout using the considered scheme is achievable in various cavity-QED type systems (see Table 4.1). The readout can reach 99% contrast. This opens the possibility of using the readout in quantum error-correction schemes. Note our scheme is best-suited for high frequencies of both the qubit and the cavity, as follows from Eq. (4.43) and our comments on it.

Our results apply not only to a single-shot measurement but to the sequential measurements as well. In this case the measurement time discussed is replaced with the sum of durations of all measurements in a sequence.

Appendices

A Extremal points of signal-to-noise ratio are its points of maximum

If the second derivative of SNR (4.28) is negative in an extremal point D, that point is the point of maximum. The respective condition reads

$$\frac{2(D+X)^2-1}{\left[(D+X)^2+1\right]^{5/2}} = \frac{2(D-X)^2-1}{\left[(D-X)^2+1\right]^{5/2}}. \tag{4.A.1}$$

We show the condition (4.A.1) holds for every extremal point. Let us put the terms of Eq. (4.29) on the opposite sides of the equation and then square it:

$$\frac{(D+X)^2}{\left[(D+X)^2+1\right]^{3}} = \frac{(D-X)^2}{\left[(D-X)^2+1\right]^{3}}. \tag{4.A.2}$$

It was set $D^{\mathrm{opt}} \to D$ for brevity. We multiply both sides of the inequality

$$[(D-X)^2+1]^{-1/2} > [(D+X)^2+1]^{-1/2} \tag{4.A.3}$$

by the respective sides of Eq. (4.A.2) to obtain

$$\frac{(D+X)^2}{\left[(D+X)^2+1\right]^{5/2}} > \frac{(D-X)^2}{\left[(D-X)^2+1\right]^{5/2}}. \tag{4.A.4}$$

Now we use yet another inequality

$$-[(D-X)^2+1]^{-5/2} > -[(D+X)^2+1]^{-5/2}. \tag{4.A.5}$$

One adds it to the inequality (4.A.4) doubled, which yields Eq. (4.A.1). Hence every extremal point is the point of maximum.

B Cumulative distribution function of Poisson process

Here, we express the cumulative distribution function of Poissonian process in terms of incomplete Gamma function.

The probability that a Poisson random variable ξ occurs with a value less than or equal to N is

$$P(\xi \leq N) = \sum_{n=0}^{N} \frac{\lambda^n}{n!} e^{-\lambda}. \tag{4.B.1}$$

This quantity is known as cumulative distribution function of the variable. Incomplete Gamma function is defined with the following expression:

$$\Gamma(n,x) = \int_x^\infty dt\, t^{n-1} e^{-t}. \tag{4.B.2}$$

A basic property of the incomplete Gamma function reads

$$\Gamma(n+1,x) = n\Gamma(n,x) + x^n e^{-x}. \tag{4.B.3}$$

It can be derived integrating by parts the definition (4.B.2). Noticing that

$$\Gamma(1,x) = e^{-x} \tag{4.B.4}$$

and applying induction to Eq. (4.B.3), one arrives at

$$\Gamma(n+1,x) = e^{-x}\sum_{k=0}^{n} x^k n(n-1)\cdot\ldots\cdot(n-k+1) = e^{-x}n!\sum_{k=0}^{n}\frac{x^k}{k!}. \tag{4.B.5}$$

In obtaining Eq. (4.B.5) it was assumed that n is a positive integer or zero. With Eq. (4.B.5), the cumulative distribution function (4.B.1) is expressed as follows:

$$P(\xi \le N) = \frac{\Gamma(N+1,\lambda)}{\Gamma(N+1)}, \quad N = 0,1,\ldots \tag{4.B.6}$$

C Conditions for contrast maximum at the extremal point

In this appendix, we show that the extrema D^{opt} given by Eq. (4.77) are the maxima of contrast.

First of all, the highest D^{opt} possible, D^{hi} (4.79), maximizes contrast C. This follows from the fact that the derivative $\partial C/\partial D|_{n_{\mathrm{th}}^{\mathrm{cont}}\equiv\mathrm{const}}$ changes its sign from plus to minus while D^{opt} passes D^{hi}.

We now check that the solutions of Eq. (4.77) give maxima in the rest of the region between two jumps, i.e., for $D^{\mathrm{opt}} < D^{\mathrm{hi}}$. In this region, extremum of C is a maximum if

$$\left.\frac{\partial^2 C}{\partial D^2}\right|_{n_{\mathrm{th}}\equiv\mathrm{const}} < 0. \tag{4.C.1}$$

Performing differentiation, one obtains

$$\frac{(D+X)^2+1+2(\tau_{\mathrm{m}}-n_{\mathrm{th}}-1)(D+X)}{\left[(D+X)^2+1\right]^{n_{\mathrm{th}}+2}}\cdot e^{-\overline{n}_{\downarrow}} < \frac{(D-X)^2+1+2(\tau_{\mathrm{m}}-n_{\mathrm{th}}-1)(D-X)}{\left[(D-X)^2+1\right]^{n_{\mathrm{th}}+2}}\cdot e^{-\overline{n}_{\uparrow}}. \tag{4.C.2}$$

For $X > 0$ the stronger inequality can be obtained by multiplying the denominator of the right-hand side of Eq. (4.C.2) by $[(D-X)^2+1]/[(D+X)^2+1]$. Simplifying the resulting inequality using Eq. (4.77) and taking logarithm of both sides of it, we have

$$\overline{n}_{\uparrow} - \overline{n}_{\downarrow} < n_{\mathrm{th}} \log\frac{\overline{n}_{\uparrow}}{\overline{n}_{\downarrow}}. \tag{4.C.3}$$

Using the definition (4.55) of $n_{\mathrm{th}}^{\mathrm{cont}}$, Eq. (4.C.3) reduces to

$$n_{\mathrm{th}}^{\mathrm{cont}} < n_{\mathrm{th}} \tag{4.C.4}$$

which is the identity for $D^{\mathrm{opt}} < D^{\mathrm{hi}}$ due to the definition of n_{th} (4.56).

Chapter V

Qubit decoherence due to weak dispersive measurement

The measurement-induced decoherence in the dispersive readout was first studied in Refs. [19, 79, 86]. Essentially, that decoherence arises as the resonator occupancy fluctuates and induces the fluctuations in the qubit frequency. Two methods were used in the work [79]: the first one assumes, similarly to Refs. [19, 86], that the qubit *phase* fluctuations are Gaussian, and the other one uses the positive-P-function technique. Thermal photons were neglected in both approaches. In Refs. [87, 88] the resonator is not driven and is occupied by thermal photons only; for that case, the two-time correlator of the photon number fluctuations was found in Ref. [87]. Both thermal and drive photons were taken into account in Ref. [89] using the Wigner function approach; a complex expression for the decoherence rate was provided.

While the more formal methods in Refs. [79, 88, 89] are applicable to a wider range of parameters, the method based on the Gaussian approximation for the phase provides a solid physical insight into the process of decoherence. Using that approach, the decoherence rate was calculated in my Master's thesis [90] while taking into account the influence of both thermal and coherent photons. However, in that thesis the transition to the dressed picture [see Eq. (1.34)] and back is not always performed thoroughly. The whole derivation is not fully coherent, and there are some claims that invalidate the approximations used. Finally, the result seemed to be obtained without any assumption about the measurement strength. On the other hand, it was shown in Ref. [79] with other methods that the Gaussian approximation only works the weak measurement—when the qubit shifts the cavity resonance only negligibly compared to its linewidth.

Here we use the method based on the Gaussian approximation to derive the rate of the measurement-induced dephasing while taking into account the influence of thermal photons. For finding the decoherence rate, we first calculate the two-time correlator of the photon number fluctuations, which can be useful for other applications. Unlike Refs. [19, 79, 86, 90], we consistently use the Heisenberg equations of motion for our derivation. With that approach, we want to achieve a clear and relatively rigorous and simple calculation of the dephasing rates. Simultaneously, we would like to keep our reasoning valid for any statistics of the *frequency* noise. This can be especially useful as non-Gaussian extrinsic noise is known to arise in superconducting qubits [91]. Hence we ground the Gaussian assumption for the phase by the central limit theorem for long measurement times as in Refs. [19, 87, 90]. However, we argue that either the Gaussian phase assumption should be postulated as in Ref. [79], or the measurement should be considered weak to neglect the time ordering while solving for the qubit coherence operator.

1 Definition of the qubit coherence

First, let us discuss how to express the qubit coherence. For that, we need to take into account its environment. Their full state can be denoted as

$$|\mathrm{q},\mathrm{r},\mathrm{b}\rangle = \sum_{\{n_\mathrm{e}\}} \Big(c_{\downarrow,\{n_\mathrm{e}\}} |\downarrow,\{n_\mathrm{e}\}\rangle + c_{\uparrow,\{n_\mathrm{e}\}} |\uparrow,\{n_\mathrm{e}\}\rangle \Big). \tag{5.1}$$

The qubit state is spanned by its ground $|\downarrow\rangle$ and excited $|\uparrow\rangle$ states. The environment state is labeled by the quantum numbers $\{n_\mathrm{e}\}$. We denote the expansion over all its states mnemonically with $\sum_{\{n_\mathrm{e}\}}$. In our case, the environment consists of the resonator and the waveguides connected to it. The waveguides play a role of thermal bath in our model. Strictly speaking, there are other systems that provide additional noise in the qubit transition frequency. However, as we model that with a classical noise process $F(t)$ in the Hamiltonian (3.1), this part of the environment does not enter Eq. (5.1).

While that is not important for the core calculations of this chapter, we briefly discuss how to span the state of the qubit environment in Eq. (5.1). One can use the states

$$|\{n_\mathrm{e}\}\rangle = |n\rangle |\mathrm{w}^{\mathrm{I}}_{k_1 \ldots k_N}\rangle |\mathrm{w}^{\mathrm{II}}_{l_1 \ldots l_M}\rangle \tag{5.2}$$

each denoting a state with the n-photon Fock state in the resonator, N photons in the first waveguide with wavevectors $k_1 \ldots k_M$, and similarly for M photons in the second waveguide. The expansion in Eq. (5.1) then reads

$$\sum_{\{n_\mathrm{e}\}} \equiv \sum_{N=0}^{\infty} \int_0^\infty dk_1 \ldots \int_0^\infty dk_N \sum_{M=0}^{\infty} \int_0^\infty dl_1 \ldots \int_0^\infty dl_M \sum_{n=0}^{\infty}. \tag{5.3}$$

Should we have used the discrete representation of the waveguide modes, Eq. (5.3) would have comprised a sum over all possible combinations of photon number states in these modes. However, in the continuous limit that we use throughout this thesis, the math is different. In Eq. (5.3), we sum over the total number N of the first waveguide photons which are then distributed, in all possible manners, over the continuous modes by N integrations. That is the approach we used in Ref. [29] to express the unitary operator of a waveguide field; that very piece is also presented in Ch. VI of this thesis.

Now for the concept of coherence to naturally occur, consider some measurable A of the qubit. Its average reads

$$\langle A \rangle = \overline{\langle \mathrm{q},\mathrm{r},\mathrm{b}|A|\mathrm{q},\mathrm{r},\mathrm{b}\rangle} \tag{5.4}$$

$$= \rho_{00}\langle\downarrow|A|\downarrow\rangle + \rho_{\downarrow\uparrow}\langle\uparrow|A|\downarrow\rangle + \rho_{\uparrow\downarrow}\langle\downarrow|A|\uparrow\rangle + \rho_{\uparrow\uparrow}\langle\uparrow|A|\uparrow\rangle = \mathrm{Tr}(\rho A), \tag{5.5}$$

where $\overline{\bullet}$ means averaging of $\bullet$ over the ensemble of baths and over the realizations of the noise $F(t)$ in the qubit frequency, while

$$\rho_{ij} = \sum_{n,n_1,n_2,\ldots} \overline{c^*_{i,n,n_1 n_2 \ldots} c_{j,n,n_1 n_2 \ldots}} = \langle i|\rho|j\rangle, \quad i,j = \downarrow,\uparrow. \tag{5.6}$$

It is seen that ρ is the qubit density matrix. Quantities $\rho_{\downarrow\downarrow}$, $\rho_{\uparrow\uparrow}$ are the probabilities of finding the qubit in either of its eigenstates. Each of the other two matrix elements, $\rho_{\downarrow\uparrow}$ and $\rho_{\uparrow\downarrow}$, expresses the ability to interfere of the amplitudes of probability $\langle \mathrm{q},\mathrm{r},\mathrm{b}|\downarrow\rangle$ and $\langle \mathrm{q},\mathrm{r},\mathrm{b}|\uparrow\rangle$. In other words, it is those non-diagonal density matrix elements that store the qubit state coherence.

It is straightforward to find the evolution of $\rho_{\downarrow\uparrow}$ and $\rho_{\uparrow\downarrow}$ through the corresponding operators in the Heisenberg picture. From Eq. (5.4) and the definition of the qubit lowering operator one finds at time t:

$$\begin{aligned}\rho_{\downarrow\uparrow}(t) &= \rho^*_{\uparrow\downarrow}(t) = \overline{\langle \mathrm{q,r,b}:t|\sigma_-|\mathrm{q,r,b}:t\rangle} \\ &= \overline{\langle \mathrm{q,r,b}:0|U^\dagger(t)\sigma_- U(t)|\mathrm{q,r,b}:0\rangle} = \overline{\langle \mathrm{q,r,b}:0|\sigma_-(t)|\mathrm{q,r,b}:0\rangle} \\ &= \langle\sigma_-(t)\rangle,\end{aligned} \tag{5.7}$$

where σ_- and $\sigma_-(t)$ denote the lowering operators in the Schrödinger and the Heisenberg pictures respectively, and $U(t)$ denotes the evolution operator of the system. Here and in what follows $\langle\bullet\rangle$ denotes both the expectation value of $\bullet$ and its averaging $\overline{\bullet}$ by the ensemble of baths.

We conclude that the magnitude of $\langle\sigma_-(t)\rangle$ is the qubit coherence. In what follows, the average $\langle\sigma_-(t)\rangle$ is found, using the Heisenberg equations of motion.

2 Cavity population

To calculate $\langle\sigma_-\rangle$, we first need to find the cavity population. It consists of the photons due to the coherent drive, and the thermal photons.

We use the expression (3.35) for the photon annihilation operator a to arrive at

$$\langle n\rangle \approx n_\mathrm{b} + n_\mathrm{d}, \quad n = a^\dagger a, \tag{5.8}$$

where we neglect the $\propto \lambda^2$ terms and higher. Here

$$n_\mathrm{d} = \Big\langle \frac{f^2|c|^2}{\tilde\omega_\mathrm{dr}^2 + \kappa^2/4}\Big\rangle \tag{5.9}$$

is the number of the drive photons in the resonator, and

$$n_\mathrm{b} = \int_0^\infty dk \,\Big\langle \frac{f_k^2}{\tilde\omega_{k\mathrm{r}}^2 + \kappa^2/4}\Big\rangle \sum_{\alpha=\mathrm{I,II}} \langle b_k^{\alpha\dagger}(0) b_k^\alpha(0)\rangle \tag{5.10}$$

is the number of the bath photons in it. Here the operators $\tilde\omega_\mathrm{dr}$ and $\tilde\omega_{k\mathrm{r}}$ of effective detuning with the cavity are as defined in Eq. (3.36). Also, in obtaining Eq. (5.8), it was taken into account that $\sigma_\mathrm{z} \approx \sigma_\mathrm{z}(0)$ in the accuracy of Eq. (3.35), and therefore σ_z commutes with $b_k^\alpha(0)$. In addition, averages of the mixed products with drive and noise terms from Eq. (3.35) vanish. Indeed, these products split into the products of averages. The respective noise averages are negligible as discussed in the derivation of Eq. (3.39) for $\langle a\rangle$.

We calculate the thermal population in the equilibrium with the bath which is comprised by the waveguide modes. In Ch. III we have split the waveguide operators into the drive and the drive operators with a unitary transformation as in Ref. [16]. Here we assume that in the resulting frame the waveguides are in the thermal state. The density matrix of the first waveguide is

$$\rho^\mathrm{I} = \sum_N^\infty \int_0^\infty dk_1 \ldots \int_0^\infty dk_M \,|\mathrm{w}^\mathrm{I}_{k_1\ldots k_N}\rangle\, C e^{\hbar v(k_1+\ldots+k_N)/k_B T}\, \langle \mathrm{w}^\mathrm{I}_{k_1\ldots k_N}|, \tag{5.11}$$

and similarly for the second one. That is, there is no coherence between the waveguide

energy states, and the probabilities to find each state are due to the Gibbs distribution [92]. Here T is the cryostat temperature, k_B is the Boltzmann constant, vk is the frequency of the mode with wavevector k, and C is the normalization constant such as $C\,\mathrm{Tr}\,\rho = 1$. The state vectors $|\mathrm{w}^{\mathrm{I}}_{k_1\ldots k_N}\rangle$ are as explained for Eq. (5.2). Consider the thermal population due to the first waveguide n_b^{I}, which is given by the $\alpha = \mathrm{I}$ part of the sum in Eq. (5.10). Using that $\langle \mathrm{w}^{\mathrm{I}}_{k_1\ldots k_N}|b^{\mathrm{I}\dagger}b^{\mathrm{I}}|\mathrm{w}^{\mathrm{I}}_{k_1\ldots k_N}\rangle = N$, we find

$$n_b^{\mathrm{I}} = C\,\mathrm{Tr}\left\{\rho^{\mathrm{I}}\int_0^\infty dk \frac{f_k^2\, b_k^{\mathrm{I}\dagger} b_k^{\mathrm{I}}}{\omega_{\mathrm{kr}}^2 + \kappa^2/4}\right\} \approx C\int_{-\infty}^{\infty} dk \sum_{N=0}^{\infty} \frac{f^2 N e^{-\hbar v k N/k_B T}}{\omega_{\mathrm{kr}}^2 + \kappa^2/4}. \tag{5.12}$$

In the spirit of the Markov approximation, we have extended the integration to $-\infty$ and assumed constant coupling $f_k \approx f$. Also, we neglect the dispersive shift here as it is small compared to the resonator frequency. Performing the complex integration, and summing up over N yields

$$n_b^{\mathrm{I}} \approx C\sum_{N=0}^{\infty} \frac{2\pi i f^2}{v}\frac{N e^{-\hbar\omega_{\mathrm{r}} N/k_B T}}{i\kappa} = \frac{1}{2}\,\frac{1}{e^{\hbar\omega_{\mathrm{r}}/k_B T} - 1}, \tag{5.13}$$

where we have used the definition (3.28) of the decay rate κ. Also, we have plugged in the value of $C = 1 - e^{-\hbar\omega_{\mathrm{r}}/k_B T}$ which can be found similarly to the above calculations. The same amount of thermal excitations comes from the second waveguide. Hence, as expected, we recover the Bose-Einstein distribution for the photon population [92]:

$$n_b = \frac{1}{e^{\hbar\omega_{\mathrm{r}}/k_B T} - 1}. \tag{5.14}$$

This result can be obtained in a simpler manner using the discrete representation of the bath modes [27].

3 Equation for the qubit lowering operator

Here we find the Langevin equation for the qubit lowering operator σ_-. We take into account the noise coming from the resonator state and the waveguides. We model other noise sources with the classical noise F in the qubit frequency.

From the form of the Hamiltonian (3.16), the equation of motion of σ_- is

$$\dot\sigma_- = -i\Omega_{\mathrm{q}}\sigma_- + i\lambda\sigma_{\mathrm{z}}\Big(\int_0^\infty dk f_k(b_k^{\mathrm{I}} + b_k^{\mathrm{II}}) + fc - Fa\Big) + o(\lambda), \tag{5.15}$$

where

$$\Omega_{\mathrm{q}}(t) = \omega_{\mathrm{q}} + 2g\lambda(a^\dagger a|_t + 1/2) + F(t) \tag{5.16}$$

is the effective qubit frequency.

Next, along the lines we have obtained the Langevin equation (1.60), we obtain the Langevin equation for $\sigma_-(t)$,

$$\begin{aligned}\dot\sigma_-(t) = -i\Omega_{\mathrm{q}}(t)\sigma_-(t) + \lambda\sigma_{\mathrm{z}}\Big(i\int_0^\infty dk f_k[b_k^{\mathrm{I}}(0) + b_k^{\mathrm{II}}(0)]e^{-i\omega_k t} \\ + ifc(t) + \frac{\kappa}{2}a(t) - iF(t)a(t)\Big) + o(\lambda).\end{aligned} \tag{5.17}$$

We dropped the dependency of σ_{z} on time, as taking account of it exceeds the accuracy of the equation.

4 Coherence in the weak measurement

In this section, we calculate the qubit coherence for the case of weak measurement,

$$g\lambda \ll \kappa. \tag{5.18}$$

In this regime, we avoid assumptions about the statistics of the frequency fluctuations. For that, we make a physically motivated guess in finding the solution of Eq. (5.17).

Consider the time-dependent frequency term in that equation. Photon-number dependent parts there are operators, thus $[a^\dagger(t_2)a(t_2), a^\dagger(t_1)a(t_1)] \neq 0$ and the qubit frequency Ω_q does not commute with itself at different times. Therefore, in general, the solution of Eq. (5.17) requires time ordering.

However, we assume that the time ordering can be neglected if the condition (5.18) holds. We present an intuitive reasoning to back that assumption. When $|t_2 - t_1| \ll 1/g\lambda$, dispersive interaction has not yet changed $a^\dagger(t_2)a(t_2)$ enough to not commute with $a^\dagger(t_1)a(t_1)$. On the other hand, for $|t_2 - t_1| \gg 1/\kappa$ dissipation has already diminished the quantumness of $a^\dagger a$ and the respective two-time commutator is negligible. Due to the condition (5.18), these two intervals of $|t_2 - t_1|$ overlap and the commutator is negligible for all times. In that case the solution of Eq. (5.17) takes the form:

$$\begin{aligned}\sigma_-(t) \approx \sigma_-(0) \exp\left(-i\int_0^t dt' \Omega_\mathrm{q}(t')\right) + \lambda\sigma_\mathrm{z}\int_0^t dt' \exp\left(-i\int_{t'}^t dt'' \Omega_\mathrm{q}(t'')\right) \\ \times \left(i\int_0^\infty dk f_k[b_k^\mathrm{I}(0) + b_k^\mathrm{II}(0)]e^{-i\omega_k t'} + ifc(t') + \frac{\kappa}{2}a(t') - iF(t')a(t')\right).\end{aligned} \tag{5.19}$$

It is convenient to split the phase of each of the exponents in Eq. (5.19) into deterministic and fluctuating part. We separate deterministic and noise parts in the effective qubit frequency,

$$\Omega_\mathrm{q}(t) = \langle\Omega_\mathrm{q}\rangle + 2g\lambda\Delta n(t) + F(t), \tag{5.20}$$

$$\Delta n(t) = n(t) - \langle n(t)\rangle. \tag{5.21}$$

This yields the following expression for the phase:

$$\int_{t'}^t dt'' \Omega_\mathrm{q}(t'') = \langle\tilde{\omega}_\mathrm{q}\rangle(t - t') + \Delta\phi_n(t', t) + \Delta\phi_F(t', t), \tag{5.22}$$

where $\tilde{\omega}_\mathrm{q}$ is defined in Eq. (1.40). In the course of obtaining the last expression we used that $\langle F(t)\rangle = 0$ and $\langle n\rangle = \mathrm{const}$ by Eqs. (5.8)–(5.10). Also, we have introduced the following notations: the phase noise

$$\Delta\phi_n(t_1, t_2) = 2g\lambda\int_{t_1}^{t_2} dt' \Delta n(t') \tag{5.23}$$

caused by the fluctuations Δn of photon number, and the noise

$$\Delta\phi_F(t_1, t_2) = \int_{t_1}^{t_2} dt' F(t') \tag{5.24}$$

caused by the natural fluctuations $F(t)$ in the qubit frequency.

4.1 Averaging to find the coherence

In finding $\langle\sigma_-\rangle$, we neglect the second term in Eq. (5.19). It gives rise to small oscillations of magnitude about $\lambda f|c(0)|/\omega_{\rm qr}$ due to the integrand term with the drive signal $c(t')$. Also, we expect the noise terms there to provide a small amount of coherence on averaging, similarly to the estimate in Eq. (3.38). We leave the proper averaging of the noise terms for future work. Here we assume that

$$\langle\sigma_-(t)\rangle \approx \langle\sigma_-(0)\rangle\Big\langle\exp\Big[-i\int_0^t dt'\Omega_{\rm q}(t')\Big]\Big\rangle. \tag{5.25}$$

We confine ourselves to the time scales much greater than both $2/\kappa$ the resonator photon lifetime and τ_F the coherence time of $F(t)$:

$$t \gg 2/\kappa, \tau_F. \tag{5.26}$$

Under this assumption, average of the solution (5.25) simplifies. Qubit frequency fluctuations taken at the moments separated by their coherence time, $F(t)$ and $F(t+\tau_F)$, can be considered to be independent random variables. The same holds for the photon number fluctuations, $\Delta n(t)$. Those fluctuations coherence is estimated by the time $2/\kappa$ the system "remembers" a photon state in the resonator. Hence, for times qualifying the condition (5.26), integrals in Eqs. (5.23), and (5.24) become infinite sums of independent random variables. With assumption of $\Delta n(t)$ and $\Delta F(t)$ stationary, the integrals yield normally distributed random variables by the central limit theorem. It is shown in Appendix III.A that $\langle e^x\rangle = \exp\frac{\langle x^2\rangle}{2}$ for an x normally distributed. Using this identity for normally-distributed $i\phi_n$ and $i\phi_F$, one obtains from Eq. (5.25) and Eq. (5.22) that

$$\langle\sigma_-(t)\rangle = \langle\sigma_-(0)\rangle e^{-i\langle\tilde{\omega}_{\rm q}\rangle t}\exp\left(-\frac{1}{2}\langle\Delta\phi_n^2(t)\rangle - \frac{1}{2}\langle\Delta\phi_F^2(t)\rangle\right). \tag{5.27}$$

We follow Ref. [70] in finding $\langle\Delta\phi_F^2(t)\rangle$. It is assumed that $F(t)$ is stationary and

$$\langle\Delta\phi_F^2(t)\rangle = \int_0^t\int_0^t dt_1 dt_2\langle F(0)F(t_2-t_1)\rangle; \tag{5.28}$$

with the Wiener-Khinchin theorem, it is expressed as

$$\langle\Delta\phi_F^2(t)\rangle = \int_{-\infty}^{+\infty} d\omega S_{FF}(\omega)W(\omega), \tag{5.29}$$

where

$$W(\omega) = \int_0^t\int_0^t dt_1 dt_2 e^{i\omega(t_2-t_1)} = \frac{\sin^2(\omega t/2)}{(\omega/2)^2}. \tag{5.30}$$

is the spectral weight of those fluctuations in the phase noise. Due to the form of $W(\omega)$, it is the region $|\omega| < 2\pi/t$ which influences $\langle\Delta\phi_F^2(t)\rangle$ most. According to the condition (5.26), we approximate $S(\omega)\approx S(0)$ in this region. Therefore,

$$\langle\Delta\phi_F^2(t)\rangle \approx 2\Gamma_0 t, \tag{5.31}$$

where

$$\Gamma_0 = \pi S_{FF}(0), \tag{5.32}$$

and

$$S_{FF} = \frac{1}{2\pi}\int_{-\infty}^{+\infty} dt e^{-i\omega t}\langle F(t)F(0)\rangle \tag{5.33}$$

is the spectral density of the fluctuations in the qubit frequency. In other words, we assume F to be a delta-correlated white noise on the timescales t that we are interested in. As can be seen from Eqs. (5.27) and (5.31), Γ_0 is the natural decoherence rate of the qubit.

To find $\langle\Delta\phi_n^2(t)\rangle$, the correlator $\langle\Delta n(t_1)\Delta n(t_2)\rangle$ is needed first. $\langle b_k(0)\rangle = 0$ as the transmission lines are thermalized. By the same reason, we assume the waveguide modes including the drive mode to be not entangled at the initial moment of time. Hence $\langle b_k^{\alpha(\dagger)}(0)c(0)\rangle = 0$, $\langle b_k^{\alpha(\dagger)}(0)b_l^{\beta}(0) = 0\rangle$ for $k \neq l$ or $\alpha \neq \beta$. By virtue of Eq. (3.35) and these assumptions, the correlator can be expressed as

$$\begin{aligned}\langle\Delta n(t_1)\Delta n(t_2)\rangle = &\sum_{k,\alpha}\langle B_{k1}^{\alpha\dagger}B_{k2}^{\alpha}\rangle\sum_{l,\beta}\langle B_{l1}^{\beta}B_{l2}^{\dagger\beta}\rangle \\ &+ C_2^*C_1\sum_{k,\alpha}\langle B_{k1}^{\alpha\dagger}B_{k2}^{\alpha}\rangle + C_1^*C_2\sum_{l,\beta}\langle B_{l1}^{\beta}B_{l2}^{\beta\dagger}\rangle + o(\lambda),\end{aligned} \tag{5.34}$$

where $B_{ki}^{\alpha} = f_k b_k^{\alpha}(0)e^{-i\omega_k t_i}/(\tilde{\omega}_{kr} + i\kappa/2)$, $C_i = fc(0)e^{-i\omega_d t_i}/(\tilde{\omega}_{dr} + i\kappa/2)$ with $\omega_{dr} = \omega_d - \omega_r$ the bare detuning. The expression can be simplified. We assume the modes to be closely spaced. Also, in the narrow range cut by the resonator Lorentzian, those modes number of photons is taken to be constant. Thus,

$$\sum_k\langle B_{k1}^{\alpha\dagger}B_{k2}^{\alpha}\rangle = \frac{n_b}{2}e^{-i\tilde{\omega}_r(t_2-t_1)-\frac{\kappa}{2}|t_2-t_1|}, \tag{5.35}$$

where the definition (3.28) of κ was used and n_b is given by Eq. (5.14). With help of Eq. (5.35), the correlator is finally obtained,

$$\begin{aligned}\langle\Delta n(t_1)\Delta n(t_2)\rangle = &\, n_b(n_b+1)e^{-\kappa|t_2-t_1|} \\ &+ n_d\left(2n_b\cos\omega_{dr}(t_2-t_1) + e^{-i\omega_{dr}(t_2-t_1)}\right)e^{-\frac{\kappa}{2}|t_2-t_1|} + O(\lambda).\end{aligned} \tag{5.36}$$

We have neglected the frequency shift $g\lambda$ as it is not visible on top of the decay rate $\kappa/2$ under the condition (5.18) of the weak measurement. The expression (5.36) shows that the photon number fluctuations become uncorrelated when $|t_2 - t_1| > 2/\kappa$. Previously, in obtaining Eq. (5.27), we explained this intuitively.

Let us check some limiting cases of the photon number statistics. For the limit of negligible thermal occupation

$$n_b \ll n_d, \frac{1}{2}, \tag{5.37}$$

it is seen from Eqs. (5.36) and (5.8) that $\langle\Delta n^2\rangle \approx \langle n\rangle$. This is a hallmark of a coherent state. On the other hand, for $n_b \gg n_d$ one has $\langle\Delta n^2\rangle \approx \langle n\rangle + \langle n\rangle^2$. A thermal state possesses such a statistics.

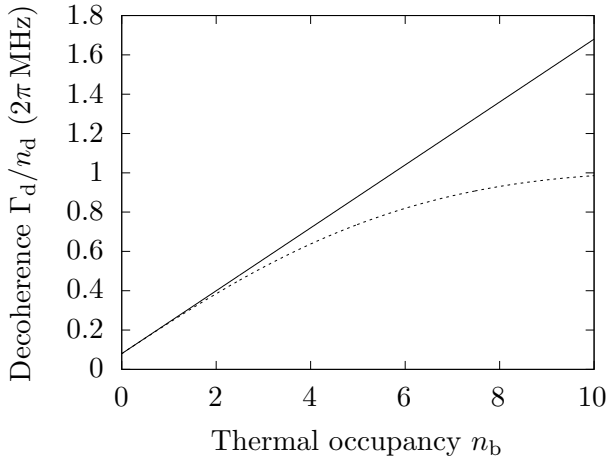

FIGURE 5.1: Dependence of the measurement-induced qubit dephasing on the thermal occupancy for small temperatures: Γ_d as given by the simple expression (5.39) (solid) and the expression given in Ref. [89] (dashed). Measurement is weak with $\kappa = 2\pi\,100\,\text{MHz}$ and $\chi = 2\pi\,1\,\text{MHz}$. Thermal occupancy n_b is much smaller than the number of photons due to the coherent drive n_d.

Now we are in position to calculate $\langle\Delta\phi^2\rangle$ and $\langle\sigma_-\rangle$. We set $\omega_{dr} = 0$. Using Eqs. (5.36) and (5.23) and taking the appropriate integrals, we obtain

$$\frac{\langle\Delta\phi_n^2\rangle}{2} = (\Gamma_d + \Gamma_b)t, \tag{5.38}$$

$$\Gamma_d = \frac{16g^2\lambda^2}{\kappa} n_d \left(n_b + \frac{1}{2}\right), \tag{5.39}$$

$$\Gamma_b = \frac{4g^2\lambda^2}{\kappa} n_b(n_b + 1), \tag{5.40}$$

where it was taken into account that $t \gg 2/\kappa$ according to Eq. (5.26). By means of Eq. (5.38), the expression for coherence (5.27) reduces to

$$\langle\sigma_-(t)\rangle = \langle\sigma_-(0)\rangle e^{-i\langle\tilde{\omega}_q\rangle t} \exp[-(\Gamma_0 + \Gamma_d + \Gamma_b)t], \tag{5.41}$$

where Γ_0 the natural dephasing rate of the qubit is defined in Eq. (5.32). We conclude that here $\Gamma_d + \Gamma_b$ is the decay rate that arises due to the photon fluctuations. Its drive-induced part Γ_d can be "amplified" by the presence of thermal photons, according to Eq. (5.39). The purely thermal part Γ_b is negligible for reasonably low temperatures and strong enough drive. One can show that in the weak measurement limit (5.18), the expressions (5.39)–(5.40) stay intact for $\omega_{dr} \sim \chi$.

Limiting cases of the expressions given are known in the literature. The correlator (5.36) and $\langle\sigma_+(t_1)\sigma_-(t_2)\rangle$ were found in Refs. [79, 86] in the case of no thermal photons. In the limit (5.37), $\langle\sigma_+(t_1)\sigma_-(t_2)\rangle$ from the reference is proportional to the exponent in Eq. (5.41). In the same limit, the correlator (5.36) coincides with that found in the literature. In Refs. [87, 88] a resonator occupied solely by thermal photons was considered. Our expression (5.40) for Γ_b equals that of Ref. [87]. Also, it is the same as the golden-rule part of the expression from Ref. [88]. In Ref. [89] both parts induced by the drive and the thermal photons are found. The thermal part, in the Fermi's golden rule approximation, coincides with the expression (5.40).

A different expression for the drive-induced part of the decoherence was found in

Ref. [89] with the effect of thermal photons taken into account. In our notations and for $\omega_{\rm dr} = 0$, the expression from the reference reads

$$\Gamma_{\rm d} = n_{\rm d}\frac{\kappa^2\chi}{2}\frac{\Delta_{\rm th}(\kappa + 2\Gamma'_{\rm b})}{[\Delta_{\rm th}^2 + (\kappa + 2\Gamma'_{\rm b})^2/4]^2}, \tag{5.42}$$

where $\Delta_{\rm th} = \frac{\kappa}{2}\,{\rm Im}\,\xi$, $\Gamma'_{\rm b} = \frac{\kappa}{2}({\rm Re}\,\xi - 1)$, and $\xi = \sqrt{(1 + 2i\chi/\kappa)^2 + 8i\chi n_{\rm b}/\kappa}$. It is claimed to be valid beyond the weak measurement regime. When both the condition (5.18) of weak measurement and the condition $n_{\rm b}^2 \ll \kappa^2/32\chi^2$ hold, Eq. (5.42) coincides with Eq. (5.39). A comparison between the two formulas is plot in Fig. 5.1.

In the case of resonant drive $\omega_{\rm d} = \omega_{\rm r}$, the correlator (5.35) was obtained in my Master's thesis [90]. While the decoherence rates (5.39)–(5.40) can be deduced from Eq. (3.41) in the Master's thesis, here we have clearly provided the expressions for them, properly taking into account the Gaussian approximation (5.26) we use. These expressions were obtained in a rather careless way in the Master's thesis. Most importantly, the time ordering in the solution for the qubit phase was disregarded there, despite the presence of the operator $a^\dagger a$ in the qubit frequency. Here we have used a more solid approach overall, and we have heuristically motivated that the time ordering can be neglected in Eq. (5.19) for the weak measurement case (5.18).

5 Summary and discussion

We have determined the effect of thermal photons on the measurement-induced decoherence for the case of weak measurement [see the criterion (5.18)] and when the Gaussian approximation is valid [see the criterion (5.26)]. Also, the two-time correlator of the photon number fluctuations has been found. The decoherence rate consists of three parts [see Eq. (5.39)]: a part due to the drive photons alone, a part proportional to both the drive and the thermal population, and a part quadratic in the thermal population that does not depend on the drive. When the quadratic term is negligible, $n_{\rm b}$ thermal photons entering the resonator increase the qubit dephasing rate proportionally to $n_{\rm b} + 1/2$.

Since the publication of my Master's thesis [90], we have been able to find the analogous results in the literature. Compared to the result of Ref. [89], our expression for the measurement-induced decoherence rate is much easier to interpret. The expression from the reference coincide with Eq. (5.39) in the limit of weak measurement and small number of thermal photons.

Compared to the results of the Master's thesis [90], here we have provided explicit expressions for the decoherence rates (5.39)–(5.40) in the proper approximation. Our derivation is now more rigorous and straightforward and does not contain a hidden approximation about the time ordering in the solution for the qubit variables. We claim that the time ordering can be neglected in the weak measurement regime. In that approximation, qubit phase noise can be considered Gaussian for any type of its frequency noise.

Still, there are several issues that we consider unresolved. First, we were not able to thoroughly estimate the dressing correction in the qubit coherence which we have neglected in Eq. (5.27). Finding out the average of the term with the natural noise in the qubit frequency F in the second term of Eq. (5.19) may require the knowledge of the natural noise statistical properties, as described for superconducting qubits in Refs. [65, 66, 93, 94]. Estimate of the waveguide-related terms with operators $b_k^{\alpha(\dagger)}$ may be found using a quasiprobability distribution as in Refs. [79, 88, 89]. Second, it is not very clear to us now, how our theory breaks at higher number of thermal photons

n_b. That happens even if it is compared to the treatment of Ref. [89], which also does not take into account the higher-order nonlinearities [21, 28] in the dispersive Hamiltonian (1.35). The comparison in Fig. (5.1) suggests that our theory breaks already for $n_\mathrm{b} > 5$, which is worse than we expected. A possible explanation is that the time ordering that we have neglected in Eq. (5.19) becomes more important for higher populations. In the future, it might be interesting to properly prove that one can drop the time ordering in the weak measurement limit. Another explanation is that the non-Gaussian nature of frequency fluctuations becomes more pronounced for higher photon numbers.

We provide more detail to back this claim. For higher powers of the frequency noise, decoherence occurs already on small timescales [79, 86, 95, 96]. Following Ref. [96], we estimate $\langle e^{i\phi} \rangle \approx \langle e^{i\frac{d\phi}{dt}t} \rangle$ for small times t. Statistics of the *frequency* noise $d\phi/dt$ then determines the average. This approximation may be used in future research.

Chapter VI

Fock photons transport beyond the rotating-wave approximation

In this chapter, we provide a theory of transport of photons in a Fock state through the resonator and the qubit beyond the RWA. Previous studies of the few-photon transport through the resonator coupled to a qubit (see, e.g., Refs. [97–101]) use the RWA to describe the resonator-qubit interaction. Here go beyond the RWA in treating the photon transport by systematically taking into account the Bloch-Siegert shift.

Dissipation to the waveguides of the qubit and the resonator beyond the RWA should be treated carefully [102]. While a suitable master equation for that case is derived in that reference, we choose a different method to treat the system. Our treatment of the system dynamics and photon transport is based on the Heisenberg-Langevin equations for the entire system including the waveguides. The approach is inspired by Refs. [27, 74]. It allows us to highlight some subtle moments that arise due to the break of the RWA. While we focus on the superconducting qubit readout, our treatment is applicable to other types of qubits that couple strongly to a cavity.

1 Hamiltonian

We model the system as shown in Fig. 6.1. The system Hamiltonian reads

$$H = H_{\mathrm{q}} + H_{\mathrm{qr}} + H_{\mathrm{r}} + H_{\mathrm{rI}} + H_{\mathrm{rII}} + H_{\mathrm{I}} + H_{\mathrm{II}}, \tag{6.1}$$

where

$$H_{\mathrm{q}} = \frac{1}{2}\hbar\omega_{\mathrm{q}}\sigma_{\mathrm{z}}, \quad H_{\mathrm{r}} = \hbar\omega_{\mathrm{r}}\left(a^{\dagger}a + \frac{1}{2}\right), \tag{6.2}$$

$$H_{\mathrm{qr}} = \hbar g\sigma_{\mathrm{x}}(a + a^{\dagger}) \tag{6.3}$$

are the Hamiltonians of the qubit, the resonator, and the qubit-resonator interaction, respectively. Together, these three comprise the Rabi Hamiltonian. Here and below we use the following notations: σ_{x}, σ_{y}, and σ_{z} for the Pauli operators of the qubit (quasi)spin; $\sigma_{\pm} = \frac{1}{2}(\sigma_{\mathrm{x}} \pm i\sigma_{\mathrm{y}})$ for the raising and lowering operators of the qubit; $a^{\dagger}$

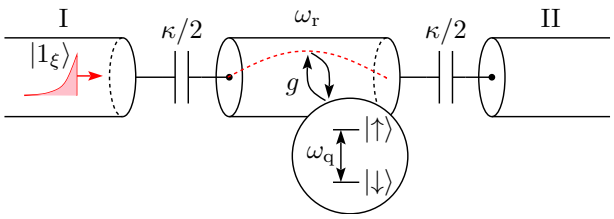

FIGURE 6.1: The system. Semi-infinite waveguides I and II couple to the resonator. They model the lack of back action on the cavity and the qubit: after a photon scatters off the resonator, it does not return. A single-photon pulse $|1_\xi\rangle$ of exponentially damped shape is incident on the first port of a cavity. The cavity resonant frequency is ω_r and its leakage is $\kappa/2$ to each of its ports. The cavity is dispersively coupled to a qubit with rate g. The qubit transition frequency is ω_q.

and a for the resonator photon creation and annihilation operators; g for the qubit-resonator coupling strength. Hamiltonians of the waveguide fields are

$$H_\alpha = \hbar \int_0^\infty dk\, \omega_k b_k^{\alpha\dagger} b_k^\alpha, \quad \alpha = \mathrm{I}, \mathrm{II}, \tag{6.4}$$

where the contribution of the zero-point oscillations is omitted. $b_k^{\alpha\dagger}$ and b_k^α are the operators of creation and annihilation of a photon with wave vector k and frequency ω_k in the waveguide with index α. The term responsible for the interaction of the waveguides with the resonator is

$$H_{\mathrm{r}\alpha} = i\hbar \int_0^\infty dk f_k (a - a^\dagger)(b_k^\alpha + b_k^{\alpha\dagger}). \tag{6.5}$$

We assumed that the resonator couples to both waveguides in the same manner and with equal strength. With a unitary transformation, one can move from $H_{\mathrm{r}\alpha}$ to the Hamiltonian (2.43) derived before. H_qr (6.3) is then transformed to the Hamiltonian (1.20) up to a unitary transformation in the qubit variables. Therefore, under the convention of Eqs. (1.6)–(1.7), our Hamiltonian describes the inductive qubit-resonator coupling and the capacitive interaction with the waveguides—exactly the situation we considered in Ch. II.

In general, the choice of signs in the Hamiltonians (6.3) and (6.5) captures the case of different-type couplings: capacitive waveguide-resonator coupling and inductive qubit-resonator interaction, or vice versa. If we do not drop the fast-oscillating terms in the Hamiltonians, they are not equivalent to those with same-type couplings (see Sec. I.2 and Ref. [20]). However, the change of the coupling type does not alter the main results of this chapter. Section 3 outlines the changes in the case of a general linear transversal coupling. A partial case of a same-type interaction is discussed there as well.

1.1 Bloch-Siegert regime

The case of the qubit strongly detuned from the resonator is of interest. If $\omega_\mathrm{q} - \omega_\mathrm{r} \sim \omega_\mathrm{q} + \omega_\mathrm{r}$, the RWA breaks down. We assume, however, that the frequencies are of the same order of magnitude,

$$\omega_\mathrm{q} \sim \omega_\mathrm{r}, \tag{6.6}$$

and there is a small parameter

$$\Lambda^2 \ll 1, \quad \Lambda = g/(\omega_\mathrm{q} + \omega_\mathrm{r}). \tag{6.7}$$

We also assume that there are not more than two photons in the cavity: one photon can come from the single-photon input pulse and another one can appear due to the excitation exchange with the qubit. Under these assumptions, the terms proportional to $a^\dagger\sigma_+ + a\sigma_-$ in the Rabi Hamiltonian can be treated as a perturbation and eliminated via the unitary transformation

$$U_\mathrm{BS} = \exp(\Lambda a\sigma_- - \Lambda a^\dagger\sigma_+). \tag{6.8}$$

Transforming the Rabi Hamiltonian (6.2)–(6.3) with U_BS gives

$$\begin{aligned} H_\mathrm{q} + H_\mathrm{qr} + H_\mathrm{r} &\to U_\mathrm{BS}^\dagger(H_\mathrm{q} + H_\mathrm{qr} + H_\mathrm{r})U_\mathrm{BS} \\ &= H_\mathrm{q} + H'_\mathrm{qr} + H'_\mathrm{r} + O(\Lambda^2), \end{aligned} \tag{6.9}$$

$$H'_\mathrm{qr} = \hbar g(\sigma_+ a + a^\dagger\sigma_-), \tag{6.10}$$

$$H'_\mathrm{r} = \hbar(\omega_\mathrm{r} + g\Lambda\sigma_\mathrm{z})\left(a^\dagger a + \frac{1}{2}\right). \tag{6.11}$$

The shift $g\Lambda\sigma_\mathrm{z}$ in the cavity resonance is known as the Bloch-Siegert shift [102].

We have omitted $\hbar g\Lambda\sigma_\mathrm{z}a^2$ and its conjugate in Eq. (6.9). Upon integration of the equations of motion for $\sigma_\pm$ and $a^{(\dagger)}$, these terms contribute in the order of $g\Lambda/\omega_\mathrm{r}$. Due to the condition (6.6), this is of order Λ^2 and should be neglected. In the same approximation, the transform (6.8) is identical to that used in Ref. [102].

Now we transform the rest of the terms in the full Hamiltonian (6.1). Using Eqs. (6.9)–(6.11) and $a \to U_\mathrm{BS}^\dagger a U_\mathrm{BS} = a - \Lambda\sigma_+ + O(\Lambda^2)$, one gets

$$H \to H' = H_\mathrm{q} + H_\mathrm{qr} + H'_\mathrm{r} + H_\mathrm{rI} + H_\mathrm{rII} + H'_\mathrm{qI} + H'_\mathrm{qII} + H_\mathrm{I} + H_\mathrm{II} + O(\Lambda^2). \tag{6.12}$$

The term

$$H'_{\mathrm{q}\alpha} = \hbar\Lambda\int_0^\infty dk f_k\sigma_\mathrm{y}(b_k^\alpha + b_k^{\alpha\dagger}) \tag{6.13}$$

describes the direct coupling between the dressed qubit and the waveguide. The Hamiltonian (6.12) allows for Purcell decay in which the qubit relaxes to the waveguides via the resonator. To take account of the Purcell decay, the Hamiltonian (6.12) is used in Ref. [29] to model the single-photon transport through the resonator-qubit system.

In the next two sections, we assume that the qubit relaxation is negligible. It is possible to obtain analytical results for that case.

1.2 Dispersive Bloch-Siegert picture

The Hamiltonian (6.9)–(6.11) of the qubit-resonator subsystem is of the Jaynes-Cummings form. It is possible to diagonalize it with a treatment similar to that of Sec. 2.2 and Ref. [19]. The resonator-qubit detuning is large,

$$4\lambda^2 \ll 1, \quad \lambda = g/(\omega_\mathrm{q} - \omega_\mathrm{r}). \tag{6.14}$$

That is the critical photon number criterion (1.33) (see also Refs. [19, 21]) for a cavity populated by a single photon. The photon comes from the input pulse. The dispersive approximation is valid under the condition (6.14), and we neglect the possibility that

the qubit will provide another photon. As $|\lambda| > \Lambda$, the inequality (6.7) follows from the last one, and $O(\Lambda^2) + O(\lambda^2) = O(\lambda^2)$ as well as $O(\Lambda\lambda) = O(\lambda^2)$. The dispersive transform (1.34) then approximately diagonalizes the Hamiltonian (6.9). Applying the transform yields

$$\begin{aligned} H \to{}& H_{\rm q} + \widetilde{H}_{\rm r} \\ &+ H_{\rm rI} + H_{\rm rII} + \widetilde{H}_{\rm qI} + \widetilde{H}_{\rm qII} \\ &+ H_{\rm I} + H_{\rm II} + O(\lambda^2), \end{aligned} \tag{6.15}$$

$$\widetilde{H}_{\rm r} = \hbar(\omega_{\rm r} + g\Lambda\sigma_{\rm z} + g\lambda\sigma_{\rm z})\left(a^\dagger a + \frac{1}{2}\right), \tag{6.16}$$

$$\widetilde{H}_{\rm q\alpha} = \hbar(\lambda + \Lambda)\int_0^\infty dk f_k \sigma_{\rm y}(b_k^\alpha + b_k^{\alpha\dagger}). \tag{6.17}$$

It was used that $a \to U_{\rm d}^\dagger a U_{\rm d} = a + \lambda\sigma_- + O(\lambda^2)$ and $\sigma_- \to \sigma_- + \lambda a\sigma_{\rm z} + O(\lambda^2)$. The total shift

$$\chi = g(\lambda + \Lambda) \tag{6.18}$$

in the resonator frequency is identical to that given in Ref. [103]. It sets the performance of a dispersive readout. As shown in Sec. 3, it does not change when the qubit-resonator and the resonator-waveguide couplings are of the same type. The Bloch-Siegert shift $g\Lambda$ becomes comparable with the dispersive one $g\lambda$ when $\omega_{\rm q} - \omega_{\rm r} \sim \omega_{\rm q} + \omega_{\rm r}$. Equations (6.15)–(6.17) constitute the Hamiltonian in the dispersive Bloch-Siegert picture. That is the picture we use in the next sections and in Ch. VII.

2 Photon transport

Here we calculate the density of transmitted photons for a single-photon Fock pulse with a given shape. First we link the density to the cavity population; then we express the population in terms of the incoming pulse spectrum. The result is generalized for an N-photon pulse.

2.1 Density of transmitted photons

The density of transmitted photons [73, 74] is

$$\langle\rho_{\rm tr}(x,t)\rangle = \frac{1}{2\pi}\int_0^\infty\int_0^\infty dk dl \langle b_k^{\rm II\dagger}(t) b_l^{\rm II}(t)\rangle e^{-i(k-l)x}, \tag{6.19}$$

where $x > 0$.

From the Hamiltonian (6.15), one obtains the equations of motion for the annihilation operators of a waveguide photon:

$$\begin{aligned} \dot{b}_k &= \frac{1}{i\hbar}[b_k, H] \\ &= -i\omega_k b_k + f_k[a - a^\dagger - i(\lambda + \Lambda)\sigma_{\rm y}]. \end{aligned} \tag{6.20}$$

Their formal solution is given by

$$b_k(t) = b_k(0)e^{-i\omega_k t} + f_k\int_0^t dt' e^{-i\omega_k(t-t')}[a - a^\dagger - i(\lambda+\Lambda)\sigma_{\rm y}]_{t'}. \tag{6.21}$$

Waveguide indices are omitted for brevity. The first term on the right-hand side of Eq. (6.21) represents the free-propagating part of the waveguide field and the second one describes the influence of the qubit and the resonator.

Now we derive two useful identities. Multiplying Eq. (6.21) by e^{ikx} and integrating over k, one obtains

$$\int_0^\infty dk\, b_k(t)e^{ikx} = \int_0^\infty dk\, e^{-ikv(t-x/v)}b_k(0) + \int_0^t dt' \int_0^\infty dk f_k e^{-ikv(t-t'-x/v)} \times [a - a^\dagger - (\lambda+\Lambda)(\sigma_+ - \sigma_-)]_{t'}, \quad (6.22)$$

where the dispersion relation (2.30) was used. Consider the second term on the right-hand side. Approximately, a, $a^\dagger$, σ_-, and σ_+ vary as $e^{-i\omega_\mathrm{r}t'}$, $e^{i\omega_\mathrm{r}t'}$, $e^{-i\omega_\mathrm{q}t'}$, and $e^{i\omega_\mathrm{q}t'}$. We drop the terms proportional to $\sigma_+(t')e^{ikvt'}$ and $a^\dagger(t')e^{ikvt'}$ since they oscillate rapidly and vanish after integration over t'. By a similar argument, we can extend the integration by k to $-\infty$ as in Sec. I.6.1. The remaining parts of the integrand comprise $\sigma_-(t')e^{ikvt'}$ and $a(t')e^{ikvt'}$ and oscillate fast for $k<0$. Next, due to integration over t', only narrow regions around respective frequencies of a and σ_- contribute significantly. We assume that the coupling strength f_k is approximately constant in these regions. Extending the integration to $-\infty$ and using that $\int_{-\infty}^{+\infty} dk\, e^{ikx} = 2\pi\delta(x)$ yields

$$\int_0^\infty dk\, b_k(t)e^{ikx} = \int_0^\infty dk\, e^{-ikv(t-x/v)}b_k(0) + \frac{2\pi}{v}\theta\Big(t-\frac{x}{v}\Big)\theta(x)[f_\mathrm{r}a + f_\mathrm{q}(\lambda+\Lambda)\sigma_-]_{t-x/v}, \quad (6.23)$$

where $f_{\mathrm{r,q}} = f(\omega_{\mathrm{r,q}}/v)$ and

$$\theta(t) = \begin{cases} 0 & \text{for } t<0, \\ 1/2 & \text{for } t=0, \\ 1 & \text{for } t>0 \end{cases} \quad (6.24)$$

is the Heaviside step function. Step functions arise due to integration of $\delta(t'-t+x/v)$ from $t'=0$ to t. At time t a point x in a waveguide is influenced by the qubit and the resonator states at time $t-x/v$ due to finite velocity of propagation. $\theta(t-x/v)$ ensures that the resonator and the qubit do not influence a point x in a waveguide for $t<x/v$. The reasoning analogous to that used in obtaining Eq. (6.23) leads to a similar identity,

$$\int_0^\infty dk f_k b_k(t) = \int_0^\infty dk f_k e^{-ikvt}b_k(0) + \frac{1}{4}\theta(t)[\kappa a + \kappa_\mathrm{q}(\lambda+\Lambda)\sigma_-]_t, \quad (6.25)$$

where

$$\kappa = 4\pi f_\mathrm{r}^2/v, \quad \kappa_\mathrm{q} = 4\pi f_\mathrm{q}^2/v. \quad (6.26)$$

It will be seen from what follows that κ is the total decay rate of the resonator. κ_q is the decay rate of the resonator as seen by the Purcell decay [102]. Equations (6.23) and (6.25) are written in the Markov approximation, similarly to Eqs. (1.60), (3.26), and (4.5).

In deriving Eqs. (6.23) and (6.25) we drop the terms under the integral which are proportional to $\sigma_+(t')e^{ikvt'}$ and $a^\dagger(t')e^{ikvt'}$. This relates to the RWA made to write out Eq. (A3) of Ref. [102]. In contrast to the reference, our approach allows making

this approximation naturally.

Substituting Eq. (6.23) into Eq. (6.19), one has

$$\langle\rho_{\rm tr}(x,t)\rangle = \frac{1}{2\pi}\int_0^\infty\!\!\int_0^\infty dkdl\langle b_k^{\rm II\dagger}(0)b_l^{\rm II}(0)\rangle e^{-iv(k-l)(t-x/v)} + \frac{\kappa/2}{v}\langle a^\dagger a\rangle_{t-x/v} + \frac{2\pi f_{\rm q}f_{\rm r}}{v^2}(\lambda+\Lambda)\big(\langle a^\dagger\sigma_-\rangle_{t-x/v} + \text{c. c.}\big) + \Big(\frac{1}{v}\Big\langle[f_{\rm r}a^\dagger + f_{\rm q}(\lambda+\Lambda)\sigma_+]_{t-x/v}\int_0^\infty dk\, e^{-ikv(t-x/v)}b_k^{\rm II}(0)\Big\rangle + \text{c. c.}\Big) + O(\lambda^2) \quad (6.27)$$

for $t > x/v > 0$.

Now we show that only the second term in Eq. (6.27) should be retained. First, we consider the averages that involve $b_k^{\rm II}$. Both waveguides, the resonator, and the qubit are entangled in the ground state due to the counter-rotating terms like $\sigma_- b_k^\alpha$ and ab_k^α in $\widetilde{H}_{{\rm q}\alpha}$ (6.17) and $H_{{\rm r}\alpha}$ (6.5). However, far from overdamping [104],

$$\kappa, \kappa_{\rm q} \ll \omega_{\rm r}, \omega_{\rm q}, \quad (6.28)$$

and for a narrow-band pulse, the system state is approximately separable. Then the second waveguide state is close to vacuum at $t = 0$. Indeed, the system is thermalized at a low temperature, $k_{\rm B}T \ll \hbar\omega_{\rm r}$. In this case, the number of thermal photons in the waveguides and the resonator is negligibly small. The input pulse has no effect on the second waveguide at $t = 0$. Hence the resonator-waveguide subsystem is in the ground state. Therefore, the first term in Eq. (6.27) vanishes. So does the term with $\langle a^\dagger(t)b_k^{\rm II}(0)\rangle$ and its conjugate. Now we treat the qubit-related averages. We assume that the qubit and the cavity are not initially correlated. The correlation arises, over the course of time, in the first order of interaction parameters λ and Λ, $\langle a^\dagger\sigma_\pm\rangle = O(\lambda)$. Then the terms with $\lambda+\Lambda$ in (6.27) are of second order in λ, which is beyond the accuracy of Eq. (6.27). Thus finally,

$$\langle\rho_{\rm tr}(x,t)\rangle = \frac{\kappa}{2v}\langle a^\dagger a\rangle_{t-x/v}, \quad t > \frac{x}{v} > 0. \quad (6.29)$$

This expression is interpreted as follows. In a time Δt, $\kappa\Delta t/2$ photons leak to the waveguide, where they propagate over a distance $v\Delta t$. The shape of a propagating pulse follows the cavity population dynamics. The delay x/v is due to finite velocity of propagation v.

2.2 Cavity population

Using the Hamiltonian (6.15), one obtains the equation of motion for the resonator variable

$$\dot a(t) = -i\widetilde{\omega}_{\rm r}(t)a(t) - \sum_{\alpha={\rm I,II}}\int_0^\infty dk f_k(b_k^\alpha + b_k^{\alpha\dagger})_t + O(\lambda^2), \quad (6.30)$$

$$\widetilde{\omega}_{\rm r}(t) = \omega_{\rm r} + g\Lambda\sigma_{\rm z}(t) + g\lambda\sigma_{\rm z}(t). \quad (6.31)$$

Applying Eq. (6.25) to Eq. (6.30) leads to the Heisenberg-Langevin equation for $t \geq 0$

$$\dot{a}(t) = \left[-i\widetilde{\omega}_{\mathrm{r}}(t) - \frac{\kappa}{2}\right] a(t) - \frac{\kappa}{2}a^{\dagger}(t) - \frac{\kappa_{\mathrm{q}}}{2}(\lambda+\Lambda)\sigma_{\mathrm{x}}(t) - \sum_{\alpha=\mathrm{I,II}} \int_0^{\infty} dk f_k (b_k^{\alpha}(0)e^{-ikvt} + \text{h. c.}) + O(\lambda^2). \quad (6.32)$$

It follows from the equation that κ is the decay rate of the resonator. Equations (6.30)–(6.32) are correct to the first order in λ. This follows from the accuracy of the Hamiltonian (6.15).

Now we solve Eq. (6.32). Since $\dot{\sigma}_{\mathrm{z}}(t) = O(\lambda)$, the time dependence of $\widetilde{\omega}_{\mathrm{r}}(t)$ is of the second order in λ. This exceeds the accuracy of Eq. (6.32) and should be neglected. Integrating Eq. (6.32), one obtains

$$a(t) = a(0)e^{-(i\widetilde{\omega}_{\mathrm{r}}+\kappa/2)t} - \int_0^t dt' e^{-(i\widetilde{\omega}_{\mathrm{r}}+\kappa/2)(t-t')} \left\{ \frac{\kappa}{2}a^{\dagger}(t) + \frac{\kappa_{\mathrm{q}}}{2}(\lambda+\Lambda)\sigma_{\mathrm{x}}(t') + \sum_{\alpha=\mathrm{I,II}} \int_0^{\infty} dk f_k [b_k^{\alpha}(0)e^{-ikvt'} + \text{h. c.}] \right\}. \quad (6.33)$$

We assume that the coupling is strong and $\kappa_{\mathrm{q}} \lesssim g$. Then the integrands proportional to $\kappa_{\mathrm{q}}/2$ contribute beyond the accuracy of Eq. (6.32):

$$\int_0^t dt' e^{-(i\widetilde{\omega}_{\mathrm{r}}+\kappa/2)(t-t')}(\lambda+\Lambda)\frac{\kappa_{\mathrm{q}}}{2}\sigma_{\pm}(t') \sim \frac{\kappa_{\mathrm{q}}}{g}\frac{\lambda g}{|\omega_{\mathrm{q}} \pm \omega_r|} \lesssim \lambda^2. \quad (6.34)$$

Moreover, the term with $b_k^{\alpha\dagger}(0)e^{i(vk+\widetilde{\omega}_{\mathrm{r}})t'}$ oscillates fast and becomes negligible after integration over t'. The same holds for the term with $a^{\dagger}(t')e^{i\omega_{\mathrm{r}}t'}$, the contribution of which is negligible under the condition (6.28). One can also extend the integration over t' to $-\infty$, as for $t' < 0$ the input pulse does not appreciably influence the cavity. Then carrying out the integration yields

$$a(t) \approx a(0)e^{-(i\widetilde{\omega}_{\mathrm{r}}+\kappa/2)t} - \frac{if_{\mathrm{r}}}{\sqrt{\kappa/2}} \sum_{\alpha=\mathrm{I,II}} \int_0^{\infty} dk R(vk) b_k^{\alpha}(0)e^{-ivkt}, \quad (6.35)$$

$$R(\omega) = \frac{\sqrt{\kappa/2}}{i(\widetilde{\omega}_{\mathrm{r}} - \omega) + \kappa/2}. \quad (6.36)$$

It was taken into account that $f(\omega/v) \approx f_{\mathrm{r}}$ in the vicinity of $\omega = \omega_{\mathrm{r}} \pm g(\lambda+\Lambda)$.

To calculate the cavity population, one can use an expansion of unity in the whole system Hilbert space,

$$\mathbb{1} = \mathbb{1}^{\mathrm{q}}\mathbb{1}^{\mathrm{r}}\mathbb{1}^{\mathrm{I}}\mathbb{1}^{\mathrm{II}}. \quad (6.37)$$

Here the unity operators of the system parts are:

$$\mathbb{1}^{\mathrm{q}} = |\uparrow\rangle\langle\uparrow| + |\downarrow\rangle\langle\downarrow| \quad (6.38)$$

for the qubit space,

$$\mathbb{1}^{\mathrm{r}} = \sum_{n^{\mathrm{r}}=0}^{\infty} |n^{\mathrm{r}}\rangle\langle n^{\mathrm{r}}| \quad (6.39)$$

for the cavity space, and

$$\mathbb{1}^{\alpha} = \sum_{n=0}^{\infty} \int_0^{\infty} dk_1 \ldots \int_0^{\infty} dk_n |\mathrm{w}^{\alpha}_{k_1\ldots k_n}\rangle\langle \mathrm{w}^{\alpha}_{k_1\ldots k_n}|, \tag{6.40}$$

$$|\mathrm{w}^{\alpha}_{k_1\ldots k_n}\rangle = \nu^{\alpha}(n) \prod_{k=k_1,\ldots k_n} b^{\alpha\dagger}_k(0)|0^{\alpha}\rangle \tag{6.41}$$

for the α-th waveguide space. In Eq. (6.41), ν^{α} is a normalization constant which satisfies $\langle \mathrm{w}^{\alpha}_{k_1\ldots k_n}|\mathrm{w}^{\alpha}_{k_1\ldots k_n}\rangle = 1$.

First we express $\langle a^{\dagger}a\rangle$ for an arbitrary state of the input pulse. By insertion of the unity operator one gets

$$\langle a^{\dagger}a\rangle = \langle\psi|a^{\dagger}\mathbb{1}a|\psi\rangle, \tag{6.42}$$

where

$$|\psi\rangle = |\mathrm{q}\rangle|0^{\mathrm{r}}\rangle|\mathrm{w}^{\mathrm{I}}\rangle|0^{\mathrm{II}}\rangle \tag{6.43}$$

is the initial state of the entire system. It is comprised of wavefunctions of the system parts. $|\mathrm{q}\rangle$ is the qubit wavefunction and $|0^{\mathrm{r}}\rangle$ is that of the resonator; $|\mathrm{w}^{\mathrm{I}}\rangle$ is the wavefunction of the first waveguide and $|0^{\mathrm{II}}\rangle$ is that of the second one. As explained in the course of derivation of Eq. (6.29), the initial state (6.43) can indeed be considered separable. The resonator and the second waveguide are in the vacuum state initially. We substitute the unity expansion (6.37)–(6.41) into Eq. (6.42) and use Eq. (6.35). Then, using the initial state of the system (6.43), one arrives at

$$\langle a^{\dagger}a\rangle_t = \frac{f_{\mathrm{r}}^2}{\kappa/2} \sum_{n=0}^{\infty} \int_0^{\infty} dk_1 \ldots \int_0^{\infty} dk_n \times \langle \mathrm{q}| \Big| \int_0^{\infty} dk \langle \mathrm{w}^{\mathrm{I}}_{k_1\ldots k_n}|R(vk) b^{\mathrm{I}}_k(0) e^{-ivkt}|\mathrm{w}^{\mathrm{I}}\rangle \Big|^2 |\mathrm{q}\rangle. \tag{6.44}$$

It was used that $a(0)|0^{\mathrm{r}}\rangle = 0$ and $b^{\mathrm{II}}(0)|0^{\mathrm{II}}\rangle = 0$. We also employed the property

$$\sum_{q'=\uparrow,\downarrow} |\langle q'|\zeta(\sigma_{\mathrm{z}})|\mathrm{q}\rangle|^2 = |\langle\uparrow|\mathrm{q}\rangle\,\zeta(1)|^2 + |\langle\downarrow|\mathrm{q}\rangle\,\zeta(-1)|^2 = \langle \mathrm{q}|\big|\zeta(\sigma_{\mathrm{z}})\big|^2|\mathrm{q}\rangle, \tag{6.45}$$

where ζ is a function of σ_{z}.

Note that Eq. (6.44) can also be obtained by writing out the explicit form of the system state vector and finding the relevant amplitudes first. This approach was used in Appendix C of Ref. [29] and in Chs. 4.6.1–4.6.3 of the thesis [105]. Also, we use it in Sec. VII.2 where we consider a decay of a two-level system into a waveguide.

Now we provide an expression for the population, given the input pulse is in a single-photon Fock state:

$$|\mathrm{w}^{\mathrm{I}}\rangle = |1^{\mathrm{I}}_{\xi}\rangle \equiv \int_{-\infty}^{+\infty} dk\, \xi'(k) b^{\mathrm{I}\dagger}_k(0)|0^{\mathrm{I}}\rangle. \tag{6.46}$$

Here $\xi'(k)$ is the incident pulse spectrum. That is, $\xi'(k)$ is the amplitude of the probability density of finding a monochromatic photon with a wave vector k. It holds that $\int_{-\infty}^{+\infty} |\xi'(k)|^2 = 1$ due to normalization. We assume the pulse to be narrow-band, i.e., its spectral width is much smaller than its central frequency. Hence the limits of integration in Eq. (6.46) were extended to $-\infty$. Using Eqs. (6.46) and (6.44), one

arrives at

$$\langle a^\dagger a\rangle_t = \langle \mathrm{q}|\big|\mathcal{F}[R(\omega)\xi(\omega)](t)\big|^2|\mathrm{q}\rangle. \tag{6.47}$$

The equation is only applicable for $t \geq 0$ due to the original restriction in the Langevin equation (6.32). We have defined the pulse Fourier transform $\mathcal{F}[\xi(\omega)](t) = (2\pi)^{-1/2}\int_{-\infty}^{+\infty} d\omega \exp(-i\omega t)\xi(\omega)$, where

$$\xi(\omega) = \frac{\xi'(\omega/v)}{\sqrt{v}}. \tag{6.48}$$

The last expression follows from the dispersion relation (2.30) and $n'(k)dk = n(\omega)d\omega$ with $n'(k) = |\xi'(k)|^2$ and $n(\omega) = |\xi(\omega)|^2$. Density of photons in an increment $d\omega$ is the same as for the corresponding increment dk.

2.3 Generalization to an N-photon pulse

Due to the linearity of the system in the dispersive approximation, an N-photon Fock pulse populates the resonator N times the one-photon pulse:

$$\langle a^\dagger a\rangle_t = N\langle \mathrm{q}|\big|\mathcal{F}[R(\omega)\xi(\omega)](t)\big|^2|\mathrm{q}\rangle. \tag{6.49}$$

The expression of the same form was obtained in Ref. [106] for a coherent input pulse. Also, the formula (6.29) was obtained without any assumptions on the input state. However, for this generalization to be valid, the condition (1.33) should be taken instead of the condition (6.14).

3 Other types of qubit-resonator and resonator-waveguide couplings

The coupling Hamiltonians (6.3) and (6.5) can be of more general form. If any type of linear transversal coupling is allowed,

$$H_{\mathrm{qr}}^{\mathrm{gen}} = \hbar(g^*\sigma_+ a + G\sigma_- a + \mathrm{h.\ c.}), \tag{6.50}$$

$$H_{\mathrm{r}\alpha}^{\mathrm{gen}} = \hbar\int_0^\infty dk(f_k b_k^{\alpha\dagger} a + F_k b_k a + \mathrm{h.\ c.}), \tag{6.51}$$

where the constants of interaction g, f_k, and F_k are complex. Each coupling here is a mixture of inductive coupling, capacitive coupling, and a coupling described by charge-flux terms like $Q\Phi$.

One partial case of Eqs. (6.50) and (6.51) is important from a practical standpoint. In the main part of Ch. VI and in Ch. VII, the qubit-resonator coupling is capacitive, and the resonator-waveguide coupling is inductive, or vice versa. Let us consider the case when the qubit-resonator and the resonator-waveguide interactions are both either capacitive or inductive. To describe it, one could alter the Hamiltonian (6.5) of the cavity-waveguide coupling to

$$H_{\mathrm{r}\alpha}^{\text{same-type}} = \hbar\int_0^\infty dk f_k(a + a^\dagger)(b_k^\alpha + b_k^{\alpha\dagger}). \tag{6.52}$$

Should we use these Hamiltonians, our treatment would change only trivially. Consider the general case of Hamiltonians (6.50) and (6.51). It is straightforward to generalize the unitary transformations (6.8) and (1.34) to that case. The total

magnitude of the qubit-dependent shift of the cavity resonance changes to

$$\chi = \mathrm{Re}(g^*\lambda + G^*\Lambda). \tag{6.53}$$

In the case of the same-type couplings, χ stays intact and is given by Eq. (6.18). Photon transport in the dispersive regime does not depend on whether the qubit-resonator and the resonator-waveguide couplings are different or of the same type. Indeed, one can show that Eqs. (6.29), (6.44), and all the subsequent ones are the same for any type of coupling.

4 Conclusion

We have treated a cavity quantum electrodynamics system with a method based on the Heisenberg-Langevin equations. This approach has allowed us to make the RWA naturally for the coupling to the waveguides and to highlight the condition (6.28) of its validity. We have considered a situation when the RWA for the qubit-resonator coupling breaks, but the counter-rotating terms in the Hamiltonian can be treated as a perturbation. For this case, a theory of multi-photon transport through the system has been developed in the dispersive regime, neglecting the exchange of excitations between the resonator and the qubit. Explicit expressions have been given for the resonator population and the transmitted density of photons. The expressions we have provided hold for other combinations of the qubit-resonator and the resonator waveguides couplings.

Chapter VII

Qubit readout with a single-photon pulse and a photodetector

Dispersive measurement [19, 51] is an established method for readout of a superconducting qubit [14, 18]. In the dispersive readout, a qubit is weakly coupled to a resonator. Depending on the qubit state, the cavity resonance is shifted either to the blue or to the red side. To probe the cavity, homodyne detection is usually used. When the cavity is probed with a resonant coherent signal, it acquires a phase shift that depends on the qubit state. This shift is measured by homodyning after several amplification stages. To approach quantum-limited amplification, parametric amplifiers [34] are used. This requires additional circulators and drive tones in the cryostat, which makes the setup hard to scale with the number of qubits.

An alternative approach is to use a photodetector [37, 49]. Suppose the probe frequency is chosen at the cavity resonance for a particular qubit state. Depending on the state of the qubit, the radiation either mostly passes through the cavity or reflects off it. A photodetector on the cavity output port provides a click for a particular qubit eigenstate. The click can be picked up by room-temperature electronics, with no need for a complex and bulky amplification chain [37]. The photodetector scheme was demonstrated in Ref. [2].

A coherent probe is used in most of the implemented and proposed readout schemes. States of the output radiation—different for the qubit in the ground and the excited states—are approximately coherent, too. As coherent states are non-orthogonal, it is impossible to discriminate them without errors. This contributes to the readout error. To overcome this, in Refs. [106, 107] the homodyne readout is modified in a way that the output radiation is squeezed. However, even more circulators and drives are needed in the input chain. The proposed protocols make the homodyne measurement even harder to scale.

A Fock-state probe in the photodetector scheme can be used to avoid the errors due to the non-orthogonality. In this work, we study the dispersive readout with the smallest possible amount of energy—a single photon—in the probe pulse of a given spatial form. That is also the simplest case for both experiment and theory. A single-photon pulse can be generated with a single element: an artificial atom decaying into a waveguide [108]. A simple vacuum detector such as a Josephson photomultiplier [1, 2], which can only distinguish a vacuum input state, is suitable for the measurement. Some of the results for that case might be helpful for approximate analysis of a more sophisticated case of a multi-photon input pulse. We expect that the scheme studied

Chapter VII, except for Sec. 2, was published in "A. M. Sokolov and E. V. Stolyarov, Phys. Rev. A 101, 042306 (2020)". All figures except Fig. 7.3 were created by A. M. Sokolov. The majority of the text was written by A. M. Sokolov. Calculations described in this chapter were carried out by A. M. Sokolov.

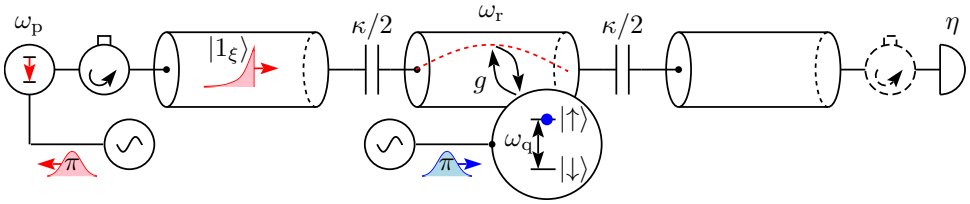

FIGURE 7.1: Measurement scheme. Notations regarding the pulse, the qubit, and the cavity are as in Fig. 6.1. The qubit is prepared at the initial moment of time. To prepare the excited state $|\uparrow\rangle$, a π pulse is used. On the second port there is an vacuum detector with a quantum efficiency η. The pulse can be generated by decay of a two-level system with the transition frequency ω_p. The two-level system is protected from a reflected photon by a circulator. The dashed circulator indicates there is no back-action on the cavity due to reflection off the detector.

The back-action can also be avoided without a circulator [2].

can be scaled reasonably well. Indeed, compared to the readout method reported in Ref. [2], our scheme only requires an additional circulator.

It is challenging to perform a readout with a single photon. We enhance the readout efficiency by increasing the qubit-resonator coupling. With other parameters unchanged, this increases an unwanted exchange of excitations between the qubit and the resonator. To suppress it, the qubit-resonator detuning $\omega_\mathrm{q} - \omega_\mathrm{r}$ should also be increased. Eventually, $\omega_\mathrm{q} - \omega_\mathrm{r}$ becomes of the same order of magnitude as $\omega_\mathrm{q} + \omega_\mathrm{r}$, which invalidates the rotating-wave approximation (RWA). To remedy this, the counter-rotating terms in the Hamiltonian can be treated in the first order of perturbation theory. This gives a Bloch-Siegert shift in the cavity resonance [102, 103] as demonstrated in the experiment of Ref. [109]. We show how this shift can be used to improve readout.

In what follows, we provide the theory of the single-photon readout and show how to optimize the parameters of the system with a simple analytical approach. Example parameters are then given, for which we calculate the contrasts and the qubit population in the end of the measurement. The latter is calculated with the numerics described in Ref. [29]. The numerical approach is also used to calculate contrasts more precisely and to further optimize the system parameters.

1 Measurement scheme

The readout setup is schematically depicted in Fig. 7.1. The resonance ω_r of the cavity is shifted to $\omega_\mathrm{r} + \chi$ for the excited qubit state $|\uparrow\rangle$, and $\omega_\mathrm{r} - \chi$ for its ground state $|\downarrow\rangle$. At one of the resonances, a probe photon is incident on the cavity. Suppose the photon central frequency is $\omega_\mathrm{p} = \omega_\mathrm{r} + \chi$. If the qubit is in the excited state, it is most likely that the photon passes through the cavity. Then the detector delivers a click, which indicates that the qubit is excited. If there is no click, we decide that the qubit is in the ground state. Due to a large qubit-resonator detuning, it is unlikely that they exchange an excitation. Hence the measurement scheme can be highly quantum-non-demolition [26].

In what follows, we use the following convention on the measurement sequence. At $t = 0$ the probe photon is far from the resonator, so its influence on the cavity, the qubit, and the detector is negligible. The pulse front reaches the cavity port at $t = t_0$. One waits for the detector clicks from $t = 0$ to t_m, where t_m is referred to as the measurement time.

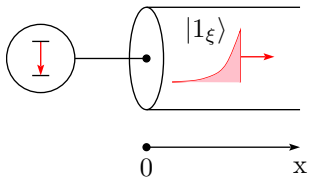

FIGURE 7.2: Generation of a single-photon pulse by a two-level system

2 Generation of an exponentially damped pulse

Here we show how the decay of a two-level system generates an exponentially damped pulse.

The system we consider in this section is depicted in Fig. 7.2. The circulator between the two-level system and the cavity (see Fig. 7.1) prevents any signal from coming to the two-level system. This is modeled by a semi-infinite waveguide connected to the two-level system. The Hamiltonian of the whole system is

$$H = \frac{1}{2}\hbar\omega_{\mathrm{p}}\sigma_{\mathrm{z}} + f\hbar\int_0^\infty dk(\sigma_+ b_k + \text{h. c.}) + \hbar\int_0^\infty dk\,\omega_k b_k^\dagger b_k. \tag{7.1}$$

We have used the RWA here. The Hamiltonian is in fact the well-known Fano-Anderson model, originally used to describe a discrete state coupled to a continuum in an atom [110, 111] and in a solid [112]. In the interaction picture the Hamiltonian reads

$$H \to U^\dagger H U - i\hbar U^\dagger \dot{U} = f\hbar\int_0^\infty dk(\sigma_+ b_k e^{i(\omega_{\mathrm{p}}-\omega_k)t} + \text{h. c.}), \tag{7.2}$$

where $U = \exp\frac{1}{i\hbar}H_0 t$ with $H_0 = \frac{1}{2}\hbar\omega_{\mathrm{p}}\sigma_{\mathrm{z}} + \hbar\int_0^\infty dk\,\omega_k b_k^\dagger b_k$.

The Hamiltonian conserves the number of excitations. Therefore, if initially the two-level system is excited and the waveguide is empty, the wavefunction of the system reads

$$|\psi\rangle = c|0\rangle|\uparrow\rangle + \int_0^\infty dk\,\xi'(k)b_k^\dagger|0\rangle|\downarrow\rangle \tag{7.3}$$

at any time. From the Schröinger equation

$$i\hbar|\dot{\psi}\rangle = H|\psi\rangle \tag{7.4}$$

follows that

$$\dot{\xi}'(k) = -ifce^{i(\omega_k-\omega_{\mathrm{p}})t}, \tag{7.5}$$

$$\dot{c} = -if\int_0^\infty dk\,\xi'(k)e^{-i(\omega_k-\omega_{\mathrm{p}})t}. \tag{7.6}$$

The equations are easy to solve. Substituting Eq. (7.5) into Eq. (7.6) yields

$$\dot{c}(t) = -f^2\int_0^\infty dk\int_0^t dt' ce^{i(\omega_k-\omega_{\mathrm{p}})t}. \tag{7.7}$$

By the same argument as used in the derivation of Eq. (1.60), the integration by k can be extended to the negative values. The resulting integral is expressed in terms

of the delta function; then, simplifying the expression gives rise to

$$\dot{c} = -\gamma c/2, \tag{7.8}$$

where $\gamma = 2\pi f^2/v$. Taking into account that $c(0) = 1$, one finds the solution to the equation:

$$c(t) = e^{-\gamma t/2}. \tag{7.9}$$

Substituting the solution into Eq. (7.5) and integrating yields

$$\xi'(k) = \sqrt{\frac{\gamma v}{2\pi}} \frac{1}{\omega_k - \omega_\mathrm{p} + i\gamma/2} (1 - e^{i(\omega_k - \omega_\mathrm{p})t - \gamma t/2}), \tag{7.10}$$

where it was used that $\xi' = 0$ at $t = 0$. For $t \gg \gamma^{-1}$ the excitation has mostly gone into the waveguide and

$$\xi'(k) \approx \sqrt{\frac{\gamma v}{2\pi}} \frac{e^{-i\omega_k t}}{\omega_k - \omega_\mathrm{p} + i\gamma/2} \tag{7.11}$$

in the Schrödinger picture. We have applied U to go back from the interaction picture:

$$|\psi\rangle_\mathrm{Sch} = U|\psi\rangle = ce^{-i\omega_\mathrm{p} t}|0\rangle|\uparrow\rangle + \int_0^\infty dk\, \xi'(k) e^{-i\omega_k t} b_k^\dagger |0\rangle|\downarrow\rangle, \tag{7.12}$$

hence $\xi' \to \xi' e^{-i\omega_k t}$. We call $\xi'(k)$ the pulse spectrum. The amplitude of the probability density to find the photon at point x in the resulting pulse is

$$\varrho'(x) = \mathcal{F}^{-1}[\xi'(k)](x) = \sqrt{\frac{\gamma}{v}} e^{(i\frac{\omega_\mathrm{p}}{v} + \frac{\gamma}{2v})(x - vt)} \theta(-x + vt) \tag{7.13}$$

up to a non-relevant phase. The resulting pulse is called exponentially-damped [113].

Now we rewrite the amplitude of the photon density of the pulse and its spectrum in the coordinate system related to the cavity (see Fig. 6.1). We assume that the process of forming of an exponentially damped pulse does not influence the cavity. Again, due to the presence of the circulator, the waveguide connected to the cavity first port can be considered infinite. At the initial instant of time the pulse front is located at $vt = -vt_0$:

$$\xi'(k) = \frac{1}{\sqrt{2\pi v t_\mathrm{p}}} \frac{e^{ikvt_0}}{k - k_\mathrm{p} + i(2vt_\mathrm{p})^{-1}}, \tag{7.14}$$

$$\varrho'(x) = \frac{1}{\sqrt{vt_\mathrm{p}}} e^{[ik_\mathrm{p} + (2vt_\mathrm{p})^{-1}](x + vt_0)} \theta(-x - vt_0). \tag{7.15}$$

where $k_\mathrm{p} = \omega_\mathrm{p}/v$ and $t_\mathrm{p} = 1/\gamma$. The photon density $|\varrho'(x)|^2$ decays over the length vt_p, hence t_p is regarded as the pulse duration. After traveling for time t_0, the pulse front arrives at the cavity first port at time t_0.

A related problem of a single-photon absorption by a three-level atom was solved in Ref. [114]. There, a formalism of non-Hermitian "Hamiltonians" was used to describe the evolution of the atom "wavefunction" non-unitary dynamics [16]. Apart from that technical difference, the treatment in the reference is equivalent to ours. The cornerstone of both approaches is to assume that the coupling rate does not vary with frequency.

3 Readout contrast

Having obtained a description of photon transport in Ch. VI, we can now assess the performance of our readout scheme. In this section, an expression for the readout contrast in our measurement scheme is derived.

The measurement outcome is based on the state of an vacuum photodetector on the second cavity port. We assign the readout result to be "↑" when there is a click and "↓" in the other case. Hence Eq. (1.43) becomes

$$C = P_{\mathrm{cl}|\uparrow}[\xi(\omega)] - P_{\mathrm{cl}|\downarrow}[\xi(\omega)], \tag{7.16}$$

where $P_{\mathrm{cl}|q}$ is the probability of a click, given that the qubit is prepared in an eigenstate $q = \uparrow, \downarrow$, and the cavity is irradiated by a pulse with spectrum $\xi(\omega)$.

The way we decide on the readout outcome is easy to justify in the dispersive regime when the condition (6.14) holds. In this regime, the qubit does not decay to the waveguides. Also, recall the input pulse is single-photon. Then at most one photon reaches the second waveguide and the detector. In this case, the probability of a click is

$$P_{\mathrm{cl}} = \eta \langle \mathcal{N}_{\mathrm{tr}} \rangle, \tag{7.17}$$

where $\mathcal{N}_{\mathrm{tr}} = \int_0^{t_{\mathrm{m}}} dt v \rho_{\mathrm{tr}}(t)$ is the total number of photons transmitted through the cavity, t_{m} denotes the counting time, and η is a quantum efficiency of the photodetector. It is clear from the form of Eqs. (7.17), (7.16) and the results of Ch. VI that the contrast depends on the types of the qubit-resonator and the resonator-waveguides couplings only through χ. With Eq. (6.29), Eq. (7.17) yields

$$P_{\mathrm{cl}} = \eta \frac{\kappa}{2} \int_0^{t_{\mathrm{m}}} dt \langle a^\dagger a \rangle_t. \tag{7.18}$$

Suppose we have a high-Q resonator and a narrow-band incoming pulse. Let the pulse be in resonance with the cavity if the qubit is excited:

$$\omega_{\mathrm{p}} = \langle \uparrow | \widetilde{\omega}_{\mathrm{r}} | \uparrow \rangle = \omega_{\mathrm{r}} + \chi, \tag{7.19}$$

where $\widetilde{\omega}_{\mathrm{r}} = \omega_{\mathrm{r}} + \chi \sigma_{\mathrm{z}}$ analogously to Eq. (1.41) but with χ the total shift of the cavity resonance (6.18). Then by Eqs. (6.47) and (6.36) the resonator reflects most of a pulse if the qubit is in the ground state. Most likely, the detector does not click in this case. On the other hand, if the qubit is excited, the resonator transmits most of the pulse to the detector port. It is most probable then for the detector to deliver a click.

In the dispersive regime, Eq. (7.16) simplifies. Cavity population (6.47) is symmetrical with respect to a qubit flip and a shift of $\xi(\omega)$:

$$\uparrow \to \downarrow, \quad \xi(\omega) \to \xi(\omega + 2\chi), \quad \langle a^\dagger a \rangle \to \langle a^\dagger a \rangle; \tag{7.20}$$

$$\downarrow \to \uparrow, \quad \xi(\omega) \to \xi(\omega - 2\chi), \quad \langle a^\dagger a \rangle \to \langle a^\dagger a \rangle. \tag{7.21}$$

Due to Eq. (7.18) the symmetry applies to the click probability, too. Hence

$$C = P_{\mathrm{cl}|\uparrow}[\xi(\omega)] - P_{\mathrm{cl}|\uparrow}[\xi(\omega - 2\chi)]. \tag{7.22}$$

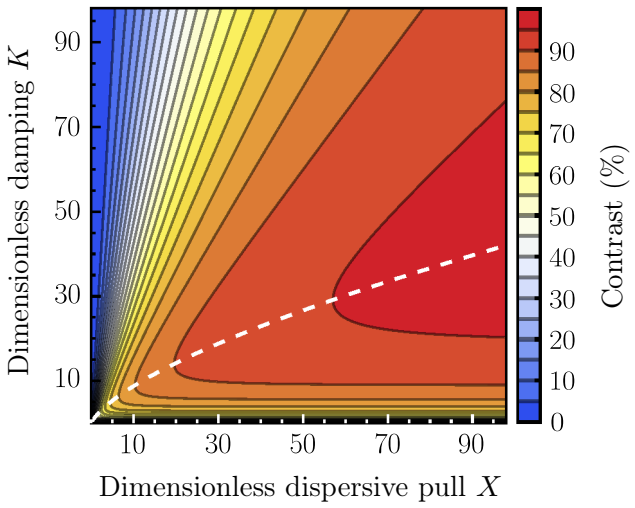

FIGURE 7.3: Readout contrast as a function of the dimensionless dispersive pull X (7.24) and cavity leakage K (7.23). The dashed line shows the position of maximum for each X.

It is convenient to introduce dimensionless quantities

$$\tau = \frac{t - t_0}{t_\mathrm{p}}, \quad K = \kappa t_\mathrm{p}, \tag{7.23}$$

$$D = (\omega_\mathrm{r} + \chi\sigma_\mathrm{z} - \omega_\mathrm{p})t_\mathrm{p}, \quad X = \chi t_\mathrm{p}. \tag{7.24}$$

Equations (6.47)–(6.48), upon insertion of Eq. (7.14) yield

$$\langle a^\dagger a\rangle = \theta(\tau)\langle q|\frac{4Ke^{-(K+1)\tau/2}}{(K-1)^2+4D^2}\big[\cosh\frac{(K-1)\tau}{2} - \cos D\tau\big]|q\rangle. \tag{7.25}$$

If $K = 1$ and $D = 0$, one obtains

$$\langle a^\dagger a\rangle = \theta(\tau)\tfrac{1}{2}e^{-\tau}\tau^2. \tag{7.26}$$

Using this result, one can check that for the exponentially damped pulse

$$C = P_\mathrm{cl}|_{D=0} - P_\mathrm{cl}|_{D=2X}\,. \tag{7.27}$$

The contrast is compromised by unwanted scattering. The first term in Eq. (7.27) is less than unity, as a non-monochromatic photon can reflect off the cavity even in resonance. The second term describes the loss of contrast due to the false photon count. It occurs when a photon passes the cavity off-resonance.

Suppose the measurement is long enough for the detector to absorb most of the outgoing pulse energy. That is, $t_\mathrm{m} \gg t_\mathrm{p}, \kappa^{-1}$. Then one can integrate to ∞ in Eq. (7.18). Performing the integration using Eqs. (7.26) and (7.25) gives

$$P_\mathrm{cl}|_{D=0} = \frac{\eta K}{K+1}, \tag{7.28}$$

$$P_\mathrm{cl}|_{D=2X} = \frac{\eta K(K+1)}{(K+1)^2+16X^2}. \tag{7.29}$$

Equations (7.27)–(7.29) and (7.23)–(7.24) constitute the expression for the contrast. The contrast is shown in Fig. 7.3.

Detuning the probe photon from a cavity resonance, i.e. $\omega_\mathrm{p} \neq \omega_\mathrm{r} \pm \chi$, lowers the contrast. To check this, one can straightforwardly generalize the expressions for the contrast for a non-zero detuning. Note that when a coherent-state probe is used, the maximum of contrast is away from the resonance due to the shot noise [49].

For a given X, the contrast is maximized for

$$K = u + \frac{1}{4u} - \frac{1}{2}, \quad u = \sqrt[3]{X\sqrt{16X^2+1} + \frac{16X^2+1}{4}} - \frac{1}{8}. \tag{7.30}$$

The position of maximum is shown in Fig. 7.3. For $2X^{2/3} \gg 1$ one obtains that

$$K \approx 2X^{2/3}. \tag{7.31}$$

Note it follows that $\chi > \kappa$.

As C grows with X, the case of a large dispersive pull is of interest. In this case, one can give a simple expression for the maximal contrast. It is shown in Appendix A that the contrast can be approximated as

$$C \approx \eta\left(1 - \frac{3}{2\kappa t_\mathrm{p}}\right) \tag{7.32}$$

if the cavity decay rate $K = \kappa t_\mathrm{p}$ is optimal, as given by Eq. (7.31), and

$$X = \chi t_\mathrm{p} \gtrsim 100, \tag{7.33}$$

with χ given by Eq. (6.18). As follows from the derivation of Eq. (7.32), a third of the contrast loss is due to the false photon count off the resonance. The other two-thirds are from the absence of a count in the resonance.

Equations (7.32) and (7.31) are the quantitative version of the general considerations given in Ref. [69]. To readout the qubit in our setup means to distinguish a change 2χ in the resonator frequency. This can only be accomplished if

$$2\chi t_\mathrm{m} > 1, \tag{7.34}$$

where the measurement time t_m is of the same order of magnitude as the pulse duration t_p.

4 Analytical optimization

Here we use our analytical results to choose the system parameters; the qubit relaxation is neglected. The main idea is to relate the minimal measurement time for obtaining a given contrast with the time for the qubit to stay intact. One also takes care to get acceptable errors due to finite counting time and to avoid qubit relaxation due to the counter-rotating terms in the Hamiltonian.

4.1 Minimal pulse duration to get a given error

Here we determine a pulse duration t_p that suffices to perform a readout with a given accuracy. The counting time is considered infinite.

It is convenient to argue in terms of the probability of an erroneous readout (1.47). By expressing it in terms of contrast with Eq. (1.46) and using the approximation (7.32) for the latter, one gets

$$\varepsilon = \frac{1-\eta}{2} + \frac{3\eta}{8(\chi t_\mathrm{p})^{2/3}}. \tag{7.35}$$

Let us assume $\eta = 1$. Then

$$t_\mathrm{p} \geq \frac{1}{\chi}\left(\frac{3}{8\varepsilon}\right)^{3/2} \tag{7.36}$$

suffices to get an error not exceeding ε.

4.2 Error due to a finite counting time

Let us calculate the degradation of contrast due to finite counting time. Integration in Eq. (7.18) with limits from $t = 0$ to t_m gives

$$P_\mathrm{cl}(t_\mathrm{m}) = P_\mathrm{cl}(\infty) - \Delta(t_\mathrm{m}), \tag{7.37}$$

where

$$\Delta(t_\mathrm{m}) = \left(\frac{Ke^{-\tau_\mathrm{m}} + e^{-K\tau_\mathrm{m}}}{2K} + \frac{2e^{-(K+1)\tau_\mathrm{m}/2}[(K+1)\cos D\tau_\mathrm{m} + D\sin D\tau_\mathrm{m}]}{(K+1)^2 + 4D^2}\right) \times \frac{2K^2}{(K-1)^2 + 4D^2}, \tag{7.38}$$

$P_\mathrm{cl}(\infty)$ is the click probability given by Eq. (7.29), and $\tau_\mathrm{m} = t_\mathrm{m}/t_\mathrm{p}$. In the spirit of the approximations used to obtain Eq. (7.32), one has

$$\Delta(\tau_\mathrm{m})|_{D=0} \approx (1 + 2/K)e^{-\tau_\mathrm{m}}, \tag{7.39}$$

$$\Delta(\tau_\mathrm{m})|_{D=2X} \approx 0. \tag{7.40}$$

Then, from Eqs. (1.43) and (7.24) it follows that

$$C(\tau_\mathrm{m}) = C(\infty) - \Delta(\tau_\mathrm{m}), \tag{7.41}$$

where $C(\infty)$ is given by Eqs. (7.22) and (7.28)–(7.29).

To have $\Delta \approx 0.3\%$, one chooses $t_\mathrm{m} = 6t_\mathrm{p}$. In comparison, for $t_\mathrm{m} = 3t_\mathrm{p}$ the degradation in contrast is already around 5%. For both cases, one needs $K \gtrsim 10$.

4.3 Maximal readout duration for the qubit not to relax

Qubit relaxation time T_1 is limited by the time of its Purcell decay T_P. From Refs. [19, 28], one has

$$T_1 < T_\mathrm{P}, \quad T_\mathrm{P} \approx \frac{1}{\kappa\lambda^2}. \tag{7.42}$$

Here we assume that $\kappa_\mathrm{q} \approx \kappa$.

Thus the readout duration is limited by the condition

$$t_\mathrm{m} \ll T_\mathrm{P} \tag{7.43}$$

The ratio $T_\mathrm{P}/t_\mathrm{m}$ is chosen to avoid significant errors due to the qubit relaxation. Using Eqs. (7.42), (7.23), and (7.31), one obtains

$$t_\mathrm{p} < \left(\frac{t_\mathrm{p}}{2T_\mathrm{P}}\right)^{3/2} \frac{1}{\lambda^3\chi}. \tag{7.44}$$

The ratio $t_\mathrm{m}/t_\mathrm{p}$ is chosen to limit the error due to finite integration time. The error is given by Eqs. (7.41) and (7.39).

We don't take into account the correction to the qubit relaxation due to the Bloch-Siegert dressing. This is justified for

$$\Lambda^2 \ll \lambda^2. \tag{7.45}$$

Combining Eqs. (7.36) and (7.44) yields the limit on readout error,

$$(1-C)/2 = \varepsilon > \frac{3T_\mathrm{P}}{4t_\mathrm{p}}\lambda^2. \tag{7.46}$$

To express ε in terms of contrast C, Eqs. (1.47) and (1.46) were used. A reasonable choice $t_\mathrm{m} = T_\mathrm{P}/10$ and $t_\mathrm{m} = 6t_\mathrm{p}$ yields $\varepsilon = 45\lambda^2$.

4.4 Parameter choice

Now one can determine all of the system parameters. By virtue of Eq. (7.46), λ is set by the readout contrast to be attained. The other parameters are chosen as follows. The ratio λ/Λ is set by the requirement (7.45) which limits the relaxation due to the Bloch-Siegert dressing. In terms of this ratio,

$$\omega_\mathrm{r} = \frac{\lambda/\Lambda - 1}{\lambda/\Lambda + 1}\,\omega_\mathrm{q}. \tag{7.47}$$

With this and the definition (6.14) of λ one gets

$$g = 2\lambda\omega_\mathrm{q}(\lambda/\Lambda + 1)^{-1}. \tag{7.48}$$

Plugging the latter expression into Eq. (7.44) and using Eq. (6.18) results in

$$t_\mathrm{p} = \frac{\lambda}{2\Lambda}\left(\frac{t_\mathrm{p}}{2T_\mathrm{P}}\right)^{3/2} \frac{1}{\lambda^5\omega_\mathrm{q}}. \tag{7.49}$$

Measurement duration t_m is related to t_p by choosing an acceptable error due to finite integration time, which is given by Eqs. (7.41) and (7.39). Resonator leakage κ can be obtained with Eqs. (7.31) and (7.49), and definitions (7.23) and (7.24).

Equations (7.49) and (7.46) elucidate what parameters to alter for achieving fast and high-fidelity readout. Higher ω_q is favorable for our readout scheme. As shown in Ch. IV and Ref. [49], a related scheme with a photodetector also favors higher frequencies. Higher λ is especially beneficial if the qubit does not decay.

The dispersive shift $g\lambda$ and the Bloch-Siegert shift $g\Lambda$ should be of the same sign to maximize the total pull χ (6.18). This is the case for $\omega_\mathrm{q} > \omega_\mathrm{r}$. For $\lambda/\Lambda = 10$ [which satisfies Eq. (7.45)], the pull χ is about 20% larger for $\omega_\mathrm{q} > \omega_\mathrm{r}$ than in the opposite case. Hence t_p (7.36) and t_m decrease by the same percentage.

In the approximations used, the optimal parameters are the same for the case of a multi-photon input. In the dispersive approximation, the system is linear with respect to the number of input photons. Therefore, the contrast of the multi-photon readout

TABLE 7.1: Parameters for high-fidelity readout. Contrasts C_d are calculated in the dispersive approximation using Eq. (7.32). Contrasts C_n and the post-measurement qubit populations $P_\uparrow(t_\mathrm{m})$ are obtained numerically. An ideal detection is assumed with $\eta = 1$. The integration time relates to the pulse duration as $t_\mathrm{m} = 7t_\mathrm{p}$. For analytical estimates of parameters, $t_\mathrm{m} = T_\mathrm{P}/15$ is chosen.

$\omega_\mathrm{q}/2\pi$ (GHz)	$\omega_\mathrm{r}/2\pi$ (GHz)	λ	$g/2\pi$ (MHz)	$\kappa/2\pi$ (kHz)	t_m (ms)	C_d (%)	C_n (%)	$P_\uparrow$ (%)
Parameters optimized analytically:								
5.00	4.09	0.006	5.7	7.2	36.9	99.3	98.1	92.3
20.00	16.36	0.006	22.9	28.9	9.2	99.3	98.1	92.2
Parameters optimized numerically:								
5.00	4.09	0.005	4.4	3.8	36.9	98.8	98.5	97.5
20.00	16.36	0.005	18.1	16.9	9.2	98.8	98.5	97.2

depends only on the probability of a single photon passing through the cavity when the photon is off-resonant and the probability of reflecting it when the photon is in resonance with the cavity. However, as explained for Eq. (7.32), these probabilities are proportional to $1 - C$. By increasing C these probabilities decrease, which increases the contrast in the multi-photon case.

5 Estimates and comparison with numerics

In this section, we provide the system parameters optimized with the analytical approach of Sec. 4 and the parameters optimized with the numerical approach described in Ref. [29]. We also compare the contrasts obtained with the analytical theory and the numerics.

First let us discuss the cases when the analytical approach works well. The higher the post-readout qubit population $P_\uparrow$ is, the better C_d approximates C_n. This is seen from Tables 7.1 and 7.2. As for the parameters optimization, here the analytics provides good results if high fidelities are targeted. We compare the resulting contrasts with those obtained by numerical optimization; the details of the numerical method are described below. One can see from Table 7.1 that numerical optimization gives only a slight improvement of less than 0.5% for the contrast.

Note the readout times given in Table 7.1 are far beyond the best accessible lifetimes of superconducting qubits as of 2022 [115–118]. The contrasts given in the table do not take into account the intrinsic sources of the qubit decay, which start to play a role at such times. The purpose of this table is to demonstrate the regime when the formula (7.32) and the analytical optimization work perfectly well.

Numerical optimization provides considerably higher contrasts than the analytical optimization if we optimize for a fast readout (see Table 7.2). This is explained as follows. The qubit decay shifts the cavity resonance

$$\langle\widetilde{\omega}_\mathrm{r}\rangle = \omega_\mathrm{r} + \chi\langle\sigma_\mathrm{z}\rangle \tag{7.50}$$

during readout. This raises the probability of unwanted scattering due to the detuning with the probe photon. According to Eqs. (7.50), (6.18), and (7.48), the shift susceptibility to the decay in $\langle\sigma_\mathrm{z}\rangle$ increases proportionally to λ^2. However, the pulse spectral

TABLE 7.2: Parameters for fast readout. Here the measurement time is $t_\mathrm{m} = 6t_\mathrm{p}$, where t_p is the pulse duration. For analytical parameter estimates we set $t_\mathrm{m} = T_\mathrm{P}/10$. Other parameters, as well as notations, are the same as in Table 7.1. To calculate C_d, Eqs. (7.27)–(7.29) are used here as χt_m does not satisfy the condition (7.33).

$\omega_\mathrm{q}/2\pi$ (GHz)	$\omega_\mathrm{r}/2\pi$ (GHz)	λ	$g/2\pi$ (MHz)	$\kappa/2\pi$ (MHz)	t_m (μs)	C_d (%)	C_n (%)	$P_\uparrow$ (%)
Parameters optimized analytically:								
5.00	4.09	0.059	53.6	4.08	1.0	71.0	67.9	89.2
20.00	16.36	0.050	180.0	9.99	0.6	79.1	75.9	88.9
Parameters optimized numerically:								
5.00	4.09	0.095	86.4	5.80	1.0	82.0	75.8	66.5
20.00	16.36	0.074	269.0	12.90	0.6	86.3	80.6	71.9

density widens as λ^5 according to Eq. (7.49), which reduces unwanted scattering due to decay. The reduction is more effective with larger λ. Based on Eq. (7.49), it is the increase of λ that is the best strategy to readout faster. As explained before, one can sustain more qubit decay in that case. Therefore, $t_\mathrm{m}/T_\mathrm{P}$ should be increased to allow longer pulses and decrease the error (7.46) due to the pulse non-monochromaticity. This is not taken into account in the analytical optimization: see Eq. (7.49), where the ratio is fixed. As the numerical optimization yields larger $t_\mathrm{m}/T_\mathrm{P}$, the population $P_\uparrow$ is smaller for the relevant sets in Table 7.2. Note that $P_\uparrow$ is better for the numerically optimized sets in Table 7.1. Indeed, λ is chosen small there to achieve high contrasts. However, $t_\mathrm{m}/T_\mathrm{P}$ in analytical optimization is too large to get relaxation errors that are small enough.

6 Discussion and outlook

A protocol for the dispersive readout that uses merely a single photon has been considered in this chapter. We have managed to develop an analytical model of the readout by neglecting the Purcell decay of the qubit. Using this theory, we have derived a compact expression for the readout contrast. Optimal parameters of the system have been expressed too. Both the readout time and its contrast are set by the characteristic frequencies of the system ω_q and ω_r and by the ratio $\lambda = g/(\omega_\mathrm{q} - \omega_\mathrm{r})$ of the coupling strength to the detuning. We have complemented our analytical approach with the numerical model, which accounts for the relaxation. We have used the model to check the analytical contrasts and to optimize the system parameters further. Making the measurement time closer to the qubit lifetime results in more relaxation, but gives less error due to the scattering. Numerical optimization allows one to find a compromise between the relaxation and the scattering errors. It is particularly helpful for designing a fast measurement reaching contrasts up to 90%. In that case, it gives an increase in contrast of more than 5%. For the contrasts above 98%, numerics gives an improvement of about 0.5%. We stress that the only sources of errors in our scheme are qubit relaxation and unwanted scattering of the probe pulse.

There are no errors caused by the non-orthogonality of the states being distinguished by the detector. Despite the absence of these errors, our scheme is slower than the state-of-the-art readout. We attribute this to the fact that it uses just one photon. As the photon is non-monochromatic, it can pass or reflect the cavity when

it is not wanted. By using more photons to probe the cavity, one can significantly decrease the probability of those errors. For example, there are a few tens of photons in the measurement pulse in Ref. [51], as can be shown by simple estimates with Eq. (20) of Ref. [69]. The case of multiple input photons is left for future work. Some of the results obtained in this chapter might be helpful for the investigation of that case. Due to the linearity of the system in the dispersive approximation, the scheme parameters optimized analytically are the same as for the single-photon case. Besides, we have obtained the formula for the photon transport in the multi-photon case. We also believe that the features of the system behavior due to the excitation exchange between the qubit and the resonator we have studied are qualitatively retained in the multi-photon case.

There are other possibilities to improve our scheme performance. One can use stronger qubit-resonator coupling g to obtain the higher magnitude $g(\lambda + \Lambda)$ of the qubit-dependent cavity pull. To retain the non-demolition character of the readout, $\lambda = g/(\omega_\mathrm{q} - \omega_\mathrm{r})$ and the Purcell decay rate $T_\mathrm{P}^{-1} = \kappa\lambda^2$ should be kept constant. However, to minimize quasiparticle generation, the cavity and the qubit frequencies ω_r and ω_q are limited by the superconducting gap. One can only increase the $|\Lambda/\lambda| = |\omega_\mathrm{q} - \omega_\mathrm{r}|/(\omega_\mathrm{q} + \omega_\mathrm{r})$ ratio to overcome the Purcell decay. While doing so additionally improves the readout due to the higher Bloch-Siegert shift, one would need to account for the qubit relaxation due to the counter-rotating terms in the Hamiltonian. Interestingly, this type of relaxation depends on the combination of the qubit-resonator and the resonator-waveguide couplings (see Ref. [20] and Sec. VI.3). Alternatively, a Purcell filter [51] could be used to suppress the qubit relaxation while increasing the coupling g. In this case, κ_q, the resonator decay rate as seen by the qubit, differs significantly from the resonance decay rate κ. One can check that Eqs. (7.44), (7.46), and (7.49) are then modified with the replacement $t_\mathrm{p}/T_\mathrm{P} \to (\kappa/\kappa_\mathrm{q})(t_\mathrm{p}/T_\mathrm{P})$. Furthermore, if λ is replaced with $\lambda\sqrt{\kappa/\kappa_\mathrm{q}}$, the measurement error ε (7.46) does not change. The measurement time $t_\mathrm{m} \propto t_\mathrm{p}$, however, decreases by the ratio of κ/κ_q. As can be deduced from Ref. [32], $\kappa/\kappa_\mathrm{q} \sim 100$ is achievable for the typical parameters we use.

We expect that the studied setup for the superconducting qubit readout is favorable for on-chip integration. On-chip circulators were already demonstrated [119–121]. The same holds for single-photon sources [108, 122] and photodetectors [1, 2, 42, 45, 48]. Moreover, we only need one type of classical signals: those to prepare the states of the qubit and the photon source. This may simplify the integration of control circuitry on a chip using the single flux quantum logic. Such control was already demonstrated [123], and some promising proposals for it were put forward [124–126].

In addition to the study of the single-photon readout, our work provides some general results. We have shown that under the conditions (6.7), (6.6), and (7.45), a change of coupling types does not change the magnitude of the dispersive pull. Hence it does not alter the performance of a dispersive readout with any type of detector and probe. Also, it has been found that the Bloch-Siegert shift can aid dispersive readout. A proper choice of its sign increases the qubit-dependent cavity pull without a substantial impact on the qubit lifetime.

In conclusion, a theory of a single-photon dispersive measurement with a photodetector has been developed. Using this theory, we have assessed the performance of the scheme. Hence we were able to quantitatively analyze an ultimate limit of dispersive readout with an elementary portion of electromagnetic energy—a single photon. Sources of the readout errors have been identified. The role of the Bloch-Siegert shift and the coupling types has been elucidated. Some of our results are also valid for the multi-photon input. For future work, considering multi-photon Fock pulses is of interest.

Appendices

A Derivation of the approximate formula for the readout contrast

Here we show how to approximate Eqs. (7.27)–(7.29) with Eq. (7.32). Equations (7.27)–(7.29) yield

$$\frac{C}{\eta} = \frac{K}{K+1} - \frac{4K^2}{(K-1)^2+16X^2}\left(\frac{1}{4}+\frac{1}{4K}-\frac{K+1}{(K+1)^2+16X^2}\right). \quad (7.A.1)$$

In what follows, we drop the terms that contribute below 0.1% to C/η. As $\eta \sim 1$, these terms contribute with the same order of magnitude to C too.

The Taylor expansion of the first term in Eq. (7.A.1) is $K/(K+1) = 1 - 1/K + 1/2K^2 + \ldots$ We drop the terms starting from $1/2K^2$, as they contribute to the order of magnitude 10^{-3} or less if $X \gtrsim 40$. This can be shown using Eq. (7.31). The second term in Eq. (7.A.1) is approximated as $K^2/16X^2$, which is below or of order 10^{-2} for $X \gtrsim 100$. In the Taylor expansion $4K^2/[(K-1)^2+16X^2] = K^2/4X^2[1-(K-1)^2/16X^2+\ldots]$ we neglect the terms starting with the second one. $(K-1)^2/X^2 \sim 10^{-1}$ contributes as 10^{-3} to C since $K \gtrsim 10$ for $X \gtrsim 100$. Also, we neglected the terms $1/4K$ and $(K+1)/[(K+1)^2+16X^2]$ as these terms contribute not more than 10^{-3}. Finally,

$$C \approx \eta\left(1-\frac{1}{K}-\frac{K^2}{16X^2}\right) = \eta\left(1-\frac{3}{2K}\right), \quad (7.A.2)$$

for $X \gtrsim 100$; we used Eq. (7.31) in obtaining the last equality.

Chapter VIII

Counting microwave photons to two

1 Introduction

Quantum optics deals with indivisible units of electromagnetic radiation on an elementary level. It is not restricted to optical frequencies or interactions with single atoms. In fact, the platform of circuit quantum electrodynamics based on guided microwaves and superconducting circuits containing Josephson junctions has proven successful in implementing the functionality necessary for quantum optics [1, 19, 127] and to reach unparalleled coupling strengths of microwave photons to matter [128, 129]. It is also a successful platform for quantum computing [130]. Unlike natural atoms, the matter component of circuit quantum electrodynamics can be specially tailored to perform a certain function [127]. For example, one can design a counter of microwave photons which is based on Josephson junctions [1, 2, 38, 40–48, 53, 131, 132].

There are several reasons to have such a detector. At the end of a quantum microwave experiment one usually amplifies a signal and then measures its amplitude with a homo- or a heterodyne. To achieve a decent signal-to-noise ratio, several amplification stages are required. Moreover, a cold stage with a quantum-limited amplifier [34] is used. This requires bulky circulators and additional drive tones (see e.g. Ref. [51]). In the optical range one usually uses a photon detector, which reacts to a certain amount of energy. Photodetectors were also demonstrated in the microwave range. In Refs. [42–44] quantum non-demolition detectors were demonstrated. In Ref. [45] a destructive detector was demonstrated that uses only coherent quantum dynamics and hence allows rapid resetting. In Ref. [46], dissipation engineering was used to implement a destructive detector. However, these detectors rely on the readout of an ancillary qubit and their use in the readout of another qubit does not reduce overhead. Moreover, the detectors include circulators and a several-stage amplification sequence, which rules out the possibility for a compact design with the current technology. The destructive detector demonstrated in Refs. [47, 48] is quite compact as it only requires a resonator coupled to a Josephson junction. However, it is slow, requiring seconds for a photon to be detected. Josephson photomultipliers (JPMs) [1, 2] are especially compact, fast, and simple destructive detectors. The use of JPM in a microwave quantum optics experiment allows one to avoid complex and bulky amplification and promises integration with cold classical electronics [133].

Chapter VIII—except for Sec. 8, Appendix C, changes in Fig. 8.3, and various corrections—was published in "A. M. Sokolov and F. K. Wilhelm, Phys. Rev. Appl. 14.6, 064063 (2020)". The majority of the text was written by A. M. Sokolov. Calculations described in this chapter were carried out by A. M. Sokolov.

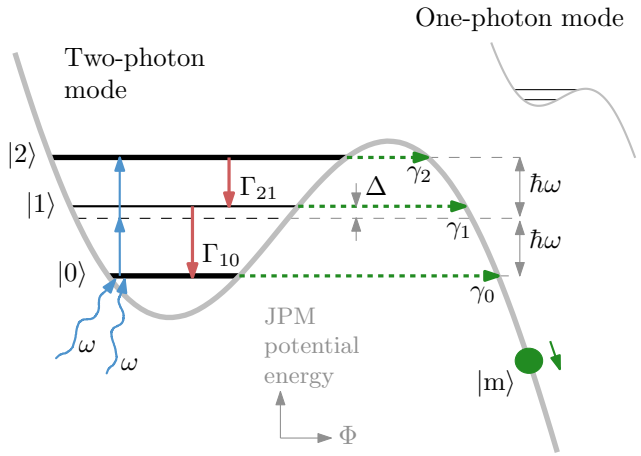

FIGURE 8.1: Two modes of operation of the JPM that counts to two. In the two-photon mode, the JPM possesses three metastable states. A single photon rarely excites the JPM to $|1\rangle$ due to detuning Δ. Two photons excite it to $|2\rangle$, which then tunnels quickly to the (quasi) continuum. JPM then "rolls" down the potential. This provides a macroscopic voltage on the junction, which is interpreted as a click. In the one-photon mode, the JPM possesses two metastable states. A single photon can deliver a click.

This might be useful for faster control and data acquisition, as well as for building quantum information processing devices with more qubits.

Most designs for microwave photodetectors demonstrated so far only discriminate the vacuum state vs. the states with a non-zero number of photons, i.e., they are called vacuum detectors [134]. However, for certain applications a detector that resolves the input photon number is desirable. In the dispersive readout with a photodetector [2, 37, 135], photon number resolution can improve fidelity in certain schemes [49]. Other uses include optimal discrimination of coherent states [136] and characterization [137] of microwave single-photon sources [108, 122]. Detectors of microwave photons were demonstrated [43, 44] and envisioned [42, 47] that possess limited capabilities for number resolution. However, they have a large footprint and other disadvantages discussed before, and they are only able either to distinguish a certain Fock state against all other states [42, 44], react to photon number above a threshold [47], or determine parity of the photon number [43]. The detector demonstrated in Ref. [41] resolves up to three photons, but relies on readout of an auxiliary qubit and includes a pump. To the best of our knowledge, no compact photodetectors with photon number resolution were demonstrated or proposed in the microwave range.

We propose a compact, photon-number resolving JPM based on the two-photon transition (see Fig. 8.1). It works as follows. First the JPM is set in the two-photon mode and its ground state is prepared. In this mode, the JPM clicks if two or more photons are present. This can be seen as an extension of a vacuum detector. Note that, after a click, it is a slow process to return the JPM to a state where it is sensitive to photons. If there are fewer than two photons, the JPM is tuned to the single-photon mode. This can be done fast. Here it works as a vacuum detector and fires if a photon is present. Hence the detector discriminates the vacuum state, single-photon state, and states with two or more photons. We present a theory of this detector in Sections 2–5 and evaluate its performance in Sections 6–7.

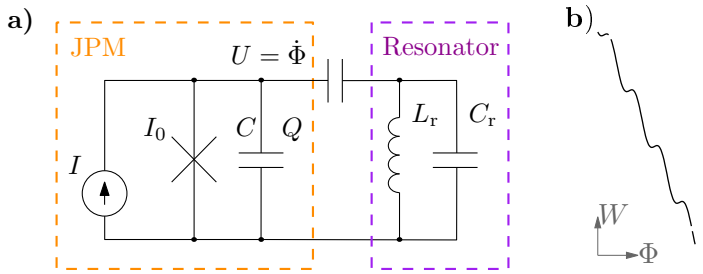

FIGURE 8.2: a) Circuit diagram of a resonator mode coupled to a JPM. The latter is a Josephson junction with a critical current I_0 and contact capacitance C. The junction is biased with an external current I. Voltage U is read out by an external voltmeter. b) The potential energy of the JPM.

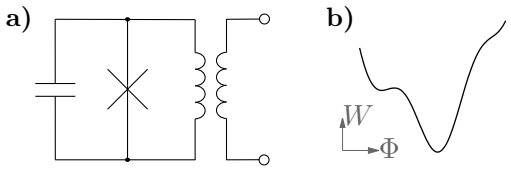

FIGURE 8.3: a) Another variant of JPM schematics: a flux-biased loop with a Josephson junction. b) Energy landscape of this JPM variant, as explained in Sec. 3.2.1 of Ref. [138].

2 Model

In this section, we write out the Hamiltonian of our system. Then, we treat dissipation and tunneling with the Lindblad equation formalism. For simplicity, a current-biased Josephson junction (Fig. 8.2) serves as a JPM model. However, we discuss why our results are also applicable to the flux-biased JPM (Fig. 8.3).

2.1 Hamiltonian

We consider a resonator coupled to a JPM (see Fig. 8.2). Full system Hamiltonian is

$$H = H_{\mathrm{JPM}} + H_{\mathrm{c}} + H_{\mathrm{r}}. \tag{8.1}$$

Here, the resonator Hamiltonian is given by

$$H_{\mathrm{r}} = \frac{Q_{\mathrm{r}}^2}{2\tilde{C}_{\mathrm{r}}} + \frac{\Phi_{\mathrm{r}}^2}{2L_{\mathrm{r}}}, \tag{8.2}$$

where Q_{r} denotes the charge on the resonator capacitance C_{r}, and Φ_{r} is the drop of node flux on it. A tilde denotes that a capacitance is renormalized by the JPM-resonator interaction. The JPM Hamiltonian is of the form

$$H_{\mathrm{JPM}} = \frac{Q^2}{2\tilde{C}} + W, \quad W = -\Phi_0 I_0 \cos 2\pi \frac{\Phi}{\Phi_0} - I\Phi. \tag{8.3}$$

Here, Φ_0 denotes the flux quantum. Q is the charge of the JPM capacitance C, Φ is its node flux. The JPM resides in a washboard potential W, which is plotted in Fig. 8.1. The resonator and the JPM interact through a coupling capacitance C'. The

coupling Hamiltonian is

$$H_{\mathrm{c}} = \frac{\tilde{C}'}{C C_{\mathrm{r}}} Q Q_{\mathrm{r}}. \tag{8.4}$$

The expressions for $\tilde{C}$, $\tilde{C}_{\mathrm{r}}$, and $\tilde{C}'$, as well as a detailed derivation of the circuit Hamiltonian are given in Appendix A. One can promote our canonical variables to operators. Their commutators are:

$$[\Phi, Q] = [\Phi_{\mathrm{r}}, Q_{\mathrm{r}}] = i\hbar, \tag{8.5}$$

while the other pairs commute. For two related circuits, a similar Hamiltonian was obtained in Ref. [139], which only differs in the type of coupling.

It is convenient to rewrite the Hamiltonian (8.1) in terms of ladder operators. In the Hamiltonian model, we restrict the JPM dynamics to the metastable states in a well—$|0\rangle$, $|1\rangle$, and $|2\rangle$ in Fig. 8.1. For the resonator, we make a usual substitution (1.9)–(1.10). The resulting Hamiltonian is

$$\begin{aligned} H =& \hbar(\omega + \Delta)|1\rangle\langle 1| + \hbar 2\omega |2\rangle\langle 2| + \hbar\omega a^\dagger a \\ &+ \hbar g_1(|1\rangle\langle 0|a + \text{h. c.}) + \hbar g_2(|2\rangle\langle 1|a + \text{h. c.}), \end{aligned} \tag{8.6}$$

where[1] $g_1 = \tilde{C}'(CC_{\mathrm{r}})^{-1}\sqrt{\hbar/2\rho}\,\langle 1|Q|0\rangle$ and $g_2 = \tilde{C}'(CC_{\mathrm{r}})^{-1}\sqrt{\hbar/2\rho}\,\langle 2|Q|1\rangle$. The JPM is designed for its $0 \to 2$ transition frequency to match 2ω, where $\omega = 1/\sqrt{L_{\mathrm{r}}\tilde{C}_{\mathrm{r}}}$ is the resonator frequency. The rotating-wave approximation was used in obtaining the Hamiltonian. The coupling of the JPM to the resonator is assumed to be linear in the field quadrature, hence its matrix elements in the Fock basis couple states that are different by exactly one photon.

2.2 Lindbladian

The model given so far does not take into account the interaction with the external degrees of freedom. First, in the Hamiltonian (8.6), we have excluded the states the system tunnels to. Hence the tunneling is a non-unitary process in this model. Moreover, even the non-truncated Hamiltonian (8.1) does not take account of the non-radiative transitions in the JPM and its dephasing. However, it would turn out that these processes, along with the tunneling, set the JPM performance.

To model them, we use the master equation formalism [60]. The Lindblad equation for our system reads

$$\dot{\rho} = \hat{L}\rho, \quad \hat{L}\rho = \frac{1}{i\hbar}[H, \rho] + (\hat{L}_0 + \hat{L}_1 + \hat{L}_2)\rho. \tag{8.7}$$

Lindbladians $\hat{L}_0$, $\hat{L}_1$, and $\hat{L}_2$ describe the incoherent processes involving the JPM states $|0\rangle$, $|1\rangle$, and $|2\rangle$:

$$\hat{L}_0 = \gamma_0 D[|\mathrm{m}\rangle\langle 0|], \tag{8.8}$$

$$\hat{L}_i = \Gamma_{i\,i-1} D[|i-1\rangle\langle i|] + \Gamma_{i\,i} D[|i\rangle\langle i|] + \gamma_i D[|\mathrm{m}\rangle\langle i|], \quad i = 1, 2. \tag{8.9}$$

Losses in the resonator are neglected. Here $D[\bullet]\rho = \bullet\rho\,\bullet^\dagger - \frac{1}{2}[\bullet^\dagger\bullet, \rho]_+$ with $[a, b]_+ = ab + ba$. For an i-th excited state of the JPM, γ_i is its tunneling rate, $\Gamma_{i\,i-1}$ is the relaxation rate, and $\Gamma_{i\,i}$ is the pure decoherence rate. In abbreviations like these, we

[1] Expressions for the coupling rates given in this thesis differ by the factor of i from our published work [140] due to the difference in the definition of a and $a^\dagger$.

mean double index in a subscript. $|\mathrm{m}\rangle$ denotes an amalgamation of the many possible states the JPM can tunnel into [38].

We have also considered another model for the tunneling [141]. The model is derived in Appendix C. It is also claimed in the appendix that for the model to be valid, the metastable levels should be separated by a frequency of order of the tunneling rates. In this case the JPM will not work, as the $|1\rangle$ width is more than the anharmonicity and a single photon can excite the JPM. However, for completeness we also provide the dressed superoperator $\hat{L}$ for this type of tunneling in Appendix D. It turns out that this model reproduces the Lindblad tunneling in the RWA.

2.3 Flux-biased variation

A flux-biased loop with a junction [2] can be more convenient to operate. It avoids voltages above the gap and hence quasiparticle production; therefore, the JPM can be reset much faster. The circuit diagram of this JPM variant and its energy landscape is shown in Fig. 8.3. Here, tunneling occurs to bound states in the global minimum. One aims at a regime where the global minimum resides in a wide and deep well. Then it is unlikely for an excitation to bounce back to the local minimum and get re-emitted back to the resonator. In fact, there is a large number of densely separated bound states, which can be treated as a continuum. Tunneling here can be described in the same way as in the current-biased JPM we consider. Qualitatively, we expect the same results for the flux-biased JPM variant.

3 Effective description of the two-photon processes

It is convenient to move to the frame where the first excited state of the JPM takes no part in the system dynamics. The two-photon terms appear then in the Hamiltonian explicitly. We use a Schrieffer-Wolff transform (see Ref. [142] and references therein) to obtain the Hamiltonian in that frame. Also, one needs to know how the relaxation processes are dressed in this picture. Therefore, the very transform is also applied to the Lindbladian.

3.1 Effective Hamiltonian

One can decouple the first excited state of the JPM with the unitary transform [143]

$$U = \exp(-\lambda_1|1\rangle\langle 0|a + \lambda_2|2\rangle\langle 1|a - \text{h. c.}), \tag{8.10}$$

where

$$\lambda_{1,2} = g_{1,2}/\Delta. \tag{8.11}$$

Hamiltonian (8.6) is then transformed as

$$\begin{aligned} H \to U^\dagger H U \approx{}& \hbar(\omega + \Delta + \chi_1)|1\rangle\langle 1| + \hbar(2\omega - \chi_2)|2\rangle\langle 2| \\ &+ \hbar\tilde{g}(|2\rangle\langle 0|a^2 + \text{h. c.}) + \hbar(\omega + \chi_1\sigma_\mathrm{z}^{01} - \chi_2\sigma_\mathrm{z}^{12})a^\dagger a \end{aligned} \tag{8.12}$$

with

$$\sigma_\mathrm{z}^{ij} = |j\rangle\langle j| - |i\rangle\langle i|, \quad \chi_i = \frac{g_i^2}{\Delta}, \tag{8.13}$$

$$\tilde{g} = \frac{g_1 g_2}{\Delta}. \tag{8.14}$$

By regrouping the terms in Eq. (8.12), one can check that χ_1 and χ_2 are the Stark shifts [19] per photon in the respective JPM levels.

The resulting Hamiltonian describes the system in the first order of perturbation theory. We have neglected the terms which contribute to the H matrix elements as $\lambda_{1,2}^2 N_{\rm ch}$ or $\lambda_1\lambda_2 N_{\rm ch}$, where $N_{\rm ch}$ is a characteristic number of photons in the resonator. Hence the Hamiltonian (8.12) holds if

$$\lambda_{1,2}^2 N_{\rm ch} \ll 1. \tag{8.15}$$

A transform is known [144], that *exactly* decouples the first excited state of a three-level atom interacting with a resonator mode. However, it does not accomplish this in the presence of the environment and is hence not useful here.

3.2 Interaction picture

It is convenient to move to the interaction picture with a unitary transform $U_{\rm i} = \exp(H_0 t/i\hbar)$, where H_0 is given by the first and the last lines in the right-hand side of Eq. (8.12). That is, H_0 is the effective Hamiltonian of the qubit and the resonator including the parametric interaction terms. This gives rise to

$$H \to U_{\rm i}^\dagger H U_{\rm i} - i\hbar U_{\rm i}^\dagger \dot{U}_{\rm i} = \hbar\tilde{g}|2\rangle\langle 0|e^{irt}a^2 + \text{h. c.}, \tag{8.16}$$

$$r = 2\chi_1 - \chi_2 + (\chi_1 - \chi_2)N, \quad N = a^\dagger a. \tag{8.17}$$

We used the facts that $|2\rangle\langle 0| \to |2\rangle\langle 0| \exp[i\{2\omega - \chi_2(N+1) + \chi_1 N\}t]$ and $a^2 \to a^2 \exp[-2i(\omega + \chi_1\sigma_{\rm z}^{01} - \chi_2\sigma_{\rm z}^{12})t]$.

In the interaction picture, the non-diagonal elements of the density matrix (coherences) do not oscillate with a high frequency. This simplifies the differential equations that govern the matrix elements. What is more important, in the interaction picture decoherence becomes the fastest process. This would allow us to make crucial approximations in Sec. 5.

Before that, one needs to check how the Lindbladian changes in the working frame.

3.3 Effective Lindbladian

Here we transform the Lindbladian first with the unitary transform U, as given in Eq. (8.10), and then with $U_{\rm i}$ as in Eq. (8.16). Transition to another frame with U changes the rates of non-unitary processes. In that frame, a resonator photon gets dressed by the JPM, thus acquiring new channels of tunneling and decay. The subsequent move to the interaction picture is also not completely trivial due to the parametric interaction terms in H_0.

While the density matrix transforms by $\rho \to U\rho U^\dagger$, jump operators of Lindbladians transform as

$$|i\rangle\langle j| \to U^\dagger|i\rangle\langle j|U, \quad i,j = 0,1,2,\text{m}. \tag{8.18}$$

An explicit form of the Lindbladian transformed with U is given in Appendix B. It contains the jump operators a and $a^\dagger$ of the dressed resonator.

When moving further to the interaction picture, $|i\rangle\langle j|$ and $a^{(\dagger)}$ in the Lindbladian pick up oscillating factors with photon number operator in the exponent, similarly to the operators in Eq. (8.16). These operator terms are due to the parametric interaction in the effective Hamiltonian (8.12). The conservative part of the Lindbladian is transformed by taking into account of the changes in the Hamiltonian, as in Eq. (8.16). As for the dissipative part, one can check that the regular non-operator phases cancel out

in the Lindbladian (8.B.1). On the other hand, the operator phases remain, as they do not commute with ρ and a. It is straightforward to write down the dressed Lindbladian in the interaction picture $\hat{L}'$. For that, one performs the substitutions (8.18) with U_i as well as $a^{(\dagger)} \to U_\mathrm{i}^\dagger a^{(\dagger)} U_\mathrm{i}$ in the dressed Lindbladian (8.B.1).

4 Equations for the click probability

Probability of the detector click is given by the occupation of $|\mathrm{m}\rangle$ disregarding the resonator state,

$$P = \sum_{N=0}^{\infty} \rho_{N\mathrm{m},N\mathrm{m}}. \tag{8.19}$$

Here

$$\rho_{Mi,Nj} = \langle M|\rho_{ij}|N\rangle, \quad \rho_{ij} = \langle i|\rho|j\rangle, \tag{8.20}$$

where $i, j = 0, 1, 2, \mathrm{m}$ index the JPM states while M and N index the Fock states of the resonator. In this section, we write out the exact equations that allows one to calculate P.

First the equation on ρ_mm is given. Transforming the dressed Lindbladian (8.B.1) to the interaction picture $\hat{L} \to \hat{L}'$ and projecting it on $|\mathrm{m}\rangle$ gives rise to

$$\begin{aligned}\dot{\rho}_\mathrm{mm} =& \hat{\gamma}_0\rho_{00} + \hat{\gamma}_1\rho_{11} + \hat{\gamma}_2\rho_{22} \\ &- (\gamma_1\lambda_2\tilde{\rho}_{12}a - \gamma_0\lambda_1\tilde{\rho}_{01}a - \gamma_2\lambda_2 a\tilde{\rho}_{12} + \gamma_1\lambda_1 a\tilde{\rho}_{01} + \mathrm{h.\,c.}),\end{aligned} \tag{8.21}$$

where $\tilde{\rho}_{10} = e^{i(\chi_1+\chi_2)Nt}\rho_{10}e^{-i\chi_2 Nt}$ and $\tilde{\rho}_{21} = e^{i\chi_2 Nt}\rho_{21}e^{-i(\chi_1+\chi_2)Nt}$ due to the transformation to the interaction picture of the dressing correction $\hat{L}^{(1)}$ in the Lindbladian (8.B.1). The equation is given up to and including terms of order λ_1 and λ_2. In Eq. (8.21) and in the following equations, we use the superoperators

$$\hat{\gamma}_0\rho = \gamma_0 e^{i\chi_1 Nt}\rho e^{-i\chi_1 Nt}, \tag{8.22}$$

$$\hat{\gamma}_1\rho = \gamma_1 e^{-i(\chi_1+\chi_2)Nt}\rho e^{i(\chi_1+\chi_2)Nt}, \tag{8.23}$$

$$\hat{\gamma}_2\rho = \gamma_2 e^{i\chi_2 Nt}\rho e^{-i\chi_2 Nt}, \tag{8.24}$$

$$\hat{\Gamma}_{10}\rho = \Gamma_{10} e^{-i(2\chi_1+\chi_2)Nt}\rho e^{i(2\chi_1+\chi_2)Nt}, \tag{8.25}$$

$$\hat{\Gamma}_{21}\rho = \Gamma_{21} e^{i(\chi_1+2\chi_2)Nt}\rho e^{i(\chi_1+2\chi_2)Nt} \tag{8.26}$$

that take into account the effect of moving to the interaction picture on the bare part (8.7) of the dressed Lindbladian. The only terms that change there are those responsible for the accumulation in the JPM populations due to the incoherent processes.

To complete Eq. (8.21), one needs equations for $\dot{\rho}_{00}$, $\dot{\rho}_{11}$, and $\dot{\rho}_{22}$ with the same accuracy. For $\dot{\rho}_{12}$ and $\dot{\rho}_{01}$, the zeroth approximation in λ_1 and λ_2 would suffice. Equations (8.B.1) and (8.16)–(8.17) yield

$$\dot{\rho}_{00} = (i\tilde{g}\rho_{02}e^{irt}a^2 + \mathrm{h.\,c.}) - \gamma_0\rho_{00} + \hat{\Gamma}_{10}\rho_{11} + \langle 0|\hat{L}'^{(1)}\rho|0\rangle, \tag{8.27}$$

$$\dot{\rho}_{11} = -(\gamma_1 + \Gamma_{10})\rho_{11} + \hat{\Gamma}_{21}\rho_{22} + \langle 1|\hat{L}'^{(1)}\rho|1\rangle, \tag{8.28}$$

$$\dot{\rho}_{22} = (-i\tilde{g}e^{irt}a^2\rho_{02} + \mathrm{h.\,c.}) - (\gamma_2 + \Gamma_{21})\rho_{22} + \langle 2|\hat{L}'^{(1)}\rho|2\rangle \tag{8.29}$$

in the first order in λ_1 and λ_2. Next we express

$$\dot{\rho}_{01} = -i\tilde{g}a^{\dagger 2}e^{-irt}\rho_{21} - \frac{1}{2}d_{01}\rho_{01} + O(\lambda_1 + \lambda_2), \tag{8.30}$$

$$\dot{\rho}_{12} = i\tilde{g}\rho_{10}a^{\dagger 2}e^{-irt} - \frac{1}{2}d_{12}\rho_{12} + O(\lambda_1 + \lambda_2), \tag{8.31}$$

as well as

$$\dot{\rho}_{02} = i\tilde{g}\rho_{00}a^{\dagger 2}e^{-irt} - i\tilde{g}a^{\dagger 2}e^{-irt}\rho_{22} - \frac{1}{2}d_{02}\rho_{02} + \langle 0|\hat{L}'^{(1)}\rho|2\rangle + O(\lambda_1^2 + \lambda_2^2 + \lambda_1\lambda_2), \tag{8.32}$$

where

$$d_{01} = \gamma_0 + \gamma_1 + \Gamma_{10} + \Gamma_{11}, \tag{8.33}$$

$$d_{12} = \gamma_1 + \gamma_2 + \Gamma_{10} + \Gamma_{21} + \Gamma_{22}, \tag{8.34}$$

$$d_{02} = \gamma_0 + \gamma_2 + \Gamma_{21} + \Gamma_{22} \tag{8.35}$$

are the full decoherence rates of the $0 \to 1$, the $1 \to 2$, and the $0 \to 2$ transitions, respectively. Due to the form of Eqs. (8.27) and (8.29), we have calculated $\dot{\rho}_{02}$ in the first order in λ_1 and λ_2.

It is straightforward to write out a full set of equations to calculate ρ_{mm} and P. To do that, one transforms the dressed Lindbladian $\hat{L}$ in Appendix B into the interaction picture as described in Sec. 3.3, arriving at the working frame Lindbladian $\hat{L}'$ with a dressed correction $\hat{L}'^{(1)}$. Then one uses the $\hat{L}'^{(1)}$ matrix elements and projects Eqs. (8.21) and (8.27)–(8.32) on the photon number states. However, in the regime the device operates well, much simpler equations can be used.

5 Fast decoherence

If there are two photons in the resonator, the JPM should fire as fast as possible. After the photons excite the JPM, it should tunnel immediately. More precisely, this should happen much faster than the excitation bounces back coherently to the cavity or the JPM relaxes non-radiatively. In this regime, the JPM decoheres instantaneously; hence the system state is determined by the probabilities of the excitation to occupy either the cavity or the JPM. Here we obtain the rate equations for the case of fast decoherence.

For that case we assume that

$$\tilde{\Gamma}_1 + \Gamma_{11} \gg t^{-1}, \quad \tilde{\Gamma}_2 + \Gamma_{22} \gg \tilde{\Gamma}_1, t^{-1}, \tag{8.36}$$

where t is the time we observe the system at, and

$$\tilde{\Gamma}_1 = \gamma_1 + \Gamma_{10}, \quad \tilde{\Gamma}_2 = \gamma_2 + \Gamma_{21}. \tag{8.37}$$

By Eqs. (8.36), and given that

$$\gamma_0 \ll \gamma_1 \ll \gamma_2, \tag{8.38}$$

Eqs. (8.33) and (8.34) yield $d_{01} \approx \tilde{\Gamma}_1 + \Gamma_{11}$ and $d_{12} \approx \tilde{\Gamma}_2 + \Gamma_{22}$. Moreover, at time t the coherences between the neighbor JPM levels have already died out,

$$\rho_{01} \approx \rho_{12} \approx 0, \tag{8.39}$$

which follows from the form of Eqs. (8.30)–(8.31) and the conditions (8.36). Equation (8.21) then simplifies to

$$\dot{\rho}_{\mathrm{mm}} = \gamma_0\rho_{00} + \gamma_1\rho_{11} + \gamma_2\rho_{22}. \tag{8.40}$$

One can show the system is then governed by rate equations. First we express ρ_{02} in terms of the probabilities ρ_{00} and ρ_{22}. The formal solution of Eq. (8.32) reads

$$\rho_{02}(t) \approx \rho_{02}(0)e^{-\frac{1}{2}(\tilde{\Gamma}_2+\Gamma_{22})t} + i\tilde{g}\int_0^t dt' e^{-\frac{1}{2}(\tilde{\Gamma}_2+\Gamma_{22})(t-t')} \times [\rho_{00}a^{\dagger 2}e^{-irt'} - a^{\dagger 2}e^{-irt'}\rho_{22}e^{\tilde{\Gamma}_2 t'}e^{-\tilde{\Gamma}_2 t'}]. \tag{8.41}$$

We took into account that $\langle 0|\hat{L}'^{(1)}\rho|2\rangle \approx 0$ due to Eq. (8.39). The first term in the right-hand side vanishes due to Eqs. (8.36). Now we make an approximation similar to the Weisskopf-Wigner one: we assume $a^\dagger(t')$, $e^{-irt'}$, $\rho_{00}(t')$, and $\rho_{22}(t')e^{\tilde{\Gamma}_2 t'}$ to change slowly in comparison to the rate $\tilde{\Gamma}_2$. Treating these terms as constants allows one to perform the integration, which yields

$$\rho_{02}(t) \approx i\frac{2\tilde{g}}{\tilde{\Gamma}_2 + \Gamma_{22}}\rho_{00}a^{\dagger 2}e^{-irt}. \tag{8.42}$$

Substituting this into Eqs. (8.27)–(8.29) and projecting them on the resonator Fock states gives rise to

$$\begin{aligned}
\dot{\rho}_{N\,0,N\,0} &\approx -B_{N\,N-2}\rho_{N\,0,N\,0} - \gamma_0\rho_{N\,0,N\,0} + \Gamma_{10}\rho_{N\,1,N\,1}, \quad N \geq 2\\
\dot{\rho}_{N-2\,2,N-2\,2} &\approx B_{N\,N-2}\rho_{N\,0,N\,0} - \tilde{\Gamma}_2\rho_{N-2\,2,N-2\,2}, \quad N \geq 2\\
\dot{\rho}_{N\,0,N\,0} &\approx -\gamma_0\rho_{N\,0,N\,0} + \Gamma_{10}\rho_{N\,1,N\,1}, \quad N = 0, 1\\
\dot{\rho}_{N\,1,N\,1} &\approx -\tilde{\Gamma}_1\rho_{N\,1,N\,1} + \Gamma_{21}\rho_{N\,2,N\,2}.
\end{aligned} \tag{8.43}$$

It was used that the matrix elements $\langle i|\hat{L}'^{(1)}\rho|i\rangle \approx 0$ for $i = 0, 1, 2$ due to Eq. (8.39). We have defined

$$B_{N\,N-2} = \frac{4\tilde{g}^2}{\tilde{\Gamma}_2 + \Gamma_{22}}N(N-1) \tag{8.44}$$

the rate of absorption of two photons from an N-photon state. $B_{N\,N-2}$ is also the stimulated emission rate; however, Eqs. (8.43) do not contain stimulated emission terms, as the stimulated emission is slow compared to the competing processes. One can figure out from Eqs. (8.43) that the condition

$$B_{N\,N-2} \ll \tilde{\Gamma}_2 + \Gamma_{22} \tag{8.45}$$

should hold, as we have assumed ρ_{00} and ρ_{22} to change slowly. Also, as $e^{-irt'}$ is assumed to change slowly as well, the condition

$$\chi_2 N_{\max} \ll \tilde{\Gamma}_2 + \Gamma_{22} \tag{8.46}$$

is required to hold. In the course of its derivation, it was taken into account that $\chi_2 - \chi_1 \sim \chi_2$ as

$$g_2 \approx \sqrt{2}g_1 \tag{8.47}$$

in the harmonic approximation of the JPM potential. $N_{\max}$ in Eq. (8.46) is the highest number of a Fock state such that its occupation is not negligible. The condition (8.46)

is easy to interpret in the laboratory frame. It makes sure that the two-photon transition is not detuned from the Stark-shifted second excited level more than by its linewidth. This interpretation suggests that the condition might be weakened to use the "<" inequality sign.

As manifested by Eqs. (8.43), the dressing does not change the rates of non-unitary processes if the decoherence is fast; this can be explained as follows. Consider $|1\,0\rangle$ the dressed state of a photon and the ground-state JPM. In terms of the bare states, it is a photon entangled with the excited JPM, $|1\,0\rangle \approx |1\,0\rangle_\mathrm{b} + \lambda_1 |0\,1\rangle_\mathrm{b}$. Admixture of the bare excited JPM adds its decay channels to the dressed state. However, due to the rapid decoherence, the state collapses to a statistical mixture. The addition to the decay rate is then of order of λ_1^2, which is negligible.

In the next subsections, we calculate the click probabilities for vacuum, single-photon, and two-photon inputs. In the two-photon mode, a click should be delivered if more than one photon dwells in the resonator; no click should occur in the opposite case. Clicks that do occur for vacuum or single-photon inputs we call false counts.

5.1 Vacuum input

Here we determine the probability of a JPM click in the case there are no photons in the resonator.

First we determine the initial state of the system. In the laboratory frame, both the JPM and the cavity are in the ground state at the initial instant:

$$|\Psi_\mathrm{b}(0)\rangle = |0\,0\rangle. \tag{8.48}$$

So are they in our working frame,

$$|\Psi(0)\rangle = U^\dagger |\Psi_\mathrm{b}(0)\rangle = |0\,0\rangle, \tag{8.49}$$

where U is defined in Eq. (8.10). Therefore,

$$\rho(0) = |0\,0\rangle\langle 0\,0|. \tag{8.50}$$

For this case, Eqs. (8.43), (8.19) and (8.40) simplify to

$$\dot{P}_\mathrm{f} = \gamma_0 \rho_{00,00} \quad \text{and} \quad \dot{\rho}_{00,00} = -\gamma_0 \rho_{00,00}. \tag{8.51}$$

With the initial conditions given by Eq. (8.50) and

$$P_\mathrm{f}(0) = 0, \tag{8.52}$$

these equations yield

$$P_\mathrm{f}(t) = 1 - e^{-\gamma_0 t} \tag{8.53}$$

with γ_0 the false count rate. The JPM can tunnel even while in the ground state, hence delivering a false count.

5.2 One-photon input

Analogously to the previous case, one can determine the initial state. In the laboratory frame

$$|\Psi_\mathrm{b}(0)\rangle = |1\,0\rangle, \tag{8.54}$$

while in the working frame

$$\begin{aligned} |\Psi(0)\rangle =& U^\dagger |\Psi_\mathrm{b}(0)\rangle \\ =& |1\,0\rangle + \lambda_1 |0\,1\rangle + O(\lambda_1^2) + O(\lambda_2^2), \end{aligned} \tag{8.55}$$

$$\rho(0) = |1\,0\rangle\langle 1\,0| + \lambda_1 |1\,0\rangle\langle 0\,1| + \lambda_1 |0\,1\rangle\langle 1\,0| + O(\lambda_1^2) + O(\lambda_2^2). \tag{8.56}$$

Recall that, in our working frame, there is no interaction with the JPM's first excited state. However, in this frame, a bare photon acquires a part of it according to Eq. (8.55). This may cause a click if the excitation from the first level tunnels.

In the limit of fast decoherence, the dressed initial state coincides with the bare one. Due to Eq. (8.39), coherences vanish on times (8.36) we are interested in and

$$\rho(0) \approx |1\,0\rangle\langle 1\,0|. \tag{8.57}$$

Solving Eqs. (8.43), (8.19) and (8.40) with the initial conditions given by Eqs. (8.57) and (8.52) yields

$$P_\mathrm{f}(t) = 1 - e^{-\gamma_0 t}. \tag{8.58}$$

The false count rate for the single-photon input is the same as for the vacuum input. This can be explained as follows. As commented before, the one-photon admixture in Eq. (8.56) may deliver a click. However, it relies on the system coherence. The coherence dies out momentarily and the admixture decays before the JPM excitation can tunnel.

This does not hold in the next order of perturbation theory. Luckily, there is a simple way to estimate the next-order false count rate. This rate will provide the limit of applicability of Eq. (8.58).

Let us calculate the tunneling rate due to the one-photon transition in the next order of perturbation theory. As the conditions (8.36) of the fast decoherence are secured, one can argue in terms of probabilities and transition rates. From Eq. (8.55), probability of the JPM residing in the first excited state is

$$\langle 1|\rho(0)|1\rangle = \lambda_1^2 + O(\lambda_1^3) + O(\lambda_2^3). \tag{8.59}$$

According to Eqs. (8.43), the first excited state tunnels with rate γ_1. Therefore, for the initial state $\rho(0)$, the rate of the first-level tunneling is $\lambda_1^2\gamma_1$. Note the Eqs. (8.43) are obtained up and including terms of the order of $\lambda_{1,2}$ only. However, higher-order terms in the equations only give rise to corrections of order beyond $\lambda_{1,2}^2$ in the rate.

The tunneling rate via the first excited state sets the limit of validity of Eq. (8.58),

$$t \ll \gamma_1^{-1}\lambda_1^{-2}. \tag{8.60}$$

For the two-photon input we consider below, the limit of validity is the same. It can be obtained analogously.

5.3 Two-photon input

To determine initial conditions, one applies the same reasoning as for the vacuum and the one-photon input. This gives rise to

$$\rho(0) = |2\,0\rangle\langle 2\,0| + \lambda_1 |2\,0\rangle\langle 1\,1| + \lambda_1 |1\,1\rangle\langle 2\,0|. \tag{8.61}$$

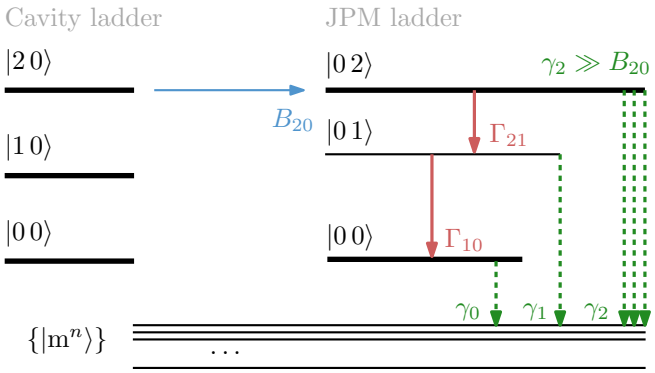

FIGURE 8.4: Two-photon absorption in the limit of fast decoherence and tunneling. $\{|m^n\rangle\}$ are the states the JPM can tunnel to.

Due to the fast decoherence, the initial state should be approximated as

$$\rho(0) \approx |2\,0\rangle\langle 2\,0|. \tag{8.62}$$

This can be shown analogously to the case of one-photon input.

Equations (8.43), (8.19) and (8.40) become

$$\dot{\rho}_{20,20} = -B_{20}\rho_{20,20} - \gamma_0\rho_{20,20}, \tag{8.63}$$
$$\dot{\rho}_{02,02} = B_{20}\rho_{20,20} - \tilde{\Gamma}_2\rho_{02,02}, \tag{8.64}$$
$$\dot{\rho}_{01,01} = -\tilde{\Gamma}_1\rho_{01,01} + \Gamma_{21}\rho_{02,02}, \tag{8.65}$$
$$\dot{\rho}_{00,00} = -\gamma_0\rho_{00,00} + \Gamma_{10}\rho_{01,01}, \tag{8.66}$$
$$\dot{P}_\mathrm{b} = \gamma_0\rho_{20,20} + \gamma_2\rho_{02,02} + \gamma_1\rho_{01,01} + \gamma_0\rho_{00,00} \tag{8.67}$$

with

$$B_{20} = 8\tilde{g}^2/(\tilde{\Gamma}_2 + \Gamma_{22}) \tag{8.68}$$

the two-photon absorption rate. The rate equations are illustrated in Fig. 8.4. Equations, similar to Eqs. (8.63)–(8.67) were obtained in Ref. [38] for the one-photon transition in a two-state JPM well. As compared to the reference, our equations lack the stimulated emission terms. This is explained for Eqs. (8.43). Moreover, the ground level tunneling was not accounted for in the reference.

We solve Eqs. (8.63)–(8.67) by carrying out the Laplace transform. The initial conditions are given by Eqs. (8.62) and $P_\mathrm{b}(0) = 0$. The solution in the Laplace domain is

$$\tilde{P}_\mathrm{b}(s) = \frac{\gamma_0 B_{20}\Gamma_{21}\Gamma_{10}}{s(s+\gamma_0)(s+\tilde{\Gamma}_1)\Delta_2} + \frac{\gamma_1 B_{20}\Gamma_{21}}{s(s+\tilde{\Gamma}_1)\Delta_2} + \frac{\gamma_0(B_{20}+\tilde{\Gamma}_2)+\gamma_2 B_{20}}{s\Delta_2} + \frac{\gamma_0}{\Delta_2}, \tag{8.69}$$

where

$$\Delta_2 = (s+\tilde{\Gamma}_2)(s+B_{20}+\gamma_0). \tag{8.70}$$

Now we find an expression for the click probability in the time domain. It is found by calculating the inverse Laplace transform,

$$P_\mathrm{b}(t) = \frac{1}{2\pi i}\int_{\sigma-i\infty}^{\sigma+i\infty} ds\, e^{st}\tilde{P}_\mathrm{b}(s). \tag{8.71}$$

By carrying out the integrals and doing approximations, one arrives at

$$P_{\mathrm{b}}(t) = 1 - e^{-B_{20}t} - \frac{\Gamma_{21}}{\gamma_2 + \Gamma_{21}} \frac{\Gamma_{10}}{\gamma_1 + \Gamma_{10}} e^{-\gamma_0 t}. \tag{8.72}$$

We used the condition (8.38) and

$$\gamma_0 \ll B_{20} \ll \tilde{\Gamma}_2, \tag{8.73}$$

where the last inequality is a more stringent version of the condition (8.45). This allowed us to drop the terms proportional to $B_{20}/\tilde{\Gamma}_2$ and $\gamma_{0,1}/\tilde{\Gamma}_2$. These terms are negligibly small in comparison to the second term in the equation. While it will turn out the last term is also small, it decays much slower than the second one. Hence it is considerable for $t > 1/B_{20}$. Equation (8.72) holds for the times (8.36) coherence has already vanished.

One can interpret Eq. (8.72). The second term there is the population of the state $|2\,0\rangle$ of the resonator in the two-photon Fock state and the JPM in the ground state. Tunneling from this state is negligible due to Eq. (8.73). After an excitation transfers from $|2\,0\rangle$ to $|0\,2\rangle$ with the rate B_{20}, it tunnels immediately due to the condition (8.45). Hence $1 - \exp(-B_{20}t)$ is the tunneling probability for the times before the resonator is depleted. Afterward, the third term in Eq. (8.72) starts to matter. While absorbing photons, the JPM can also relax to its first excited state $|1\rangle$. After all photons are absorbed, the JPM relaxes to $|1\rangle$ with a small probability $\Gamma_{21}/(\gamma_2+\Gamma_{21})$. From $|1\rangle$ the JPM relaxes to the ground state with the probability $\Gamma_{10}/(\gamma_1+\Gamma_{10})$. There it is stuck due to the slow ground-state tunneling of rate γ_0, which only becomes substantial for the longer times. While tunneling can also occur from $|1\rangle$, this mostly happens while the resonator is not yet depleted and the tunneling from $|0\,2\rangle$ is ongoing. Due to the condition (8.38), this process is much faster than the tunneling from $|1\rangle$ and the respective term does not play a role in Eq. (8.72).

5.4 Error probability

One can now calculate the probability of false discrimination between the state with $N = 2$ photons and the states with $N = 1$ or $N = 0$ photons. This error is expressed as

$$\varepsilon = P_{0,1} P_{\mathrm{f}} + P_2(1 - P_{\mathrm{b}}) \tag{8.74}$$

where $P_{0,1} = P_0 + P_1$ and P_N is a probability of an input state with N photons to occur. P_{b} denotes a probability of a bright count—i.e., a probability of registering a two-photon state when it dwells in the resonator. It was taken into account that the probability of a false count P_{f} is the same for both $N = 0$ and $N = 1$.

If we know nothing about the resonator state beforehand, $P_{0,1} = P_2 = 1/2$. Using the expressions (8.53) and (8.58) for P_{f} and Eq. (8.72) for P_{b} yields

$$\varepsilon = \frac{1}{2}(1 + e^{-B_{20}t} + \Big(\frac{\Gamma_{21}}{\tilde{\Gamma}_2} \frac{\Gamma_{10}}{\tilde{\Gamma}_1} - 1\Big) e^{-\gamma_0 t}). \tag{8.75}$$

The error probability is plot in Fig. 8.5.

With Eq. (8.75), it is possible to find the minimal error and the optimal waiting time t. At

$$t \approx \frac{1}{B_{20}} \ln \frac{B_{20}}{\gamma_0} \tag{8.76}$$

TABLE 8.1: JPM Parameters. The decay rates are from Ref. [145]. Coupling strength g_1 is chosen as described in the text.

C (pF)	I_0 (μA)	I/I_0	$\Gamma_{10}/2\pi$ (kHz)	$\Gamma_{22}/2\pi$ (MHz)	$g_1/2\pi$ (MHz)
2	10	0.97987	318	2.1	13.8

TABLE 8.2: Estimates for the JPM.

$\gamma_0/2\pi$ (Hz)	$\gamma_1/2\pi$ (kHz)	$\gamma_2/2\pi$ (MHz)	$\omega/2\pi$ (GHz)	$\Delta/2\pi$ (MHz)	$B_{20}/2\pi$ (MHz)	$N_{\max}$
37	54	41	8.2	194	0.35	14

one attains the minimal error

$$\varepsilon \approx \frac{\gamma_0}{2B_{20}}\Big(1+\ln\frac{B_{20}}{\gamma_0}\Big)+\frac{1}{2}\frac{\Gamma_{21}}{\tilde{\Gamma}_2}\frac{\Gamma_{10}}{\tilde{\Gamma}_1}. \tag{8.77}$$

One can check the expression is the same if the condition with γ_0 in Eq. (8.73) is not used in obtaining Eq. (8.72).

5.5 More than two photons in the input

For the case there are $N > 2$ photons in the cavity, a two-photon transition occurs, leaving $N-2$ photons in the cavity. To describe this, one only need to change the state labels and $B_{20} \to B_{N\,N-2}$ in Eqs. (8.61)–(8.77). The bright count probability $P_{\rm b}$ improves, as $B_{N\,N-2} > B_{20}$ by Eq. (8.44). By the same reason, the error ε gets smaller if one needs to discriminate a state with $N > 2$ photons against the states with one or no photons. Moreover, the error is smaller even if N breaks the condition (8.15) but the requirement (8.46) still holds. In that case, additional clicks are provided by the single-photon transition and the subsequent tunneling from the first level.

6 Distinguishing a multi-photon state

In this section, example parameters for the JPM in the two-photon mode are provided. For those parameters, we estimate the probabilities of bright and false counts, the time to distinguish a multi-photon state, and the probability of false discrimination.

First let us summarize the requirements for our JPM to work as described above. The energy of the junction plasma oscillations should much exceed that of a thermal excitation, $\hbar\omega_{\rm p} \gg k_{\rm B}T$, where T is the temperature of the JPM environment. On the other hand, we do not want to spur quasiparticles while exciting the JPM. Hence

$$\omega_{\rm p} \ll \Delta_{\rm gap}, \tag{8.78}$$

where $\Delta_{\rm gap}$ is the superconductor gap. Furthermore, the effective Lindbladian (8.B.1) we have used is correct if the conditions (8.15) and (8.60) hold. Finally, we have required the JPM to decohere fast by the conditions (8.36) and (8.45)–(8.46).

It is convenient to introduce the Josephson energy

$$E_{\rm J} = \frac{I_0\Phi_0}{2\pi} \tag{8.79}$$

TABLE 8.3: JPM performance in the detection of the two-photon state. The bright P_b (8.72) and the false P_f count probabilities [Eqs. (8.53) and (8.58)] are given for the optimal waiting time t (8.76).

t (μs)	P_f %	P_b %
4.2	0.1	98.6

and the capacitive energy

$$E_\mathrm{C} = \frac{e^2}{2C}. \tag{8.80}$$

The ratio

$$\beta = I/I_0 \tag{8.81}$$

is given in Table 8.1. For that ratio, three levels fit in the well.

One needs to know the position of the levels in the well. For that, we expand the potential around the well minimum up to the cubic terms:

$$\frac{W}{E_\mathrm{J}} \approx \frac{\sqrt{1-\beta^2}}{2}\delta^2 - \frac{\beta}{6}\delta^3, \tag{8.82}$$

where $\delta = 2\pi\Phi/\Phi_0 - \phi_\mathrm{min}$ is the dimensionless flux with respect to the well minimum at $\phi_\mathrm{min} = \arcsin\beta$. To determine the level structure correctly, the cubic approximation should be accurate in the region up to the barrier maximum at $\delta_\mathrm{max} = 2\cot\phi_\mathrm{min}$. For a weak anharmonicity, one can calculate the position of the levels using the second-order perturbation theory [146, 147]. It is useful to define

$$n_0 = \frac{(1-\beta^2)^{5/4}}{3\beta^2}\sqrt{\frac{E_\mathrm{J}}{2E_\mathrm{C}}} \tag{8.83}$$

the barrier height in the units of

$$\omega_\mathrm{p} = \frac{1}{\hbar}\sqrt{8E_\mathrm{J}E_\mathrm{C}}(1-\beta^2)^{1/4} \tag{8.84}$$

the level separation in harmonic approximation. Expressions (8.83) and (8.84) coincide with those given in Ref. [147]. Transition frequency from the ground to the first excited state is $\omega_{10} = \omega_\mathrm{p}(1 - 5/36n_0)$. Transition frequency to the second excited state is $\omega_{20} = \omega_\mathrm{p}(2 - 5/12n_0)$ [70]. We aim to detect photons of frequency

$$\omega = \omega_{02}/2. \tag{8.85}$$

This photon is detuned from the $0 \to 1$ transition by

$$\Delta = \omega_{10} - \omega = \frac{5}{72}\frac{\omega_\mathrm{p}}{n_0}. \tag{8.86}$$

We provide the value of Δ in Table 8.2.

Knowledge of Δ allows one to set g_1 and g_2. One can use the criterion (8.15) for that. To be sure that no clicks are delivered when there is a single photon in the resonator, Eq. (8.15) should hold for $N_\mathrm{ch} = 1$. This requirement does not matter for bigger photon numbers—by the reasoning similar to that at the end of Section 5.4. So, we choose $\lambda_2 = 0.1$ which fulfills one of the requirements (8.15) for $N_\mathrm{ch} = 1$. By virtue

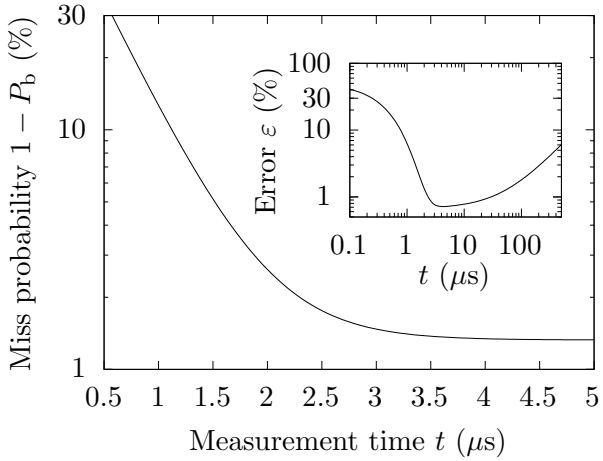

FIGURE 8.5: Probability of missing a two-photon state for a device with the parameters given in Table 8.1. (Inset) Error in the discrimination of the two-photon state against the states with fewer photons.

of Eq. (8.47), the part of the condition (8.15) with λ_1 (8.11) holds automatically. From the definition (8.11) of λ_1 and λ_2 and the relationship (8.47), one gets that

$$g_2 = \lambda_2 \Delta, \quad g_1 = \lambda_2 \Delta / \sqrt{2}. \tag{8.87}$$

One also needs to make sure that the condition (8.46) holds. This yields the biggest photon number $N_{\max}$ that can be distinguished from the single-photon and the vacuum states. Its value is given in Table 8.2.

Let us calculate the rate B_{20} of the two-photon absorption. It follows from the Eqs. (8.68), (8.14), (8.87), and (8.11) that

$$B_{20} \approx 4\lambda_2^4 \Delta^2 / (\tilde{\Gamma}_2 + \Gamma_{22}). \tag{8.88}$$

Assuming flat density of states of the thermal reservoir, one can estimate in the harmonic approximation that

$$\Gamma_{21} \approx 2\Gamma_{10}. \tag{8.89}$$

Tunneling rates γ_0, γ_1, and γ_2 are calculated with the WKB method [146] and are given in Table 8.2. We used the expression [147]

$$\gamma_n = \frac{\omega_n}{n!\sqrt{2\pi}} \left(\frac{n+1/2}{e} \right)^{n+1/2} \exp\left(-\frac{2S}{\hbar} \right) \tag{8.90}$$

for the tunneling rate. The integral in the action $S = \int_{\Phi_1}^{\Phi_2} d\Phi \sqrt{2C(W - \hbar\omega_n)}$ was carried out numerically [2] for the exact potential W given by Eq. (8.3). The n-th level eigenfrequencies ω_n and the barrier boundaries Φ_1 and Φ_2 were determined using the cubic approximation. With all the necessary quantities obtained, one can calculate B_{20}. Its value is provided in the table.

Now one can estimate the JPM performance. The error (8.75) and the probability to miss a two-photon state $1 - P_b$ [see Eq. (8.72)] are shown in Fig. 8.5. The dominant contribution to the false counts at the optimal counting time (8.76) is due to the ground level tunneling as given by Eqs. (8.53) and (8.58). The false count probability is given in Table 8.3. Transitions to the first excited state $|1\rangle$ in the second-order

[2] The respective PYTHON codes are available as a part of the GitLab repository [148].

perturbation theory in $\lambda_{1,2}$ contribute as well. However, one can check that by the criterion (8.60) their effect is still vanishing for the relevant times. Also, $|1\rangle$ could be excited by an off-resonant single photon due to the level widening. However, this is highly improbable, as

$$\tilde{\Gamma}_1 + \Gamma_{11} \ll \Delta. \tag{8.91}$$

7 Counting to two

A two-step procedure (see Fig. 8.1 and Section 1) is to be performed to count photons to two. To switch from the two-photon mode to the single-photon one, bias current I [see Fig. 8.2 and the Hamiltonian (8.3)] is changed so that the JPM possesses two metastable states instead of three. Here we estimate the error in discrimination between the vacuum input state, a one-photon state, and a multi-photon state. The total time of the discrimination is estimated as well.

Full time to count to two is approximately the same as the time to distinguish a multi-photon state vs. the vacuum or the single-photon state. Additional time consists of the time to switch to the single-photon mode and the time to discriminate the vacuum state. To spur no excitations in the JPM, the switching should be much slower than the inverse transition frequencies. For the parameters in Table 8.1, the switching can be as fast as 10 ns. Now let us compare the waiting times. Time to discriminate a multi-photon state is determined by B_{20}, as it follows from Eq. (8.72). Time to discriminate the vacuum is set by γ_1 in the two-state configuration and B_{10} the single-photon absorption rate. The latter can be calculated analogously to the two-photon absorption rate (8.68). This yields $B_{10} = 4g_1^2/(\tilde{\Gamma}_1 + \Gamma_{11})$. With Eq. (8.14) one has

$$\frac{B_{20}}{B_{10}} = 2\lambda_2^2 \frac{\tilde{\Gamma}_1 + \Gamma_{11}}{\tilde{\Gamma}_2 + \Gamma_{22}} \approx \lambda_2^2. \tag{8.92}$$

Equation (8.89) and the fact that decay is much faster than the pure decoherence were used in obtaining the last equality in Eq. (8.92). WKB estimate for the tunneling rate from the excited state gives

$$\gamma_1 \approx 2\pi\, 19\,\mathrm{MHz}. \tag{8.93}$$

We chose $I/I_0 = 0.98473$ to fit two levels in the well. By Eq. (8.93), as well as by the value of B_{20} from Table 8.2 and Eq. (8.92), discrimination of the vacuum state is much faster than that of a multi-photon state.

Now we find the probability to incorrectly determine the number of input photons. Let $P_\mathrm{b}^{0/1}$ denote the probability to correctly identify a single-photon state in the second stage; P_b denotes that in the first stage as before. Probability of error in the two-step discrimination is then

$$\varepsilon^{0/1/2} = P_0 P_\mathrm{f} + P_1[P_\mathrm{f} + (1 - P_\mathrm{f})(1 - P_\mathrm{b}^{0/1})] + P_2(1 - P_\mathrm{b}). \tag{8.94}$$

It was taken into account that the false count probability is negligible for the second stage, as compared to P_f the false count probability in first stage. This is due to the detection time in the second stage being much smaller than that in the first one. We assume that nothing is known about the input and $P_0 = P_1 = P_2 = 1/3$. One can rewrite Eq. (8.94) in a more convenient form:

$$\varepsilon^{0/1/2} = \tfrac{1}{3}[P_\mathrm{f}(1 + P_\mathrm{b}^{0/1}) + 1 - P_\mathrm{b}^{0/1} + 1 - P_\mathrm{b}]. \tag{8.95}$$

To compute $\varepsilon^{0/1/2}$, one needs to estimate $P_{\rm b}^{0/1}$. For the optimal counting time, a photon is most probably absorbed by the JPM. However, this does not necessarily give a click: a photon could get stuck in the ground state due to the JPM relaxation with a probability $\Gamma_{10}/(\Gamma_{10}+\gamma_1)$. Therefore,

$$P_{\rm b}^{0/1} \approx \gamma_1/(\Gamma_{10}+\gamma_1) \approx 98.3\%, \tag{8.96}$$

where the estimate (8.93) was used. The expression (8.96) was also given in Ref. [54]. With the estimate (8.96) and the values from Table 8.3 one obtains

$$\varepsilon^{0/1/2} \approx 1.1\%. \tag{8.97}$$

The optimal time can be chosen to minimize the full counting error (8.95) instead of that in the discrimination of a multi-photon state (8.75). However, this does not improve the full error substantially.

As explained in Sec. 5.5, $P_{\rm b}$ increases for more than two photons in the input; hence $\varepsilon^{0/1/2}$ decreases if one accounts for the higher photon numbers. However, the difference for the photon numbers not much larger than two is not substantial, while the cases with much more photons are unlikely in practice. Therefore, $\varepsilon^{0/1/2}$ is a good approximation to the error in discrimination between the vacuum state, single-photon, and a multiphoton state.

8 Fast pure decoherence

In this section we consider the case when the pure decoherence dominates other rates:

$$\Gamma_{11} \gg t^{-1}, \gamma_0, \gamma_1, \Gamma_{10}, \tag{8.98}$$

$$\Gamma_{22} \gg t^{-1}, \gamma_1, \gamma_2, \Gamma_{10}, \Gamma_{21}, \chi_2 N_{\max}, B_{20}. \tag{8.99}$$

where t is operation time. Historically, we first considered this very case, as we were motivated by Ref. [38]. However, this regime is unpractical for our JPM. The reason for that are JPM coupling rates limited by its nonlinearity according to Eqs. (8.15) and (8.60). With the coupling rates fixed and $\Gamma_{22} \gg \gamma_2$, the two-photon absorption rate B_{20} (8.68) is at least one degree of magnitude smaller for the case of fast pure decoherence. Detection time is then changed accordingly. Moreover, reaching pure decoherence that is faster than the $|2\rangle$ tunneling probably requires sophisticated environment engineering and does not provide any benefits. Below, we give the results for this regime for the sake of completeness.

Analogously to the derivation of Eqs. (8.43) one obtains

$$\begin{aligned}
\dot\rho_{N\,0,N\,0} &= -B_{20}(\rho_{N\,0,N\,0} - \rho_{N-2\,2,N-2\,2}) - \gamma_0\rho_{N\,0,N\,0} + \Gamma_{10}\rho_{N\,1,N\,1}, \quad N \geq 2,\\
\dot\rho_{N-2\,2,N-2\,2} &= B_{20}(\rho_{N\,0,N\,0} - \rho_{N-2\,2,N-2\,2}) - (\gamma_2+\Gamma_{21})\rho_{N-2\,2,N-2\,2}, \quad N \geq 2,\\
\dot\rho_{N\,0,N\,0} &= -\gamma_0\rho_{N\,0,N\,0} + \Gamma_{10}\rho_{N\,1,N\,1}, \quad N = 0, 1,\\
\dot\rho_{N\,1,N\,1} &= -(\gamma_1+\Gamma_{10})\rho_{N\,1,N\,1} + \Gamma_{21}\rho_{N\,2,N\,2}.
\end{aligned} \tag{8.100}$$

8.1 Vacuum and one-photon input

The derivation and the resulting click probabilities are the same as in the Secs. 5.1–5.2.

8.2 Two-photon input

Analogously to the derivation of (8.63)–(8.66) one obtains:

$$\dot{\rho}_{20,20} = -B_{20}(\rho_{20,20} - \rho_{02,02}) - \gamma_0\rho_{20,20}, \tag{8.101}$$
$$\dot{\rho}_{02,02} = B_{20}(\rho_{20,20} - \rho_{02,02}) - (\gamma_2 + \Gamma_{21})\rho_{02,02}, \tag{8.102}$$
$$\dot{\rho}_{01,01} = -(\gamma_1 + \Gamma_{10})\rho_{01,01} + \Gamma_{21}\rho_{02,02}, \tag{8.103}$$
$$\dot{\rho}_{00,00} = -\gamma_0\rho_{00,00} + \Gamma_{10}\rho_{01,01}. \tag{8.104}$$

Equations (8.101) and (8.102) describe the induced emission and absorption caused by a two-photon process, as well as the non-radiative processes. Equations of the same form were obtained in Ref. [38] for a one-photon transition between the ground and the first excited state.

We solve Eqs. (8.101-8.104) by carrying out the Laplace transform. The initial conditions are given by Eqs. (8.62) and (8.52). This allows one to find the Laplace transform of the click probability,

$$\tilde{P}(s) = \frac{\gamma_0 B_{20}\Gamma_{21}\Gamma_{10}}{s(s+\gamma_0)(s+\tilde{\Gamma}_1)\Delta_2} + \frac{\gamma_1 B_{20}\Gamma_{21}}{s(s+\tilde{\Gamma}_1)\Delta_2} + \frac{\gamma_0(B_{20}+\tilde{\Gamma}_2)+\gamma_2 B_{20}}{s\Delta_2} + \frac{\gamma_0}{\Delta_2}, \tag{8.105}$$

where

$$\Delta_2 = s^2 + s(s + 2B_{20} + \tilde{\Gamma}_2 + \gamma_0) + B_{20}(\gamma_0 + \tilde{\Gamma}_2) + \gamma_0\tilde{\Gamma}_2 \tag{8.106}$$
$$\tilde{\Gamma}_1 = \Gamma_{10} + \gamma_1, \quad \tilde{\Gamma}_2 = \Gamma_{21} + \gamma_2, \tag{8.107}$$
$$B_{20} = 8\tilde{g}^2/\Gamma_{22} \tag{8.108}$$

Now we find an expression for the click probability in the time domain. It is found by calculating the inverse Laplace transform,

$$P(t) = \frac{1}{2\pi i}\int_{\sigma-i\infty}^{\sigma+i\infty} ds\, e^{st}\tilde{P}(s). \tag{8.109}$$

This yields, after some algebra,

$$\begin{aligned} P(t) = 1 &- \frac{\Gamma_{21}\Gamma_{10}e^{-\gamma_0 t}}{(\tilde{\Gamma}_1-\gamma_0)(\tilde{\Gamma}_2-\gamma_0)} + \frac{(\gamma_1-\gamma_0)B_{20}\Gamma_{21}e^{-\tilde{\Gamma}_1 t}}{(\tilde{\Gamma}_1+s_+)(\tilde{\Gamma}_1+s_-)(\gamma_0-\tilde{\Gamma}_1)} \\ &+ \frac{1}{s_+-s_-}\Big[e^{s_+t}\Big(\frac{\gamma_0 B_{20}\Gamma_{21}\Gamma_{10}}{s_+(s_++\gamma_0)(s_++\tilde{\Gamma}_1)} + \frac{\gamma_1 B_{20}\Gamma_{21}}{s_+(s_++\tilde{\Gamma}_1)} \\ &\qquad + \frac{B_{20}(\gamma_0+\gamma_2)+\gamma_0\tilde{\Gamma}_2}{s_+} + \gamma_0\Big) \;+\; s_+ \to s_-\Big]. \end{aligned} \tag{8.110}$$

Here $s_+ \to s_-$ denotes the repetition of the previous term with s_+ changed to s_-. Also,

$$s_\pm = \tfrac{1}{2}(-2B_{20} - \tilde{\Gamma}_2 - \gamma_0 \pm \sqrt{4B_{20} + (\Gamma_2 - \gamma_0)^2}), \tag{8.111}$$

and the combined rates of non-radiative processes in the first and the second excited states are denoted by

$$\tilde{\Gamma}_1 = \Gamma_{10} + \gamma_1, \quad \tilde{\Gamma}_2 = \Gamma_{21} + \gamma_2. \tag{8.112}$$

Below we consider some limiting cases of the expression (8.110). But first we describe a convenient technique to approximate $P(t)$.

8.2.1 Approximations in the Laplace domain

It is not always convenient to analyze the limiting cases of $P(t)$ (8.110) directly. Instead, it may be easier to approximate $\tilde{P}(s)$ first. The approximate $P(t)$ is then found by the inverse Laplace transform.

We approximate $\tilde{P}(s)$ by approximating position of its poles. Three rules should be obeyed:

(i) Neglecting ϵ in a pole position makes the approximation valid for $\epsilon t \ll 1$ only.

(ii) An approximated pole can be "merged" with another one.

(iii) An approximated pole should be much further from any other—except for the one it is possibly merged with—as compared to the neglected quantity ϵ.

Also, in the time domain, we would often give prefactors of an exponent with accuracy lower than its argument.

8.2.2 The limit of overwhelming ground-state tunneling

Let us approximate $P(t)$ for $\gamma_0 \gg B_{20}, \Gamma_{21}$. In that case, poles $s_\pm$ (8.111) are approximately $-\gamma_0$ and $-\gamma_2$. We have neglected a quantity of order $O(B_{20}) + O(\Gamma_{21})$ in the poles. Using the rules from the previous subsection,

$$\tilde{P}(s) \approx \frac{\gamma_0 B_{20}\Gamma_{21}\Gamma_{10}}{s(s+\gamma_0)^2(s+\tilde{\Gamma}_1)(s+\gamma_2)} + \frac{\gamma_1 B_{20}\Gamma_{21}}{s(s+\tilde{\Gamma}_1)(s+\gamma_0)(s+\gamma_2)} + \frac{\gamma_0\gamma_2}{s(s+\gamma_0)(s+\gamma_2)} + \frac{\gamma_0}{(s+\gamma_0)(s+\gamma_2)} \quad (8.113)$$

for

$$B_{20}, \Gamma_{21} \ll t^{-1}, \gamma_0, |\gamma_2 - \gamma_0|, |\tilde{\Gamma}_1 - \gamma_{0,2}|. \quad (8.114)$$

Inverse Laplace transform gives

$$P(t) = 1 - e^{-\gamma_0 t}. \quad (8.115)$$

The expression holds when the conditions (8.114) and (8.60) are satisfied.

Equation (8.115) is not hard to interpret. Ground state tunneling is much faster than the excitation to the second excited state. Hence, only the ground state tunneling can fire the JPM. That is the same situation as in the case of vacuum and one-photon cavity. In this regime, the JPM cannot distinguish the two-photon state.

8.2.3 The limit of fast two-photon absorption and emission

Here we find $P(t)$ for the case, when the two-photon processes are faster than any other process captured by Eq. (8.110). As before, we first approximate $s_\pm$ (8.111). Consider $(\tilde{\Gamma}_2 - \gamma_0)/(2B_{20})$ is small. One can expand the square root in $s_\pm$ in this quantity, which yields

$$s_+ = -\frac{1}{2}(\tilde{\Gamma}_2 + \gamma_0) + O\left(\frac{\tilde{\Gamma}_2 - \gamma_0}{2B_{20}}\right)^2 \frac{B_{20}}{2}. \quad (8.116)$$

We approximate the other pole as

$$s_- = -2B_{20} + O(\tilde{\Gamma}_2/2) + O(\gamma_0/2). \quad (8.117)$$

Now one can approximate $\tilde{P}(s)$,

$$\tilde{P}(s) \approx \frac{\gamma_0 B_{20}\Gamma_{21}\Gamma_{10}}{s^3(s+2B_{20})(s-s_+)} + \frac{\gamma_1 B_{20}\Gamma_{21}}{s^2(s+2B_{20})(s-s_+)} + \frac{(\gamma_0+\gamma_2)B_{20}}{s(s+2B_{20})(s-s_+)} + \frac{\gamma_0}{(s+2B_{20})(s-s_+)}. \quad (8.118)$$

According to the rules from Sec. 8.2.1, the expression is valid for

$$2B_{20} \gg \gamma_2, \Gamma_{21}, \quad \tilde{\Gamma}_1, \gamma_0 \ll 2B_{20}, \tilde{\Gamma}_2/2, \quad (8.119)$$

$$t \ll \Gamma_1^{-1}, \gamma_0^{-1}, 8B_{20}/\tilde{\Gamma}_2^2. \quad (8.120)$$

Inverse Laplace transform of $\tilde{P}(s)$ yields

$$P(t) = \frac{\gamma_2}{\Gamma_{21}+\gamma_2}(1 - e^{-(\Gamma_{21}+\gamma_2)t/2}). \quad (8.121)$$

The limit of applicability of this expression is set by conditions (8.119), (8.120) and (8.60).

It is possible to interpret Eq. (8.121). First, we explain why $\exp[-(\Gamma_{21}+\gamma_2)t/2]$ gives the total population of the ground state $|0\rangle$ and the second excited state $|2\rangle$. Two-photon absorption and emission are much faster than any other process. They redistribute the population of $|0\rangle$ and $|2\rangle$ equally. Hence, at the initial instant of time $t = 0$ those populations should be considered $1/2$. In a small period of time Δt, the population of $|2\rangle$ decays by $(\gamma_2 + \Gamma_{21})\rho_{02,02}\Delta t$. This gets immediately redistributed with $|0\rangle$. In the end, $|2\rangle$ looses $\frac{1}{2}(\gamma_2 + \Gamma_{21})\Delta t\rho_{02,02}$ of its population, and so does $|0\rangle$. It follows that, at time t, there are $\frac{1}{2}\exp[(\gamma_2 + \Gamma_{21})t/2]$ excitations at each of $|0\rangle$ and $|2\rangle$. On the other hand, $1 - \exp[(\gamma_2 + \Gamma_{21})t/2]$ excitations were lost due to incoherent processes. Of those, γ_2 of $\gamma_2 + \Gamma_2$ has tunneled and provided a click.

9 Discussion and outlook

We have proposed a detector of microwave photons with limited photon number resolution. We were able to provide a simple analytical theory of the detector using that its decoherence is fast compared to other processes due to the fast tunneling. Note that the case of fast *pure* decoherence is unpractical, as in this case the two-photon absorption is much slower. Realistic parameters have been provided that allow distinguishing between the vacuum, single-photon, and a multi-photon state in 4.2 μs with 1.1% error probability. The most time-consuming part in the device operation is the discrimination of a multi-photon state vs. the single-photon or vacuum one. The speed of this step is limited by the two-photon absorption rate, which in turn is set by the coupling strength of the JPM to the cavity. To avoid single-photon transitions, the coupling should be much weaker than the JPM anharmonicity. A larger anharmonicity can lead to faster detection. Moreover, faster detection decreases the false count probability P_f. The probability to count photons incorrectly is determined by P_f and the probabilities to miss a multi- and the single-photon state. As for the probabilities to miss photons, they are determined by branching ratios between the excited state tunneling and relaxation.

For the proposed parameters, the 8.2 GHz photons are detected. The frequency can be chosen at the design stage in the range from 1 GHz to 20 GHz. The upper limit on the frequency is set by the superconducting gap of aluminum, which

is about 82 GHz, and the condition (8.78). As for the lower limit, it is determined by the requirement (8.91) for the intermediate level being narrow enough to exclude single-photon transitions, the relationship (8.86) between the plasma frequency and the anharmonicity, and an estimate for the decoherence of the JPM first excited state, which is about 1 MHz.

Let us consider some avenues for development of the detector. One possibility is to modify it for the detection of itinerant photons. It seems that the most straightforward option is to attach a waveguide directly. This introduces reflection losses; to minimize them, the detector should be matched to its input [113]. What is more important, a detector can analyze only a part $\eta\tau$ of a pulse of duration τ for photon pairs and the remaining part for single photons. In the second stage lasting $(1-\eta)\tau$, the probability of a photon click diminishes as $P_{\rm b}^{0/1} \to (1-\eta)P_{\rm b}^{0/1}$ compared to the case when the whole pulse is available. In the first stage that lasts $\eta\tau$, the probability of a JPM detecting a pair of photons diminishes as $P_{\rm b} \to \eta^2 P_{\rm b}$. The resulting error in counting to two is $\varepsilon^{0/1/2} \leq (1+\eta-\eta^2)/3 \leq 5/12$, where, to obtain the first inequality, we have considered the case of no false counts, $P_{\rm f} = 0$. Besides, the incoming pulse should be no shorter than about 4 μs for the JPM to detect a pair of photons reliably. Note that using two detectors—first one in the two-photon mode and the next one in the one-photon mode—is ruled out for the JPM described. Indeed, in that case the incoming pulse first needs to interact with the two-photon detector solely. Interaction with the one-photon detector can result in a absorption of a photon, which spoils the results of the two-photon detector. Hence one needs a delay line between those; however, as the incoming pulse duration is no shorter than 4 μs, the delay line length should be about 1 km to isolate the detectors. More viable option is to attach the resonator to a waveguide; it will function as a capture cavity from Ref. [2, 41]. Instead of resonator, one can also store the incoming photons in a low-loss loop, so that a short pulse constantly returns back to the detector if its photons are not detected.

As another possibility, one can envision is a JPM that counts photons up to N. This device might use an N-photon transition through $N-2$ auxiliary levels at the first stage to discriminate the states with N or more photons. Afterward, it can be sequentially tuned to discriminate the states with $N-1$, $N-2$, and down to 1 photon. However, as the interaction strength for the JPM transition from $|n\rangle$ to $|n-1\rangle$ is approximately $g_n = \sqrt{N}g_1$, the effective N-photon transition strength is $\tilde{g}^{(N)} = g_1 \ldots g_N/\Delta^{N-1} = g_1^N\sqrt{N!}/\Delta^{N-1}$. This decays rapidly with N, which makes the idea unpractical. However, it still might work if one can engineer stronger N-photon coupling. The use of non-linear coupling that includes a Josephson junction looks promising for that. A stronger coupling also improves the detection speed. Another possibility to detect faster is to use a coherent Rabi oscillation between the cavity and the JPM [2, 135]. To capture photons, the JPM can be operated in a deep-well regime where tunneling is negligible for the first three of its states; after that, one can tilt the JPM potential for the tunneling to occur from $|2\rangle$. As compared to incoherent absorption [see Eq. (8.44)], this process is not compromised by the JPM decoherence. The excitation fully transfers to the JPM in Rabi half-period $\pi/2\tilde{g}N(N-1)$. However, this time depends on the number N of resonator photons, which severely restricts the detection efficiency of an arbitrary multiphoton state. On the other hand, that might be another way to reach photon number resolution.

Appendices

A Derivation of the circuit Hamiltonian

Lagrangian of the system in Fig. 8.2 is given by

$$\mathcal{L} = \mathcal{L}_{\mathrm{JPM}} + \mathcal{L}_{\mathrm{r}} + \mathcal{L}_{\mathrm{c}}, \tag{8.A.122}$$

$$\mathcal{L}_{\mathrm{JPM}} = \frac{C\dot{\Phi}^2}{2} + E_{\mathrm{J}} \cos 2\pi \frac{\Phi}{\Phi_0} + I\Phi, \tag{8.A.123}$$

$$\mathcal{L}_{\mathrm{c}} = \frac{C'(\dot{\Phi} - \dot{\Phi}_{\mathrm{r}})^2}{2}, \tag{8.A.124}$$

$$\mathcal{L}_{\mathrm{r}} = \frac{C_{\mathrm{r}}\dot{\Phi}_{\mathrm{r}}^2}{2} - \frac{\Phi_{\mathrm{r}}^2}{2L_{\mathrm{r}}}. \tag{8.A.125}$$

Here E_{J} is defined by Eq. (8.79).

Generalized momenta are

$$Q = \partial \mathcal{L} / \partial \dot{\Phi} = (C + C')\dot{\Phi} - C'\dot{\Phi}_{\mathrm{r}}, \tag{8.A.126}$$

$$Q_{\mathrm{r}} = \partial \mathcal{L} / \partial \dot{\Phi}_{\mathrm{r}} = -C'\dot{\Phi} + (C_{\mathrm{r}} + C')\dot{\Phi}_{\mathrm{r}}. \tag{8.A.127}$$

The system Hamiltonian is given by the Legendre transform,

$$H = Q\dot{\Phi} + Q_{\mathrm{r}}\dot{\Phi}_{\mathrm{r}} - \mathcal{L}\,. \tag{8.A.128}$$

One needs to find the kinetic energy part T of H. It is a quadratic form in Q and Q_{r},

$$T = \frac{1}{2}\frac{\partial^2 H}{\partial Q^2}Q^2 + \frac{1}{2}\frac{\partial^2 H}{\partial Q_{\mathrm{r}}^2}Q_{\mathrm{r}}^2 + \frac{\partial^2 H}{\partial Q \partial Q_{\mathrm{r}}}QQ_{\mathrm{r}} + \left.\frac{\partial H}{\partial Q}\right|_{Q,Q_{\mathrm{r}}=0} Q + \left.\frac{\partial H}{\partial Q_{\mathrm{r}}}\right|_{Q,Q_{\mathrm{r}}=0} Q_{\mathrm{r}}. \tag{8.A.129}$$

It was used that potential energy, which composes the rest of H, does not depend on the momenta. Differentiating Eq. (8.A.128) and using the expressions for generalized momenta (8.A.126)–(8.A.127) gives rise to

$$\partial^2 H / \partial Q^2 = \partial \dot{\Phi} / \partial Q \tag{8.A.130}$$

and $\partial H/\partial Q|_{Q,Q_{\mathrm{r}}=0} = 0$. Other coefficients are given by the similar formulas. One then determines the renormalized capacitances

$$\tilde{C} = \frac{C + C'(1 + C/C_{\mathrm{r}})}{1 + C'/C_{\mathrm{r}}}, \quad \tilde{C}_{\mathrm{r}} = \frac{C_{\mathrm{r}} + C'(1 + C_{\mathrm{r}}/C)}{1 + C'/C}, \tag{8.A.131}$$

$$\tilde{C}' = (1/C' + 1/C + 1/C_{\mathrm{r}})^{-1} \tag{8.A.132}$$

in the Hamiltonian (8.1)–(8.4).

B Dressed Lindblad equation

Here we write out the explicit form of the first-order corrections in the Lindbladian in our working frame.

On applying the transform U (8.10), the Lindbladian (8.7) becomes

$$\hat{L} \to \hat{L} + \hat{L}^{(1)}, \tag{8.B.1}$$

where $\hat{L}^{(1)}$ is first-order in λ_1 and λ_2. It can be given in terms of its matrix elements:

$$\begin{aligned}
\langle 0|\,\hat{L}^{(1)}\rho\,|0\rangle =& -\lambda_2\,\Gamma_{10}\,a^\dagger\,\langle 2|\,\rho\,|1\rangle + \frac{1}{2}\,\lambda_1\,\left(\Gamma_{10}+\Gamma_{11}-\gamma_0+\gamma_1\right)\,a^\dagger\,\langle 1|\,\rho\,|0\rangle \\
&-\lambda_1\,\Gamma_{10}\,a\,\langle 0|\,\rho\,|1\rangle + \text{c. c.}, && \text{(8.B.2)}\\
\langle 1|\,\hat{L}^{(1)}\rho\,|1\rangle =& -\frac{1}{2}\,\lambda_2\,\left(-\Gamma_{10}+\Gamma_{11}+\Gamma_{21}+\Gamma_{22}-\gamma_1+\gamma_2\right)\,a^\dagger\,\langle 2|\,\rho\,|1\rangle \\
&+\lambda_2\,\Gamma_{21}\,a\,\langle 1|\,\rho\,|2\rangle + \frac{1}{2}\,\lambda_1\,\left(\Gamma_{10}-\Gamma_{11}-\gamma_0+\gamma_1\right)\,a\,\langle 0|\,\rho\,|1\rangle + \text{c. c.}, && \text{(8.B.3)}\\
\langle 2|\,\hat{L}^{(1)}\rho\,|2\rangle =& -\frac{1}{2}\,\lambda_2\,\left(-\Gamma_{10}-\Gamma_{11}+\Gamma_{21}-\Gamma_{22}-\gamma_1+\gamma_2\right)\,a\,\langle 1|\,\rho\,|2\rangle + \text{c. c.}, && \text{(8.B.4)}\\
\langle \mathrm{m}|\,\hat{L}^{(1)}\rho\,|\mathrm{m}\rangle =& -\lambda_2\,\gamma_1\,a^\dagger\,\langle 2|\,\rho\,|1\rangle + \lambda_1\,\gamma_0\,a^\dagger\,\langle 1|\,\rho\,|0\rangle \\
&+\lambda_2\,\gamma_2\,a\,\langle 1|\,\rho\,|2\rangle - \lambda_1\,\gamma_1\,a\,\langle 0|\,\rho\,|1\rangle + \text{c. c.}, && \text{(8.B.5)}\\
\langle 0|\,\hat{L}^{(1)}\rho\,|1\rangle =& -\lambda_1\,\Gamma_{21}\,a^\dagger\,\langle 2|\,\rho\,|2\rangle + \frac{1}{2}\,\lambda_1\,\left(\Gamma_{10}-\Gamma_{11}-\gamma_0+\gamma_1\right)\,a^\dagger\,\langle 1|\,\rho\,|1\rangle \\
&+\lambda_1\,\Gamma_{10}\,\langle 1|\,\rho a^\dagger\,|1\rangle + \frac{1}{2}\,\lambda_1\,\left(\Gamma_{10}+\Gamma_{11}-\gamma_0+\gamma_1\right)\,\langle 0|\,\rho a^\dagger\,|0\rangle \\
&-\frac{1}{2}\,\lambda_2\,\left(-\Gamma_{10}-\Gamma_{11}+\Gamma_{21}+\Gamma_{22}-\gamma_1+\gamma_2\right)\,\langle 0|\,\rho a\,|2\rangle\,, && \text{(8.B.6)}\\
\langle 1|\,\hat{L}^{(1)}\rho\,|2\rangle =& -\frac{1}{2}\,\lambda_2\,\left(-\Gamma_{10}-\Gamma_{11}+\Gamma_{21}-\Gamma_{22}-\gamma_1+\gamma_2\right)\,a^\dagger\,\langle 2|\,\rho\,|2\rangle \\
&+\frac{1}{2}\,\lambda_1\,\left(\Gamma_{10}+\Gamma_{11}-\gamma_0+\gamma_1\right)\,a\,\langle 0|\,\rho\,|2\rangle - \lambda_2\,\Gamma_{21}\,\langle 2|\,\rho a^\dagger\,|2\rangle \\
&-\frac{1}{2}\,\lambda_2\,\left(-\Gamma_{10}+\Gamma_{11}+\Gamma_{21}+\Gamma_{22}-\gamma_1+\gamma_2\right)\,\langle 1|\,\rho a^\dagger\,|1\rangle\,, && \text{(8.B.7)}\\
\langle 0|\,\hat{L}^{(1)}\rho\,|2\rangle =& -\frac{1}{2}\,\lambda_2\,\left(-\Gamma_{10}-\Gamma_{11}+\Gamma_{21}+\Gamma_{22}-\gamma_1+\gamma_2\right)\,\langle 0|\,\rho a^\dagger\,|1\rangle \\
&+\frac{1}{2}\,\lambda_1\,\left(\Gamma_{10}+\Gamma_{11}-\gamma_0+\gamma_1\right)\,a^\dagger\,\langle 1|\,\rho\,|2\rangle\,, && \text{(8.B.8)}\\
\langle \mathrm{m}|\,\hat{L}^{(1)}\rho\,|0\rangle =& \frac{1}{2}\,\lambda_1\,\left(\Gamma_{10}+\Gamma_{11}-\gamma_0+\gamma_1\right)\,\langle \mathrm{m}|\,\rho a\,|1\rangle\,, && \text{(8.B.9)}\\
\langle \mathrm{m}|\,\hat{L}^{(1)}\rho\,|1\rangle =& -\frac{1}{2}\,\lambda_2\,\left(-\Gamma_{10}-\Gamma_{11}+\Gamma_{21}+\Gamma_{22}-\gamma_1+\gamma_2\right)\,\langle \mathrm{m}|\,\rho a\,|2\rangle \\
&+\frac{1}{2}\,\lambda_1\,\left(\Gamma_{10}+\Gamma_{11}-\gamma_0+\gamma_1\right)\,\langle \mathrm{m}|\,\rho a^\dagger\,|0\rangle\,, && \text{(8.B.10)}\\
\langle \mathrm{m}|\,\hat{L}^{(1)}\rho\,|2\rangle =& -\frac{1}{2}\,\lambda_2\,\left(\gamma_2-\gamma_1+\Gamma_{22}+\Gamma_{21}-\Gamma_{11}-\Gamma_{10}\right)\,\langle \mathrm{m}|\,\rho a^\dagger\,|1\rangle\,. && \text{(8.B.11)}
\end{aligned}$$

For the calculation of the matrix elements, a custom simplifier was programmed for the Maxima computer algebra system. The simplifier allows for a limited set of manipulations with the JPM bras and kets, and the resonator creation and annihilation operators. The respective codes are available as a part of GitLab repository [148].

C The Ping-Li-Gurvitz tunneling master equation

In this appendix, we derive a master equation for tunneling in which each level tunnels to the same set of states. In this case, tunneling can excite the system to a higher metastable state for a short time. We generalize the Ping-Li-Gurvitz [141] derivation of the master equation to arbitrary number of the metastable states. Besides, we make an assumption that the derivation and the resulting equation is applicable to

the tunneling of states from the same potential well [54]. Finally, we claim that this theory is only applicable to closely separated metastable states.

C.1 Hamiltonian

Tunneling from the metastable states $|i\rangle$ to the continuum states $|c\rangle$ is described by the Hamiltonian

$$H = \sum_i \hbar\Omega_i |i\rangle\langle i| + \sum_c \hbar\omega_c |c\rangle\langle c| + \sum_{c,i} (\hbar f_{ic} |c\rangle\langle i| + \text{h. c.}) \tag{8.C.1}$$

It is useful to compare the Hamiltonian (8.C.1) with the Hamiltonian describing relaxation to a reservoir. The Hamiltonian of a subsystem with levels $|i\rangle$ that is in contact with a thermal bath with N modes is

$$H_\text{r} = \sum_i \hbar\Omega_i |i,0\rangle\langle i,0| + \sum_{i,j} \hbar\omega_{ij} |i,0_1,\dots 1_j,\dots 0_N\rangle\langle i,0_1,\dots 1_j,\dots 0_N| + \sum_{\substack{i=1,\dots \\ j}} (\hbar f_{ij} |i-1,0_1,\dots 1_j,\dots 0_N\rangle\langle i,0| + \text{h. c.}) \tag{8.C.2}$$

Before the relaxation the bath is in the vacuum state and the state of the full system is $|i,0\rangle$. On relaxation, the subsystem falls down from the level $|i\rangle$ to the level $|i-1\rangle$ while a mode j acquires a photon, resulting in the state $|0_1,\dots 1_j,\dots 0_N\rangle$ of the bath. The resulting state of the full system is different for each level $|i\rangle$. In this respect the relaxation Hamiltonian (8.C.2) differs from the Ping-Li-Gurvitz tunneling Hamiltonian (8.C.1). However, if each metastable state tunnels to a separate set of the states across the barrier, the tunneling is described by mostly the same Hamiltonian. The only difference is that the ground state can tunnel but cannot relax, and the respective term is absent in the relaxation Hamiltonian.

C.2 The master equation

The system state

$$|\Psi\rangle = \sum_i \alpha_i |i\rangle + \sum_c \beta_c |c\rangle \tag{8.C.3}$$

is governed by the Schrödinger equation

$$ih|\dot{\Psi}\rangle = H|\Psi\rangle. \tag{8.C.4}$$

Using the Hamiltonian (8.C.1) and the form of the system state (8.C.3) one obtains the equations

$$\dot{\alpha}_i = -i\Omega_i\alpha_i - i\sum_c f_{ic}\beta_c \tag{8.C.5}$$

$$\dot{\beta}_c = -i\omega_c\beta_c - i\sum_i f_{ic}\alpha_i \tag{8.C.6}$$

Formal solution of for β_c is

$$\beta_c(t) = \beta_c(0)e^{-i\omega_c t} - i\int_0^t dt' e^{-i\omega_c(t-t')} \sum_i f_{ic}\alpha_i(t'). \tag{8.C.7}$$

We assume that the states $|c\rangle$ are very dense with the density of states $\rho(\omega_c)$ and

$$\sum_c f_{ic}\beta_c(t) \approx \sum_c f_{ic}\beta_c(0)e^{-i\omega_c t} - i\int_0^t dt' \int_{-\infty}^{+\infty} d\omega_c f_{ic}\rho(\omega_c)e^{-i\omega_c(t-t')}\sum_j f_{jc}\alpha_j(t'). \tag{8.C.8}$$

As $\alpha_i \propto e^{-i\Omega_i t-\gamma_i t}$, the integration by time yields a function that cuts a narrow region in ω_c. Only this region gives a substantial contribution to the integral by ω_c [see the derivation of Eq. (1.60)]. We assume that in this narrow region $\rho(\omega_c) \approx \rho$, $f_{ic} \approx f_i$. Then, with $\int_{-\infty}^{+\infty} d\omega_c e^{-i\omega_c(t-t')} = 2\pi\delta(t-t')$, one has

$$\sum_c f_{ic}\beta_c(t) \approx -i\pi\rho\sum_j f_i f_j \alpha_j(t), \tag{8.C.9}$$

where it was taken into account that the states $|c\rangle$ are unoccupied initially,

$$\beta_c(0) = 0. \tag{8.C.10}$$

Substituting Eq. (8.C.9) into Eq. (8.C.5) gives rise to

$$\dot{\alpha}_i = -i\Omega_i\alpha_i - \sum_j \eta_{ij}\frac{\sqrt{\gamma_i\gamma_j}}{2}\alpha_j, \tag{8.C.11}$$

where $\gamma_i = 2\pi\rho f_i^2$ and $\eta_{ij} = f_i f_j/|f_i f_j|$. According to Ref. [141], when the wavefunctions of $|i\rangle$ and $|j\rangle$ have the same pairness, $\eta_{ij} = 1$, otherwise $\eta_{ij} = -1$. However, all $\eta_{ij} = 1$ in Ref. [54].

One now can write out the master equation

$$\dot{\rho}_{ij} = i(\Omega_j - \Omega_i)\rho_{ij} - \sum_k(\eta_{ik}\frac{\sqrt{\gamma_i\gamma_j}}{2}\rho_{kj} + \eta_{jk}\frac{\sqrt{\gamma_j\gamma_k}}{2}\rho_{ik}) \tag{8.C.12}$$

on the density matrix $\rho_{ij} = \alpha_i\alpha_j^*$.

It is instructive to consider the case with two metastable states in the well and $\gamma_1 = \gamma_2 = \gamma$. For the initial conditions $\rho_{00} = 1$, $\rho_{11} = 0$, and $\rho_{01} = \rho_{10} = 0$, the solution of Eqs. (8.C.12) reads:

$$\rho_{00} = \frac{\gamma^2\cosh^2\frac{t}{2}\sqrt{\gamma^2-\epsilon^2} - \epsilon^2}{\gamma^2-\epsilon^2}e^{-\gamma t}, \tag{8.C.13}$$

$$\rho_{11} = \frac{\gamma^2\sinh^2\frac{t}{2}\sqrt{\gamma^2-\epsilon^2}}{\gamma^2-\epsilon^2}e^{-\gamma t}, \tag{8.C.14}$$

$$\rho_{01} = \rho_{10}^* = -\frac{i\epsilon(1-\cosh t\sqrt{\gamma^2-\epsilon^2}) + \sqrt{\gamma^2-\epsilon^2}\sinh t\sqrt{\gamma^2-\epsilon^2}}{2(\gamma^2-\epsilon^2)}\gamma e^{-\gamma t}, \tag{8.C.15}$$

where $\epsilon = \Omega_1 - \Omega_0$. The same equations are given in Ref. [141] for the case of small level separation $\gamma > \epsilon$. In the form (8.C.13)–(8.C.15) we present the equations, they are also applicable for the case of $\epsilon > \gamma$ if one uses the rule that $\sqrt{-\beta} = i\sqrt{\beta}$ for $\beta > 0$. In that case the oscillatory behavior appears.

A striking feature of this system is that $|1\rangle$ can be excited due to the tunneling. Coherence arises between $|0\rangle$ and $|1\rangle$ as, during the leakage to the continuum, both states interact with the leaked part of the quantum. This coherence results in the possibility of $|1\rangle$ to be excited. However, according to Eq. (8.C.14) the excitation lasts only for time $1/\gamma$. Due to the Heisenberg inequality, $\hbar(\Omega_1 - \Omega_0)/\gamma \lesssim h$. It

follows that

$$\Omega_1 - \Omega_0 \lesssim \gamma/2\pi. \tag{8.C.16}$$

Therefore, the theory is applicable to closely separated levels only. A possible explanation is that with a wider separation each level tunnels to a separate continuum of levels. Note that in the $\Omega_1 - \Omega_0 \gg \gamma$ case this feature does not appear in the population (8.C.14). That is what one should expect. In that case one can throw out the rapidly oscillating terms in the master equation (8.C.12) that link the coherence and the populations. Then it reproduces the Lindblad master equation for tunneling. The latter can be obtained from Eq. (8.7).

D The JPM with the Ping-Li-Gurvitz tunneling

Here we determine the first-order correction $\hat{L}^{(1)}$ to the dissipative part of the JPM master equation superoperator for the Ping-Li-Gurvitz tunneling model. It is argued that, in the RWA, the model is equivalent to the Lindblad tunneling.

The superoperator is defined similarly to the case of Lindblad tunneling as in Eq. (8.B.1), but for the case of the tunneling described by Eqs. (8.C.12). The bare part of the superoperator can be figured out from these equations. We then determine its dressed correction $\hat{L}^{(1)}$. Its matrix elements read:

$$\begin{aligned}
\langle 0|\,\hat{L}^{(1)}\rho\,|0\rangle =& -\lambda_2\,\Gamma_{10}\,a^\dagger\,\langle 2|\,\rho\,|1\rangle - \frac{1}{2}\,(\lambda_1\sqrt{\gamma_1\,\gamma_2} + \lambda_2\sqrt{\gamma_0\,\gamma_1})\;a^\dagger\,\langle 2|\,\rho\,|0\rangle \\
&+ \frac{1}{2}\,\lambda_1\,(\gamma_1 - \gamma_0 + \Gamma_{11} + \Gamma_{10})\;a^\dagger\,\langle 1|\,\rho\,|0\rangle - \frac{1}{2}\,\lambda_1\sqrt{\gamma_0\,\gamma_1}\,a^\dagger\,\langle 0|\,\rho\,|0\rangle \\
&- \frac{1}{2}\,\lambda_2\sqrt{\gamma_0\,\gamma_2}\,a\,\langle 1|\,\rho\,|0\rangle - \lambda_1\,\Gamma_{10}\,a\,\langle 0|\,\rho\,|1\rangle - \frac{1}{2}\,\lambda_1\sqrt{\gamma_0\,\gamma_1}\,a\,\langle 0|\,\rho\,|0\rangle \\
&+ \text{c. c.},
\end{aligned} \tag{8.D.1}$$

$$\begin{aligned}
\langle 1|\,\hat{L}^{(1)}\rho\,|1\rangle =& -\frac{1}{2}\,\lambda_2\,(\gamma_2 - \gamma_1 + \Gamma_{22} + \Gamma_{21} + \Gamma_{11} - \Gamma_{10})\;a^\dagger\,\langle 2|\,\rho\,|1\rangle \\
&+ \frac{1}{2}\,(\lambda_2\sqrt{\gamma_1\,\gamma_2} + \lambda_1\sqrt{\gamma_0\,\gamma_1})\;a^\dagger\,\langle 1|\,\rho\,|1\rangle - \frac{1}{2}\,\lambda_2\sqrt{\gamma_0\,\gamma_2}\,a^\dagger\,\langle 0|\,\rho\,|1\rangle \\
&- \frac{1}{2}\,\lambda_1\sqrt{\gamma_0\,\gamma_2}\,a\,\langle 2|\,\rho\,|1\rangle + \lambda_2\,\Gamma_{21}\,a\,\langle 1|\,\rho\,|2\rangle \\
&+ \frac{1}{2}\,(\lambda_2\sqrt{\gamma_1\,\gamma_2} + \lambda_1\sqrt{\gamma_0\,\gamma_1})\;a\,\langle 1|\,\rho\,|1\rangle \\
&+ \frac{1}{2}\,\lambda_1\,(\gamma_1 - \gamma_0 - \Gamma_{11} + \Gamma_{10})\;a\,\langle 0|\,\rho\,|1\rangle + \text{c. c.},
\end{aligned} \tag{8.D.2}$$

$$\begin{aligned}
\langle 2|\,\hat{L}^{(1)}\rho\,|2\rangle =& -\frac{1}{2}\,\lambda_2\sqrt{\gamma_1\,\gamma_2}\,a^\dagger\,\langle 2|\,\rho\,|2\rangle - \frac{1}{2}\,\lambda_1\sqrt{\gamma_0\,\gamma_2}\,a^\dagger\,\langle 1|\,\rho\,|2\rangle - \frac{1}{2}\,\lambda_2\sqrt{\gamma_1\,\gamma_2}\,a\,\langle 2|\,\rho\,|2\rangle \\
&- \frac{1}{2}\,\lambda_2\,(\gamma_2 - \gamma_1 - \Gamma_{22} + \Gamma_{21} - \Gamma_{11} - \Gamma_{10})\;a\,\langle 1|\,\rho\,|2\rangle \\
&+ \frac{1}{2}\,(-\lambda_1\sqrt{\gamma_1\,\gamma_2} - \lambda_2\sqrt{\gamma_0\,\gamma_1})\;a\,\langle 0|\,\rho\,|2\rangle + \text{c. c.},
\end{aligned} \tag{8.D.3}$$

$$\begin{aligned}
\langle 0|\,\hat{L}^{(1)}\rho\,|1\rangle =& -\lambda_1\,\Gamma_{21}\,a^\dagger\,\langle 2|\,\rho\,|2\rangle - \frac{1}{2}\,(\lambda_1\sqrt{\gamma_1\,\gamma_2} + \lambda_2\sqrt{\gamma_0\,\gamma_1})\;a^\dagger\,\langle 2|\,\rho\,|1\rangle \\
&+ \frac{1}{2}\,\lambda_1\,(\gamma_1 - \gamma_0 - \Gamma_{11} + \Gamma_{10})\;a^\dagger\,\langle 1|\,\rho\,|1\rangle - \frac{1}{2}\,\lambda_1\sqrt{\gamma_0\,\gamma_1}\,a^\dagger\,\langle 0|\,\rho\,|1\rangle \\
&- \frac{1}{2}\,\lambda_2\sqrt{\gamma_0\,\gamma_2}\,a\,\langle 1|\,\rho\,|1\rangle - \frac{1}{2}\,\lambda_1\sqrt{\gamma_0\,\gamma_1}\,a\,\langle 0|\,\rho\,|1\rangle + \lambda_1\,\Gamma_{10}\;\langle 1|\,\rho a^\dagger\,|1\rangle \\
&- \frac{1}{2}\,\lambda_1\sqrt{\gamma_0\,\gamma_2}\;\langle 0|\,\rho a^\dagger\,|2\rangle + \frac{1}{2}\,(\lambda_2\sqrt{\gamma_1\,\gamma_2} + \lambda_1\sqrt{\gamma_0\,\gamma_1})\;\langle 0|\,\rho a^\dagger\,|1\rangle
\end{aligned}$$

$$
\begin{aligned}
&+\frac{1}{2}\,\lambda_1\,(\gamma_1-\gamma_0+\Gamma_{11}+\Gamma_{10})\,\langle 0|\,\rho a^\dagger\,|0\rangle\\
&-\frac{1}{2}\,\lambda_2\,(\gamma_2-\gamma_1+\Gamma_{22}+\Gamma_{21}-\Gamma_{11}-\Gamma_{10})\,\langle 0|\,\rho a\,|2\rangle\\
&+\frac{1}{2}\,(\lambda_2\sqrt{\gamma_1\,\gamma_2}+\lambda_1\sqrt{\gamma_0\,\gamma_1})\,\langle 0|\,\rho a\,|1\rangle-\frac{1}{2}\,\lambda_2\sqrt{\gamma_0\,\gamma_2}\,\langle 0|\,\rho a\,|0\rangle\,,
\end{aligned}
\tag{8.D.4}
$$

$$
\begin{aligned}
\langle 1|\,\hat{L}^{(1)}\rho\,|2\rangle =&-\frac{1}{2}\,\lambda_2\,(\gamma_2-\gamma_1-\Gamma_{22}+\Gamma_{21}-\Gamma_{11}-\Gamma_{10})\,a^\dagger\,\langle 2|\,\rho\,|2\rangle\\
&+\frac{1}{2}\,(\lambda_2\sqrt{\gamma_1\,\gamma_2}+\lambda_1\sqrt{\gamma_0\,\gamma_1})\,a^\dagger\,\langle 1|\,\rho\,|2\rangle-\frac{1}{2}\,\lambda_2\sqrt{\gamma_0\,\gamma_2}\,a^\dagger\,\langle 0|\,\rho\,|2\rangle\\
&-\frac{1}{2}\,\lambda_1\sqrt{\gamma_0\,\gamma_2}\,a\,\langle 2|\,\rho\,|2\rangle+\frac{1}{2}\,(\lambda_2\sqrt{\gamma_1\,\gamma_2}+\lambda_1\sqrt{\gamma_0\,\gamma_1})\,a\,\langle 1|\,\rho\,|2\rangle\\
&+\frac{1}{2}\,\lambda_1\,(\gamma_1-\gamma_0+\Gamma_{11}+\Gamma_{10})\,a\,\langle 0|\,\rho\,|2\rangle-\lambda_2\,\Gamma_{21}\,\langle 2|\,\rho a^\dagger\,|2\rangle\\
&-\frac{1}{2}\,\lambda_2\sqrt{\gamma_1\,\gamma_2}\,\langle 1|\,\rho a^\dagger\,|2\rangle-\frac{1}{2}\,\lambda_1\sqrt{\gamma_0\,\gamma_2}\,\langle 1|\,\rho a\,|1\rangle\\
&-\frac{1}{2}\,\lambda_2\,(\gamma_2-\gamma_1+\Gamma_{22}+\Gamma_{21}+\Gamma_{11}-\Gamma_{10})\,\langle 1|\,\rho a^\dagger\,|1\rangle\\
&-\frac{1}{2}\,(\lambda_1\sqrt{\gamma_1\,\gamma_2}+\lambda_2\sqrt{\gamma_0\,\gamma_1})\,\langle 1|\,\rho a^\dagger\,|0\rangle-\frac{1}{2}\,\lambda_2\sqrt{\gamma_1\,\gamma_2}\,\langle 1|\,\rho a\,|2\rangle\,,
\end{aligned}
\tag{8.D.5}
$$

$$
\begin{aligned}
\langle 0|\,\hat{L}^{(1)}\rho\,|2\rangle =&-\frac{1}{2}\,(\lambda_1\sqrt{\gamma_1\,\gamma_2}+\lambda_2\sqrt{\gamma_0\,\gamma_1})\,a^\dagger\,\langle 2|\,\rho\,|2\rangle\\
&+\frac{1}{2}\,\lambda_1\,(\gamma_1-\gamma_0+\Gamma_{11}+\Gamma_{10})\,a^\dagger\,\langle 1|\,\rho\,|2\rangle-\frac{1}{2}\,\lambda_1\sqrt{\gamma_0\,\gamma_1}\,a^\dagger\,\langle 0|\,\rho\,|2\rangle\\
&-\frac{1}{2}\,\lambda_2\sqrt{\gamma_0\,\gamma_2}\,a\,\langle 1|\,\rho\,|2\rangle-\frac{1}{2}\,\lambda_1\sqrt{\gamma_0\,\gamma_1}\,a\,\langle 0|\,\rho\,|2\rangle\\
&-\frac{1}{2}\,\lambda_2\sqrt{\gamma_1\,\gamma_2}\,\langle 0|\,\rho a^\dagger\,|2\rangle-\frac{1}{2}\,\lambda_1\sqrt{\gamma_0\,\gamma_2}\,\langle 0|\,\rho a\,|1\rangle\\
&-\frac{1}{2}\,\lambda_2\,(\gamma_2-\gamma_1+\Gamma_{22}+\Gamma_{21}-\Gamma_{11}-\Gamma_{10})\,\langle 0|\,\rho a^\dagger\,|1\rangle\\
&-\frac{1}{2}\,(\lambda_1\sqrt{\gamma_1\,\gamma_2}+\lambda_2\sqrt{\gamma_0\,\gamma_1})\,\langle 0|\,\rho a^\dagger\,|0\rangle-\frac{1}{2}\,\lambda_2\sqrt{\gamma_1\,\gamma_2}\,\langle 0|\,\rho a\,|2\rangle\,.
\end{aligned}
\tag{8.D.6}
$$

The matrix elements were calculated with a MAXIMA script that is available in the GitLab repository [148]. We used $\eta_{ij}=(-1)^{i+j}$ in the course of obtaining Eqs. (8.D.1)–(8.D.6). Unlike the approach of Sec. 5, here we do not find the $\hat{L}^{(1)}$ matrix elements with $|\mathrm{m}\rangle$. Probability of the detector click can be obtained as $P=1-\sum_{N=0}^{\infty}(\rho_{N\,0,N\,0}+\rho_{N\,1,N\,1}+\rho_{N\,2,N\,2})$. One can then obtain the rate equations as described in Sec. 4.

However, there is no need to do that in practice. The superoperator $\hat{L}$ as given by the equations (8.C.12) contains the rapidly-oscillating terms like the one proportional to $\sqrt{\gamma_0\gamma_2}|0\rangle a^\dagger\langle 2|\rho|0\rangle\langle 0|$. We consider the case when the tunneling rates are orders of magnitude smaller than the JPM level separation (see Table 8.2). In that case, the rapidly-oscillating terms can be neglected. Then one arrives at the Lindblad superoperator as given by Eq. (8.B.1) and the subsequent equations. This approximation can be done one step earlier, as discussed in Appendix C. Note also that, as explained in Sec. 2.2, the JPM does not work under the conditions we expect the Ping-Li-Gurvitz tunneling to occur.

Chapter IX

Conclusion

The thesis has considered several methods of dispersive readout, measurement-induced qubit decoherence, and a photon-number resolving detector of microwave photons. We have also provided some background theory relevant to the field.

Chs. II–III derive the results which are known in literature, albeit with original self-containing methods. In Ch. II, we have quantized a semi-infinite waveguide connected to a resonator, which is a part of the system that is used for dispersive readout of a superconducting qubit. Ch. III presents the full Hamiltonian of the system in the RWA, for the case of continuous coherent radiation incident on the cavity. The model is used to determine the quadratures of the radiation transmitted through the cavity. When performing a dispersive readout with a homodyne detection, it is these quadratures which are monitored to infer the state of the qubit. The Hamiltonian of Ch. III is used in Chs. IV and V.

In Chs. IV and VII, we have considered some schemes of dispersive readout that use a photodetector. Ch. IV considers a readout with a continuous coherent radiation and an ideally photon-number-resolving detector. The readout is optimized using the two figures of merit: SNR and the readout contrast. During the readout process, the cavity resonance gets shifted depending on the qubit state (ground or excited). One can probe the cavity with coherent radiation at the frequency that is resonant for the qubit in the excited state. Then if the qubit is excited, large amount of photons gets transmitted through the cavity, and very few photons are transmitted otherwise. However, to obtain the maximal SNR in the difference in photon counts between the qubit states, one should detune the probe from the resonance. Other optimal parameters also exhibit non-trivial dependence on each other, as discussed in Sec. IV.6. We have found that it is enough to maximize the SNR to achieve a close-to-the-best contrast for most practical purposes. Ch. VII considers a readout with a Fock pulse and a vacuum detector. To achieve better readout contrasts, we use the parameters that invalidate the RWA; hence we provide a description of the readout that is valid beyond the RWA. In Ch. VI, we provide a theory of the Fock pulse transport through the cavity-qubit system beyond the RWA in the dispersive approximation. With a Fock pulse, there is no shot noise in the transmitted radiation and hence no associated measurement error—unlike the standard schemes that use a coherent probe. The readout error in that case is due to the unwanted reflection of a photon in resonance with the cavity and transmission of an off-resonant photon. These processes occur due to finite linewidths of the cavity resonance and the photon. Despite the absence of shot noise in the probe, the single-photon readout performance is behind that of standard schemes, where tens of photons are used in the probe. Some possibilities to improve the readout are discussed in Sec. VII.6. It might be interesting to study the use of several-photon Fock pulses.

Ch. V considers an effect of the cavity thermal photons on the measurement-induced qubit decoherence. We have considered a qubit that is read out dispersively

with a coherent radiation. As the qubit frequency depends on the cavity photon number, its fluctuations—both thermal and the shot noise fluctuations—cause qubit decoherence. We obtain a simple formula valid for the weak measurement regime, that is, when the dispersive shift of the cavity due to the interaction with the qubit is much smaller than the cavity decay rate. For n_b thermal photons in the cavity, the decoherence rate grows proportionally to $n_\mathrm{b} + 1/2$ when n_b is small. We have used a physically motivated approximation regarding time ordering in the weak measurement limit. It might be worth proving this approximation in the future. Note that in the case of a Fock-state probe, there is no photon shot noise in the cavity. The qubit decoherence in that case is due to the process of photodetection and might be interesting to study.

In Ch. VIII, we have proposed a JPM that is able to count microwave photons up to two. It can be used in a scheme of dispersive readout from Ch. IV, where the ability to count photons starts to matter if one aims at fidelities of about 73% and higher. The detector uses a two-photon transition through an intermediate level to test for the states with two and more photons. The main limiting factors for the JPM performance are the anharmonicity of its potential (the bigger the anharmonicity the better) and the rate of non-radiative decay (the less the decay rate the better). It might be possible to design a much faster two-photon JPM by using a Josephson nonlinearity in the JPM-photon coupling. Our preliminary calculations show that such a nonlinearity allows for fast two-photon transitions. If this can be scaled to higher multi-photon processes, a JPM may arise that is able to count photons up to three or four. Also, with use of a capture cavity, the JPM can be utilized to count flying photons. As discussed in Sec. VIII.9, other possibilities to do that are not practical. Beside, we discuss the idea to load photons to the counting JPM with Rabi oscillations and the idea to extend the original JPM to count higher photon numbers with multi-photon transitions via intermediate levels—both ideas have been found unpractical.

Bibliography

[1] Y.-F. Chen, D. Hover, S. Sendelbach, L. Maurer, S. T. Merkel, E. J. Pritchett, F. K. Wilhelm, and R. McDermott, Phys. Rev. Lett. **107**, 217401 (2011).

[2] A. Opremcak, I. V. Pechenezhskiy, C. Howington, B. G. Christensen, M. A. Beck, E. Leonard, J. Suttle, C. Wilen, K. N. Nesterov, G. J. Ribeill, T. Thorbeck, F. Schlenker, M. G. Vavilov, B. L. T. Plourde, and R. McDermott, Science **361**, 1239 (2018).

[3] M. H. Devoret, in *Quantum Fluctuations* (Elsevier, New York, 1997) Chap. 10.

[4] P. A. M. Dirac, *The principles of quantum mechanics* (Oxford university press, 1981).

[5] T. Niemczyk, *From strong to ultrastrong coupling in circuit QED architectures*, Ph.D. thesis, Technische Univ. München (2011).

[6] B. D. Josephson, Phys. Lett. **1**, 251 (1962).

[7] E. M. Lifshitz and L. P. Pitaevskii, *Statistical physics: theory of the condensed state*, Vol. 9 (Elsevier, 2013).

[8] A. A. Golubov, M. Y. Kupriyanov, and E. Il'ichev, Rev. Mod. Phys. **76**, 411 (2004).

[9] S. Shapiro, Phys. Rev. Lett. **11**, 80 (1963).

[10] R. Feynman, R. Leighton, and M. Sands, *The Feynman Lectures on Physics Vol. III* (Addison-Wesley Publ. Comp, New York, 1965) current version is available online at `https://www.feynmanlectures.caltech.edu/III_toc.html`.

[11] A. Barone and G. Paterno, *Physics and applications of the Josephson effect* (Wiley, 1982).

[12] J. Clarke and A. Braginski, *The SQUID Handbook* (John Wiley & Sons, Ltd, 2004).

[13] D. Cardwell, D. Larbalestier, and A. Braginski, eds., *Handbook of Superconductivity: Characterization and Applications, Volume Three*, 2nd ed. (CRC Press, 2021).

[14] G. P. Berman, A. R. Bishop, A. A. Chumak, D. Kinion, and V. I. Tsifrinovich, arXiv:0912.3791 (2009).

[15] M. O. Scully and M. S. Zubairy, *Quantum Optics* (Cambrisge University Press, Cambridge, 1997).

[16] B. R. Mollow, Phys. Rev. A **12**, 1919 (1975).

[17] C. Flühmann, T. L. Nguyen, M. Marinelli, V. Negnevitsky, K. Mehta, and J. P. Home, Nature **566**, 513 (2019).

[18] J. Clarke and F. K. Wilhelm, Nature **453**, 1031 (2008).

[19] A. Blais, R.-S. Huang, A. Wallraff, S. M. Girvin, and R. J. Schoelkopf, Phys. Rev. A **69**, 062320 (2004).

[20] M. Bamba and T. Ogawa, Phys. Rev. A **89**, 023817 (2014).

[21] M. Boissonneault, J. M. Gambetta, and A. Blais, Phys. Rev. A **79**, 013819 (2009).

[22] P. Carbonaro, G. Compagno, and F. Persico, Phys. Lett. A **73**, 97 (1979).

[23] D. Braak, Phys. Rev. Lett. **107**, 100401 (2011).

[24] D. P. DiVincenzo, Fortschr. Phys. **48**, 771 (2000).

[25] M. A. Nielsen and I. L. Chuang, *Quantum computation and quantum information* (Cambridge University Press, 2010).

[26] V. B. Braginsky and F. Y. Khalili, Rev. Mod. Phys. **68**, 1 (1996).

[27] G. P. Berman and A. A. Chumak, Phys. Rev. A **83**, 042322 (2011).

[28] E. A. Sete, J. M. Gambetta, and A. N. Korotkov, Phys. Rev. B **89**, 104516 (2014).

[29] A. M. Sokolov and E. V. Stolyarov, Phys. Rev. A **101**, 042306 (2020).

[30] D. M. Pozar, *Microwave engineering* (John Wiley & Sons, 2009).

[31] D. I. Schuster, *Circuit quantum electrodynamics*, Ph.D. thesis, Yale University (2007).

[32] E. Jeffrey, D. Sank, J. Y. Mutus, T. C. White, J. Kelly, R. Barends, Y. Chen, Z. Chen, B. Chiaro, A. Dunsworth, A. Megrant, P. J. J. O'Malley, C. Neill, P. Roushan, A. Vainsencher, J. Wenner, A. N. Cleland, and J. M. Martinis, Phys. Rev. Lett. **112**, 190504 (2014).

[33] A. A. Clerk, M. H. Devoret, S. M. Girvin, F. Marquardt, and R. J. Schoelkopf, Rev. Mod. Phys. **82**, 1155 (2010).

[34] A. Roy and M. Devoret, Phys. Rev. B **98**, 045405 (2018).

[35] R. Vijay, D. H. Slichter, and I. Siddiqi, Phys. Rev. Lett. **106**, 110502 (2011).

[36] G. de Lange, D. Ristè, M. J. Tiggelman, C. Eichler, L. Tornberg, G. Johansson, A. Wallraff, R. N. Schouten, and L. DiCarlo, Phys. Rev. Lett. **112**, 080501 (2014).

[37] L. C. G. Govia, E. J. Pritchett, C. Xu, B. L. T. Plourde, M. G. Vavilov, F. K. Wilhelm, and R. McDermott, Phys. Rev. A **90**, 062307 (2014).

[38] L. C. G. Govia, E. J. Pritchett, S. T. Merkel, D. Pineau, and F. K. Wilhelm, Phys. Rev. A **86**, 032311 (2012).

[39] C. K. Andersen, G. Oelsner, E. Il'ichev, and K. Mølmer, Phys. Rev. A **89**, 033853 (2014).

[40] B. Peropadre, G. Romero, G. Johansson, C. M. Wilson, E. Solano, and J. J. García-Ripoll, Phys. Rev. A **84**, 063834 (2011).

[41] R. Dassonneville, R. Assouly, T. Peronnin, P. Rouchon, and B. Huard, Phys. Rev. Applied **14**, 044022 (2020).

[42] J.-C. Besse, S. Gasparinetti, M. C. Collodo, T. Walter, P. Kurpiers, M. Pechal, C. Eichler, and A. Wallraff, Phys. Rev. X **8**, 021003 (2018).

[43] J.-C. Besse, S. Gasparinetti, M. C. Collodo, T. Walter, A. Remm, J. Krause, C. Eichler, and A. Wallraff, Phys. Rev. X **10**, 011046 (2020).

[44] B. R. Johnson, M. D. Reed, A. A. Houck, D. I. Schuster, L. S. Bishop, E. Ginossar, J. M. Gambetta, L. DiCarlo, L. Frunzio, S. M. Girvin, and R. J. Schoelkopf, Nat. Phys. **6**, 663 (2010).

[45] K. Inomata, Z. Lin, K. Koshino, W. D. Oliver, J.-S. Tsai, T. Yamamoto, and Y. Nakamura, Nat. Commun. **7**, 12303 (2016).

[46] R. Lescanne, S. Deléglise, E. Albertinale, U. Réglade, T. Capelle, E. Ivanov, T. Jacqmin, Z. Leghtas, and E. Flurin, Phys. Rev. X **10**, 021038 (2020).

[47] G. Oelsner, C. K. Andersen, M. Rehák, M. Schmelz, S. Anders, M. Grajcar, U. Hübner, K. Mølmer, and E. Il'ichev, Phys. Rev. Applied **7**, 014012 (2017).

[48] G. Oelsner and E. Il'ichev, J. Low Temp. Phys. **192**, 169 (2018).

[49] A. Sokolov, Phys. Rev. A **93**, 032323 (2016).

[50] J. Gambetta, W. A. Braff, A. Wallraff, S. M. Girvin, and R. J. Schoelkopf, Phys. Rev. A **76**, 012325 (2007).

[51] T. Walter, P. Kurpiers, S. Gasparinetti, P. Magnard, A. Potočnik, Y. Salathé, M. Pechal, M. Mondal, M. Oppliger, C. Eichler, and A. Wallraff, Phys. Rev. Applied **7**, 054020 (2017).

[52] J. E. Johnson, E. M. Hoskinson, C. Macklin, D. H. Slichter, I. Siddiqi, and J. Clarke, Phys. Rev. B **84**, 220503(R) (2011).

[53] B. Fan, G. Johansson, J. Combes, G. J. Milburn, and T. M. Stace, Phys. Rev. B **90**, 035132 (2014).

[54] A. Poudel, R. McDermott, and M. G. Vavilov, Phys. Rev. B **86**, 174506 (2012).

[55] B. Yurke and J. S. Denker, Phys. Rev. A **29**, 1419 (1984).

[56] A. A. Clerk, M. H. Devoret, S. M. Girvin, F. Marquardt, and R. J. Schoelkopf, arXiv:0810.4729 (2010), see also the Supplemental material to Ref. [33].

[57] C. W. Gardiner and M. J. Collett, Phys. Rev. A **31**, 3761 (1985).

[58] G. Lindblad, Commun. Math. Phys. **48**, 119 (1976).

[59] P. K. Schuhmacher, *Decoherene as a Resource for Quantum Information*, Ph.D. thesis, Universität des Saarlandes (2021).

[60] H.-P. Breuer and F. Petruccione, *The theory of open quantum systems* (Oxford University Press, New York, 2002).

[61] A. Ishizaki and G. R. Fleming, J. Chem. Phys. **130**, 234110 (2009).

[62] M. Malekakhlagh and H. E. Türeci, Phys. Rev. A **93**, 012120 (2016).

[63] J. Bourassa, J. M. Gambetta, A. A. Abdumalikov, O. Astafiev, Y. Nakamura, and A. Blais, Phys. Rev. A **80**, 032109 (2009).

[64] R.-S. Huang, *Qubit-resonator system as an application to quantum computation*, Ph.D. thesis, Indiana University (2004).

[65] S. Schlör, J. Lisenfeld, C. Müller, A. Bilmes, A. Schneider, D. P. Pappas, A. V. Ustinov, and M. Weides, Phys. Rev. Lett. **123**, 190502 (2019).

[66] J. J. Burnett, A. Bengtsson, M. Scigliuzzo, D. Niepce, M. Kudra, P. Delsing, and J. Bylander, npj Quantum Information **5**, 54 (2019).

[67] K. J. Blow, R. Loudon, S. J. D. Phoenix, and T. J. Shepherd, Phys. Rev. A **42**, 4102 (1990).

[68] M. Boissonneault, J. M. Gambetta, and A. Blais, Phys. Rev. A **77**, 060305 (2008).

[69] G. P. Berman, A. A. Chumak, and V. I. Tsifrinovich, J. Low Temp. Phys. **170**, 172 (2013).

[70] J. M. Martinis, S. Nam, J. Aumentado, K. M. Lang, and C. Urbina, Phys. Rev. B **67**, 094510 (2003).

[71] R. Bianchetti, S. Filipp, M. Baur, J. M. Fink, M. Göppl, P. J. Leek, L. Steffen, A. Blais, and A. Wallraff, Phys. Rev. A **80**, 043840 (2009).

[72] С. Ахманов, Ю. Дьяков, and А. Чиркин, *Введение в статистическую радиофизику и оптику* (Наука. Гл. ред. физ.-мат. лит., М., 1981).

[73] O. Chumak and N. Sushkova, Ukr. J. Phys. **57**, 30 (2012).

[74] O. O. Chumak and E. V. Stolyarov, Phys. Rev. A **88**, 013855 (2013).

[75] P. L. Kelley and W. H. Kleiner, Phys. Rev. **136**, A316 (1964).

[76] L. Mandel and E. Wolf, *Optical coherence and quantum optics* (Cambridge University Press, 1995).

[77] W. Vogel and D.-G. Welsch, *Quantum Optics* (John Wiley & Sons, Ltd, 2006).

[78] C. Müller, J. Lisenfeld, A. Shnirman, and S. Poletto, Phys. Rev. B **92**, 035442 (2015).

[79] J. Gambetta, A. Blais, D. I. Schuster, A. Wallraff, L. Frunzio, J. Majer, M. H. Devoret, S. M. Girvin, and R. J. Schoelkopf, Phys. Rev. A **74**, 042318 (2006).

[80] A. A. Clerk and D. W. Utami, Phys. Rev. A **75**, 042302 (2007).

[81] J. Gambetta, A. Blais, M. Boissonneault, A. A. Houck, D. I. Schuster, and S. M. Girvin, Phys. Rev. A **77**, 012112 (2008).

[82] A. M. Sokolov, GIT repository at `https://gitlab.com/matan-bebop/steady` (2016), accessed 4 Jan. 2024.

[83] K. Hennessy, A. Badolato, M. Winger, D. Gerace, M. Atatüre, S. Gulde, S. Fält, E. L. Hu, and A. Imamoğlu, Nature **445**, 896 (2007).

[84] F. Brennecke, T. Donner, S. Ritter, T. Bourdel, M. Köhl, and T. Esslinger, Nature **450**, 268 (2007).

[85] V. Ranjan, G. de Lange, R. Schutjens, T. Debelhoir, J. P. Groen, D. Szombati, D. J. Thoen, T. M. Klapwijk, R. Hanson, and L. DiCarlo, Phys. Rev. Lett. **110**, 067004 (2013).

[86] D. I. Schuster, A. Wallraff, A. Blais, L. Frunzio, R.-S. Huang, J. Majer, S. M. Girvin, and R. J. Schoelkopf, Phys. Rev. Lett. **94**, 123602 (2005).

[87] P. Bertet, I. Chiorescu, C. J. P. M. Harmans, and J. E. Mooij, "Dephasing of a flux-qubit coupled to a harmonic oscillator," (2005), arXiv:cond-mat/0507290 [cond-mat.mes-hall] .

[88] I. Serban, E. Solano, and F. K. Wilhelm, Europhysics Letters **80**, 40011 (2007).

[89] A. A. Clerk and D. W. Utami, Phys. Rev. A **75**, 042302 (2007).

[90] A. M. Sokolov, *Температурна залежність дефазування надпровідного кубіта при дисперсійному вимірюванні*, Master's thesis, National University of Kyiv-Mohyla Academy (2011).

[91] Y. Sung, F. Beaudoin, L. M. Norris, F. Yan, D. K. Kim, J. Y. Qiu, U. von Lüpke, J. L. Yoder, T. P. Orlando, S. Gustavsson, L. Viola, and W. D. Oliver, Nature Communications **10**, 3715 (2019).

[92] L. D. Landau and E. M. Lifshitz, *Statistical Physics: Part 1*, 3rd ed. (Butterworth-Heinemann, New York, 1980).

[93] J. Bylander, S. Gustavsson, F. Yan, F. Yoshihara, K. Harrabi, G. Fitch, D. G. Cory, Y. Nakamura, J.-S. Tsai, and W. D. Oliver, Nature Physics **7**, 565 (2011).

[94] P. J. J. O'Malley, *Superconducting qubits: dephasing and quantum chemistry*, Ph.D. thesis, University of California, Santa Barbara (2016).

[95] S. Stenholm, *Foundations of laser spectroscopy* (John Wiley & Sons, 1984).

[96] O. Chumak, *Квантова оптика* (Євросвіт, Lviv, 2012).

[97] J.-T. Shen and S. Fan, Phys. Rev. A **79**, 023837 (2009).

[98] E. Rephaeli and S. Fan, IEEE J. Sel. Top. Quantum Electron. **18**, 1754 (2012).

[99] D. Oehri, M. Pletyukhov, V. Gritsev, G. Blatter, and S. Schmidt, Phys. Rev. A **91**, 033816 (2015).

[100] Q. Hu, B. Zou, and Y. Zhang, Phys. Rev. A **97**, 033847 (2018).

[101] E. V. Stolyarov, Phys. Rev. A **99**, 023857 (2019).

[102] F. Beaudoin, J. M. Gambetta, and A. Blais, Phys. Rev. A **84**, 043832 (2011).

[103] D. Zueco, G. M. Reuther, S. Kohler, and P. Hänggi, Phys. Rev. A **80**, 033846 (2009).

[104] P. Forn-Díaz, J. J. García-Ripoll, B. Peropadre, J.-L. Orgiazzi, M. A. Yurtalan, R. Belyansky, C. M. Wilson, and A. Lupascu, Nat. Phys. **13**, 39 (2016).

[105] E. V. Stolyarov, *Транспорт фотонів у одновимірних хвилеводах та неадіабатична молекулярна динаміка*, Ph.D. thesis, Institute of Physics of the National Academy of Sciences of Ukraine, Kyiv (2020).

[106] S. Barzanjeh, D. P. DiVincenzo, and B. M. Terhal, Phys. Rev. B **90**, 134515 (2014).

[107] N. Didier, A. Kamal, W. D. Oliver, A. Blais, and A. A. Clerk, Phys. Rev. Lett. **115**, 093604 (2015).

[108] Z. H. Peng, S. E. de Graaf, J. S. Tsai, and O. V. Astafiev, Nat. Commun. **7**, 12588 (2016).

[109] P. Forn-Díaz, J. Lisenfeld, D. Marcos, J. J. García-Ripoll, E. Solano, C. J. P. M. Harmans, and J. E. Mooij, Phys. Rev. Lett. **105**, 237001 (2010).

[110] U. Fano, Phys. Rev. **124**, 1866 (1961).

[111] U. Fano, Il Nuovo Cimento (1924-1942) **12**, 154 (1935).

[112] P. W. Anderson, Phys. Rev. **124**, 41 (1961).

[113] M. Schöndorf, L. C. G. Govia, M. G. Vavilov, R. McDermott, and F. K. Wilhelm, Quantum Sci. Technol. **3**, 024009 (2018).

[114] N. Trautmann and G. Alber, Phys. Rev. A **93**, 053807 (2016).

[115] C. Rigetti, J. M. Gambetta, S. Poletto, B. L. T. Plourde, J. M. Chow, A. D. Córcoles, J. A. Smolin, S. T. Merkel, J. R. Rozen, G. A. Keefe, M. B. Rothwell, M. B. Ketchen, and M. Steffen, Phys. Rev. B **86**, 100506(R) (2012).

[116] H. Paik, A. Mezzacapo, M. Sandberg, D. T. McClure, B. Abdo, A. D. Córcoles, O. Dial, D. F. Bogorin, B. L. T. Plourde, M. Steffen, A. W. Cross, J. M. Gambetta, and J. M. Chow, Phys. Rev. Lett. **117**, 250502 (2016).

[117] F. Yan, S. Gustavsson, A. Kamal, J. Birenbaum, A. P. Sears, D. Hover, T. J. Gudmundsen, D. Rosenberg, G. Samach, S. Weber, J. L. Yoder, T. P. Orlando, J. Clarke, A. J. Kerman, and W. D. Oliver, Nat. Commun. **7**, 12964 (2016).

[118] C. Wang, X. Li, H. Xu, Z. Li, J. Wang, Z. Yang, Z. Mi, X. Liang, T. Su, C. Yang, G. Wang, W. Wang, Y. Li, M. Chen, C. Li, K. Linghu, J. Han, Y. Zhang, Y. Feng, Y. Song, T. Ma, J. Zhang, R. Wang, P. Zhao, W. Liu, G. Xue, Y. Jin, and H. Yu, npj Quantum Inf. **8**, 3 (2022).

[119] B. J. Chapman, E. I. Rosenthal, J. Kerckhoff, B. A. Moores, L. R. Vale, J. A. B. Mates, G. C. Hilton, K. Lalumière, A. Blais, and K. W. Lehnert, Phys. Rev. X **7**, 041043 (2017).

[120] A. C. Mahoney, J. I. Colless, S. J. Pauka, J. M. Hornibrook, J. D. Watson, G. C. Gardner, M. J. Manfra, A. C. Doherty, and D. J. Reilly, Phys. Rev. X **7**, 011007 (2017).

[121] N. R. Bernier, L. D. Tóth, A. Koottandavida, M. A. Ioannou, D. Malz, A. Nunnenkamp, A. K. Feofanov, and T. J. Kippenberg, Nat. Commun. **8**, 604 (2017).

[122] P. Forn-Díaz, C. W. Warren, C. W. S. Chang, A. M. Vadiraj, and C. M. Wilson, Phys. Rev. Applied **8**, 054015 (2017).

[123] V. K. Kaplunenko and A. V. Ustinov, Eur. Phys. J. B **38**, 3 (2004).

[124] P. J. Liebermann and F. K. Wilhelm, Phys. Rev. Applied **6**, 024022 (2016).

[125] N. V. Klenov, A. V. Kuznetsov, I. I. Soloviev, S. V. Bakurskiy, M. V. Denisenko, and A. M. Satanin, Low Temp. Phys. **43**, 789 (2017).

[126] R. McDermott and M. G. Vavilov, Phys. Rev. Applied **2**, 014007 (2014).

[127] J. Q. You and F. Nori, Nature **474**, 589 (2011).

[128] P. Forn-Díaz, L. Lamata, E. Rico, J. Kono, and E. Solano, Rev. Mod. Phys. **91**, 025005 (2019).

[129] A. Frisk Kockum, A. Miranowicz, S. De Liberato, S. Savasta, and F. Nori, Nat. Rev. Phys. **1**, 19 (2019).

[130] F. Wilhelm, R. Steinwandt, B. Langenberg, P. Liebermann, A. Messinger, and P. Schuhmacher, *Entwicklungsstand Quantencomputer*, Tech. Rep. (Federal Office for Information Security, Bonn, Germany, 2018) in English.

[131] A. L. Grimsmo, B. Royer, J. M. Kreikebaum, Y. Ye, K. O'Brien, I. Siddiqi, and A. Blais, Phys. Rev. Appl. **15**, 034074 (2021).

[132] I. Iakoupov, Y. Matsuzaki, W. J. Munro, and S. Saito, Phys. Rev. Research **2**, 033238 (2020).

[133] R. McDermott, M. G. Vavilov, B. L. T. Plourde, F. K. Wilhelm, P. J. Liebermann, O. A. Mukhanov, and T. A. Ohki, Quantum Sci. Technol. **3**, 024004 (2018).

[134] M. P. V. Stenberg, K. Pack, and F. K. Wilhelm, Phys. Rev. A **92**, 063852 (2015).

[135] A. Opremcak, C. H. Liu, C. Wilen, K. Okubo, B. G. Christensen, D. Sank, T. C. White, A. Vainsencher, M. Giustina, A. Megrant, B. Burkett, B. L. T. Plourde, and R. McDermott, Phys. Rev. X **11**, 011027 (2021).

[136] C. Wittmann, U. L. Andersen, M. Takeoka, D. Sych, and G. Leuchs, Phys. Rev. A **81**, 062338 (2010).

[137] R. H. Hadfield, M. J. Stevens, S. S. Gruber, A. J. Miller, R. E. Schwall, R. P. Mirin, and S. W. Nam, Opt. Express **13**, 10846 (2005).

[138] C. J. Howington, *Digital Readout and Control of a Superconducting Qubit*, Ph.D. thesis, Syracuse University (2019).

[139] D. V. Anghel, K. Kulikov, Y. M. Galperin, and L. S. Kuzmin, Phys. Rev. B **101**, 024511 (2020).

[140] A. M. Sokolov and F. K. Wilhelm, Phys. Rev. Applied **14**, 064063 (2020).

[141] J. Ping, X.-Q. Li, and S. Gurvitz, Phys. Rev. A **83**, 042112 (2011).

[142] G. Zhu, D. G. Ferguson, V. E. Manucharyan, and J. Koch, Phys. Rev. B **87**, 024510 (2013).

[143] M. Alexanian and S. K. Bose, Phys. Rev. A **52**, 2218 (1995).

[144] Y. Wu, Phys. Rev. A **54**, 1586 (1996).

[145] J. M. Martinis, K. B. Cooper, R. McDermott, M. Steffen, M. Ansmann, K. D. Osborn, K. Cicak, S. Oh, D. P. Pappas, R. W. Simmonds, and C. C. Yu, Phys. Rev. Lett. **95**, 210503 (2005).

[146] L. D. Landau and E. Lifshits, *Quantum Mechanics: Non-Relativistic Theory* (Butterworth-Heinemann, New York, 1991).

[147] F. W. Strauch, *Theory of superconducting phase qubits*, Ph.D. thesis, University of Maryland (2004).

[148] A. M. Sokolov and F. Wilhelm-Mauch, GIT repository at `https://gitlab.com/matan-bebop/jpm` (2020), accessed 4 Jan. 2024.